Plumes of Enceladus

Understanding Plume Variability of Enceladus by CFD Experiments

Sebastian Oliver Scholts

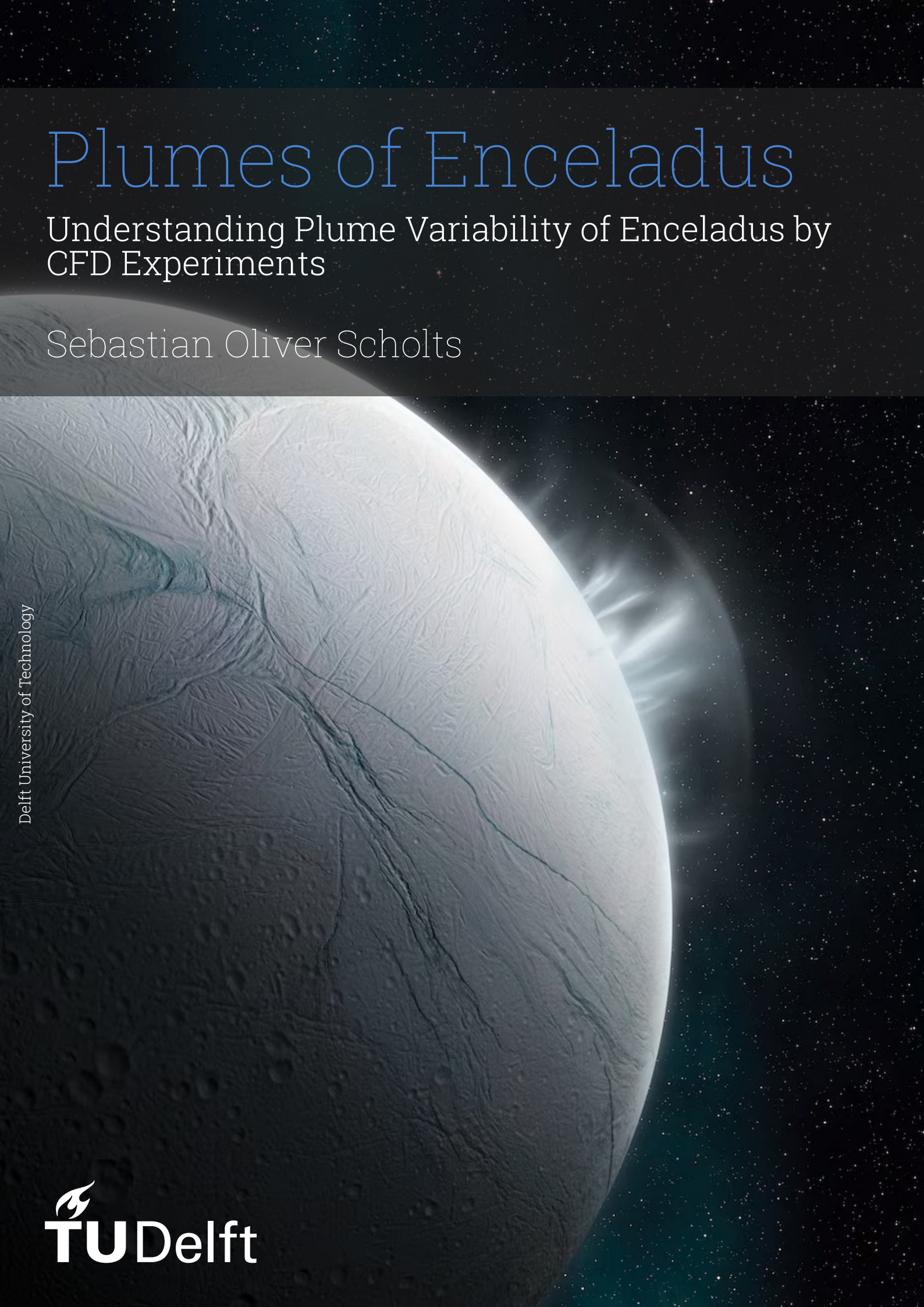

Delft University of Technology

TU Delft

Plumes of Enceladus

Understanding Plume Variability of Enceladus by CFD Experiments

by

Sebastian Oliver Scholts

to obtain the degree of Master of Science
at the Delft University of Technology,
to be defended publicly on September 26th, 2025 at 13:00.

Student number: 4547330
Supervisors: S. M. Cazaux, F.F.J. Schrijer
Project Date: November, 2024
Faculty: Faculty of Aerospace Engineering, Delft

Cover Image: Illustration of vapour plumes erupting from the surface of Enceladus by Tobias Roetsch/Future

TU Delft

Preface

This thesis report presents the research titled ”Understanding plume variability of Enceladus by CFD experiments” for the MSc in Space Exploration at the faculty of Aerospace Engineering at Delft University of Technology. This project marks the final chapter of my student life in Delft and sets the beginning of my professional career as an Aerospace Engineer.

First and foremost, I would like to express my sincere gratitude and thanks to my supervisors Professor Stéphanie Cazaux and Professor Ferry Schrijer who both introduced me to the topic of the plumes of Enceladus. Their expertise and guidance has been invaluable during our many weekly meetings, as well as introducing me to other professors and researchers to aid in my research. Although our weekly meetings were productive with the work that I had done, it was also nice to chat with Stéphanie and Ferry about what we did during our weekends and holidays.

I would also like to thank Professor Isabelle Steinke and Professor George Kelesidis on their knowledge and advice on ice nucleation. In addition, I would like to thank Professor Marc Naeije for giving me access to the TU Delft Aerospace Engineering’s Eudoxos server to run my OpenFOAM simulations. My thanks also goes to my predecessor Tomás Fontes and all of the other students who have come before me researching the modelling of Enceladus’ plumes.

During this thesis, I was part of the Plumes research group where we had bi-weekly meetings with other students to show our progress and interesting findings of our research on Enceladus. I would like to thank Stéphanie Cazaux for organising these meetings and Yaël Bourgeois, Tara Bründl, Deepanshu Kamlesh Punjabi, Aïcha van Veen and Tim Mosimann for sharing their thoughts on my work and showing me their exciting research.

Reflecting on my time in Delft, I have made many memories and friends along the way. Many of which I made when I started a full-time year in the Delft Aerospace Rocket Engineering (DARE) dream team as Chief Recovery. I would like to thank everyone in the Stratos IV team for the incredible experience I had during those 2 years. To all of my friends, thank you for being present in my life and enriching it.

I would like to thank my amazing girlfriend Demi for always being there for me and supporting me throughout my thesis. Whether I was having troubles running my simulations or I had to spend countless hours typing away at night, she always knew how to encourage and reassure me.

I could never have made it this far without the love and support of my family. My father David, being an academic has always sparked my curiosity of the world in which we live in. Our many discussions of the universe put me on the path of pursuing a degree in engineering. My mother Ingrid, has always gone out of her way to find any programme, course, or resource in the realm of physics and engineering that I would find interesting. My sister Angelica, someone I greatly admire, has always been there for me, sharing her advice and support in countless ways. Lastly, my family has always fought tooth and nail to ensure I would be able to pursue my dreams, and for that I am eternally grateful.

Sebastian Oliver Scholts
Delft, September 2025

Summary

Saturn's moon Enceladus is one of the most geologically active bodies in the Solar System. Since Cassini's discovery of towering plumes of water vapour and ice grains in 2005, Enceladus has become a central target in planetary science due to the possibility of a subsurface ocean and conditions favourable for life. While tidal stresses can explain daily and decadal variations in plume activity, Cassini observations also revealed short-term, aperiodic variability that remains unexplained. A leading hypothesis is that deposition, accretion, and sublimation of ice within subsurface fractures modulate vent geometry and thereby influence plume behaviour. This thesis addresses the question: can temporal variations in Enceladus' plume activity be explained by ice–wall interactions within the cracks?

To investigate this, a two-dimensional, two-phase computational fluid dynamics (CFD) framework was developed by extending a Wet Steam Model in OpenFOAM. The model incorporates non-equilibrium nucleation, grain growth, wall accretion, and wall sublimation, enabling the simulation of coupled plume–wall dynamics. A series of parametric studies were performed across representative geometries, including convergent–divergent channels and multi-throat channels, under varying wall temperature conditions.

The results demonstrate that channel geometry exerts a first-order control on plume dynamics. Convergent–divergent channels facilitate supersonic expansion, enhancing nucleation rates and grain production, while multi-throat channels introduce localised compression–expansion zones where nucleation preferentially occurs at the throats. The ratio of exit to throat area (A_e/A^*) strongly influences both nucleation and grain growth. Furthermore, the location of the throat within the channel dictates where particles form and evolve.

Wall interactions were found to drive significant temporal changes in channel geometry. Accretion progressively narrows channels, particularly at the inlet and throat, increasing the exit-to-throat area ratio, accelerating outflow velocities, and enhancing nucleation while reducing particle growth. Sublimation, in contrast, widens channels, decreases supersaturation, and can shift throat locations downstream. The interplay between accretion and sublimation is highly sensitive to wall temperature profiles, determining whether vents evolve toward closure or widening over time.

When compared to Cassini observations, the model reproduces aspects of aperiodic plume variability. Specifically, vent narrowing due to accretion corresponds to the observed decay in plume brightness during late August 2017. The preceding rise in plume brightness is not captured directly by mass flux, but may be explained by sublimation-driven widening based on a more complex channel wall temperature profile.

Overall, this thesis provides evidence that wall accretion and sublimation within subsurface cracks are capable of modulating vent geometry and influencing plume dynamics. While these processes alone may not fully reproduce all aspects of Enceladus' plume variability, they represent a fundamental mechanism contributing to observed short-term changes. The findings provide a framework for future studies incorporating more realistic wall temperature profiles, transient heating to further elucidate the drivers of Enceladus' enigmatic plumes.

Contents

List of Figures

List of Tables

Nomenclature

BD	Becker–Döring nucleation theory
CDA	Cosmic Dust Analyser
CFD	Computational Fluid Dynamics
CFL	Courant–Friedrichs–Lewy condition
CNT	Classical Nucleation Theory
INMS	Ion and Neutral Mass Spectrometer
ISS	Imaging Science Subsystem
RMS	Root Mean Square (error metric)
SPT	South Polar Terrain
UVIS	Ultraviolet Imaging Spectrograph
VIMS	Visual and Infrared Mapping Spectrometer
α	Interpolation weight factor
$\bar{r}$	Average droplet/grain radius
$\Delta\mu$	Change in chemical potential
ΔG	Change in total Gibbs free energy
ΔG^*	Critical Gibbs free energy barrier
ΔG_s	Gibbs free energy contribution from surface term
Δg_s	Gibbs free energy change per unit surface
ΔG_T	Change in total Gibbs free energy
ΔG_v	Gibbs free energy contribution from volume term
Δg_v	Gibbs free energy change per unit volume
ΔG_{hete}	Change in Gibbs free energy from heterogeneous nucleation
ΔG_{homo}	Change in Gibbs free energy from homogeneous nucleation
ΔH	Change in total enthalpy
ΔH_{dep}	Latent heat of deposition
Δh_{dep}	Specific enthalpy of deposition
Δh_{free}	Specific enthalpy of freezing
Δh_{vap}	Specific enthalpy of vaporisation
ΔS	Change in total entropy
Δt	Time interval
Δx	Cell length
δ_{ij}	Kronecker delta function
$\dot{E}_{tidal}$	Tidal heating rate
$\dot{m}$	Mass flux of impinging vapour molecules
$\dot{m}_a$	Accreted mass flux at wall
$\dot{m}_l$	Mass flow rate of liquid phase
$\dot{m}_s$	Sublimation mass flux at wall
$\dot{m}_{flow}$	Mass flow rate of gaseous phase
ϵ	Machine precision
γ	Specific heat ratio
γ_{IL}	Surface tension of liquid–surface interface
γ_{SI}	Surface tension of solid–surface interface
γ_{SL}	Surface tension of solid–liquid interface
λ_v	Mean free path of vapour molecules
λ_{H_2O}	Mean free path of water vapour
$\mathbf{S}_f$	Surface area vector
RMS	Root Mean Square error
μ	Dynamic viscosity
∇	Del operator
ν	Pre-exponential factor
ν	Convective heat transfer modelling correction factor
Ω	Orbital frequency
∂	Partial differential
ϕ_f	Volumetric flux
ψ	Kantrowitz's non-isothermal correction factor
ρ_i	Density of ice
ρ_l	Density of liquid

ρ_v	Density of vapour
$\rho_{eq}^{(l,v)}$	Vapour-liquid equilibrium density
$\rho_{eq}^{(l,v)}$	Vapour–liquid equilibrium density
$\sigma_{l,v}$	Surface tension of a liquid droplet in vapour
$\sigma_{s,l}$	Surface tension of the solid-liquid interface
$\sigma_{s,v}$	Surface energy of a solid grain in vapour
τ	Shear stress
τ_{ij}	Shear stress tensor
θ	Wetting angle between nucleus and surface
$\vec{U}$	Fluid velocity vector
ξ	Uniformly distributed random number
A	Interfacial area / projected surface area
A	Local area of a channel
a	Area per molecule
a	Narrowest width of the channel
a	Semi-major axis of Enceladus
a	Tidal axis (longest principal axis)
A^*	Throat area of a channel
A_e	Exit area
A_i	Amplitudes of modes
b	Intermediate equatorial axis
c	Non-isothermal nucleation correction factor
c	Polar axis
c_f	Local speed of sound at a face
c_p	Specific heat capacity at constant pressure
C_r	Average cooling rate
c_{H_2O}	Specific heat capacity of water
Co	Courant number
d	Distance of vapour particle from wall
D_h	Hydraulic diameter
D_{exit}	Diameter of the channel exit
d_{H_2O}	Effective molecular diameter of H_2O
D_{throat}	Diameter of the channel throat
E	Equivalent width (spectral absorption feature)
E	Total energy
e	Orbital eccentricity
E_a	Activation/sublimation energy
f	Solid/mass fraction
f_g	Concentration of g-mers
$f_{accretion}$	Accretion efficiency factor
g	Number of molecules per cluster
g	Surface gravitational acceleration
H	Total enthalpy
h	Spherical-cap height
H_g	Grain enthalpy
H_p	Total enthalpy of a droplet/grain
h_p	Specific enthalpy of a droplet/grain
H_v	Vapour enthalpy
I	Mass flux
I/F	Signal-to-noise ratio (Cassini data)
J	Nucleation rate
J_0	Nucleation rate kinetic prefactor
J_{CNT}	Nucleation rate from CNT
J_{ISO}	Isothermal nucleation rate
J_{NISO}	Non-isothermal nucleation rate
k_2	Tidal Love number
k_i	Wave numbers
k_v	Thermal conductivity
k_{eff}	Effective thermal conductivity
Kn	Knudsen number
Kn_p	Droplet/grain based Knudsen number
L	Channel length
L	Characteristic length
l	Mean free path
L_0	Cut-off length
L_h	Specific enthalpy of vaporisation
M	Mach number

M	Molar mass
m_p	Mass of a nucleated droplet/grain
m_{layer}	Mass of one ice molecular layer
N	Droplet/grain number density
n	Number of cluster molecules
n_1	Number density of monomers
N_A	Avogadro's constant
n_l	Number of liquid droplets
n_{ice}	Surface number density of ice molecules
Nu	Nusselt number
Nu_{Gy}	Gyamathy corrected Nusselt number
P	Perimeter of channel
$p(T)$	Equilibrium vapour pressure at T
p_0	Stagnation/total pressure
$p_\lambda(d)$	Wall collision probability at d
$p_{\lambda,\text{avg}}$	Average wall collision probability
$p_{eq}^{(l,v)}$	Vapour-liquid equilibrium pressure
$p_{eq}^{(l,v)}$	Vapour–liquid equilibrium pressure
p_{gas}	Gas pressure
$p_{sat}^{(s,g)}$	Saturation pressure at solid–vapour interface
Pr	Prandtl number
Q	Heat flux
Q	Tidal dissipation factor
q	Heat addition/removal
q_c	Condensation coefficient
R	Mean radius of Enceladus
r	Radius of droplet/grain
r^*	Critical radius for nucleation
r_a	Apoapsis distance
r_p	Periapsis distance
$r_{sublimation}$	Molecular sublimation rate
$R_{w,a}$	Wall thickness due to accretion
$R_{w,s}$	Wall thickness due to sublimation
S	Supersaturation
$S(\theta)$	Wetting angle function
S_a	Mass source term from accretion
S_a	Sink term due to the mass flux from wall accretion
S_f	Source terms for solid fraction conservation
S_h	Source/sink terms for energy conservation
S_m	Source/sink terms for mass conservation
S_N	Source terms for droplet/grain number conservation
S_s	Mass source term from sublimation
S_s	Source term due to the mass flux from wall sublimation
S_U	Source/sink terms for momentum conservation
S_{stick}	Sticking coefficient
T	Temperature
T_0	Stagnation/total temperature
T_g	Gas temperature
T_p	Temperature of a droplet/grain
T_s	Saturation pressure
T_w	Wilson temperature
t_{act}	Activation time for nucleation
T_{cr}	Critical temperature
$T_{eq}^{(l,v)}$	Liquid–vapour equilibrium temperature
$T_{eq}^{(s,v)}$	Solid–vapour equilibrium temperature
T_{sat}	Equilibrium saturation temperature
T_{wall}	Wall temperature
V	Magnitude of fluid velocity
v	Specific volume
v_{esc}	Escape velocity
V_{th}	Average thermal velocity
v_{th}	Thermal velocity of vapour molecules
Wi	Wilson number
x	Channel local length
y	Channel local height
α	Convective heat transfer modelling parameter
r_0	Size of grain when nucleation occurs
x_0	Location where nucleation occurs
Å	Angstrom

1

Introduction

Icy moons are natural satellites orbiting giant planets in our solar system with surfaces covered with ice. These icy moons are present in the solar system such as Titan, Enceladus, Iapetus, Hyperion, Dione, Rhea, Tethys, and Mimas that orbit Saturn (Farnsworth et al. 2024). In 2005, the Cassini spacecraft made a significant discovery regarding Enceladus, one of Saturn's moons (Spencer et al. 2009). During a close flyby, Cassini observed geysers of water vapour and ice particles erupting from the south polar region of Enceladus (Dotson 2018; Spencer et al. 2009). These plumes suggested the presence of a subsurface ocean beneath the moon's icy crust. Since 2005, many new discoveries have been made of Enceladus thanks to Cassini's instruments. However, there still remains many mysteries surrounding Enceladus and its plumes that are yet to be answered (Dotson 2018). The plumes of Enceladus exhibit temporal variations that are classed into three distinct variations: diurnal variations, decadal variations and aperiodic variations. The diurnal and decadal variations are well understood due to Enceladus experiencing tidal stresses due to Saturn and Dione respectively (Ingersoll et al. 2020). Since Enceladus has a 2:1 mean-motion orbital resonance with Dione, it exhibits a longer timescale compared to the diurnal variations. Lastly, the aperiodic variations are in the order of a $\sim$20 day period and were shown to be due to distinct jets appearing to turn on and off from a list of 2405 images taken from Cassini's Imaging Science Subsystem (ISS). The nature of why these plumes turn off remains a mystery but a leading hypothesis is that ice deposition & sublimation in the cracks could cause these variations, but this remains unproven (Ingersoll et al. 2020).

The literature review that was conducted identified key research gaps in understanding the mechanisms behind Enceladus' plumes, particularly how water from its subsurface ocean travels through cracks and is ejected. Existing models (e.g., quasi-1D and 2D multi-phase) lack proper coupling between the plume flow and wall processes such as wall accretion and sublimation, which may significantly affect the geometry and behaviour of the cracks over time (Fontes 2023). A major unresolved question is the aperiodic, monthly-scale variability in plume activity, which cannot be explained by known tidal effects. This issue is critical for the planning of future missions such as the Enceladus Vent Explorer that plan to explore these cracks directly (Chodas et al. 2023; Konstantinidis et al. 2015). The identified research gaps in plume variability lead to the following main research question.

Can the temporal variations in Enceladus' plume activity be explained by deposition and sublimation of ice in the cracks?

To answer this, a 2D two-phase CFD model was developed by a previous MSc student that incorporated condensation from steam to liquid water with friction and heat convection. This model provided the foundation of this work and was adapted & extended to allow for deposition and incorporated wall accretion and wall sublimation with coupling effects of the plume flow to the channel geometry. In order to answer the main research question, four sub-research questions are proposed.

Creating such a coupled wall interaction model is complex, and a concrete understanding of how the properties of plume flow behaves with different wall geometries is necessary. This forms the basis of the first sub-research question. The adapted 2D multi-phase CFD model will be used to answer

this sub-research question. For this analysis, two different channel geometries will be used such as a convergent-divergent channel, and a channel with multiple geometric throats. The tool is easily adaptable to include other channel geometries. The goal is to analyse different channel geometries and see their effect on plume characteristics.

Q1: How do different channel geometries affect the plume characteristics (velocity, number of particles, solid fraction and average particle size)?

Once the different channel geometries have been analysed, it is necessary to adapt the CFD model to include the coupling wall interactions of wall sublimation and wall accretion. This relates to the second and third sub-research question to investigate how a channel on Enceladus would behave in time when including the coupling wall interaction effects.

Q2: How does the channel geometry change in time due to the coupling between the plume flow and wall accretion?

Q3: How does the channel geometry change in time due to the coupling between the plume flow and wall sublimation?

The goal is to observe whether the geometry of the channels significantly changes in time, if they reach an equilibrium shape or if the channels tend to close completely. The two phenomena of the coupling wall interactions are separated into two research questions to better understand their separate effects on the channel geometry.

The fourth sub-research question is formed to compare the data obtained from Cassini to the results of a CFD simulation that represents the plumes.

Q4: How does a 2D CFD model with wall interactions compare to observations from the Cassini spacecraft?

The goal is to replicate the aperiodic variations data observed by Cassini on June 18th, August 2nd, and August 28th 2017 present in Figure 2.10. This means that the output of the CFD simulation is the mass flow at the vent of the channel as function of time and the final geometry of the channels. This data will then be plotted with Figure 2.10 to see if the behaviour of the curves are identical. The results of this final sub-research question will allow to answer the main research question.

These investigations aim to determine whether ice interactions within the cracks can explain the unexplained monthly plume variability and support mission planning for Enceladus exploration.

This thesis report is separated into eight chapters as is structured as follows. In chapter 2, Enceladus is introduced outlining its characteristics such as its shape, size, surface features, environment, interior, cracks and plume phenomena. In chapter 3, the physical processes that occur in the plumes of Enceladus are explored starting with the foundation of nucleation and phase changes, followed by the viscous effects on flow behaviour and nucleation phenomena in nozzles. The Wet-Steam Model which is the Navier-Stokes equations adapted for two-phase flow with a condensation model is introduced followed by the Icy-Steam model that uses a deposition model. In chapter 4, the theory of two-phase flow of water is described. The wall interactions such as wall accretion and wall sublimation are discussed with an overview of their models that was used. Finally, the methodology behind the coupled wall interactions is described which defines how the tool works and what assumptions were made. In chapter 5, the setup of the CFD model is outlined from the mesh setup, to the solver, scheme selection and boundary & initial conditions. In chapter 6, the models discussed in the preceding sections are verified and validated. In chapter 7, the results for a parametric study of the coupled wall interactions for wall accretion and wall sublimation are presented for the different channel geometries. In chapter 8 an application to Enceladus is made based on the findings of the parametric study. These results are followed by recommendations in chapter 9 that list the improvements and future work that can be done to improve the fidelity of the work. Lastly, in chapter 10, the conclusions of this work are established that tie the results to the main and sub-research question.

2

Enceladus

Enceladus is one of the many natural satellites of Saturn and is the sixth largest moon in the Saturnian system (Brown et al. 2006). In this chapter, an overview of Enceladus and its characteristics is presented with a focus on Enceladus' plumes. In section 2.1, the general background of Enceladus is presented, outlining its key characteristics. In section 2.2, the plumes are further analysed delving into their gas, solid and ion composition, and discussing the temporal variations that the plumes experience.

2.1. General Background

Enceladus was first discovered in 1789 by the German-born British astronomer William Herschel using his 1.2 m diameter, 12 m focal length telescope (Frommert and Kronberg 2013). In 1980 and 1981, Voyager 1 and Voyager 2 missions were the first to fly by Saturn and captured a glimpse of Enceladus and its features. The images revealed various different surface features such as cratered terrain, smooth terrain and fractures (Smith et al. 1982). In 2005, the Cassini spacecraft entered the Saturnian system to study Saturn and its moons (Dougherty et al. 2018). The Cassini spacecraft performed multiple flybys around Enceladus that provided constraints on the internal structure, higher resolution surface features (Spencer et al. 2009). During its first flyby on February 17th 2005, its magnetometer instrument detected a perturbation of Saturn's magnetic field and found an enhanced concentration of water group ions in the vicinity of Enceladus (Dougherty et al. 2018). In successive flybys, the magnetometer detected the presence of a diffuse atmosphere around Enceladus whereas Cassini's Ultraviolet Imaging Spectrograph (UVIS) failed to detect this atmosphere. However, the UVIS did detect water vapour over the south polar region in a subsequent flyby and confirmed that water vapour is escaping Enceladus in the south polar region (Dougherty et al. 2018). A combined analysis of imaging, mass spectrometry, and magnetospheric data from the Cassini mission indicates that the south polar plume originates from pressurised subsurface reservoirs, resembling geysers found on Earth (Porco et al. 2006). When the discovery was made about Enceladus' plumes, the Cassini team centered the focus of Cassini's Extended mission on Enceladus providing a plethora of detailed observations from February 2005 until December 2015 (Dougherty et al. 2018).

Enceladus has a mass of about 1.080318×10^{20} kg and an average radius of about 252.10 km making it Saturn's sixth largest moon (Jacobson 2022). Due to the moon's mass and size, it results in a low surface gravity of 0.113 m/s^2 and has a relatively low escape velocity of just 0.239 km/s (Solar System Exploration 2013). Enceladus' shape is characterised most accurately by a triaxial ellipsoid where a is the tidal axis which faces Saturn, c is the polar axis and b is an intermediate axis. The values for the principal axes were found to be 256.6 ± 0.5 km, 251.4 ± 0.2 km and 248.3 ± 0.2 km for a, b and c respectively by limb measurements captured by the Cassini Image Science Subsystem (ISS) that were then compared to the predicted projected ellipse with knowing the ellipsoid shape, attitude of the camera and its point of view with respect to Enceladus' axes (Thomas et al. 2007).

Enceladus is characterised by a varied and geologically active surface as seen in Figure 2.1. Its terrain includes vast regions of heavily cratered landscapes in the northern hemisphere, contrasting sharply with the smoother, younger surfaces in the south. The surface is divided into distinct geological terrains, each with unique characteristics and histories. The cratered terrain, spanning the Saturn-

facing side over the north pole to the anti-Saturn side, is marked by shallow, bowl-shaped craters—many less than 40 km in diameter suggesting significant viscous relaxation and tectonic alteration (Spencer and Nimmo 2013). Prominent rifts aligned symmetrically around the spin axis and Saturn's direction point to tidal deformation as a formation mechanism. This region is geologically inactive, with an estimated surface age of 1–4 billion years (Kirchoff and Schenk 2009). In contrast, the trailing hemisphere terrain is heavily fractured and shows signs of extensive resurfacing through tectonism, including troughs, ridges, scarps, and grooves. These features, along with possible evidence of past glacial or cryovolcanic activity, indicate a much younger surface aged between 0.01–2 billion years (Spencer and Nimmo 2013). The leading hemisphere terrain is less well-studied, with only about 30% observed in detail. It features relatively smooth plains with ridges and troughs, and retains large, ancient impact craters that show limited modification. These observations suggest that this region contains some of Enceladus' oldest preserved surface features (Crow-Willard and Pappalardo 2015; Spencer et al. 2009).

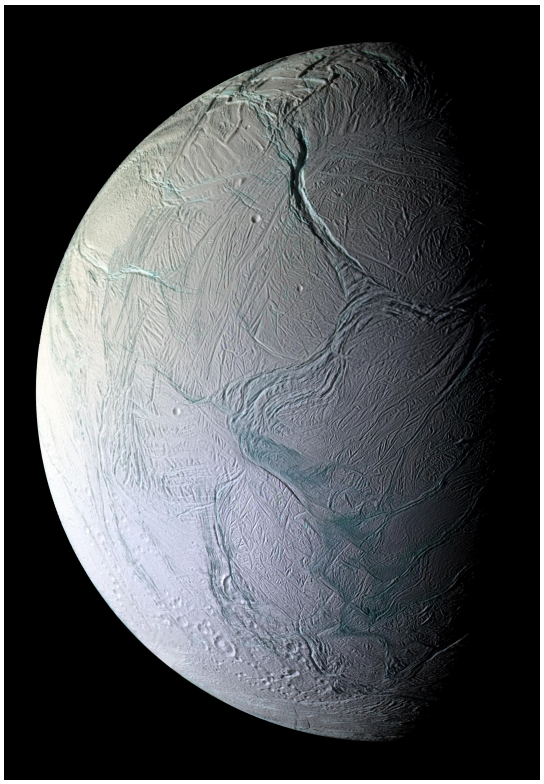

Figure 2.1: Enhanced-color mosaic of Enceladus' southern Saturn-facing hemisphere, captured by Cassini on October 9, 2008, shortly after a close flyby at 25 km altitude. The image reveals a tectonically active surface dominated by fractures, folds, and ridges, with minimal cratered terrain. Blue-green regions indicate areas coated with larger ice grains. Labtayt Sulci, a $\sim$1 km-deep chasm, is prominently visible near the center, while portions of the tiger stripe fractures and surrounding mountainous terrain appear along the lower right terminator (Cassini imaging team 2008)

The most notable region is the South Polar Terrain (SPT) shown in Figure 2.2. The SPT features prominent four distinct "tiger stripes" fissures called Damascus Sulcus, Baghdad Sulcus, Cairo Sulcus and Alexandria Sulcus as seen in Figure 2.2a. It is at these tiger stripes that plumes of water vapour and ice grains are emitted into space (Porco et al. 2006; Spencer et al. 2006). These tiger stripes are about 130 km long and spaced 35 km apart. In Figure 2.2b, the Cairo Sulcus tiger stripe is shown closer in detail, clearly showing the rift in contrast with the surrounding terrain. Enceladus also exhibits an extremely high albedo, making it one of the most reflective bodies in the Solar System, with a Bond albedo close to 0.9, indicating a surface composed primarily of clear water ice (Verbiscer et al. 2007).

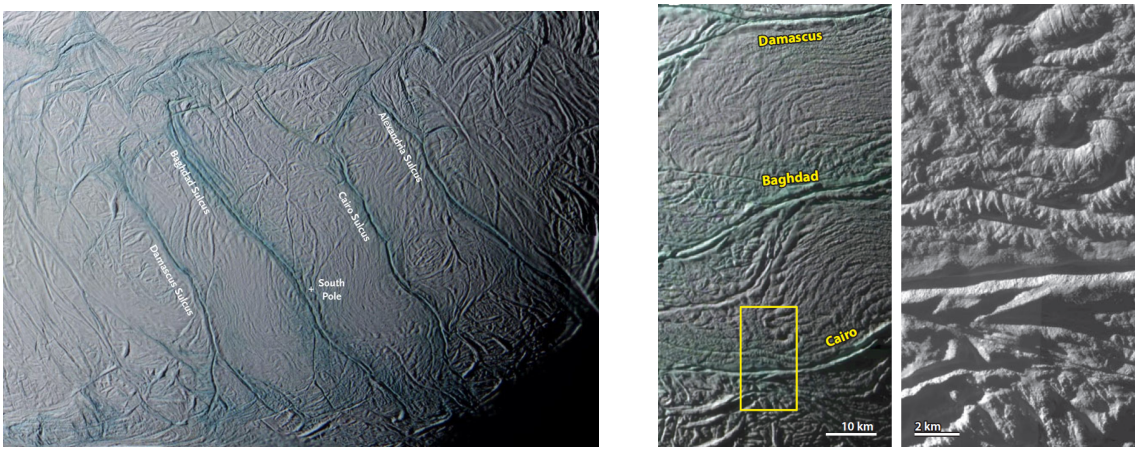

(a) Enhanced colour view of Enceladus' Tiger stripes (Cassini imaging team 2006)

(b) Zoomed-in of Cairo Sulcus and nearby terrain (Spencer and Nimmo 2013)

Figure 2.2: View of Enceladus' South polar region labelled with the four distinct Tiger stripes: Damascus Sulcus, Baghdad Sulcus, Cairo Sulcus and Alexandaria Sulcus showing the distinct terrain features

Enceladus harbours a global subsurface ocean beneath its icy crust, confirmed by gravity measurements and the analysis of plume material ejected from its South Polar Terrain (Hsu et al. 2015; Iess et al. 2014). This ocean, estimated to lie beneath a relatively thin ice shell possibly as little as a few kilometres thick near the south pole makes Enceladus a prime target in the search for extraterrestrial life. However, the source of the energy required to maintain this liquid ocean remains an open question. The amount of heat radiated from the south pole detected by the Cassini spacecraft at approximately 15.8$\pm$3.1 GW far exceeds what can be explained by standard tidal heating models alone (Howett et al. 2011; Spencer et al. 2006). This far exceeds the energy output expected from known internal heating mechanisms. Enceladus' heat is primarily thought to come from two sources: radiogenic heating and tidal heating. Radiogenic heating arises from the decay of radioactive isotopes such as ^{26}Al and ^{60}Fe, contributing an estimated 0.3 GW (Howett et al. 2011; Travis and Schubert 2015).

Tidal heating, on the other hand, is generated by the dissipation of mechanical energy due to tidal forces exerted by Saturn. It can be estimated using Equation 2.1, where Ω, e, R, and R represent Enceladus' orbital frequency, eccentricity, and radius, respectively; G is the gravitational constant; k_2 is the tidal Love number, reflecting Enceladus' internal structure; and Q is the dissipation factor, indicating energy lost per oscillation cycle (Spencer et al. 2009). However, because Ω are poorly constrained, this calculation remains uncertain. Using an estimated of 18,000 based on Mimas' orbital evolution, the upper limit of tidal heating has been calculated to be just 1.1 GW (Spencer et al. 2009), which is still an order of magnitude below the observed heat output.

$$\dot{E}_{\text{tidal}} = -\frac{21}{2}\frac{k_2}{Q}\frac{(\Omega R)^2}{G}e^2 \tag{2.1}$$

Combined, radiogenic and tidal heating account for only about 1.4 GW (Travis and Schubert 2015), leaving a large discrepancy between predicted and observed heat loss. The origin of the excess heat remains speculative. Various models have been proposed, including episodic heat release to explain long-term average output or potential overestimation of the current heat flux (Spencer and Nimmo 2013), but no single explanation fully accounts for the observed thermal output. The most widely supported hypothesis today is that Enceladus possesses a porous, water-permeable silicate core. This porosity increases the core's compressibility and allows ocean water to circulate and heat within the core, enhancing energy dissipation (Neumann and A. 2019; Rovira-Navarro et al. 2022). This model suggests a differentiated internal structure comprising a 185–205 km silicate core, a 4–70 km porous core layer, a global subsurface ocean 10–27 km thick, and an icy outer shell 30–40 km thick (Neumann and A. 2019).

Enceladus plays a central role in maintaining Saturn's diffuse E-ring, a vast torus of microscopic ice particles that extends from about 3 to 8 Saturn radii. The source of this material is Enceladus' active south polar geysers, where the some ejected water vapour and ice grains into space have speeds sufficient to escape the moon's gravity (F. Postberg et al. 2008; Spahn et al. 2006). Much of this ejected

material becomes entrained in Saturn's magnetosphere, populating the E-ring and even contributing to the planet's upper atmosphere. Observations by the Cassini spacecraft showed that Enceladus sits near the densest part of the E-ring and serves as its primary source, making it a unique example of a moon actively shaping its planetary environment (Jones et al. 2009). The constant replenishment of ring material from Enceladus is essential, as small ice particles in the E-ring would otherwise dissipate quickly due to various loss processes. The general properties of Enceladus that has been defined in the preceding paragraphs are summarised in Table 2.1.

Table 2.1: General surface, internal & orbital properties of Enceladus

Characteristic	Value
Tidal axis, a	256.6$\pm$0.5 km (Porco et al. 2006)
Intermediate equatorial axis, b	251.4$\pm$0.2 km (Porco et al. 2006)
Polar axis, c	248.3$\pm$0.2 km (Porco et al. 2006)
Radius	252.1$\pm$0.2 km (Jacobson 2022)
Mass	(1.080318$\pm$0.00028)$\times 10^{20}$ kg (Jacobson 2022)
Mean density	1609.7$\pm$3.8 kg/m^3 (Jacobson 2022)
Surface gravity	0.113 m/s^2
Moment of inertia factor	0.3305$\pm$0.0025 (Iess et al. 2014)
Geometric albedo	1.375$\pm$0.008 (Verbiscer et al. 2007)
Semi-major axis	237948 km (Solar System Exploration 2013)
Eccentricity	0.0047 (Porco et al. 2006)
Inclination	0.009° (Solar System Exploration 2013)
Orbital period	1.370218 days (Solar System Exploration 2013)
Escape velocity	0.239 km/s (Solar System Exploration 2013)
Surface mean temperature	-198°C (Spencer et al. 2006)

2.2. Plumes

Initial hints of geological activity on Encleadus came from Voyager's high-albedo surface observations, but definitive evidence emerged when Cassini entered the Saturnian system in 2005 and detected plumes emanating from the moon's south pole. Between 2005 and 2015, Cassini conducted 23 flybys of Enceladus, with several (e.g., E3, E4, E5, E7) passing directly through the plumes, enabling high-quality in-situ measurements (Dotson 2018). The plumes emanating from the tiger-stripes were captured by Cassini's ISS and one of these images is shown in Figure 2.3. The image's high resolution allows one to see not only the alignment of jets but also subtle variations in their intensity and clustering, hinting at localised differences in vent activity and possibly thermal or structural heterogeneities along the fractures. More recently, JWST's NIRSpec revealed the massive scale of the plumes, which extend more than 20 times the size of Enceladus itself (Villanueva et al. 2023).

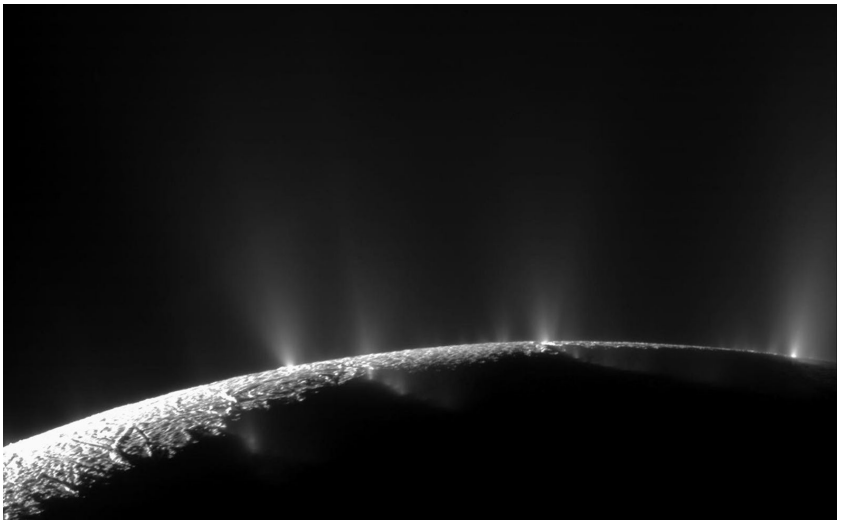

Figure 2.3: High-resolution two-image mosaic of Enceladus' southern geyser basin, captured by Cassini during its imaging survey. The image reveals the curvilinear alignment of geysers erupting from prominent fractures, identified from left to right as Alexandria, Cairo, Baghdad, and Damascus sulci (Cassini imaging team 2010).

Plumes are comprised of both discrete jets and broader curtain-like emissions (Goldstein et al. 2018; Nimmo et al. 2014). Most icy particles fall back to the surface, while vapour escapes into space due to Enceladus' low gravitational pull. Thermal observations from Cassini's CIRS showed the hottest regions lie along the tiger stripes, with estimated blackbody temperatures of 133–167 K and a radiated power of approximately 5.8 ± 1.9 GW (Abramov and S. J. 2009; Dotson 2018; Spencer et al. 2009).

Cassini's UVIS data, acquired through stellar occultations in 2005 and 2007, provided lower limits for plume temperatures of about 180 K (Hansen et al. 2008; Hansen et al. 2006). UVIS and ISS data together enabled estimates of the solid fraction (ice-to-vapour ratio) in the plumes. Initial estimates yielded a wide range of solid fractions: 0.21–0.80 (Andrew P Ingersoll and Ewald 2011). Revisions incorporating particle aggregation effects lowered this to $\sim$0.07 (Gao et al. 2016). Additional modelling based on reflectance and scattering resulting in solid fractions of 0.07–0.20 (Chan et al. 1993; Hansen et al. 2006, 2020; J. E. Hansen 1971; Kieffer et al. 2009; Nicholson et al. 1996; Porco et al. 2006). In conclusion, the variability in solid fraction estimates arises from differing methodologies, particle size distribution assumptions, and observational conditions such as time and phase angle.

2.2.1. Composition

Enceladus' plumes emanating from the four tiger stripes were found to consist of gas, micrometer sized grains and ionised particles (Dotson 2018). The correlation between Saturn's E ring and Enceladus' plumes means that one can study the composition of the E ring to infer the composition of the plumes.

2.2.2. Gas phase composition

The composition of Enceladus' plume gas was primarily determined by Cassini's Ion and Neutral Mass Spectrometer (INMS) and UVIS instruments. Early results from the INMS during the E5 flyby are shown in Figure 2.4a. The data indicate that the plume is composed mainly of water vapour, with smaller amounts of CO_2, CH_4, and a species with a mass-to-charge ratio of 28 u. Due to the low mass resolution of INMS, this 28 u signal could not be definitively identified, as overlapping signals could not be separated, introducing ambiguity in interpretation (Waite et al. 2009). The E5 flyby had the highest velocity of 17.7 km/s and a lower altitude than previous flybys, resulting in an improved signal-to-noise ratio. While the species detected were largely consistent with those from the earlier E2 flyby, E5 data showed significantly higher concentrations of H_2 and more organic compounds above 50 u. These increases are attributed to enhanced fragmentation of heavier organics at higher impact velocities, and the elevated hydrogen signal likely resulted from hypervelocity impacts of ice grains on INMS instrument surfaces. The 28 u species remains unidentified, as it was absent in the later E21 flyby. It is likely a fragmentation product, possibly CO, C_2H_4, or a heavier organic compound beyond INMS's mass range.

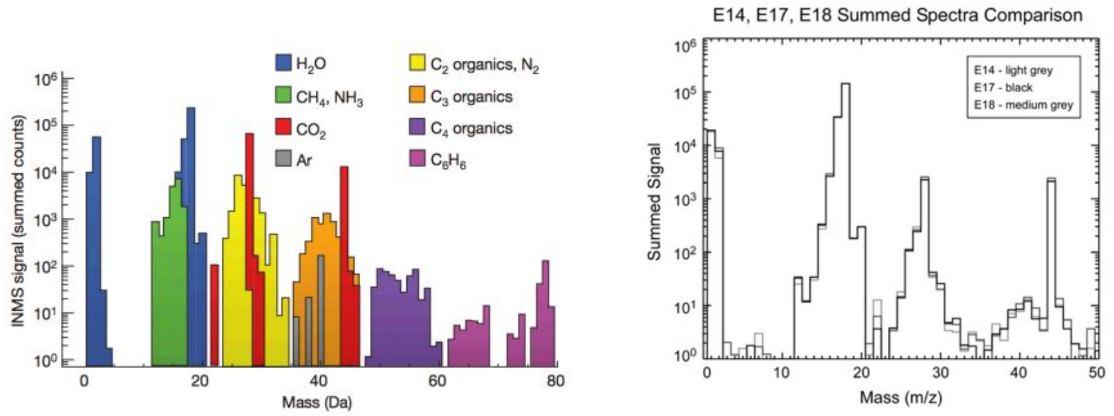

(a) INMS data from flyby E5

(b) INMS data from flybys E14, E17 and E18

Figure 2.4: The mass spectra measured by Cassini's INMS during flybys E5, E14, E17 and E18 around Enceladus (Dotson 2018)

Cassini's UVIS helped constrain the abundance of the unidentified species with a mass of 28 u (F. Postberg et al. 2018). UVIS measurements did not detect absorption features associated with N_2, placing an upper limit of less than 0.5% on its abundance (C. J. Hansen et al. 2011). Similarly, the absence of CO absorption features at 1544, 1510, 1477, and 1447 Å set an upper limit of 0.9% for CO (Hansen et al. 2006). Ethylene (C_2H_4) abundance was constrained by superimposing its absorption cross-sections, combined with water, over various column densities and comparing them to UVIS occultation data. Since no distinct ethylene features were detected, its abundance was limited to less than 5% of the water column density (C.J. Hansen et al. 2020).

Because Enceladus' subsurface ocean is believed to remain liquid, methanol and ammonia were considered possible antifreeze agents (C.J. Hansen et al. 2020). When methanol was added to pure water absorption models, the match to the observed spectrum improved, but no distinct methanol features were found. Adding methane also improved the spectral fit, and its spectral features were distinct, yet INMS did not detect methane at the required abundance. These upper limits stem from UVIS's sensitivity threshold, which requires at least a 10% decrease in signal for an absorption feature to be considered significant.

The final composition of the confirmed neutral gas species in the plume was determined to be approximately 96–99% H_2O, 0.3–0.8% CO_2, 0.4–1.3% NH_3, and 0.4–1.4% H_2 (Waite et al. 2017).

2.2.3. Solid phase composition

The composition of the solid phase of Enceladus' plume was primarily determined by Cassini's in-situ instruments, the Cosmic Dust Analyzer (CDA) and the Cassini Plasma Spectrometer (CAPS). Additional insights were derived from remote sensing data collected by the Visual and Infrared Mapping Spectrometer (VIMS). On 27 November 2005, VIMS captured 25 spectral data cubes at a phase angle of 161°, each comprising 64×64 spatial pixels representing spectral maps of Enceladus. These cubes were calibrated using standard routines to yield the reflectance parameter I/F (Hedman et al. 2009). To improve data quality, the cubes were grouped such that the spacecraft-to-Enceladus distance varied by less than 10% within each group. Within each group, spectral data was summed at each wavelength to produce composite cubes with enhanced signal-to-noise ratios.

The low optical depth of the plume and the strong forward-scattering nature of the icy particles contributed to weak absorption signals and low signal-to-noise ratios. To improve reflectance measurements, the data was integrated across rows of pixels to calculate the equivalent width, as defined in Equation 2.2 (Hedman et al. 2009):

$$E = \int I/F \, dx \tag{2.2}$$

The equivalent width was then plotted against wavelength at various altitudes, as shown in Figure 2.5. The black curve represents the best-fit spectrum, while the coloured curves show spectra scaled to the same best-fit particle size distribution. According to Mie theory, the red curve corre-

sponds to spherical particles, green to irregular shape model 3, and blue to irregular shape model 5 (Pollack and C. J. 1980), which will be discussed in more detail later. A consistent feature in the spectra is a dip near 3 μm, indicative of water ice absorption (Dotson 2018; Hedman et al. 2009). No other distinct spectral features were observed outside this region. However, variations in spectral slope with wavelength and altitude provide constraints on the particle size distribution and the dynamics of the plume (Hedman et al. 2009).

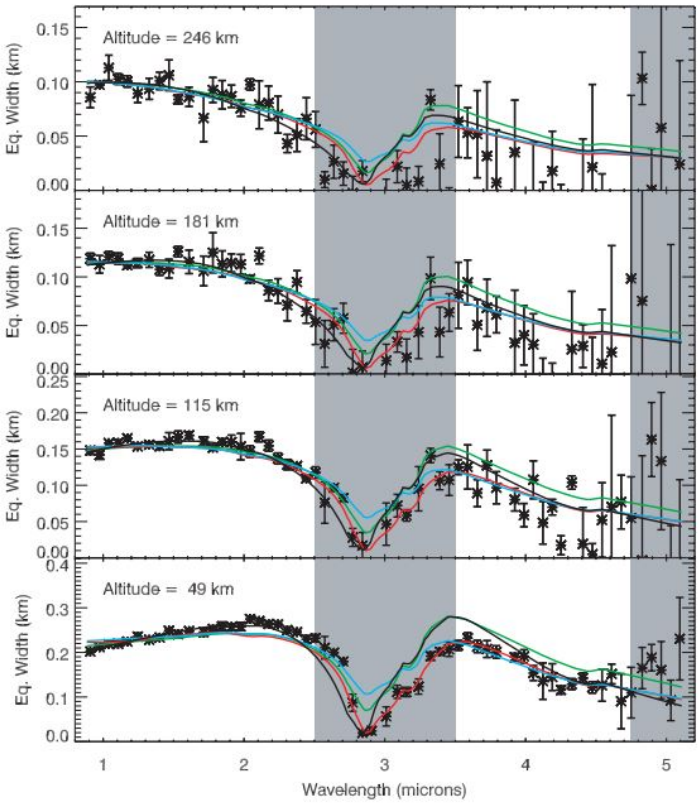

Figure 2.5: Equivalent width derived from the spectra from four altitudes in combined cube 1 (Hedman et al. 2009)

Using Mie theory, the modelled spectra for both crystalline and amorphous water ice can be compared with Cassini VIMS brightness data across various wavelengths, as shown in Figure 2.6. The comparison reveals that the crystalline ice model provides a significantly better fit to the VIMS observations than the amorphous ice model. This indicates that the plume particles are predominantly composed of nearly pure crystalline water ice (Hedman et al. 2009). Crystalline ice forms only at temperatures above approximately 130 K, suggesting that these particles originate from the warm regions along Enceladus' tiger stripe fractures, where such temperatures are thermally supported by endogenic activity (Dotson 2018).

Further evidence from VIMS spectra, as presented in Figure 2.5, confirms that Enceladus' surface is largely composed of nearly pure water ice. However, additional spectral features at 3.44 and 3.53 μm attributed to C–H stretching mode have been detected specifically in the south polar region. These features are indicative of the presence of light organic compounds (Brown et al. 2006). Although no complex organics were unambiguously detected in the VIMS spectra, these subtle features suggest the incorporation of simple hydrocarbons into the surface ice as well as CO_2, likely delivered or cycled through the plume.

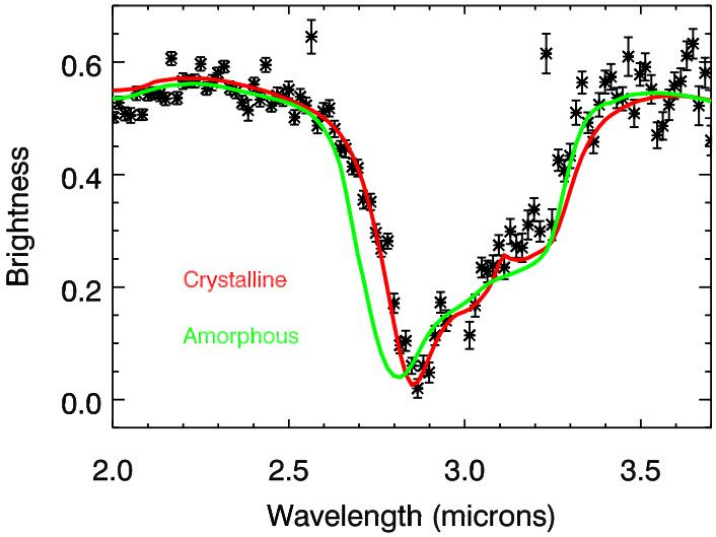

Figure 2.6: Mie-theory model spectra for crystalline and amorphous ice overlaid on VIMS data (Dotson 2018)

Observations from the James Webb Space Telescope (JWST), using its Near-Infrared Spectrograph (NIRSpec), confirmed the presence of predominantly crystalline water ice on Enceladus' surface. The spectral features detected by JWST closely match those previously observed by Cassini's VIMS instrument, reinforcing earlier findings regarding the surface composition (Villanueva et al. 2023). However, unlike VIMS, JWST did not detect any spectral signatures of CO_2 ice. This absence is likely due to the unfavourable viewing geometry during the JWST observations, which did not provide a direct line of sight to the south polar region where CO_2 ice had previously been identified by Cassini.

The lack of CO_2 detection in the JWST spectra supports the interpretation that CO_2 ice is localised and confined primarily to the south polar terrain. This region is known to be geologically active and is the origin of Enceladus' plumes. The correlation between CO_2 presence and plume activity suggests that the CO_2 ice deposits are not primordial but are instead continuously regenerated by the condensation of CO_2 gas emitted from the plumes onto the cold surface (Villanueva et al. 2023).

Cassini's CDA provided key insights into the composition of both Saturn's E-ring and the plume particles ejected from Enceladus. While CDA was originally optimised for measurements in the relatively diffuse environment of the E-ring, it was not specifically designed to operate in the dense, particle rich environment of Enceladus' plumes. To accommodate plume sampling, several instrument settings had to be adjusted, including impact ionisation thresholds and event filtering criteria. These modifications, although necessary, resulted in reduced spectral resolution and signal fidelity, thereby limiting the data quality from plume encounters. In contrast, CDA's measurements in the E-ring required no such adjustments, yielding more consistent spectra with better statistics. The compositional data collected from the E-ring revealed that the particles can be broadly categorised into three types, based on their mass spectral signatures, as shown in Figure 2.7.

Type I particles: Representing the majority ($\sim$65%) of E-ring particles, Type I is more prevalent among smaller particle sizes. These particles are composed almost entirely of pure water ice, as indicated by strong mass lines corresponding to water-cluster cations $(H_2O)_n(H_3O)^+$ in the spectra shown in Figure 2.7a. In addition to water, trace amounts of alkali metals—such as Na^+ and K^+—and their hydrated cluster ions $(H_2O)_n(Na, K)^+$ were detected, suggesting some minor contamination or surface processing of these grains.

Type II particles: Making up about 25% of the E-ring population, Type II particles are typically larger and display more complex mass spectra. Like Type I, they contain water-cluster features, but they also show additional peaks in the mass range of 27–31 u and 39–45 u shown in Figure 2.7c, consistent with C_2 and C_3 hydrocarbon fragments. However, these peaks may also contain contributions from molecules with oxygen and nitrogen. Type II particles exhibit a diverse chemical composition, with organics varying from trace levels up to several percent by mass. As shown in Figure 2.7d, some Type II spectra also contain mass lines ranging from 70 u up to 200 u, attributed to large organic

cations. These may represent aromatic and aliphatic hydrocarbons, potentially oxygen- and nitrogen-bearing, and could originate from cross-linked or polymerised macromolecules. In such structures, small aromatic units are linked by aliphatic chains, forming stable, complex molecular networks (Dotson 2018; F. Postberg et al. 2008; Frank Postberg et al. 2009).

Type III particles: The least abundant (∼10%) but chemically distinct group, Type III particles also appear to be large, given their strong ion signals. Unlike Types I and II, Type III spectra lack water-cluster features entirely. Instead, they are dominated by signatures of salts and salt-bearing clusters, most notably sodium hydroxide clusters $(NaOH)_n(Na)^+$, as well as peaks corresponding to NaCl–Na^+ and Na_2CO_3–Na^+ complexes shown in Figure 2.7b. This composition strongly suggests an oceanic origin involving brine solutions, potentially concentrated near the ice-ocean interface and subsequently entrained into the plumes during venting. The identification of salts such as sodium carbonate supports the hypothesis that Enceladus' subsurface ocean is alkaline and interacts with a rocky core, providing essential clues to the ocean's geochemistry and potential habitability (Frank Postberg et al. 2009).

Together, these three particle types sampled in the E-ring represent different stages of processing and different origins, ranging from nearly pure condensates (Type I), to organics-bearing particles (Type II), to salt-rich oceanic spray (Type III).

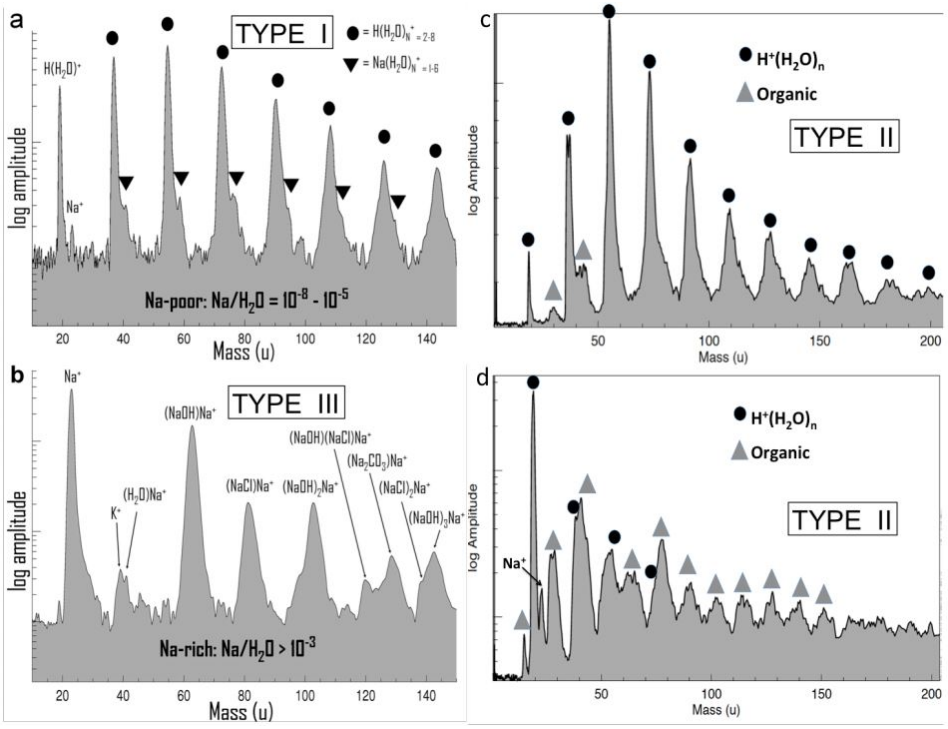

Figure 2.7: CDA mass spectra of the ice particles in the E-ring for different ice type compositions (Dotson 2018; Frank Postberg et al. 2009)

During Cassini's E5 flyby on October 9, 2008, the Cosmic Dust Analyzer (CDA) obtained in-situ compositional measurements of plume particles as the spacecraft passed through the dense vapor jets emanating from Enceladus' south polar terrain. The temporal evolution of the detected particle types—Types I, II, and III is shown in Figure 2.8, plotted as a function of time relative to the closest approach. In the seconds leading up to closest approach, the frequency of Type I spectra—dominated by nearly pure water ice—gradually decreased, while the frequency of Type III particles increased. This trend reflects the spacecraft's approach trajectory bringing it closer to the vent sources at the tiger stripes, where the heavier, salt-rich Type III particles are more concentrated. These particles, characterised by Na-rich signatures, including sodium hydroxide and sodium salts, are denser and are therefore ejected at lower velocities compared to the more volatile Type I particles, which consist primarily of water-ice nanograins (Dotson 2018). This velocity sorting means lighter particles can travel farther from their source vents, while heavier particles remain more localized near their ejection origin.

Interestingly, the abundance of Type II particles peaks after closest approach, specifically between

+45 s and +51 s, and appears relatively independent of altitude or ejection velocity. This suggests that the processes responsible for their formation or release differ from those governing Types I and III. Their spatial distribution implies a more diffuse source or different aerodynamic behaviour, possibly due to lower densities or different interactions with the surrounding vapour. This post-encounter peak in Type II particle abundance coincides with Cassini's trajectory over Damascus Sulcus. The timing and location of this enhancement suggest that Damascus Sulcus may be a particularly active vent for the release of organic-rich material. This aligns with previous inferences that different tiger stripes may contribute distinctively to the plume composition, possibly reflecting localised ocean chemistry or differing subsurface plumbing networks (Dotson 2018).

To facilitate these high-frequency measurements during the high-speed flyby, CDA's data acquisition settings were temporarily altered to increase the particle throughput rate. This adjustment enabled the collection of more spectra in a short time but came at the cost of reduced mass resolution and a narrower mass range. As a result, between +18 s and +35 s after closest approach, the data quality dropped significantly, and too few usable spectra were recorded. This period is shaded in Figure 2.8 to indicate the data gap. Overall, the E5 flyby provided critical insight into the compositional heterogeneity of the plume and suggested spatial variability in the sources of different materials, particularly organic compounds within Enceladus' subsurface ocean and plumes. This variability may point toward chemical gradients or localised geochemical processes within the moon's interior, further emphasising its astrobiological significance.

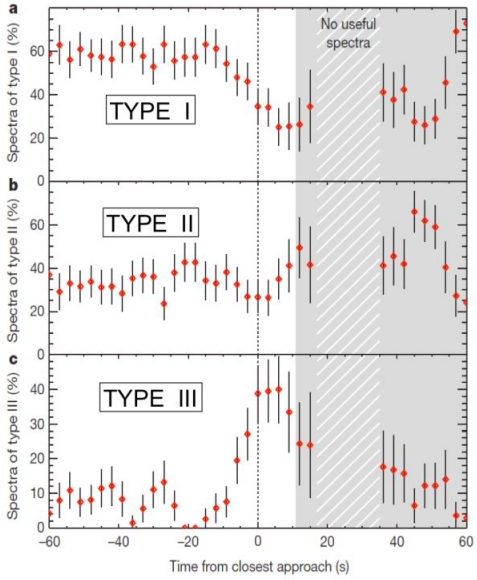

Figure 2.8: Relative frequency of spectra types of Enceladus' plumes measured by Cassini's CDA during the E5 flyby (Dotson 2018; Frank Postberg et al. 2009)

2.2.4. Charged particles composition

The composition of charged particles in Enceladus' plume environment was measured by Cassini's Cassini Plasma Spectrometer (CAPS), which included two key subsystems: the Ion Mass Spectrometer (IMS) for positive ions and the Electron Spectrometer (ELS) for negative ions (F. Postberg et al. 2018). These instruments enabled the identification of key ion species and the assessment of their dynamics within Enceladus' magnetospheric interaction region.

From CAPS data, the total plasma mass loading rate—the rate at which neutral material is ionized and added to Saturn's magnetospheric plasma—was estimated at approximately 3×10^{27} H_2O molecules per second, or roughly 100 kg/s (F. Postberg et al. 2008). This plasma mass loading arises through several ionisation mechanisms, including charge exchange, impact ionisation, and photoionisation of neutrals ejected from Enceladus' plumes.

Data collected during the E3 and E5 flybys revealed that the dominant ion population consisted of cold ions, with energies below 10 eV. Since the measurements were made in the ram direction, the detected ions were interpreted as stationary with respect to Enceladus, suggesting a relatively steady

plume ionosphere sourced primarily from the neutral exosphere (Tokar et al. 2009). This steady-state condition also supports the idea of a persistent and continuous source of neutral material from the subsurface ocean.

The mass spectra obtained from the CAPS IMS subsystem during these encounters as shown in Figure 2.9a revealed several key positive ion species, including O^+, OH^+, H_2O^+, and H_3O^+, along with heavier water-group ions likely in the form of $(H_xO_2)^+$ clusters, where $x = 1$–4 (Tokar et al. 2009). These species reflect the progressive ionisation and hydration of water molecules in the near-plume plasma environment.

The negative ion population, characterised by CAPS ELS as depicted in Figure 2.9, exhibited clear peaks in the differential flux versus energy per charge spectrum. These peaks correspond to water-based anions, including OH^-, O^-, and H^- (Tokar et al. 2009). The formation of such species is attributed to dissociative electron attachment which is a low-energy process in which an electron attaches to a neutral molecule, causing it to fragment into an anion and one or more neutral fragments. For water, this can be represented by:

$$H_2O + e^- \rightarrow OH^- + H \tag{2.3}$$

$$H_2O + e^- \rightarrow O^- + H_2 \tag{2.4}$$

This process is particularly efficient at the low electron energies prevalent in Enceladus' plume ionosphere (Fabrikant et al. 2017), and the presence of negative ions offers strong evidence for low-energy plasma processes operating close to the moon's surface.

The identification of both positive and negative water-group ions by CAPS has critical implications for understanding the plasma-neutral coupling at Enceladus, the role of the plumes in magnetospheric dynamics, and the chemical environment that may affect the surface and near-subsurface chemistry that is potentially relevant for prebiotic or biotic processes.

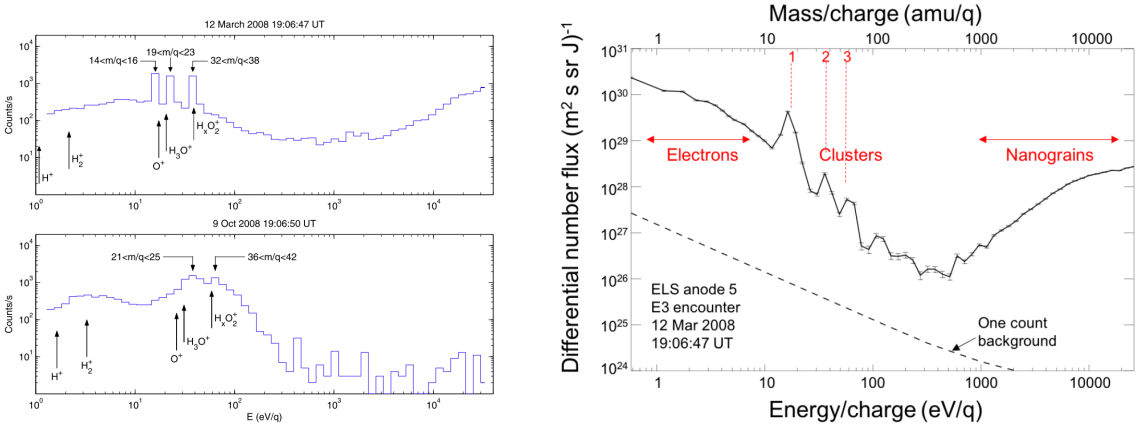

(a) Ion counting rate against energy per charge from Cassini CAPS IMS during flyby E3 and E5 (Tokar et al. 2009)

(b) Negative ion spectrum from Cassini CAPS ELS during flyby E3 (F. Postberg et al. 2018)

Figure 2.9: Positive and negative ion spectra in Enceladus plume ionosphere

2.3. Temporal variations

Enceladus' active cryovolcanism is a highly dynamic process, exhibiting both spatial and temporal variability. Spatially, the activity is concentrated along the "tiger stripe" where localised variations in temperature, vent geometry, and subsurface pressure influence plume behavior (Spencer et al. 2006). Temporally, the plumes show three primary types of variation: periodic diurnal, periodic decadal, and aperiodic fluctuations (Ingersoll et al. 2020).

The diurnal variation is the most well-characterised, modulated by Enceladus' eccentric orbit around Saturn. The tidal stresses acting on the moon vary with its position in orbit, leading to periodic flexing of the icy crust and opening or closing of fissures. Observations from Cassini's ISS and VIMS revealed that plume brightness peaks near apoapsis, the farthest point in Enceladus' orbit, when the tidal stresses pull the tiger stripes open widest (Hedman et al. 2013; Nimmo et al. 2014). This effect results in a 4-fold

variation in plume brightness throughout the orbit (Andrew P. Ingersoll and Ewald 2017), highlighting the influence of tidal mechanics on subsurface venting.

Early measurements from VIMS in 2005 reported plume brightness about 50% higher than in subsequent observations, suggesting that long-term (decadal) variability also affects plume output (Hedman et al. 2013). This could be linked to internal processes such as thermal evolution, changes in vent morphology, or modulations in ocean pressure over time.

Additionally, long-term analysis of ISS data spanning 2005 to 2017 has allowed researchers to separate periodic variations from aperiodic events, such as transient changes in vent activity or episodic clogging and clearing of fissures (Ingersoll et al. 2020). These irregular variations could result from shifting subsurface conditions, ice grain accumulation near vent throats, or abrupt shifts in local ice shell stress.

Overall, the interplay between Enceladus' orbital dynamics, subsurface ocean, and icy crust creates a complex and evolving cryovolcanic system. The multi-scale temporal variability of the plumes is crucial for understanding the internal plumbing system, habitability potential, and long-term stability of ocean–ice interactions.

2.3.1. Periodic diurnal variations

Due to Enceladus' slightly eccentric orbit around Saturn, the moon experiences tidal stresses that vary periodically throughout its orbit. These tidal stresses reach their maximum amplitude at periapsis and conversely reach their minimum amplitude at apoapsis. Given that Enceladus completes an orbit approximately every 1.37 Earth days, these cyclical changes induce diurnal oscillations in the tidal stresses acting on its icy shell (Ingersoll et al. 2020).

In Figure 2.10, the variations in slab density at 100 km altitude are plotted against Enceladus' mean anomaly, which corresponds to the orbital position. Here, the slab density refers to the mass per unit thickness of material within a horizontal slab located at 100 km altitude, serving as a proxy for plume density or material transport above the tiger stripes. The data is grouped into five distinct sets: magenta, blue, orange, red, and black each spanning approximately three years of observations. Each day's data is represented by unique alphanumeric symbols, with repeated measurements from the same day sharing the same symbol. The figure shows that all datasets follow a similar sinusoidal pattern, with consistent shapes but offset vertically by a nearly constant value.

This consistent, phase-shifted pattern aligns well with the theory that tidal stresses cyclically compress and stretch the fissures and subsurface channels along the tiger stripes, modulating the flow and density of plume material (Ingersoll et al. 2020). When the tiger stripe fractures are under tensile stress, the cracks open wider, allowing increased venting and higher slab densities. Conversely, during compressive stress, the fissures narrow, reducing plume output. These observations support a direct mechanical link between Enceladus' orbital dynamics and the variability of its plume activity, reinforcing the idea that the moon's tidally-driven cryovolcanism is tightly coupled to its orbital position and the resulting stress field within its ice shell.

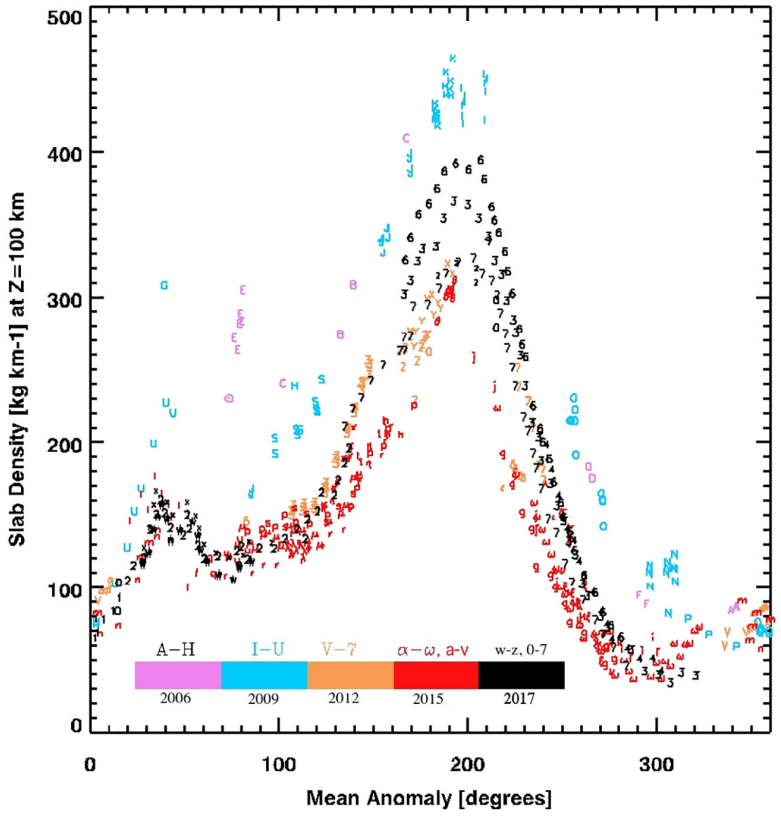

Figure 2.10: Slab density at 100 km against mean anomaly of Enceladus split into five groups of 3 years length each (Ingersoll et al. 2020)

Furthermore, two distinct peaks are observed in Figure 2.10: a primary peak around a mean anomaly of 200°, and a smaller secondary peak between 25° and 60°. The smaller peak may be attributed to cross-cutting fractures on Enceladus' surface that open and close at different intervals compared to the main tiger stripe fractures (Helfenstein and Porco 2015). These fractures could respond to tidal stresses with different phase shifts or stress thresholds, producing additional periodic variations in plume activity.

Interestingly, the main peak occurs shortly after 180°, which corresponds to apoapsis, the point in the orbit farthest from Saturn. This timing implies a 6 to 7 hour lag between Enceladus reaching apoapsis and the observed maximum in slab density (Ingersoll et al. 2020; Nimmo et al. 2014). There are three plausible explanations for this observed time lag:

Eruption Trigger Delay: It may take time for plume eruptions to commence after being triggered by tidal stress changes. This phenomenon is analogous to terrestrial volcanism, where eruptions sometimes occur days after being initiated by earthquakes or other geophysical triggers (Manga and Brodsky 2006).

Viscoelastic Response of the Ice Shell: The ice shell behaves as a viscoelastic material with a characteristic viscosity on the order of $3 \times 10^4\ Pa\ s$ (Goldsby and Kohlstedt 2001). Such a viscosity implies that the ice shell's response to tidal stresses is not instantaneous but delayed, with a characteristic relaxation timescale comparable to Enceladus' orbital period (about 1.37 days). This lag in the mechanical response of the ice shell can account for the observed delay in plume activity following changes in tidal stress (Schoenfeld and Yin 2024).

Strike-slip Motion Driving the Geysers: A recent 3D finite-element modeling study suggests that the geyser activity and its timing can be explained by strike-slip fault motions along the tiger stripes (Berne et al. 2023). In this model, the relative sliding of the crustal blocks may create transient openings or modulate flow pathways with a phase lag consistent with the observed delay.

Moreover, (Teolis et al. 2017) found that jets emanate from a series of fissures in a curvilinear arrangement, with varying intensities depending on the orbital position. This spatial heterogeneity also contributes to variability in the observed time lag, as different fissures may respond differently to

the same tidal forcing. Additionally, (Vidmachenko 2023) demonstrated that both the brightness and geometry of the jets change seasonally, consistent with changing solar illumination and viewing angles but also suggestive of deeper structural and thermal evolution.

Finally, (Schoenfeld and Yin 2024) demonstrated that seasonal effects and long-term orbital evolution modulate not only the amplitude of plume activity but also shift its timing. Their work confirms that the strike-slip model, combined with viscoelastic behaviour, provides the most robust explanation for the observed lag and amplitude variability in Enceladus' cryovolcanic activity. In summary, the temporal variability of Enceladus' plume activity results from a combination of diurnally varying tidal stresses, viscoelastic and fracture mechanical delays, strike-slip faulting dynamics, and possibly seasonal effects.

2.3.2. Periodic decadal variations

Due to Enceladus' 2:1 mean-motion orbital resonance with Dione, the tidal stresses experienced by Enceladus also vary on longer timescales of approximately 3.9 and 11.1 years (Porco et al. 2018). These longer-period variations superimpose on the primary diurnal tidal stress cycle caused by Enceladus' own orbit around Saturn, potentially modulating plume activity over multi-year intervals.

To isolate and analyse these longer timescale variations in the observational data, it is assumed that the overall shape of the diurnal variation curve remains consistent across different epochs but is scaled by a multiplicative factor. A template diurnal curve was constructed by interpolating data points from days 2 to 7 in the 2017 dataset, capturing the characteristic daily variation pattern during that period (Ingersoll et al. 2020).

By dividing the full dataset by this template, the diurnal variations are effectively normalised out, allowing the residual signal to highlight variations occurring on longer, decadal timescales. This processed data is shown in Figure 2.11, where the right-hand axis displays the difference between Enceladus' apoapsis and periapsis positions, calculated using the NASA NAIF/SPICE toolkit.

The plotted data points use alphanumerical symbols representing the average slab density measured on individual days, while the five circled points correspond to UVIS occultation observations (Ingersoll et al. 2020). This comparison suggests a correlation between the longer-term tidal forcing due to resonance and observed changes in plume density, supporting the idea that orbital resonances play an important role in modulating Enceladus' cryovolcanic activity on timescales beyond the daily tidal cycle.

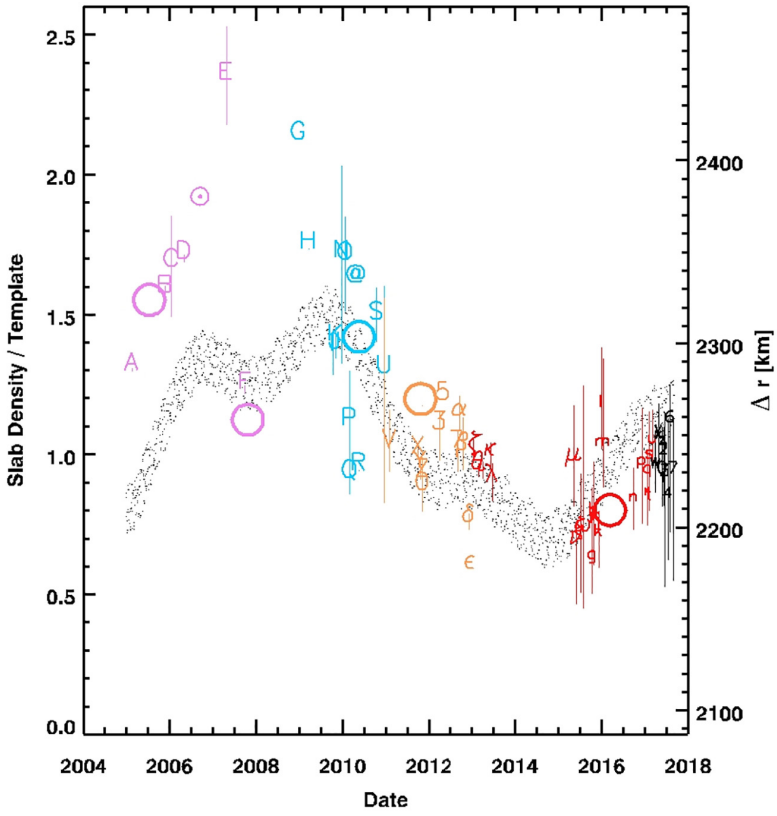

Figure 2.11: Ratio of slab density of the measurements to the slab density of a template (Ingersoll et al. 2020)

It is observed that the shape of the Δr curve and a curve fitting through the alphanumerical data points matches. The Δr is dependent on eccentricity by Equation 2.5 where r_a is the apoapsis distance, r_p is the periapsis distance, and a is the semi-major axis. Both curves peak around 2007-2009 and then have a trough around 2013-2015. Furthermore, the curves rise around 2006 and in 2017 which corresponds to the 11.1 years cycle. Lastly, it was seen that over this 11.1 year time-span between 2006 and 2017, Enceladus' orbit had decreased by about 5% (Ingersoll et al. 2020). On the other hand, the 3.9 periodicity is much harder to see due to the limited amount of data.

$$e = \frac{r_a - r_p}{2a} \tag{2.5}$$

2.3.3. Aperiodic variations

A large dataset of 2405 images from Cassini's ISS taken between 2005 and 2015 was analysed with a focus on images that clearly showed the collimated jets emanating from Enceladus' tiger stripes (Ingersoll et al. 2020). To facilitate this analysis, a specialised tool was developed to identify distinct jets and project their locations across different images, enabling consistent tracking of individual jets over time.

In Figure 2.12a, six distinct collimated jets are shown at two separate dates, with their projected paths clearly marked. Comparing these images reveals that almost half of the jets changed their activity or appearance within a 20-day period, highlighting significant short-term variability in the plume sources.

This variability is further supported by Figure 2.12b, which plots the slab density at 100 km altitude against Enceladus' mean anomaly for three dates in 2017: June 18, August 2, and August 28. On August 2, the plume brightness shows a $\sim$10% increase compared to the other dates, suggesting that some jets may have turned on or off during this time-frame. Although these changes are not yet conclusively understood, they strongly indicate dynamic temporal variations on monthly timescales.

Crucially, the mean anomaly values for Enceladus are nearly the same across these observations, indicating that this aperiodic variability is not correlated with the diurnal tidal stresses linked to Enceladus' orbit. This suggests that another process, independent of orbital position, modulates the plume

activity over these shorter timescales.

One compelling hypothesis is that the opening and closing of the tiger stripe fractures due to ice deposition and sublimation modulates jet activity (Ingersoll and Pankine 2010). During plume eruptions, vapour and ice particles are expelled through fractures, but over time, water vapour condenses and deposits as ice within the fractures, gradually building up ice "plugs" that can partially or fully obstruct the flow pathways. Ice sublimation is more effective near the warmer vent regions, resulting in a dynamic balance. As the cracks become blocked, pressure builds beneath the surface until it overcomes the blockage, reopening the fractures and restoring plume activity. This cycle could explain the observed aperiodic fluctuations in jet brightness and number on timescales of weeks to months.

As the cracks become blocked, pressure builds beneath the surface until it overcomes the blockage, reopening the fractures and restoring plume activity. This cycle of opening and closing could cause the observed aperiodic fluctuations in jet brightness and number on timescales of weeks to months. Such crack dynamics imply a feedback mechanism where surface and subsurface ice processes interact with the venting activity, resulting in intermittent plume behaviour that is independent from the predictable tidal forcing. Understanding this crack closing and reopening process is essential for interpreting Enceladus' plume variability and has important implications for the transport of materials from the subsurface ocean to the surface, as well as for the habitability and evolution of the icy shell.

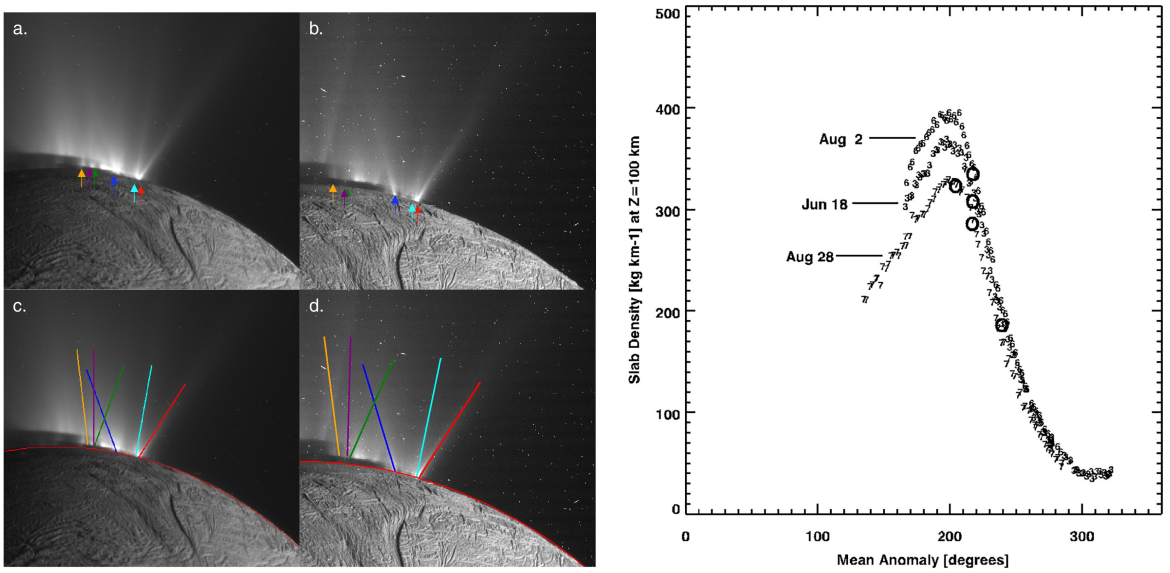

(a) Cassini ISS images of the jets between two dates November 30, 2010 shown in (a) & (c), and December 20, 2010 shown in (b) & (d)

(b) Slab density at 100 km against mean anomaly of Enceladus on June 18, 2017, August 2, 2017, and August 28, 2017

Figure 2.12: Identifying the aperiodic variations of Enceladus' jets (Ingersoll et al. 2020)

In addition to surface ice processes, aperiodic variability is further supported by Cassini INMS and UVIS observations, which revealed that gas and particle jets exhibit dramatic stochastic fluctuations up to a factor of 10 independent of orbital phase (Schoenfeld and Yin 2024; Teolis et al. 2017). These changes likely reflect subsurface dynamics, including varying gas flow rates, evolving fracture geometries, and turbulent dissipation within narrow conduits. It was shown by (Teolis et al. 2017) that supersonic gas jets can lift more particles even when total vapour flux remains stable that may contribute to the variation of measured plume activity. It has also been also suggested that stochastic strike-slip motion along faults and fracture narrowing due to lithostatic stress or pressure cycling can result in decoupled jet activation (Berne et al. 2023; Schoenfeld and Yin 2024). Furthermore, VIMS data show variations in particle launch velocities and size distributions, suggesting that mutual particle collisions and vent microphysics may also contribute to observed changes (Porco et al. 2014).

3

Processes & Ice Characteristics in Plumes Model

In this chapter, a detailed overview is given on the physical processes occuring in Enceladus' plume in the context of phase change and fluid dynamics. In section 3.1, the concept of phase changes is introduced by delving into the theory of nucleation and ice structure. This is followed by a discussion of the phenomena of nucleation in nozzles by introducing isentropic flow, then adding friction and heat transfer and finally non-homogeneous nucleation in subsection 3.2.2. The Wet Steam Model is introduced in section 3.3 which is an adapted Navier-Stokes equations model to account for the nucleation and droplet growth of water from steam. In section 3.4, the Icy Steam Model is discussed similarly to that of the Wet Steam Model but with a different nucleation and grain growth model.

3.1. Phase changes

Phase changes are physical transitions from one state of matter to another. They are defined as changes in microscopic structure resulting from variations in the system's disorder (Solé 2011). For example, boiling is a phase transition in which a liquid becomes a gas, while freezing involves the transformation of a liquid into a solid. These processes for water are illustrated in Figure 3.1. Water in the solid state, commonly known as ice has a well organised molecular structure. Due to its low kinetic energy, the individual water molecules primarily vibrate in place. This corresponds to a low degree of disorder, or in thermodynamic terms, low entropy. As heat is added to the ice, the molecules gain kinetic energy. At a certain point, the molecular arrangement transitions from the ordered structure of ice to the less ordered structure of liquid water. The point at which this occurs is typically characterised by enthalpy, a thermodynamic quantity that represents the total heat content of a system at constant pressure. The enthalpy of fusion is the energy required per mole in which the molecules holding their bonds together break apart and form a liquid.

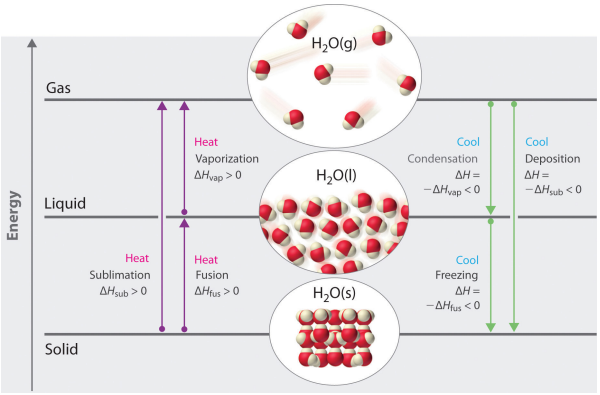

Figure 3.1: Illustration of water in its three states of matter. Purple and green arrows indicate the necessary positive and negative enthalpy changes for each phase transition respectively (Averill and Eldredge 2012). The lines for ΔH are not to scale.

Vaporisation is the endothermic phase change process in which a liquid transforms into a gas. There are two types of vaporisation processes: evaporation and boiling. Evaporation occurs on a surface level, whereas boiling occurs in the bulk of the fluid.

The process of vaporisation is governed by the enthalpy of vaporisation which for water is shown as a function of temperature in Figure 3.2a. For solid-liquid transition, the total enthalpy of fusion for ice is shown as a function of temperature in Figure 3.2b.

At 273 K the specific enthalpy of vaporisation is $\Delta h_{vap} = 2501.3$ kJ/kg (Potter and Somerton 2013). The specific enthalpy of freezing is equal to the specific enthalpy of fusion but with a negative sign. For ice at 273 K, the specific enthalpy of freezing is $\Delta h_{free} = 335$ kJ/kg (Matson et al. 2012). This means that at 273 K, about 6.74 kg of water freezes for each kilogram of water that is evaporated.

From the figures it can also be seen that the specific enthalpy of fusion firstly increases with increasing temperature but then reaches a maximum and then starts decreasing. In contrast, condensation is the exothermic phase change process in which a gas transforms into a liquid. Since condensation is the opposite process of vaporisation, its specific enthalpy is equal in magnitude to the enthalpy of vaporisation, but negative.

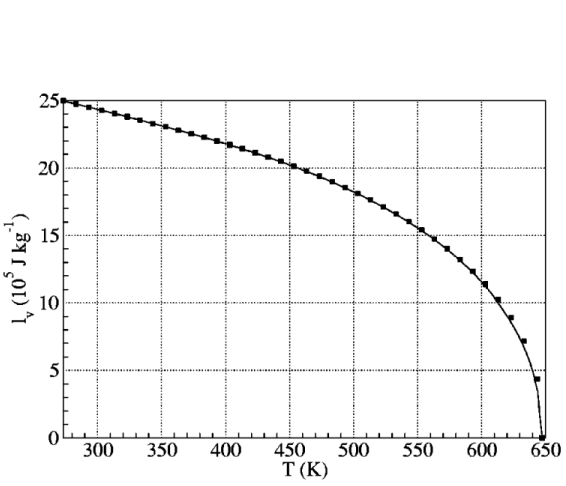

(a) Specific enthalpy of vaporisation of water (Pellicer et al. 2002)

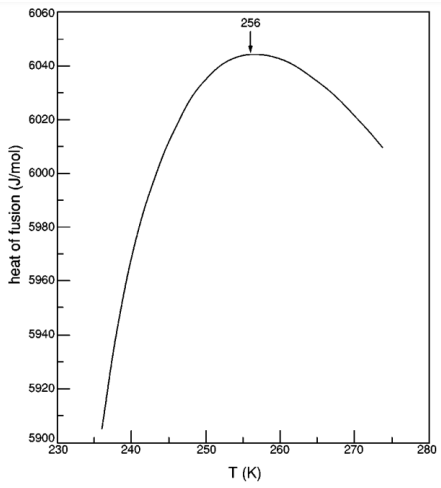

(b) Total enthalpy of fusion of water (Dougherty and Howard 1998)

Figure 3.2: Specific and total enthalpy of water as a function of temperature determined from experiments

Sublimation is the endothermic phase change process in which a solid transforms into a gas. Generally, the conditions are extreme so that the phase change skips the process of melting. For water, the enthalpy of sublimation as a function of temperature is shown in Figure 3.3. The specific sublimation enthalpy is then equal to the specific enthalpy of vaporisation plus the specific enthalpy of freezing (Feistel and Wagner 2007). Lastly, deposition is the exothermic phase change process in which a gas

transitions into a solid. This is again the opposite process of sublimation and therefore shares the same magnitude for the specific enthalpy as for sublimation but with a negative sign.

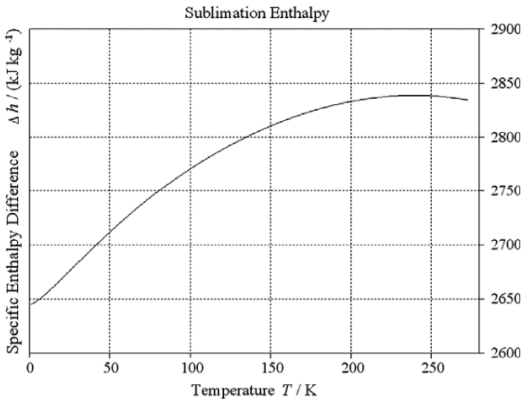

Figure 3.3: Specific enthalpy of sublimation of water as a function of temperature (Feistel and Wagner 2007)

The existence of icy particles within the Enceladus' plumes means that there must be phase changes occurring. Since it has been proven that there exists a subsurface ocean on Enceladus, there must exist a water liquid-vapour interface where the subsurface ocean transitions into water vapour and ice. Throughout literature, it has been assumed that at this interface water is at its triple point corresponding to a temperature of 273.16 K and a pressure of 611.657 Pa as seen in the water phase diagram in Figure 3.4 (Kieffer et al. 2009; Schmidt et al. 2008a,b; Yeoh et al. 2015).

Figure 3.4, shows under which conditions water exists in a certain state. For example, ice undergoes sublimation at temperatures above 273 K and for partial pressures below the triple point (Fassnacht 2004). This led scientists to hypothesise that ice sublimation was the main driving mechanism for Enceladus' cryovolcanism (Porco et al. 2006).

Looking at the phase diagram of water, at the water liquid-vapour interface, it is assumed that the water is at triple point and therefore exists in its three phases in thermodynamic equilibrium.

A blue region is marked as to where Enceladus' channel lies in the water phase diagram. At the inlet where the water flows from the reservoir to the start of the channel, it is at triple point conditions. Whereas the icy walls around the inlet will generally be at a higher pressure and lower temperature. At the vent where the channel leads to the surface, the pressure and temperature are much lower in the order of a few Pa and 133-167 K respectively (Spencer et al. 2009). As the plumes of water vapour travel along the channel, they will experience a temperature and pressure gradient resulting phase transition within the flow, as well as wall accretion & sublimation.

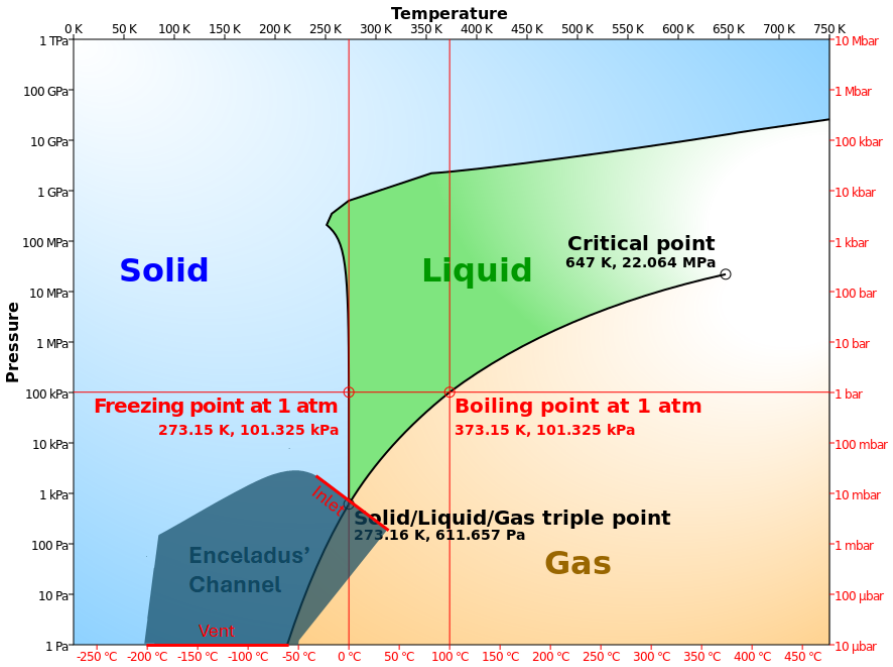

Figure 3.4: Phase diagram of water where pressure is plotted on a logarithmic y-axis and temperature on the x-axis. The ocean interface is assumed to lie at the triple point, where the temperature is about 273.16 K, the pressure is 611.657 Pa, and solid, liquid, and vapour phases coexist. This is where the inlet of Enceladus' channels begin. A pressure and temperature gradient is experienced as the flow moves from the inlet to the outlet where the pressure reaches near vacuum and the temperature is around 70-220 K (Cmglee 2014).

3.1.1. Ice Structure

Water ice is a remarkably polymorphic substance, capable of existing in numerous crystalline and amorphous forms depending on environmental conditions like pressure and temperature. At typical atmospheric pressures and temperatures below 0 °C, water crystallises into a phase known as ice I_h, or hexagonal ice, the predominant form of solid water in nature (Pruppacher et al. 1998). This phase is defined by a sixfold symmetry in its lattice structure, which arises from the unique ability of each water molecule to form four hydrogen bonds in a near-tetrahedral configuration (Pruppacher et al. 1998). Each oxygen atom in the ice lattice is surrounded by four nearest-neighbour oxygen atoms located approximately 2.76Å away. These nearly regular tetrahedra connect to form a continuous, layered hexagonal lattice shown in Figure 3.5.

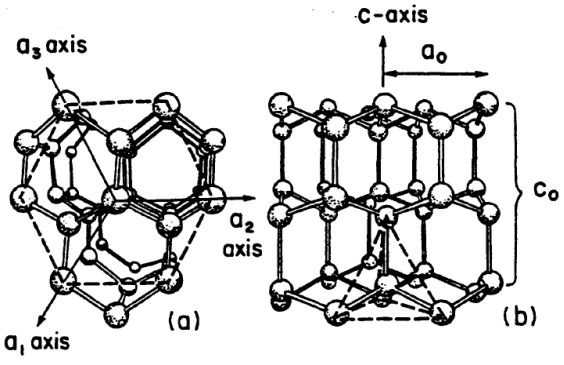

Figure 3.5: Arrangement of oxygen atoms in ice I_h: (a) viewed along the c-axis, (b) viewed perpendicular to the c-axis (Pruppacher et al. 1998)

The open, cage-like nature of the ice I_h lattice leads to a relatively low density ($\sim$0.917 g/cm^3 at 0°C) and allows for significant diffusion of water molecules, including defect-mediated processes (Pruppacher et al. 1998). Importantly, vacancies and orientational defects are present even at low

temperatures. These defects, combined with rapid reorientation of water molecules (on the order of 10^{-11} seconds), contribute to the complex dynamical behaviour of ice under stress and during sublimation (Pruppacher et al. 1998). For instance, the presence of orientational disorder and proton hopping mechanisms influences thermal conductivity and may affect the morphology of sublimating surfaces(Pruppacher et al. 1998).

According to Hou et al. (2020), hexagonal ice nucleation is heavily influenced by environmental parameters such as confinement and surface interactions. Under conditions of confinement such as nanopores less than 35 nm in diameter, or on certain substrates, water may preferentially form the cubic polymorph (ice I_c), which differs in structure from ice I_h. Nonetheless, ice I_h remains thermodynamically favoured at the low pressures and temperatures found on Enceladus.

In CFD simulations, these structural and dynamical characteristics of hexagonal ice inform boundary condition formulations, particularly for wall mass fluxes (e.g., sublimation and accretion), surface temperature models, and momentum exchange terms. Capturing the anisotropic, porous, and defect-rich nature of ice is crucial to realistically model the deposition of ice within vapour flow and the evolving wall geometry. For this work, it was assumed that the density of hexagonal ice is a function of temperature given by Equation 3.1 (Peeters et al. 2002).

$$\rho_{ice} = 916.7 - 0.175\,(T - 273.15) - 5.0 \times 10^{-4}\,(T - 273.15)^2 \quad [kg/m^3] \tag{3.1}$$

3.1.2. Nucleation

Nucleation is the random process of the formation of a new stable thermodynamic phase from a metastable phase (Mer 1952). This process can be visualised in Figure 3.6 where a system is at a metastable equilibrium at state A. A system is in equilibrium when its thermodynamic variables are constant in time. In the figure, this can be seen as the first derivative of the free energy with respect to a general thermodynamic variable is 0. For a metastable equilibrium, the system is located at a local minimum. If the system experiences small fluctuations in its thermodynamic variable, then its free energy will change but will eventually reach the same equilibrium after a certain period of time in state A. If, however, the fluctuations are large enough, then the system will move from state A to an unstable equilibrium and will then reach a new stable equilibrium at a global minimum at state B. When the system transitions from state A to state B, its free energy increases to a local maximum. At this local maximum, the system is at an unstable equilibrium state. This means that any small fluctuations will lead to a sudden collapse of system resulting in the system being in non-equilibrium and therefore in this unstable equilibrium state is short-lived (Kelton and Greer 2010).

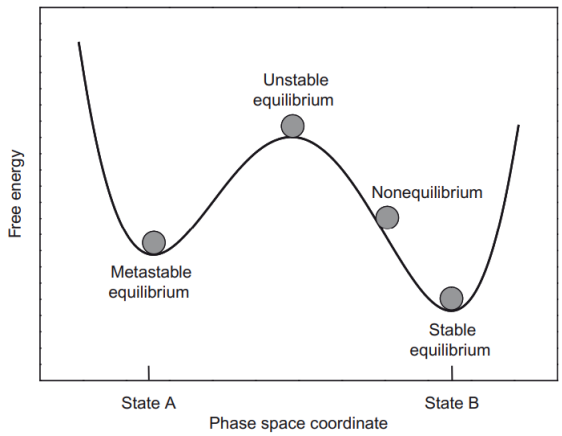

Figure 3.6: Illustration of how a system at a metastable equilibrium (State A) transitions to a state of unstable equilibrium followed by experiencing a small disturbance and finally reaching a state of stable equilibrium (State B) (Kelton and Greer 2010).

Such a system can exist in a metastable equilibrium if, for example the system becomes supersaturated; that is when the vapour pressure exceeds the saturation pressure given by Equation 3.2. Within a metastable bulk phase of water vapour, small molecular clusters occasionally form due to random collisions between water molecules (Pruppacher et al. 1998). These transient clusters are known as

embryos when the vapour pressure is below the critical threshold required for nucleation. Embryos are weakly bound and highly susceptible to disruption by thermal motion. However, as the vapour pressure increases, some embryos may reach a critical size, referred to as germs, where they exist in an unstable equilibrium with the surrounding vapour. At this critical point, the cluster is on the cusp of growth. If its size increases even slightly due to a random fluctuation in the surrounding vapour, it will begin to grow spontaneously. This marks the onset of a macroscopic phase transition, leading to the formation of the condensed phase.

$$S = \frac{p_{gas}}{p_{sat}^{(s,g)}(T_{sat})} \tag{3.2}$$

Figure 3.7 shows the process of nucleation for a pure parent gas with small liquid nuclei of a daughter phase. If the gas is at a thermodynamic state such that it becomes supersaturated then clusters will be created and disintegrated, however, if a cluster reaches a certain critical size then it will grown as seen by the bigger clusters or grains on the right side of the figure. This can also be shown in another manner considering Equation 3.3. Embryos consisting of varying numbers of molecules form within the supersaturated vapour due to statistical fluctuations. The creation-annihilation process occurs through the gradual addition and removal of individual vapour molecules A.

$$\begin{gathered} \mathrm{A} + \mathrm{A} \rightleftharpoons \mathrm{A}_2 \\ \mathrm{A}_2 + \mathrm{A} \rightleftharpoons \mathrm{A}_3 \\ \cdots\cdots \\ \mathrm{A}_{i-1} + \mathrm{A} \rightleftharpoons \mathrm{A}_i,\ i = 1, 2, ... \end{gathered} \tag{3.3}$$

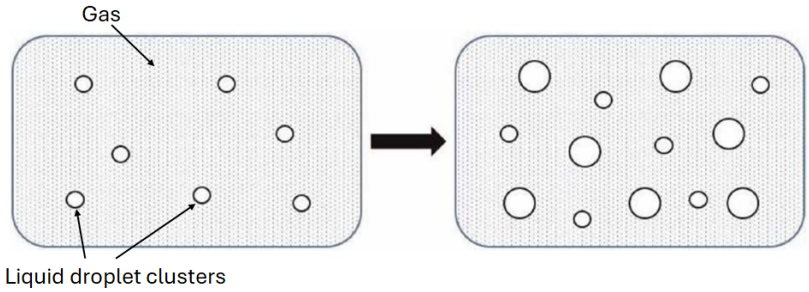

Figure 3.7: Illustration for homogeneous nucleation of liquid droplets from the parent gaseous phase. If the clusters reach a critical size known as a germ, then it will continue to grown shown by the larger clusters (Marzouki 2020).

There are two ways that nucleation can occur which are: homogeneous nucleation and heterogeneous nucleation. In homogeneous nucleation, nucleation occurs in a pure substance where there is an absence of foreign particles that may aid in the nucleation process. The random thermal fluctuations in the substance at a given temperature and pressure can lead to spontaneous formation of clusters resulting in nucleation. In contrast, heterogeneous nucleation occurs due to nucleation sites such as impurities like dust or other volatiles like salts, or due the surfaces of a container (Hou et al. 2020). Although homogeneous nucleation does occur, in reality it is rarer than heterogeneous nucleation because it requires a large degree of supersaturation.

Classical Nucleation Theory (CNT)

Classical nucleation theory (CNT) is a theoretical framework developed in 1920's to 1940's for analysing the kinetics and thermodynamic aspects of nucleation (Hodgson 1984; Wyslouzil and Wölk 2016). A useful thermodynamic parameter that is ubiquitous in CNT is the Gibbs free energy change equation represented in Equation 3.4. In this equation ΔH and ΔS denote the change in specific enthalpy and entropy between two states with different temperatures respectively, and T is the temperature. The Gibbs free energy can be used to assess whether a process will be spontaneous (ΔG < 0) or require external energy input (ΔG > 0).

$$\Delta G = \Delta H - T\Delta S \tag{3.4}$$

For a supersaturated vapour, the system is in a metastable state, the chemical potential μ of a molecule within the cluster is lower than that of the vapour phase. The chemical potential is a thermodynamic property that states the energy of a species that can be absorbed or released as a result of a change of the particle number of the given species due to a phase transition. This means that it is energetically favoured. However, as embryos form, a liquid-vapour interface is created which opposes the growth of the embryo into a germ. In other words, a germ can only form from an embryo depending on the relative magnitude of these two chemical potentials given by Equation 3.5 (Hou et al. 2020). In Equation 3.5, μ_v is the chemical potential of the supersaturated vapour phase and μ_l is the chemical potential of a molecule inside the condensed cluster phase.

$$\Delta\mu = \mu_v - \mu_l \tag{3.5}$$

For a cluster of n molecules, Equation 3.6 gives the change in Gibbs free energy, $\Delta\mu$ is the change in chemical potential for a molecule that is phase transitioning from the vapour phase to the liquid phase, $\sigma_{l,v}$ is the interfacial surface energy or in this case the surface tension between the liquid and the vapour phases, and A is the area of the interface.

$$\Delta G = -n\Delta\mu + \sigma_{l,v}A \tag{3.6}$$

For CNT applied to homogeneous nucleation, it is bound by several assumptions. It assumes that a germ forms as a spherical particle with a uniform density, and that the interface between the germ and the parent phase is isotropic, meaning it has uniform properties in all directions. The theory also assumes that the germ grows or shrinks by the addition or removal of individual molecules or atoms. The a ssumptions are summarised below.

Assumptions:

- Germs are considered as spherical clusters with uniform density.
- Germs possess macroscopic properties for their density and surface tension or interfacial energy.
- The surface tension or interfacial energy between the germ and the surrounding phase is assumed to be uniform and constant.
- Germs grow by the addition of individual molecules, one at a time.
- Nucleation is treated as a steady-state process in which the rate of nucleation is constant over time once it reaches a stable rate.
- The surface tension or interfacial energy is assumed to be constant with the radius of the germ.

If one considers that the vapour is an ideal gas and the liquid is incompressible, then the difference in chemical potentials $\Delta\mu$ can be written using Equation 3.7. The change in Gibbs free energy from vapour to liquid per unit volume is calculated using Equation 3.8 where n_L is the number density of molecules in the condensed phase, k is the Boltzmann constant, T is the temperature and S is the degree of supersaturation. Multiplying Δg_v with the volume of a spherical liquid droplet results in the change in Gibbs free energy from vapour to liquid as seen in Equation 3.9 where r is the radius of the liquid germ.

$$\Delta\mu = -kT \ln S \tag{3.7}$$

$$\Delta g_v = -n_l kT \ln S \tag{3.8}$$

$$\Delta G_v = \frac{4}{3}\pi r^3 \Delta g_v \tag{3.9}$$

When a liquid droplet is formed then there exist a liquid-vapour interface surrounding the circumference of the particle which is seen in Figure 3.8a. This interface has an associated surface energy that is represented by the surface tension $\sigma_{l,v}$ and therefore the Gibbs free energy of the interface is given by Equation 3.10.

Creating a new surface requires energy because molecules at the interface are less stably bonded than those in the bulk liquid. In other words, energy is needed to move molecules from a fully bonded environment (inside the liquid) to the less bonded surface region. Therefore, surface energy refers to the amount of energy needed to expose a unit area of new surface, because molecules at the surface are less tightly bound than those in the interior of the liquid. This is why the surface energy is positive. In fact, the surface energy $\sigma_{l,v}$ is often larger than the volumetric Gibbs free energy difference Δg_v

that drives condensation from vapour to liquid. That is why forming small droplets which have a high surface-to-volume ratio is energetically costly.

$$\Delta G_s = 4\pi r^2 \sigma_{l,v} \tag{3.10}$$

The total change in Gibbs free energy is shown in Equation 3.11 where it is plotted along with ΔG_v and ΔG_s as a function of partial radius r in Figure 3.8b. It is clear from the plot that below a certain particle radius, the surface energy term dominates the volumetric term and hence there is a creation-annihilation of clusters where nucleation and subsequent droplet growth does not occur. However, if the clusters reaches a certain radius known as the critical radius r^* then the volumetric term dominates allowing nucleation and droplet growth to happen.

$$\Delta G_T = \Delta G_V + \Delta G_s = -\frac{4}{3}\pi r^3 \Delta g_v + 4\pi r^2 \sigma_{l,v} \tag{3.11}$$

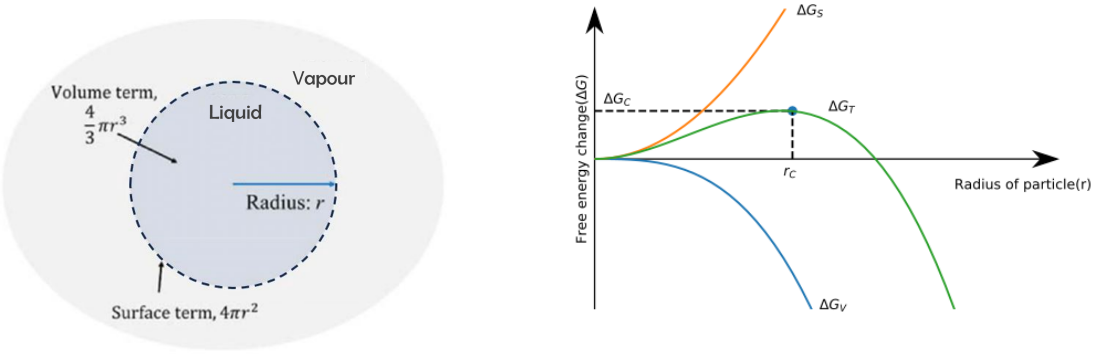

(a) Diagram of volumetric and surface tension terms (Adapted from (Kang et al. 2020))

(b) Graph of Gibbs free energy change against the radius of the nucleus (Mmarso 2020)

Figure 3.8: Illustration of homogeneous nucleation for a liquid cluster forming in the bulk vapour experiencing a surface tension

By differentiating Equation 3.11 with respect to r results in the critical radius, r^* as seen in Equation 3.12. The critical radius can be decreased by increasing the degree of supercooling in the system, or increasing the supersaturation of the system. Decreasing the critical radius leads to nucleation being much easier and will occur earlier and often resulting in smaller clusters. Plugging Equation 3.12 into Equation 3.11 results in the formation free energy of a critical cluster shown in Equation 3.13 corresponding to the maximum in Figure 3.8b. Both the critical radius and the critical Gibbs free energy are crucial for the calculation of the nucleation rate.

$$r^* = \frac{2\sigma_{l,v}}{|\Delta g_v|} = \frac{2\sigma_{l,v}}{n_l kT \ln S} = \frac{2\sigma_{l,v}}{\rho_l R T_g \ln S} \tag{3.12}$$

$$\Delta G^* = \frac{16\pi\sigma_{l,v}^3}{3\left(\rho_l R T_g \ln S\right)} \tag{3.13}$$

It is emphasised that whilst CNT has be used successfully to model phase transitions, it fails to model experimental results of vapour to liquid nucleation for Argon by severely under-predicting the nucleation rate (Fladerer and Strey 2006). Although, there are limitations of CNT possibly due to its assumptions, it is still regarded as the most common theoretical framework to use to predict the nucleation rate as a function of temperature from thermodynamic and kinetic variables (Kang et al. 2020). Several modifications have been applied to CNT to match the theory of the nucleation rate with the experimental results that is further discussed in subsection 3.1.3.

Heterogeneous nucleation

In heterogeneous nucleation, foreign particles or surfaces are present that reduce the surface free energy therefore resulting in a decrease of the energy barrier. This means that heterogeneous nucleation

occurs much more frequently compared to homogeneous nucleation since the surface free energy effect is smaller (Kang et al. 2020). Consider the phase change from liquid to solid where nucleation occurs on a surface or a foreign particle as seen in Figure 3.9. In this figure, there are three surface energies present, the liquid-surface interface γ_{IL}, the solid-liquid interface γ_{SL}, and the solid-surface interface γ_{SI}. The liquid-surface interface can be expressed as a function of the other two using Equation 3.14 where θ is the wetting angle between the nucleus and the surface (Kang et al. 2020).

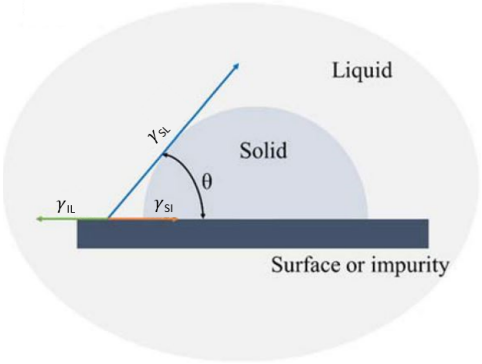

Figure 3.9: Illustration of heterogeneous nucleation of a solid germ located on a surface or impurity in a bulk liquid medium. Here there exists three interfaces: the liquid-surface interface γ_{IL}, the solid-liquid interface γ_{SL}, and the solid-surface interface γ_{SI} and θ is the wetting angle between the nucleus and the surface (Adapted from Kang et al. (2020))

$$\gamma_{IL} = \gamma_{SI} + \gamma_{SL} \cos\theta \tag{3.14}$$

Furthermore, the change in Gibbs free energy for heterogeneous nucleation is the same as that for homogeneous nucleation but scaled by a constant ranging from 0 and 1. This is represented by the $S(\theta)$ function in Equation 3.16 and can be computed knowing the wetting angle. The critical particle radius then follows similarly from the derivation of Equation 3.15 with respect to r. When comparing Equation 3.12 and Equation 3.17 using Equation 3.14, it can be confirmed that the critical radius for heterogeneous nucleation is smaller than that for homogeneous nucleation.

$$\Delta G_{\text{hete}} = \Delta G_{\text{homo}} S(\theta) \tag{3.15}$$

$$S(\theta) = \frac{(2 + \cos\theta)(1 - \cos\theta)^2}{4} \tag{3.16}$$

$$r^* = -\frac{2\gamma_{SL}}{|\Delta g_v|} \tag{3.17}$$

3.1.3. Nucleation Rate

The nucleation rate is the number of germs created by nucleation per second per volume. The foundation of all literature regarding the nucleation rate arrive at the common expression shown in Equation 3.18 where J_0 is the kinetic prefactor, ΔG^* is the formation free energy of a critical cluster given by Equation 3.13, k_B is the Boltzmann constant and T is the temperature (Wölk and Strey 2001).

$$J(T) = J_0 \exp\left(-\frac{\Delta G^*(T)}{k_B T}\right) \tag{3.18}$$

The full derivation of the kinetic prefactor and hence the nucleation rate is rather lengthy and is not presented here, but can be found in literature (Bakhtar et al. 2005; Pruppacher et al. 1998). The key idea is that during nucleation, molecular clusters continuously form and break apart at roughly equal rates, maintaining a steady concentration of clusters of a given size; for example, clusters containing g water molecules, or g-mers. However, when a favorable free energy gradient ΔG_g exists, clusters that grow beyond the critical radius are more likely to continue growing rather than disintegrate. In this case, the concentration of g-mers, denoted f_g, is no longer steady and changes over time in proportion to the rate at which g-mers grow into (g+1)-mers. This growth process can be described using a balance equation derived based on statistical thermodynamics shown in Equation 3.19.

$$\frac{\partial f_g}{\partial t} = -\frac{\partial J}{\partial g} \tag{3.19}$$

For a system where nucleation has reached steady-state, it is assumed that the concentration of clusters n that have a critical size r^* can be modelled as a Boltzmann equilibrium given by Equation 3.20 where n_1 is the number density of monomer. With this in mind, a steady-state solution to Equation 3.19 can be analytically derived using the equations for Gibbs free energy to give the nucleation rate in Equation 3.21 where k_B is the Boltzmann constant and T is the temperature.

$$n = n_1 \exp\left(-\frac{\Delta G_g}{k_B T}\right) \tag{3.20}$$

$$J = q_c \left(\frac{\rho_v^2}{\rho_l}\right) \sqrt{\frac{2\sigma_{l,v}}{\pi m^3}} \exp\left(-\frac{4\pi {r^*}^2 \sigma_{l,v}}{3k_B T}\right) \tag{3.21}$$

In this equation, q_c is the condensation coefficient, ρ_v and ρ_l are the densities of the vapour and liquid phases respectively, $\sigma_{l,v}$ is the surface tension of the liquid droplet in the vapour, m is the mass of the vapour molecule. The nucleation rate can be re-written by considering $q_c = 1$, the equation for the critical radius Equation 3.12 and using the ideal gas law: $pV = nkT$ where p is the pressure, V is the volume, n is the number of molecules and T is the temperature given by Equation 3.22.

$$J = \sqrt{\frac{2\sigma_{l,v}}{\pi m}} v_m \left(\frac{p_v}{k_b T}\right)^2 \exp\left(-\frac{16\pi v_m^3 \sigma_{l,v}^3}{3(k_b T)^3 \left(\ln S\right)^2}\right) \tag{3.22}$$

Analysing Equation 3.21 with the equation of the critical radius Equation 3.12 one may notice that surface tension is raised to the power of three in the exponential term. Therefore, the nucleation rate is extremely sensitive to the surface tension.

This equation for the nucleation rate assumes that it is in steady state. This assumption posits that the time between the onset of conditions favourable to nucleation and the point at which the nucleation rate of critical clusters reaches equilibrium is negligibly short. In conventional nozzles, this assumption is generally valid. The transient phase of nucleation typically lasts on the order of a microsecond, while the nucleation process as a whole remains active for 10–50 μs (Bakhtar et al. 2005). An extensive analysis was made by Karagiannis (2020) and studied that for a representative case for $T = 240$ K and $S = 5000$. These values, while extreme, are considered typical for micronozzles undergoing rapid expansion. Karagiannis found that the nucleation rate reaches 99% of its steady-state value after approximately 9×10^{-8} seconds. The conclusion of Karagiannis' study found that assuming that nucleation is a steady state process is reasonable. The same argument holds true for Enceladus length scales of about 150 m.

Modifications to CNT, such as those by Courtney and Kantrowitz, aim to improve quantitative accuracy, particularly for water droplet formation in steam flows (Bakhtar et al. 2005). Courtney's correction incorporates the partial pressure of clusters, leading to a revised free energy equation and nucleation rate expression shown in Equation 3.23. This correction factor reduces the classical nucleation rate value of J by a factor S. Furthermore, the correction factor can be argued on the basis that the classical form for ΔG is inconsistent with the law of mass action unless the correction factor is used (Bakhtar et al. 2005).

$$J_{CNY} = q_c \left(\frac{\rho_v}{\rho_l}\right) \left(\frac{2\sigma}{\pi m^3}\right)^{1/2} \exp\left(-\frac{4\pi {r^*}^2 \sigma}{3k_B T}\right) \tag{3.23}$$

Kantrowitz's non-isothermal correction accounts for temperature differences between vapour and droplets, introducing a factor c to the nucleation rate (Kantrowitz 1951):

$$J_{NISO} = c J_{ISO} \tag{3.24}$$

The factor c is related to energy transfer processes and is approximated by Equation 3.25 where ψ depends on heat transfer coefficients and thermodynamic properties of the vapour (Bakhtar et al. 2005). Experiments in nozzles serve as crucial validation for these theoretical models, especially at the high nucleation rates relevant to engineering applications 12, 13. While CNT offers a robust theoretical foundation, uncertainties remain regarding the precise values of interfacial energy for small clusters and energy transfer mechanisms in non-isothermal conditions (Bakhtar et al. 2005),

$$c \approx \frac{1}{(1+\psi)} \tag{3.25}$$

The value of the non-isothermal correction factor, ψ can be calculated using Equation 3.26 where Δh_{dv} is the specific latent heat of vapour released due to droplet condensation. This equation valid for low pressures was derived in Appendix 3 of Bakhtar et al. (2005) by assuming that the droplet-vapour temperature difference was independent of the droplet radius.

$$\psi = \frac{2\,(\gamma-1)}{(\gamma+1)} \frac{\Delta h_{vap}}{RT} \left(\frac{\Delta h_{vap}}{RT} - 0.5 \right) \tag{3.26}$$

Alternatively, other authors (e.g., Young (1980), Gyarmathy (1976)) propose an expression for ψ derived from kinetic theory and nucleation thermodynamics, shown in Equation 3.27. This formulation emphasises the molecular-level physics of nucleation, incorporating the vapour density ρ_v, liquid density ρ_l, surface tension $\sigma_{l,v}$, molecular mass m, and the critical radius r^* from classical nucleation theory. The exponential term captures the strong dependence of the correction on nucleation energy barriers, and thus on temperature and surface tension effects. This form is particularly useful in conditions where the vapour is highly supersaturated and nucleation plays a dominant role in the flow field evolution. While both expressions seek to correct for thermal non-equilibrium effects, they emerge from different modelling philosophies: the former grounded in macroscopic energy balance and the latter in microscopic molecular theory.

$$\psi = \frac{2\,(\gamma-1)}{(\gamma+1)} \left(\frac{\rho_v^2}{\rho_i} \right) \sqrt{\frac{2\sigma_{l,v}}{m^3\pi}} \exp\left(-\frac{4\pi {r^*}^2 \sigma_{l,v}}{3k_b T} \right) \tag{3.27}$$

In a series of condensation experiments involving water vapour in an argon carrier gas, Wölk and Strey (2001) demonstrated that classical nucleation theory (CNT) matches experimental data for temperatures of about 240 K but significantly underestimates nucleation rates away from 240 K as seen in Figure 3.10. To address this discrepancy, they proposed an empirical correction factor to the CNT-predicted nucleation rate, expressed as Equation 3.28 where A and B have been empirically determined to be -27.56 and 6500 K respectively. Using this correction proposed by Wölk and Strey (2001), Figure 3.10 shows that the nucleation rate now matches the experimental data for temperatures outside of the 240 K range.

$$J = J_{CNT} \exp\left(A + \frac{B}{T} \right) \tag{3.28}$$

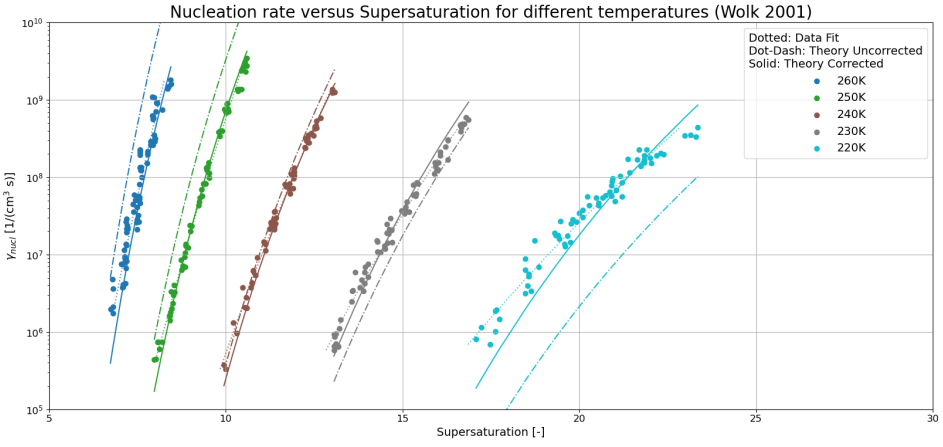

Figure 3.10: Comparison of the theoretical nucleation rate of water vapour to experimental results for a range of temperatures and supersaturations with the Wölk and Strey (2001) correction included

This exponential correction accounts for deviations from CNT predictions in the low-temperature regime, where the classical theory fails to accurately describe the energetics and kinetics of cluster

formation. The correction has been shown to yield excellent agreement with a wide range of experimental measurements beyond the original data set, including those presented by Manka et al. (2012) and reviewed by Wyslouzil and Wölk (2016). This correction results in the nucleation rate being valid for 200 < T/K < 310 and supersaturations 5 < S < 200 (Wölk et al. 2002).

3.1.4. Deposition

Deposition is the exothermic phase change process in which a gas transforms into a solid. This process occurs when the temperature or pressure of a gas is sufficiently decreased that the system becomes supersaturated allowing for nucleation to happen and skips the liquid phase. However, in literature regarding the modelling of Enceladus' plumes the term condensation has been consistently used instead of deposition (Ingersoll and Pankine 2010; Nakajima and Ingersoll 2016; Frank Postberg et al. 2009; Schmidt et al. 2008b). The reasoning is because the ice droplets that are formed on Enceladus are composed of about 20-30 water molecules which is not enough to be considered as crystalline structures (Schmidt et al. 2008b). Nevertheless, to stay consistent with the physics the term deposition will be used to throughout this work and otherwise condensation is emphasised to avoid any further ambiguities.

The change in Gibbs free energy for deposition by homogeneous nucleation is identical to that of the previous discussion shown in Equation 3.29. However, the interfacial energy is from vapour to solid and the supersaturation of the vapour to solid is defined in Equation 3.2 where p_v and $p_{sat}^{(s,g)}$ are the partial pressure and equilibrium saturated vapour pressure of the gas (Bakhtar et al. 2005; Karagiannis 2020).

$$\Delta G_T = -\frac{4}{3}\pi r^3 \rho R T_g \ln S + 4\pi r^2 \sigma_{s,v} \tag{3.29}$$

3.2. Nucleation in Nozzles

The tiger stripes on Enceladus are assumed to be cracks on the surface that extend deep within the interior until it meets the subsurface ocean (Spencer et al. 2009). Several authors have modelled this process by considering flow dynamic models. This system can be modelled as a channel where the inlet is assumed to be at triple point conditions of pure water. That is to say that the inlet has a stagnation temperature and pressure of 273.15 K and 611.657 Pa respectively (Yeoh et al. 2015). The outlet of the channel is assumed to be directly at the surface where it experiences vacuum conditions. Although the surface mean temperature was measured to be about 70 K, the temperature of the tiger stripes was calculated to have a lower limit of approximately 180-200 K (Spencer et al. 2006). This is based on the fact that a lower temperature would need a larger area of surface ice to produce the mass flux of H_2O that Cassini's UVIS observed (Spencer et al. 2006).

3.2.1. Isentropic Flow

Enceladus plume velocities at the vent can exceed Mach 5. To explain these high velocities, the crevasses can be modelled as convergent-divergent nozzle or de Laval nozzles that accelerate gas from subsonic to supersonic flow regimes (Schmidt et al. 2008b; Yeoh et al. 2015). The simplest plume model treats the flow as isentropic and quasi-one-dimensional as it expands through a de Laval nozzle, also shown in Figure 3.11. Such a model is subject to the following assumptions.

- The subsurface ocean, or reservoir, is at the triple point of water (T_0 = 273.16 K, p_0 = 611.657 Pa).
- Flow is subsonic (M < 1) in the converging section, sonic (M = 1) at the throat, and supersonic (M > 1) in the diverging section.
- The solid fraction in the plume is negligible, allowing the flow to be modelled as a perfect gas.
- Phase transitions within the plume are neglected: no ice grain nucleation or growth occurs.
- There is no heat exchange with the channel walls: no wall accretion or sublimation is considered.
- Effects of turbulence, viscosity, and wall friction are ignored.

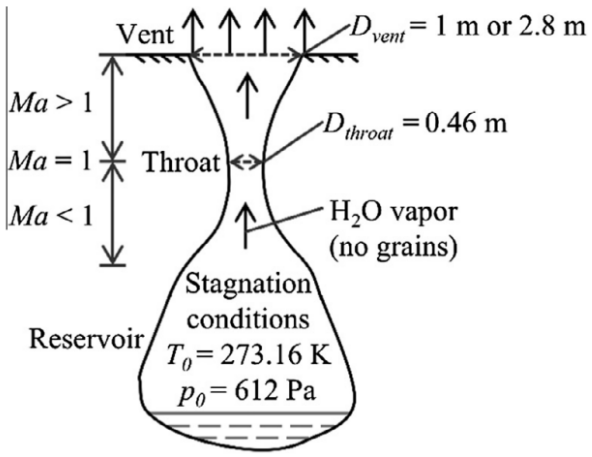

Figure 3.11: Schematic for an isentropic flow model applied to Enceladus' plumes. It is treated as a convergent-divergent nozzle with triple point conditions specified at the reservoir allowing for subsonic to supersonic flow (Yeoh et al. 2015)

The conservation equations for mass, momentum, and energy can be simplified and analytically solved for the pressure, density, and temperature with the aforementioned assumptions for the isentropic model. The derivation is not shown in this work but the reader is suggested to consult any aerodynamics textbook such as Fundamentals of Aerodynamics by Anderson (1991). The equations are shown in Equation 3.30 where p, ρ and T are denote the static conditions for the pressure, density and temperature respectively, p_0, ρ_0 and T_0 are the total conditions for the pressure, density and temperature respectively, γ is the specific heat ratio and M is the Mach number (Anderson 1991).

$$\begin{aligned}\frac{p}{p_0} &= \left(1+\frac{\gamma-1}{2}M^2\right)^{-\frac{\gamma}{\gamma-1}} \\ \frac{\rho}{\rho_0} &= \left(1+\frac{\gamma-1}{2}M^2\right)^{-\frac{1}{\gamma-1}} \\ \frac{T}{T_0} &= \left(1+\frac{\gamma-1}{2}M^2\right)^{-1}\end{aligned} \tag{3.30}$$

Furthermore, it can be shown that for isentropic flow, the Mach number can be related to the ratio of the area, A to the throat area, A^* shown in Equation 3.31. This means that for isentropic flow, the thermodynamic variables are determined solely by the area ratio and the specific heat ratio which is usually treated to be constant for a single species (Anderson 1991).

$$\frac{A}{A^*} = \frac{1}{M}\left(\frac{2+(\gamma-1)M^2}{\gamma+1}\right)^{\frac{\gamma+1}{2(\gamma-1)}} \tag{3.31}$$

The isentropic flow model is not restricted to a strictly convergent-divergent nozzle but can be considered for a channel where there exists a geometrical throat which has the minimum cross-section in the entire channel. An example of such channel used for modelling Enceladus' crevasses with the isentropic flow results for the Mach number, temperature, density, and supersaturation is shown in Figure 3.12. The isentropic model describes the flow behaviour driven by a pressure difference between the inlet and outlet, originating from a reservoir at triple point conditions. The flow accelerates to Mach 1 at the throat denoted by the vertical dashed line and continues expanding to Mach 1.76 at the vent.

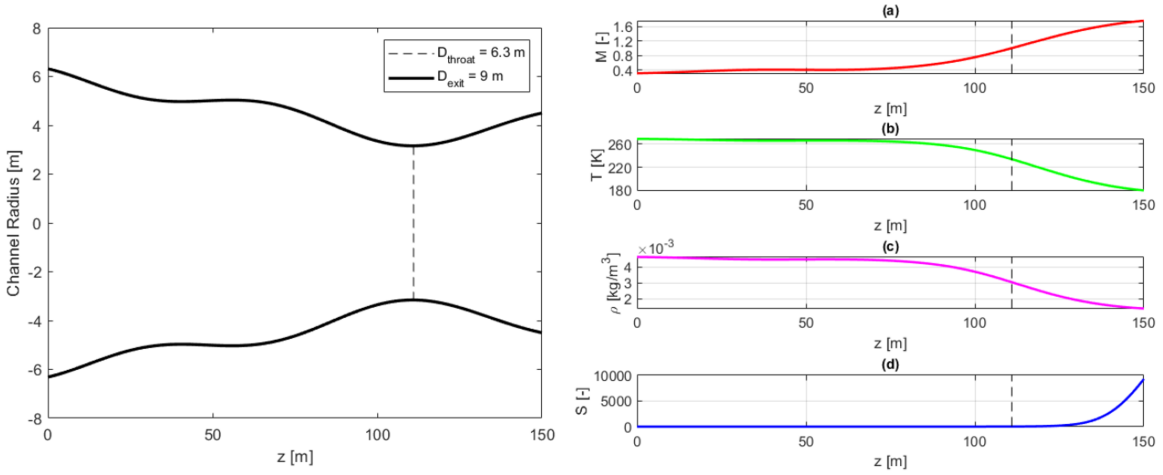

Figure 3.12: Profiles of Mach number (M), temperature (T), density (ρ), and supersaturation (S) along a channel computed using isentropic flow. The vertical dashed line indicates the location of the channel throat (van der Hijden 2021).

As the flow accelerates along the z-axis, its temperature decreases due to the conversion of internal energy into kinetic energy. The pressure drops isentropically to match the back pressure, causing a corresponding decrease in gas density. Starting at approximately 270 K near the reservoir, the gas cools to a vent temperature of around 180 K. At such low temperatures, the resulting supersaturation becomes unrealistically high, indicating that phase change should occur.

3.2.2. Viscous Effects

Considering the plumes are a fluid flowing through a channel, there will be a boundary layer formed at the walls of the channels where viscous interactions such as friction and heat convection are present. These two aspects are tackled from a theoretical qualitative perspective to analyse how they affect flow in a constant area channel and a varying area channel.

Fanno Flow

Frictional effects caused by the boundary layer along the channel walls can be analysed using the concept of Fanno flow. Fanno flow describes adiabatic flow through a constant-area duct or channel with the inclusion of frictional losses along the walls (Shapiro 1953). This model is widely used to study how friction influences compressible flow properties such as velocity, pressure, temperature, and density within ducts or conduits of fixed cross-sectional area.

The integral forms of the conservation equations can be seen in Equation 3.32, Equation 3.33, and Equation 3.35. Equation 3.32 is the continuity equation where ρ is the fluid density and V is the fluid velocity, and the area has been cancelled out since it is considering a constant area channel. Equation 3.33 is the momentum equation where p is the fluid pressure, A is the cross-sectional area, τ is the shear stress, and D_h is the hydraulic diameter given by Equation 3.34 where P is the perimeter of the channel. Equation 3.35 is the energy equation where H is the total enthalpy of the fluid, h is the specific enthalpy of the fluid (Zucker and Biblarz 2019).

$$I = \rho V = \text{constant} \tag{3.32}$$

$$pvAdv + Adp - \tau\pi D_h dx = 0 \tag{3.33}$$

$$D_h = \frac{4A}{P} \tag{3.34}$$

$$H = h + \frac{V^2}{2} = \text{constant} \tag{3.35}$$

By combining the continuity equation and the energy equation for Fanno flow, one obtains the fundamental relationship shown in Equation 3.36, which relates the specific enthalpy h and the specific volume v of the fluid. This relationship allows the plotting of a family of curves known as Fanno lines on an h-v diagram by varying the Fanno parameter I and the total enthalpy H.

Since the flow is assumed adiabatic but with friction, the second law of thermodynamics requires that the entropy of the fluid must increase along the flow direction (positive x-direction). This is because friction irreversibly dissipates mechanical energy into internal energy, increasing entropy.

In Figure 3.13, three Fanno lines are illustrated on a h-v diagram, along with another family of curves representing isentropic lines (constant entropy).

Each Fanno line intersects a single isentropic curve twice at points labelled a and b, and becomes tangent to a higher-entropy isentropic curve at point c. This tangency point c represents a critical condition where the flow reaches its maximum entropy for that Fanno line.

- Starting from a high enthalpy state $h = h_t$ (to the right on the diagram), a fluid particle moving downstream will follow the Fanno line from right to left, passing through point a and eventually approaching the tangent point c.
- Conversely, starting at a low enthalpy state $h = 0$ (to the left on the diagram), the fluid particle will move from left to right, passing through point b and also approaching point c.

The two regions defined by this behaviour correspond to:

- Above point c: flow is subsonic (Mach number < 1)
- Below point c: flow is supersonic (Mach number > 1)

Point c itself represents the sonic condition (Mach number = 1) where the flow velocity reaches the local speed of sound.

Thus, friction in a constant-area one-dimensional channel drives the flow Mach number toward unity, causing the flow to become sonic at a critical length, a phenomenon called frictional choking (Zucker and Biblarz 2019).

$$h + \frac{1}{2} I^2 \left(\frac{1}{\rho}\right)^2 = H \tag{3.36}$$

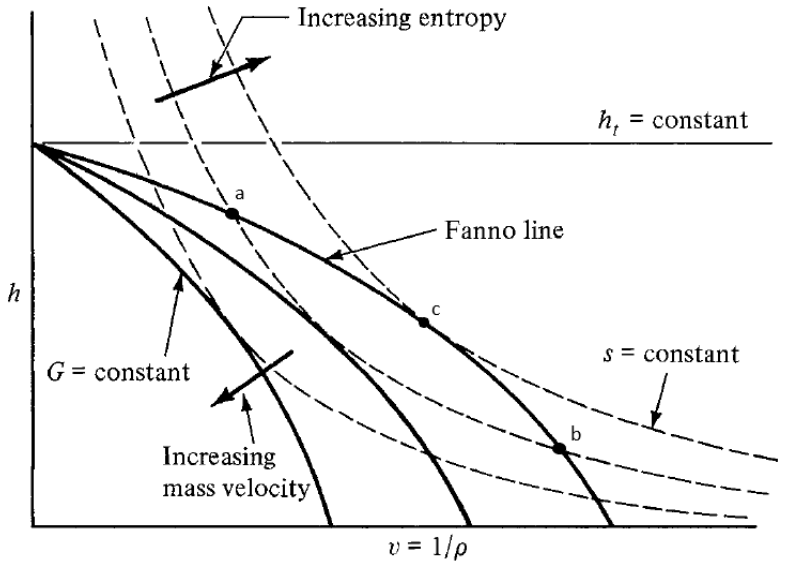

Figure 3.13: Fanno curves in the h-v plane represent compressible flow with friction in a constant area duct. The Fanno line intersects constant-entropy and constant-total-enthalpy curves, with increasing entropy and mass velocity indicated along the curve. The curve passes through a maximum entropy point corresponding to the sonic condition (M=1). The diagram illustrates the thermodynamic effect of increasing entropy and mass velocity due to wall friction, transitioning from subsonic to choked and supersonic regimes. (Adapted from Zucker and Biblarz (2019))

For channels with a variable cross-sectional area, such as those found in converging-diverging geometries, the governing flow equations must be analysed as a non-linear system of two coupled ordinary differential equations. These typically arise from the differential forms of the continuity, momentum, and energy equations, where the area $A(x)$ becomes a function of the stream-wise coordinate.

This analysis is especially relevant for converging-diverging nozzles, a common analogue used to study high-speed flows through volcanic vents or icy fissures like those on Enceladus. In an ideal, isentropic and frictionless nozzle, the flow reaches sonic speed (Mach 1) precisely at the geometric throat. However, when friction is included, this idealised behaviour changes.

Specifically, friction causes the flow to reach sonic conditions downstream of the geometric throat. This occurs because the boundary layer, generated by viscous effects along the walls, grows with downstream distance, effectively reducing the available cross-sectional area through which the flow can pass. In turn, this causes a shift in the location of the sonic point. As a result:

- Subsonic flow at the geometric throat can accelerate, but the maximum velocity may be limited by frictional losses.
- Supersonic flow downstream may decelerate, contrary to the frictionless case, due to momentum loss to wall shear stress.

Rayleigh Flow

As the plumes ascend through the subsurface channels of Enceladus, they can undergo convective heat exchange, where thermal energy is transferred between the vapour flow and the surrounding icy walls. This process is particularly relevant in regions where temperature gradients are significant, such as near the ocean-ice interface or along the frigid surface fissures. To model this, we consider Rayleigh flow, which describes steady, one-dimensional, inviscid flow with heat addition or removal (Zucker and Biblarz 2019). Considering a constant area channel, the integral forms of the conservation equations can be seen in Equation 3.37, Equation 3.38, and Equation 3.39. Equation 3.37 represents the continuity equation and is identical for Fanno flow. Equation 3.38 is the momentum equation which is identical for inviscid flow as it does not include the friction term that is present in Fanno flow. Equation 3.39 is the energy equation where H_1 and H_2 are the total enthalpy at points 1 and 2 respectively, and q is the heat addition/removal.

$$I = \rho V = \text{constant} \tag{3.37}$$

$$p + \rho V^2 = \text{constant} \tag{3.38}$$

$$H_1 + q = H_2 \tag{3.39}$$

The relationship between pressure and specific volume in Rayleigh flow can be derived by combining the continuity and momentum equations, yielding Equation 3.40. This relationship can be visualised on a p-v diagram, where the Rayleigh line appears as a straight line with a negative slope, as shown in Figure 3.14. Isothermal and isentropic curves can also be plotted on the same diagram using Equation 3.41 and Equation 3.42, respectively. These curves allow for comparison of idealised flow paths with and without heat exchange or entropy change.

It is important to note that the slope of the isentrope is always steeper than that of the isotherm at a given point on the p-v graph. This geometric relationship has direct implications for the thermodynamic path followed during heat addition or removal in Rayleigh flow. For example, consider adding heat to a subsonic flow starting from a point labelled 1. As heat is added, the temperature increases along the Rayleigh line, reaching a maximum at point 3. Entropy also increases but reaches its maximum at a point 4, the point where the Mach number reaches 1.

This divergence occurs because of how heat affects the different forms of energy in the flow. As heat is added, the density decreases (due to thermal expansion). From the continuity equation, a decrease in density leads to an increase in velocity to conserve mass flow. The increased velocity means more kinetic energy, which scales as v^2. At some point, all added heat goes into accelerating the flow (kinetic energy), and no further increase in internal energy (enthalpy or temperature) is possible. This marks the point of maximum temperature and enthalpy.

Beyond this point, continued heat addition actually causes the temperature and enthalpy to decrease in order to satisfy the total energy balance in Equation 3.39. This behaviour results in the curve bending back toward lower temperatures despite ongoing heat input.

The point of maximum entropy corresponds to the choking condition, where the Mach number equals unity. Above this point, the flow is subsonic, and below it, the flow is supersonic. Thus, just like

in Fanno flow, Rayleigh flow tends to drive the Mach number toward 1, but through the mechanism of heat transfer rather than wall friction.

This process is known as thermal choking (Zucker and Biblarz 2019). In the context of Enceladus' plume dynamics, such thermal effects could be significant in regions where latent heat is released through deposition or wall accretion or where cooling due to sublimation occurs as the vapour expands toward the surface.

$$p + I^2 v = \text{constant} \tag{3.40}$$

$$pv = \text{constant} \tag{3.41}$$

$$pv^{\gamma} = \text{constant} \tag{3.42}$$

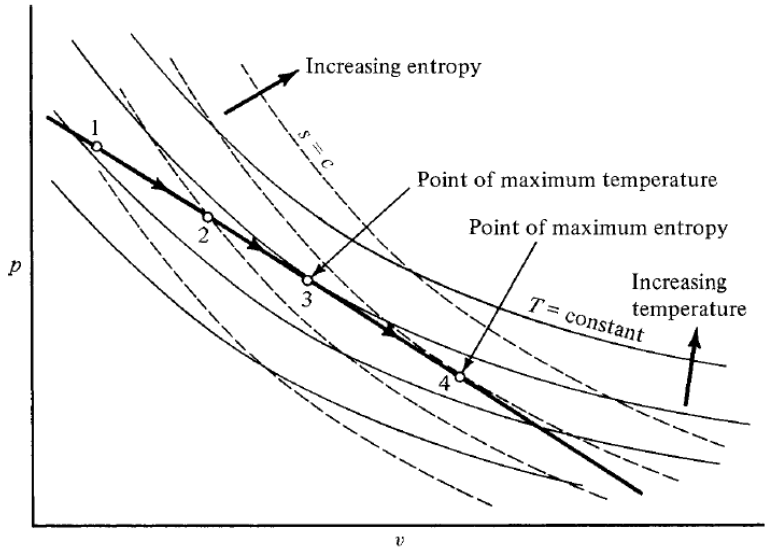

Figure 3.14: Rayleigh curves in p-v plane illustrate the behaviour of compressible flow with heat addition at constant area. The Rayleigh line intersects a family of isentropic curves, showing the increase in entropy and identifying key points such as maximum temperature and maximum entropy along the flow path. Notable points include the state of maximum entropy (choked flow at M=1) and maximum static temperature (Zucker and Biblarz 2019).

For channels with a varying cross-sectional area, the location at which the Mach number reaches unity (i.e., sonic conditions) does not necessarily coincide with the geometrical throat. In the case of Rayleigh flow, where heat addition or removal is involved, the condition for choking (Mach 1) shifts depending on the direction of heat transfer. Specifically, at the point where the Mach number equals 1, the differential area change dA must be:

- Positive (i.e., diverging geometry) when heat is added to the flow.
- Negative (i.e., converging geometry) when heat is extracted.

This condition is derived from the differential form of the quasi-one-dimensional compressible flow equations, incorporating heat transfer effects (Oosthuizen and Carscallen 1997). The implication is that the sonic point is displaced downstream or upstream of the physical throat depending on the thermal interaction with the channel walls.

In the context of Enceladus' plume channels, this is particularly important. As vapour flows upward through the channels, it may experience heat loss due to sublimation of the walls or heat gain due to deposition of vapour and wall accretion. These thermal interactions will shift the position of the choking point, and consequently the distribution of flow speed and pressure along the channel. For example, localised heating due to vapour condensation may delay the onset of choking and move the sonic point downstream, beyond the narrowest part of the channel. Conversely, cooling due to sublimation could cause the choking point to move upstream, closer to or even before the geometric throat.

3.2.3. Non-Equilibrium Homogenous Nucleation

During isentropic expansion, the temperature and pressure of the flow will drop and for a convergent-divergent nozzle it will continue to drop in the divergent section if it becomes choked at the throat. Looking at the water phase diagram in Figure 3.4 and examining the saturation curve for condensation, it can also be noted that the pressure decreases for decreasing temperature as well. Therefore, it is interesting to check whether supersaturation occurs based on the slopes of the saturation curve and for isentropic flow. Wegener (1963) derived this ratio that is a function of the specific enthalpy of vaporisation L_h, the specific heat capacity of the vapour c_p and the temperature of the gas T as shown in Equation 3.43.

$$\frac{\left(\frac{\partial p}{\partial t}\right)_{\text{condensation}}}{\left(\frac{\partial p}{\partial t}\right)_{\text{isentropic}}} = \frac{L_h}{c_p \cdot T} \tag{3.43}$$

If this ratio exceeds one, the saturated vapour pressure curve declines more steeply with temperature than the isentropic pressure path. For water and most vapours, this condition holds true across the entire temperature range from 0 °C up to the critical point. Consequently, during isentropic expansion, the vapour pressure drops faster than the static pressure of the expanding gas. If the expansion continues long enough, the vapour reaches its saturation point. Beyond this point, two outcomes are possible: either condensation begins, or the vapour enters a metastable regime, becoming supersaturated (S>1) without immediately transitioning to another phase. In the first scenario, continued expansion drives ongoing condensation, and the flow follows a saturated isentrope, maintaining S=1. In the second scenario, the vapour behaves as though the phase boundary is absent, continuing along a “dry” isentrope despite being thermodynamically supersaturated.

In compressible flows involving adiabatic expansion of saturated or near-saturated steam, condensation heat transfer occurs in regions where the local pressure falls below the saturation pressure. In transonic or supersonic regimes, flow velocity strongly influences the condensation process. If the condensation timescale is shorter than the expansion timescale, condensation is delayed. As a result, instead of undergoing an equilibrium phase change at the saturation temperature, the vapour continues to expand into a sub-cooled state.

The expansion of steam from a superheated to a wet state within a typical convergent-divergent nozzle is illustrated in Figure 3.15. Steam enters the nozzle as dry, superheated vapour at point (1) and expands to sonic conditions at point (2). As the steam continues to expand, it crosses the saturation line at point (3), which may occur either before or after the throat. Despite crossing into the thermodynamic wet region, condensation does not occur immediately due to the finite time required for droplet formation. Instead, the steam enters a metastable, supercooled (or supersaturated) state in which it remains a single-phase vapour (Hasini et al. 2012). As the expansion proceeds, the degree of supercooling increases until it reaches point (4) known as the Wilson point. This is the location where homogeneous nucleation first begins, marking the onset of droplet formation. Beyond this point, nucleation occurs rapidly and the number of droplets increases sharply. Between points (4) and (5), this nucleation zone transitions into a growth zone, where the existing nuclei grow rapidly and release latent heat, progressively restoring the flow toward thermodynamic equilibrium. The final stage of expansion, from points (5) to (6), proceeds under near-equilibrium wet steam conditions (Hasini et al. 2012).

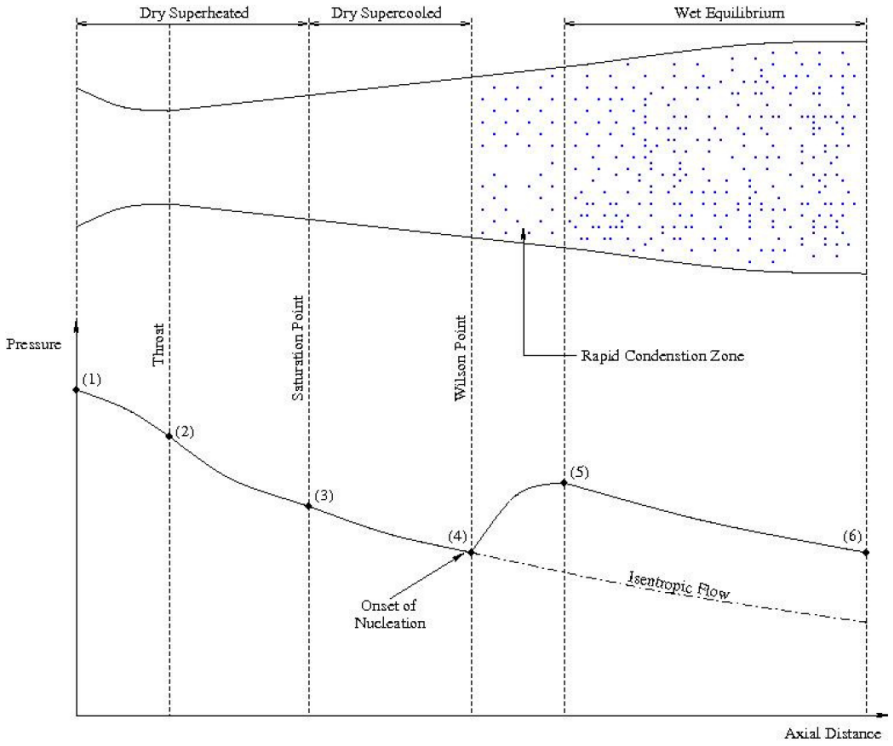

Figure 3.15: Schematic of a nozzle with spontaneous condensation with the pressure distribution shown for different locations along the channel marked with a comparison for a pure isentropic flow (Hasini et al. 2012)

Without foreign particles to act as nucleation sites, the phase change does not occur immediately due to the Gibbs free energy barrier associated with spontaneous droplet formation. This leads to a non-equilibrium condition. When the level of subcooling surpasses a critical threshold, this energy barrier is overcome, triggering a series of complex processes in the metastable vapour. These processes are typically described using kinetic theory, and nucleation begins homogeneously at numerous points throughout the flow field. The phase transition is driven by kinetic rates rather than being at the equilibrium saturation point.

Figure 3.16 shows the pressure distribution along a nozzle for homogeneous nucleation of water vapour with and without a condensation shockwave. The dashed line represents the local-to-static pressure ratio due to an isentropic expansion, whereas the solid line represents the local-to-static pressure ratio due flow with homogeneous nucleation (Matsuo et al. 1986). The Mach number of the flow is subsonic upstream of the throat, reaches sonic conditions at the throat, and becomes supersonic downstream. In Figure 3.16a, a schematic of the nozzle is shown, highlighting the region of non-equilibrium condensation, which occurs after the initial “dry” isentropic expansion and before the saturated isentropic expansion. If the latent heat released during condensation is sufficiently high, it can raise the static pressure ratio above the value at the throat leading to thermal choking (Matsuo et al. 1986). This process is typically accompanied by shock waves, referred to as condensation shocks, occurring where thermal choking sets in shown in Figure 3.16b. In this figure, the local-to-total static pressure ratio temporarily exceeds the throat value, causing the supersonic flow to decelerate to subsonic speeds over a short section. The flow then accelerates again, passing through sonic conditions and eventually returning to supersonic speeds.

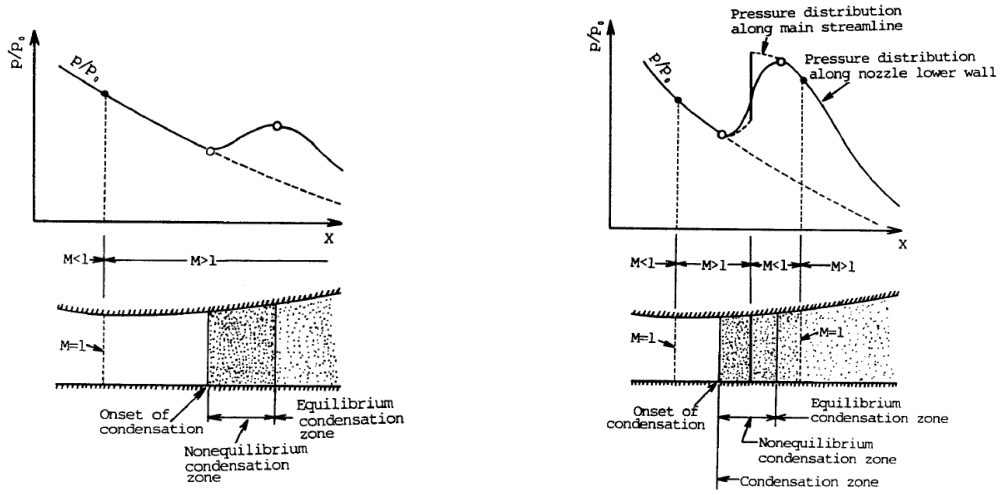

(a) Without a condensation shockwave

(b) With a condensation shockwave

Figure 3.16: Pressure distribution of steam in a nozzle with non-equilibrium homogeneous nucleation (Matsuo et al. 1986)

Wilson Point

In rapidly expanding supersonic flows, particularly those involving vapour such as steam, the Wilson point denotes the location at which homogeneous condensation/deposition initiates. This phenomenon is critically relevant to steam turbines, organic Rankine cycles, and cryovolcanic jets such as those observed on Enceladus (Azzini 2019). The delay in phase transition caused by metastable conditions alters both thermodynamics and flow behaviour, and modelling the Wilson point enables more accurate prediction of the occurrence of phase change.

When a supersaturated vapour undergoes isentropic expansion in a supersonic nozzle, it can remain in a metastable vapour state even after crossing the equilibrium saturation line. This supercooled vapour can persist until reaching the spinodal limit or until nucleation rates become high enough to trigger rapid condensation. The Wilson point marks the point where nucleation rate spikes and condensation becomes significant.

The Wilson temperature T_W at which condensation begins can be empirically correlated with the cooling rate using Equation 3.44 where T_{sat} is the equilibrium saturation temperature, T_{cr} is the critical temperature, Wi is the Wilson number and C_r is the average cooling rate defined by Equation 3.45.

$$T_W = T_{sat} - T_{cr} Wi \tag{3.44}$$

$$C_r \equiv \frac{1}{T_{cr}} \frac{dT}{dt} \tag{3.45}$$

The Wilson number Wi, a dimensionless number reflecting the delay in condensation due to finite cooling rates can be expressed using Equation 3.46 with ΔT_{cr} representing the supercooling at activation time t_{act} (Azzini 2019).

$$Wi = \frac{\Delta T_{cr}}{C_r} \tag{3.46}$$

In numerical models, the Wilson point is often identified via the inflection point in the temperature profile or via a threshold nucleation rate J, such as (Azzini 2019):

$$J > 10^{12} \text{ droplets/(m}^3 \text{ s)}$$

In the study of Enceladus' icy plumes, the Wilson point helps explain where in the subsurface channels condensation or deposition first occurs (Fontes 2023). Fontes (2023) demonstrates this through quasi-1D simulations and identifies how varying crack geometries alter the location and strength of the Wilson point. For example, increasing the crack length delays condensation onset by prolonging metastability, shifting the Wilson point downstream (Fontes 2023). Wilson points are often visualised on P–T or T–s diagrams. In these plots, the Wilson point lies between the saturation and spinodal lines, marking the sharp transition from supercooled vapour to a two-phase mixture. Experimental and numerical results frequently overlap in this regime, validating semi-empirical correlations such as those used by Azzini (2019). For water vapour expanding at typical Wilson numbers are on the order of 0.1,

which translates to temperature drops of several degrees below saturation before condensation begins (Azzini 2019).

3.3. Wet Steam Model

The condensation of steam in non-equilibrium, supersonic flow conditions has been a subject of research for more than seven decades. Rather than providing an exhaustive historical review, this section offers a concise summary of the key principles guiding the modelling of such flows. Readers seeking a broader context are referred to classic reviews by Wegener and Mack (1958), Feder et al. (1966), Hill (1966), Gyarmathy (1976), Lai and Kadambi (1993), Lamanna (2000), and Bakhtar et al. (2005), among others.

In the context of continuum fluid dynamics, the modelling of condensation typically follows one of two conceptual approaches:

- Eulerian–Lagrangian Framework: In this approach, the gaseous phase is resolved in a Eulerian framework. That is, from a fixed spatial viewpoint using standard CFD techniques like finite volume or finite element methods to solve the Navier–Stokes equations. In contrast, liquid droplets are tracked individually in a Lagrangian frame, from the perspective of a moving observer. Each droplet's trajectory is calculated via Newtonian mechanics, accounting for drag, gravitational forces, and other relevant interactions with the gas. This method provides a detailed and accurate description of droplet behaviour and flow dynamics. However, the cost of tracking individual droplets, especially in complex or turbulent flow regimes leads to a significant computational cost, which increases sharply with problem complexity.
- Eulerian–Eulerian Framework: Here, both the vapour and liquid phases are modelled as interpenetrating continua, each described by its own set of conservation equations. Rather than tracking individual droplets, the model captures phase interactions using spatially averaged quantities such as droplet number density, liquid mass fraction and an average droplet radius.

Although this approach sacrifices some fidelity, particularly during the early stages of nucleation where steep gradients exist, it offers considerable computational savings (Gerber and Kermani 2004; Young 1992). It has proven effective across a wide range of practical scenarios and is particularly advantageous when computational resources are constrained (Karagiannis 2020). A Wet Steam model developed by Gerber and Kermani (2004) was implemented by Karagiannis (2020) to analyse non-equilibrium condensation in supersonic mironozzles. This model was then adapted by Fontes (2023) to be applicable for modelling condensation in Enceladus' channels and was be used as a basis for this work.

3.3.1. Conservation Equations

The 2D wet steam model has been used to describe non-equilibrium homogeneous condensation of water vapour in supersonic flows (Wen et al. 2020). This model can be described by Equation 3.47 to Equation 3.53 (Gerber and Kermani 2004). The first equation represents the conservation of mass where ρ is the fluid density, t is time, $\vec{U}$ is the flow velocity in the channel, and S_m are the source and sink terms relevant to the conservation of mass. The second equation is the momentum equation where τ is the viscous stress tensor given by Equation 3.48, p is the fluid pressure and S_U are the source and sink terms relevant to the conservation of momentum. The third equation is the energy equation where E is the total specific energy of the flow, H is the total specific enthalpy of the flow, k_{eff} is the effective thermal conductivity (molecular conductivity and turbulent thermal conductivity), H_p is the total enthalpy of the droplet given by Equation 3.51, and L_h is the latent heat released by condensation of the vapour.

$$\begin{aligned}
&\frac{\partial \rho}{\partial t} + \nabla \cdot \left(\rho \vec{U}\right) = S_m \\
&\frac{\partial}{\partial t}\left(\rho \vec{U}\right) + \nabla \cdot \left(\rho \vec{U}\vec{U}\right) = -\nabla p + \nabla \cdot \tau + S_U \\
&\frac{\partial}{\partial t}\left(\rho E\right) + \nabla \cdot \left(\rho \vec{U} E + p\vec{U}\right) = \nabla \left(k_{\text{eff}} \nabla T + \left(\tau \cdot \vec{U}\right)\right) + S_h
\end{aligned} \tag{3.47}$$

$$\tau \equiv \tau_{ij} = \mu \left(\frac{\partial u_i}{\partial x_j} + \frac{\partial u_j}{\partial x_i} - \frac{2}{3}\frac{\partial u_k}{\partial x_k}\delta_{ij}\right) \tag{3.48}$$

$$E \equiv e + \frac{1}{2}\vec{U}^2 \quad (3.49) \qquad H \equiv h + \frac{1}{2}\vec{U}^2 \quad (3.50) \qquad H_p = H - L_h \quad (3.51)$$

In order to complete the system, two additional conservation equations need to be formulated. Two transport equations are introduced to describe the phase change process occuring within the flow for non-equilibrium condensation. To describe the evolution of the solid fraction f, Equation 3.52 is used where S_f are the sink terms relevant to the solid fraction conservation. Furthermore, Equation 3.53 is used to describe the evolution of the droplet number per unit vapour of mass, N where J is the nucleation rate and S_N are the sink terms relevant to the droplet number conservation.

$$\frac{\partial}{\partial t}(\rho f) + \nabla \cdot \left(\rho f \vec{U}\right) = S_f \quad (3.52) \qquad \frac{\partial}{\partial t}(\rho N) + \nabla \cdot \left(\rho N \vec{U}\right) = S_N \quad (3.53)$$

Source Terms

Looking at the transport equation Equation 3.53, the sink term S_f is given by Equation 3.54. This makes sense because it denotes the generation of new droplets due to the vapour undergoing nucleation, thereby increasing the droplet number. It is emphasised that the droplet number N is per unit vapour mass and therefore Equation 3.54 respects the unit dimensions for the droplet number conservation.

$$S_N = J \quad (3.54)$$

Furthermore, the sink term S_f in the transport equation Equation 3.52 is given by Equation 3.55. Here, the mass fraction f is defined by Equation 3.56 as the fraction of the mass flow of the icy grains to the total mass flow and the critical radius r^* is given by Equation 3.12. The sink term for the conservation of mass fraction depends on nucleation and the subsequent growth of the droplets. This first term is due to nucleation and represents the mass flow due to the generation of new droplets due to nucleation. The second term is due to the droplet growth and represents the mass condensation rate of all the droplets per unit volume of vapour.

$$S_f = \frac{4}{3}\pi {r^*}^3 \rho_l J + 4\pi r^2 \rho_l \frac{dr}{dt}\rho_v \quad (3.55)$$

$$f \equiv \frac{\dot{m}_l}{\dot{m}_{\text{flow}}} \quad (3.56)$$

For the conservation of mass, the source term S_m is equal and opposite to that of the liquid phase given by Equation 3.57. Then it follows that the source term in the momentum equation S_U is simply S_m convected by the velocity given by Equation 3.58 and the source term in the energy equation S_h is also S_m but multiplied by the droplet total enthalpy given by Equation 3.59.

$$S_m = -S_f \quad (3.57) \qquad S_U = \vec{U} \cdot S_m \quad (3.58) \qquad S_h = H_p \cdot S_m \quad (3.59)$$

3.3.2. Nucleation Rate

From classical nucleation theory, the nucleation rate that is commonly used is given by Equation 3.21. As previously mentioned, the surface tension has a very strong influence on the nucleation rate and therefore, the surface tension must be carefully chosen. The surface tension of water is a difficult parameter to measure and there are several different empirical formulae suggested by different authors for different temperature ranges. The surface tension of the droplet has been experimentally derived to be a function of temperature as seen in Equation 3.60 (Viisanen et al. 1993).

$$\sigma_{l,v} = 93.6635 \cdot 10^{-3} + 9.133 \cdot 10^{-6} T - 2.75 \cdot 10^{-7} T^2 \quad [N/m] \quad (3.60)$$

The supersaturation is defined as the ratio of the vapour density given by Equation 3.61 where ρ_{gas} and the vapour-liquid equilibrium densities, $\rho_{eq}^{(l,v)(T_{gas})}$. The nucleation rate of water can then be computed by applying the Wölk correction factor in Equation 3.28.

$$S \equiv \frac{\rho_{gas}}{\rho_{eq}^{(l,v)(T_{gas})}} \quad (3.61)$$

$$p_{eq}^{(l,v)}(T_{\text{gas}}) = 610.8 \exp\left(-5.1421 \ln\left(\frac{T}{273.15}\right) - 6828.77\left(\frac{1}{T} - \frac{1}{273.15}\right)\right) \quad [Pa] \quad (3.62)$$

3.3.3. Droplet Growth Model

Once liquid water clusters reach the critical size for nucleation, they form stable liquid germs, initiating the second stage of condensation, droplet growth. As the vapour expands rapidly through the nozzle (or Enceladus' channel system), it cools substantially faster than the droplets it surrounds. Initially, the droplet temperature T_p is nearly equal to the gas temperature T_g , but the steep thermal gradient caused by adiabatic expansion causes cold vapour molecules to collide with the relatively warmer droplet surface. These molecules condense onto the droplet, releasing latent heat and increasing the droplet's mass and radius.

A conceptual control volume around the droplet is shown in Figure 3.17. The figure illustrates the heat transfer process around a droplet forming in a supercooled vapour. The droplet, with radius r_1, is at temperature T_f and releases latent heat as condensation occurs at its surface. This heat is first transferred from the droplet into the thin vapour layer directly adjacent to the surface, represented by the heat flux $Q(r_1)$.

The adjacent vapour layer, however, is not the final sink for this heat. It must in turn transfer the absorbed energy outward into the surrounding supercooled bulk vapour, represented by the heat flux $Q(r_2)$. The temperature distribution reflects this transfer: the droplet temperature is highest, $T_f > T(r_1)$, the adjacent vapour is warmer than the outer vapour, $T(r_1) > T(r_2)$, and the bulk supercooled vapour remains at the lowest temperature, $T(r_2) > T_g$. Whether condensation proceeds depends on the balance between these two fluxes. If the outer vapour can reject more heat than the adjacent vapour receives, $Q(r_2) > Q(r_1)$, the adjacent vapour remains cool enough to sustain condensation. By contrast, if $Q(r_2) < Q(r_1)$, the adjacent vapour heats up, diminishing the local temperature gradient and suppressing condensation (Fontes 2023; Lai and Kadambi 1993).

Thus, the rate of condensation is limited not only by the droplet's release of latent heat but also by the efficiency with which this heat can be transported away through the surrounding vapour into the colder environment.

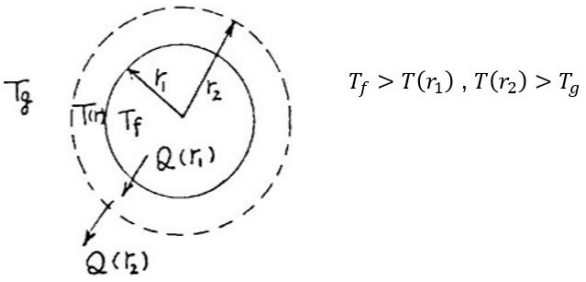

Figure 3.17: Schematic illustration of heat transfer in the vicinity of a droplet immersed in supercooled vapour. The droplet, at temperature T_f, is surrounded by a radial temperature field $T(r)$ that decreases outward toward the far-field vapour temperature T_g. Heat flows from the droplet to the surrounding vapour at radius r_1, denoted $Q(r_1)$, and is subsequently conducted away to the far-field at r_2 as $Q(r_2)$. When $Q(r_2) > Q(r_1)$, the adjacent vapour loses energy and condenses on the droplet, supporting its growth (Lai and Kadambi 1993).

The heat balance for this process can then be written out with Equation 3.63 where h_g and h_f is the specific enthalpy of the vapour and droplet respectively, m_p and r are the mass and radius of the nucleated droplet respectively, λ_v is the convective heat transfer coefficient from the gas to the droplet, T_p is the droplet temperature and $c_{\mathrm{H_2O}}$ is the specific heat capacity of water.

$$(h_g - h_p)\frac{dm_p}{dt} = 4\pi r^2 \lambda_v (T_p - T) + m_p c_{\mathrm{H_2O}} \frac{dT_p}{dt} \tag{3.63}$$

Through experimental analysis, it was found that given the nucleated droplets are so small it means their heat capacity is negligible and the thermal relaxation time is much faster leading to a small value in temperature gradient (Lamanna 2000). For this reason, the last term on the RHS of Equation 3.63 is assumed to be negligible. Furthermore, the equation can be expressed for the droplet radius leading to Equation 3.64.

$$4\rho_p \pi r^2 (h_g - h_p)\frac{dr}{dt} = 4\pi r^2 \lambda_v (T_p - T_v) \Leftrightarrow \frac{dr}{dt} = \frac{\lambda_v (T_p - T_v)}{(h_g - h_p)\rho_p} \tag{3.64}$$

The widely most accepted expression used to compute λ_v that is suitable for low pressures is given by Equation 3.65 where k_v is the thermal conductivity of the vapour, γ is the specific heat ratio of the vapour, Kn_p is the droplet based Knusden number and Pr is the Prandtl number, r_c is the Kelvin-Helmholtz critical droplet radius given by Equation 3.12, and ν is a modelling correction coefficient to account for non-equilibrium effects in droplet growth at low pressures (Gyarmathy 1976; Young 1980). The droplet based Knudsen number is given by Equation 3.66 where λ is the molecular mean free path of steam. Furthermore, the Prandtl number is given by Equation 3.67 where c_p is the specific heat of vapour and μ is the dynamic viscosity.

$$\lambda_v = \frac{k_v}{r} \frac{1 - r^*/r}{1 + 3.78\,(1-\nu)\,\frac{Kn_p}{Pr}} \tag{3.65}$$

$$Kn_p \equiv \frac{l}{2r} \tag{3.66}$$

$$Pr \equiv \frac{c_p \mu}{k_v} \tag{3.67}$$

The modelling correction coefficient ν can be computed using Equation 3.68 where $T_{eq}^{(s,g)}$ is the saturated vapour temperature at the vapour-solid equilibrium, q_c and α are the condensation coefficient and modelling parameter respectively where $q_c = 1.0$, $\alpha = 1.0$ (Wen et al. 2020). The rate of droplet growth can then be computed with Equation 3.69.

$$\nu = \frac{R_{\text{gas}} T_{eq}^{(l,v)}}{\Delta h_{vap}} \left(\alpha - 0.5 - \frac{2 - q_c}{2 q_c} \frac{(\gamma+1) c_p T_{eq}^{(l,v)}}{2\gamma \Delta h_{vap}} \right) \tag{3.68}$$

$$\frac{dr}{dt} = \frac{k_v\,(T_p - T_v)}{\rho_p L_h r} \frac{1 - r^*/\bar{r}}{1 + 3.78(1-\nu)\frac{Kn_p}{Pr}} \tag{3.69}$$

An equation for the droplet temperature can be found by deriving a kinetic expression for the droplet growth and equating it to Equation 3.69 (Gyarmathy 1976). Instead of cumbersomely solving for T_p iteratively via the full kinetic expression, Gyarmathy (1976) proposed a linearised approximation with a negligible error given by Equation 3.70 where $T_s\,(p)$ is the saturation temperature at local pressure.

$$T_p = T_s\,(p) + [T_s\,(p) - T_v]\,\frac{r^*}{r} \tag{3.70}$$

3.4. Icy Steam Model

For Enceladus, it is evident that there must be generation of ice particles from the plumes based on the data obtained by Cassini in 2005 to 2017 (Dougherty et al. 2018). Looking at the water phase diagram in Figure 3.4, one would expect that there would be solely water vapour to ice nucleation and therefore ice deposition.

3.4.1. Water-Ice vs. Ice Nucleation from the Vapour Phase

Although the previous sections focused on thermodynamic conditions well below the triple point, no explicit treatment was given to the possibility of liquid water freezing or water vapour depositing directly as ice. A substantial body of research has explored vapour nucleation at sub-freezing temperatures, with Wyslouzil and Wölk (2016) providing a broad experimental overview. From this literature, several key observations can be made on the comparison of water and ice nucleation. Even at temperatures as low as 200 K, vapour typically condenses into liquid before transitioning to ice. This stepwise process termed the Ostwald step rule first proposed by Ostwald (1897) and supported by experiments (Manka et al. 2012; Wyslouzil and Wölk 2016) delays the onset of deposition. As a result, Karagiannis (2020) found that droplets may leave a micronozzle nozzle before freezing begins.

Ostwald's Step Rule

The Ostwald step rule posits that in the formation of nuclei from supersaturated vapour, the liquid phase typically separates first, even if the vapour temperature is below the freezing point (Becker and Döring 1954). This principle has been theoretically underpinned and quantitatively refined by nucleation theories, including those that allow for the formation of both liquid and solid nuclei (Becker and Döring 1954). Peeters et al. (2002) found that nucleation rates for water vapour in helium reveal a transition at 207 K, suggesting a shift from vapour/liquid to vapour/ice nucleation as temperature decreases. This

observation aligns with Ostwald's rule, as the direct transition from vapour to ice is less likely than an intermediate vapour-to-liquid condensation, followed by liquid-to-solid (ice) nucleation (Hou et al. 2020; Manka et al. 2012). The nucleation barrier for ice crystals is generally higher than for water droplets under identical supersaturation conditions due to the greater surface free energy of ice ($\sigma_{s,v}$) compared to water ($\sigma_{l,v}$) (Hou et al. 2020). Consequently, for a given supersaturation, ice nucleation rates are significantly lower than water nucleation rates, supporting the step-wise process where supercooled water forms before ice.

Figure 3.18 illustrates the phase transitions of water within a supersonic nozzle, from vapour to liquid and then to solid ice (Manka et al. 2012). As a water-carrier gas mixture expands through the nozzle, the pressure and temperature drop, leading to supersaturation and subsequent vapour-liquid nucleation, forming nanometer-sized droplets. The heat released during this condensation process causes a temporary rise in temperature and pressure. Following droplet growth by condensation, a further decrease in temperature initiates liquid-solid nucleation, causing the droplets to freeze into ice (Manka et al. 2012). The rapid increase in condensate mass fraction correlating with the temperature increase due to latent heat release. The process culminates in the formation of solid water particles exiting the nozzle.

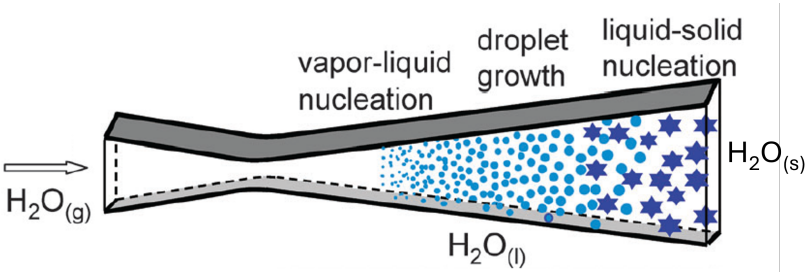

Figure 3.18: A side view of a supersonic micronozzle reveals the sequential phase transition processes obeying Ostwald's step rule: vapour–liquid nucleation initiates droplet formation, followed by droplet growth through vapour condensation, and ultimately, droplet freezing through liquid–solid nucleation (Manka et al. 2012).

Freezing of Water Droplets

Fransen et al. (2014) calculated the mean lifetime of supercooled droplets and found that freezing is negligible down to 240 K. Even at 220 K, the expected droplet lifetime exceeds 2 ms. While their results suggest that lower pressures might shorten this lifetime, the impact remains limited (Fransen et al. 2014). The latent heat released during the liquid-to-ice transition is small compared to that released during condensation. Manka et al. (2012) showed that for their nozzle experiments, the temperature rise due to freezing near 200 K is less than 1 K, only about 5% of the heating caused by condensation. The pressure and temperature signatures of condensation were distinct, while those of freezing were virtually undetectable.

The properties of supercooled water have primarily been investigated at atmospheric pressure, with reliable measurements generally limited to temperatures no lower than approximately 236–240 K. Below this range, experimental study becomes extremely challenging due to water's strong tendency to crystallise, except under conditions involving very short timescales or extremely small volumes (Amann-Winkel et al. 2016). This difficulty is so pronounced that the temperature range is often referred to as "no man's land" (Handle et al. 2017). Consequently, experimental data in this region are virtually absent, and researchers must often rely on extrapolations or theoretical approximations. Further complicating analysis is mounting evidence that water in this regime behaves in unusual ways occupying a transitional state between a liquid and amorphous ice (Handle et al. 2017).

Ice Nucleation from the Vapour Phase

There is a lack of research on the nucleation rate of ice directly from the vapour phase as this requires temperatures below 207 K (Peeters et al. 2002). Hou et al. (2020) suggests that one may simply use the CNT nucleation rate equation given by Equation 3.21 and using $S_{i,v}$, ρ_i, $\sigma_{i,v}$ and $\rho_{eq}^{(s,v)}(T_{\text{gas}})$ which can be inferred from Equation 3.71.

$$p_{eq}^{(s,v)}(T_{\text{gas}}) = \exp\left(\left(-\frac{2663.5}{T} + 12.537\right)\ln(10)\right) \quad [Pa] \tag{3.71}$$

However, as stated before the nucleation rate is extremely sensitive to the surface tension, or in this case the surface energy of ice and therefore needs to be determined carefully. Peeters et al. (2002) states that ice at temperatures above 235 K, a quasi-liquid layer envelops the ice and that the surface energy above 235 K can be determined using Antonow's rule shown in Equation 3.72.

$$\sigma_{s,v} = \sigma_{s,l} + \sigma_{l,v} \tag{3.72}$$

Then for temperatures below 235 K, this quasi-liquid layer is no longer present and the surface energy of ice $\sigma_{s,v}$ can be estimated based on the latent heat of deposition Δh_{dep} given by Equation 3.73 where a is the area per molecule on the ice surface and C is a correction factor experimentally determined to be 0.6 (Peeters et al. 2002).

$$\sigma_{s,v} = \frac{1}{2} C \Delta h_{dep} a \tag{3.73}$$

The area per molecule on the ice surface is determined by the spherical volume of an ice molecule using Equation 3.74 where N_A is Avogadro's constant, M is the molar mass of ice and ρ_{solid} is the density of the ice.

$$a = \left[4 N_A \left(\frac{3M}{4\pi N_A \rho_{\text{solid}}} \right)^{2/3} \right]^{-1} \tag{3.74}$$

Authors analysing ice crystal formation in high-pressure supersonic humid air low-temperature flow consider condensation-deposition of water vapour molecules by using the non-isothermal nucleation rate previously shown in Equation 3.25. However, they use the surface tension of water given by Equation 3.60 (Cui et al. 2011; Qiu et al. 2024; Ren et al. 2025). Furthermore, for studies on supersonic flow in Enceladus' channels, Schmidt et al. (2008b) argues that there are too few water molecules to be considered crystalline resulting in the vapour-liquid equilibrium values are favoured over the vapour-solid equilibrium values for the calculation of the supersaturation.

3.4.2. Grain Growth Model

The grain growth rate of ice grains can be derived analogously to the droplet growth rate for water droplets in subsection 3.3.3. The grain growth rate is given by Equation 3.75 where λ_v denotes the convective heat transfer coefficient between a water vapour molecule and the ice particle surface, T_g is the temperature of the grain, h_v is the specific enthalpy of the flow and h_g is the specific enthalpy of the grain defined as $h_g \equiv h_v - \Delta h_{sub}$.

$$\frac{dr}{dt} = \frac{\lambda_v \left(T_g - T_v \right)}{\rho_i \left(h_v - h_g \right)} \tag{3.75}$$

The calculation of convective heat transfer is given by Equation 3.76 and is modified to account for Knudsen number effects due to small droplets forming from homogeneous nucleation.

$$\lambda_v = \frac{N u k_g}{2\bar{r}} = \frac{k_g}{\bar{r} \left(1 + c K n_g \right)} \tag{3.76}$$

Water vapour surrounding an ice particle can be conceptualised as comprising three concentric layers. The innermost region is the deposition nucleus layer, where the ice particle has completed its initial growth and can be assumed to maintain a uniform temperature distribution due to negligible gradients. The intermediate region includes both the Knudsen layer ($Kn \leq 4.5$) and the free molecular regime (4.5<Kn $\leq$10) (Ren et al. 2025). In this zone, molecular-scale transport phenomena dominate, and the Knudsen number plays a critical role in governing the efficiency of heat and mass transfer. To model the ice crystal growth within this transition regime, the Gyarmathy model is employed, capturing non-continuum effects (Gyarmathy 1976). The outermost region corresponds to the turbulent flow regime (Kn>10), where continuum assumptions are valid and the dominant mechanisms of heat and mass transfer are strongly influenced by the macroscopic flow field, in contrast to the molecularly dominated intermediate region. Ren et al. (2025) uses Equation 3.77 for the innermost region and the intermediate region of the deposition nucleus layer.

$$Nu_{Gy} = \frac{2\bar{r}}{\left(\bar{r} + \frac{\sqrt{8\pi}}{1.5Pr_v}\frac{\gamma}{\gamma+1}\frac{2\mu\sqrt{R_v T_v}}{p_v}\right)}, \; Kn \leq 10 \tag{3.77}$$

For the outermost layer, Ren et al. (2025) uses the Hughmark model valid for high pressure gas which includes interphase momentum and energy exchange applicable for high Reynolds number conditions. Similar methods were employed by other authors (Cui et al. 2011; Qiu et al. 2024). However, for Enceladus the highest pressure in the channel is expected at the inlet to be triple point conditions (611.657 Pa) and the Reynolds number are expected to be moderate. Therefore, another method for the correction for the convective heat transfer coefficient λ_v should be used. Since the Gyarmathy model was used for ice nucleation from the vapour phase, it can be assumed that the same model developed by Gyarmathy and further refined by Young (1980) used in the droplet growth model described in subsection 3.3.3 can be used for grain growth. Equation 3.69, Equation 3.68 and Equation 3.70 can be used but then using the $T_{eq}^{s,v}$ and Δh_{dep} instead of $T_{eq}^{l,v}$ and Δh_{vap}.

4

2D Two-Phase CFD Model

In this chapter, the foundations for a 2D two-phase CFD model are presented that were used in the context of simulating the dynamics of Enceladus' plumes with an evolving wall channel. Since the flow will experience changes in its flow variables along the channel, it can for example start to accrete ice onto the walls, known as wall accretion. Furthermore, regardless if the wall is an adiabatic wall or an isothermal wall, it can also sublimate, known as wall sublimation. These two phenomena directly affect the shape of the channel and flow parameters as they act as sources/sinks in the Icy Steam model.

In section 4.1, models for the wall interactions such as wall accretion and wall sublimation are proposed. Furthermore, in section 4.2, the Icy Steam Model is combined with wall interactions to form a coupled framework that allows for CFD simulations and the channel geometry to change dynamically due to wall interactions.

4.1. Wall Interactions

The channel walls of Enceladus are presumed to be solid ice and therefore will have a certain temperature with respect to the flow. As mentioned in subsection 3.2.2, adding or removing heat to the flow has consequences on the flow development in the channel as well as nucleation. The addition or removal of heat to the flow can occur by having the wall of the channel set to a certain temperature. For an adiabatic wall, the wall will have the same temperature of the flow and therefore there will be no heat addition or removal due to the wall. However, if a fixed temperature is imposed then for a cold wall where the wall temperature is colder than the rest of the flow, it will cool down the flow and for a hot wall where the wall temperature is warmer than the rest of the flow it will heat up the flow. Since it is assumed that the cracks extend from the subsurface ocean where the temperature is at triple point conditions (273.6 K) to the surface where the temperature is about 180-200 K, that the cracks experiences a temperature gradient from the inlet of the channel to the outlet.

4.1.1. Wall Accretion: S_a

Wall accretion refers to the process by which gas-phase water molecules deposit onto a solid surface, forming layers of ice or frost. This phenomenon is particularly important in low-temperature and rarefied environments, such as planetary vents (e.g., Enceladus), cold nozzles, or microfluidic systems operating with condensable vapours (Kamenik et al. 2024; Pruppacher et al. 1998; van der Hijden 2021). Accretion is driven by molecular collisions between vapour molecules and the wall, moderated by thermophysical parameters such as temperature, thermal velocity, and sticking probability. The mass flux per unit area of gas-phase molecules impinging on a wall is given by kinetic theory using Equation 4.1.

$$\dot{m} = \rho_{\text{gas}} V_{th}, \quad \left[\text{kg/(m}^2 s)\right] \tag{4.1}$$

Here, ρ_{gas} is the vapour density and V_{th} is the thermal velocity of the molecules. For water vapour, the mean thermal velocity can be expressed using Equation 4.2 where k_B is the Boltzmann constant, T is the temperature, and $m_{\text{H}_2\text{O}}$ is the mass of a water molecule.

$$V_{th} = \sqrt{\frac{8k_bT}{\pi m_{H_2O}}} \tag{4.2}$$

This gives the average speed at which vapour molecules collide with a wall perpendicularly per unit area. However, not all molecules that collide with the wall will adhere and form ice. The actual accreted mass flux per unit area $\dot{m}_a$ depends on two additional factors: the sticking coefficient S_{stick}, which represents the probability that an impinging molecule adheres, and the accretion efficiency factor $f_{\text{accretion}}$ which is determined based on the cell size. This relationship is given by Equation 4.3 rooted in the Hertz–Knudsen model of surface mass transfer and appears widely in studies of vapour deposition and frost formation (Pruppacher et al. 1998).

$$\dot{m}_a = S_{\text{stick}}\dot{m}f_{\text{accretion}} \tag{4.3}$$

At the molecular level, the water molecules in the gas are spaced by 3Å, which means that there are $\left(\frac{1}{3\text{Å}}\right)^2$ molecules per m^2. Consider an area of 1 m^2, this means that there are roughly $\left(\frac{1}{3\times10^{-10}}\right)^2 \approx 10^{19}$ water molecules occupied in this area. Since the water molecules are spaced by 3Å, which is 1 layer, it has a mass equal to 3.3211×10^{-7} kg. The accretion rate of the ice layers can be determined independently of the area considered by dividing the mass accretion rate by the mass of one layer per unit area as shown in Equation 4.4.

$$\text{Rate of ice layers accreted} = \frac{\dot{m}_a}{\text{mass of 1 ice layer}}, \quad \left[\text{layers/(m}^2 s)\right] \tag{4.4}$$

This allows one to track the build-up of ice thickness over time. The time derivative of the change in wall thickness, assuming each added layer is 3Å thick becomes:

$$\frac{dR_{w,a}}{dt} = 3\text{Å} \cdot \text{Rate of ice layers accreted}, \quad [\text{m/s}] \tag{4.5}$$

Accretion Efficiency Factor: $f_{\text{accretion}}$

The accretion efficiency factor $f_{\text{accretion}}$ is determined based on the cell size. It is necessary to look at the Knudsen number in a cell given by Equation 4.6 where λ is the mean free path and L is a characteristic length given here as the cell height. The Knudsen number is a dimensionless parameter and indicates the degree to which a gas deviates from the continuum assumption. The ranges for the values of the Knusden number and their corresponding regions are given below. Since most CFD solvers are continuum flow solvers, it is therefore required that the Knudsen number is below 0.01. That is, the cell size should be larger than the mean free path.

$$Kn = \frac{\lambda}{L} \tag{4.6}$$

- $Kn < 0.01$: Continuum flow
- $0.01 < Kn < 0.1$: Slip flow
- $0.1 < Kn < 10$: Transitional flow
- $Kn > 10$: Free molecular flow

For water, the mean free path is given by Equation 4.7 where k_B is the Boltzmann constant, T is the vapour temperature, $d_{\text{H}_2\text{O}}$ is the molecular diameter of a water molecule, and p is the vapour pressure. At triple point conditions, the mean free path is 15.4 μm and therefore the cell size should be larger than this value. With this in mind, the accretion efficiency factor $f_{\text{accretion}}$ becomes the average probability that a molecule interacts with a wall surface.

$$\lambda_{\text{H}_2\text{O}} = \frac{k_BT}{\sqrt{2}\pi d^2_{\text{H}_2\text{O}}p} \tag{4.7}$$

For a CFD cell along the wall shown in Figure 4.1, the probability that a molecule strikes a wall is also governed by geometric constraints relative to the molecular mean free path λ. Since the thermal

velocity is random and chaotic, the vapour particles will collide with each other and the channel walls (van der Hijden 2021).

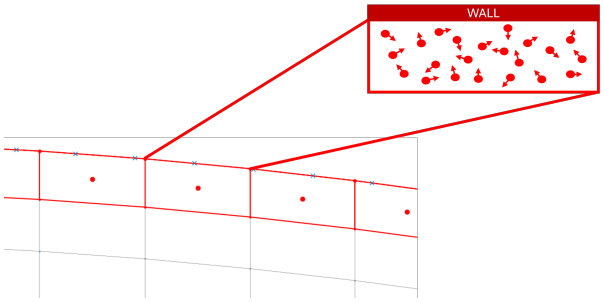

Figure 4.1: Illustration of water vapour molecules travelling in random directions with a thermal velocity v_{th} inside a CFD cell adjacent to the wall surface

The probability p_λ that a molecule moving freely will intersect with the wall before travelling a full mean free path can be approximated by a volume ratio between a wall-facing segment and the full spherical volume defined by λ shown in Figure 4.2 where h is the cap height defined as $h = \lambda - d$, which depends on the particle's distance from the wall.

$$p_\lambda = \frac{V_{\text{wall}}}{V_{\text{sphere}}} = \frac{\pi h^2 \left(\lambda - h/3\right)}{\frac{4}{3}\pi\lambda^3} \tag{4.8}$$

Vapour particles can only collide with the wall if they are located within a distance equal to the mean free path, λ, from it. This is because, following each collision, a particle's velocity is randomised and it travels in a straight path over a time interval Δt, during which it covers approximately one mean free path. Due to the high thermal velocity, the velocity distribution is assumed to fully randomise after every Δt, causing the vapour to undergo a new random flight of length λ at each step.

This motion can be visualised as the particle occupying any point on the surface of a sphere of radius λ centered at its position at time t. The probability of hitting the wall during this step depends on the particle's distance from the wall, denoted d. Specifically, the likelihood of a collision is related to how much of the spherical volume extends into the wall region.

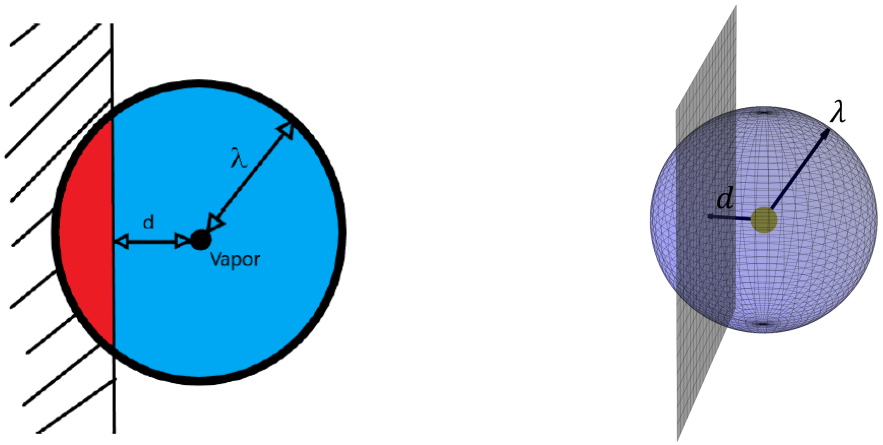

(a) 2D illustration: red area denotes the spherical cap

(b) 3D illustration

Figure 4.2: Schematic of the probabilistic wall-impact model for vapour particles near a wall surface. A particle moves in straight-line segments of length approximately equal to the mean free path λ, with its direction randomised after each step due to its thermal velocity v_{th}

If the particle lies beyond a distance λ from the wall, the probability of collision is zero. If it is exactly at the wall (i.e., $d = 0$), there is a 50% chance of striking it, since half the sphere lies in the direction of the wall. For intermediate distances, the probability is given by the ratio of the volume of a spherical cap (formed by the wall-intersecting region of the sphere) to the total volume of the sphere.

Because h is expressed relative to λ, the resulting probability function becomes independent of λ itself. This probability $p_\lambda(d)$, which quantifies the chance of wall impact as a function of distance d, is illustrated in Figure 4.3. The probability smoothly decreases from 0.5 at the wall ($d = 0$) to 0 at $d = \lambda$. The average collision probability over this range is approximately $p_{\lambda,\text{average}} = 0.188$. Then it can be assumed that the accretion efficiency factor $f_{\text{accretion}}$ is equal to this average probability $f_{\text{accretion}} = p_{\lambda,\text{average}} = 0.188$. In summary, a vapour molecule located a distance $d \leq \lambda$ from the wall has a finite probability of impacting it in the next timestep Δt, with this probability decreasing as the molecule lies farther from the surface. Beyond the mean free path, no collision with the wall can occur.

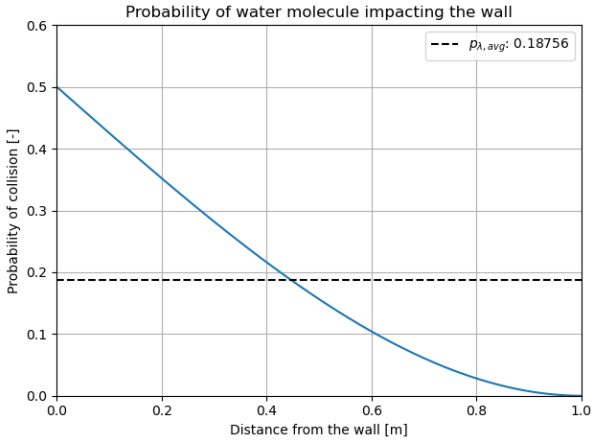

Figure 4.3: Probability function for a water vapour molecule that interacts with the wall surface as a function of distance to the wall

Sticking coefficient: S_{stick}

The sticking coefficient, or probability, of water vapour on ice is influenced by several factors, including incident energy, angle of incidence, and the molecule's orientation and reorientation time on the surface (Batista et al. 2005). In this context, "incident energy" refers to the kinetic energy that a water molecule possesses as it approaches and collides with the ice surface. It is essentially a measure of how fast the water molecule is moving towards the ice. Experimental and theoretical studies show that the sticking probability can be as high as unity for a temperature range from 300 K to 1000 K. The sticking coefficient decreases as the angle of incidence increases for higher temperatures (Batista et al. 2005). This angular dependence is attributed to the strong orientational effects of the water molecule's interaction with the ice surface and the time it takes for the molecule to reorient itself (Batista et al. 2005).

Research also indicates that the sticking coefficient is independent of the ice film's phase (crystalline versus amorphous), thickness, and temperature within a certain range (20 K < T < 120 K) (Batista et al. 2005). In specific studies, the measured sticking coefficient for water molecules on ice was found to be approximately 0.95 across various incident angles at 300 K, but at 3000 K, it decreased from 0.95 at 0 degrees to about 0.75 at 70 degrees incident angle (Batista et al. 2005). This behaviour suggests that at higher energies, the molecule's interaction with the surface and its ability to reorient are critical factors in its sticking probability (Batista et al. 2005).

Other authors found that for amorphous ice, the sticking coefficient in the region of 220-273 K was determined experimentally to vary in the range from 0.02 to 0.4 (Buch and Zhang 1991; Cuppen et al. 2010; Veeraghattam et al. 2014). While the sticking coefficient of water vapour on hexagonal ice may exhibit some temperature dependence above 200 K, several experimental and theoretical studies support the use of a sticking probability close to unity (Skrotzki et al. 2013). In Enceladus' plume environment, where gas-surface interactions often occur under non-equilibrium conditions and at near-normal incidence, the assumption of $S_{\text{stick}} = 1$ provides a physically reasonable and computationally convenient upper bound for modelling surface fluxes and vapour-solid exchange. Thus, while desorption should be explicitly treated when modelling net ice growth, the use of a unity sticking coefficient for incident molecules is justified in many microphysical and kinetic scenarios above 200 K.

4.1.2. Wall Sublimation: S_s

Wall sublimation refers to the process by which solid ice molecules at the surface of an ice layer transition directly to the vapour phase without passing through a liquid state. This process is governed by the temperature and pressure conditions at the wall, and it plays a critical role in processes such as frost evaporation, planetary atmospheric dynamics (e.g., Enceladus' plumes), and various industrial applications (Pruppacher et al. 1998; van der Hijden 2021). The rate of sublimation is influenced by both the thermodynamics of the ice and the kinetic properties of water vapour.

The rate of sublimation can be described using an Arrhenius-type expression for the molecular sublimation rate $r_{\text{sublimation}}$ given by Equation 4.9 where ν is the pre-exponential factor (the molecular frequency of encounters), E_a is the sublimation energy (or activation energy) of the ice, and T_{wall} is the wall temperature.

$$r_{\text{sublimation}} = \nu \exp\left(-\frac{E_a}{T_{\text{wall}}}\right), \quad [\text{molecules/s}] \tag{4.9}$$

This equation is derived from the statistical mechanics of molecular interactions and is widely used in models of surface evaporation and sublimation (Fletcher 1962).. The sublimation mass rate per unit area, $\dot{m}_s$ is then given by Equation 4.10 where n_{ice} is the number area density of the ice, $m_{\text{H}_2\text{O}}$ is the molar mass of water and N_A is Avogadro's constant.

$$\dot{m}_s = r_{\text{sublimation}} \cdot n_{\text{ice}} \cdot \frac{m_{\text{H}_2\text{O}}}{N_A}, \quad \left[\text{kg/(m}^2 s)\right] \tag{4.10}$$

This equation accounts for the mass of molecules leaving the surface per unit surface and per unit time. Similar to wall accretion, one ice layer of 3Å is considered leading to the change in the radius of the sublimating ice layer, $\frac{dR_{w,s}}{dt}$ over time given by Equation 4.11.

$$\frac{dR_{w,s}}{dt} = 3\text{Å} \cdot r \quad [\text{m/s}] \tag{4.11}$$

Pre-exponential factor: ν

The pre-exponential factor ν for desorption from ice surfaces is a key parameter in modelling thermal desorption kinetics in astrochemical environments (Minissale et al. 2022). Traditionally, ν has been estimated using the harmonic approximation by Hasegawa and Herbst (1993), yielding values around 10^{12} to 10^{13} s^{-1} for small physisorbed molecules. However, this method neglects entropic contributions such as molecular rotation and translation, leading to significant underestimates for larger or more complex species (Minissale et al. 2022). More accurate values are derived using transition state theory (TST), which accounts for the ratio of partition functions between the adsorbed and transition states. For water (H_2O), pre-exponential factors have been experimentally determined as high as 3.26×10^{15} s^{-1} from temperature-programmed desorption (TPD) data (Minissale et al. 2022). Theoretical estimates using TST also yield values in the 10^{15} to 10^{16} s^{-1} range when both rotational and translational degrees of freedom are included (Minissale et al. 2022).

In this work, the value of the pre-exponential factor is calibrated using the equilibrium between accretion and sublimation. That is the rate of accretion equals the rate of sublimation, when the pressure as a function of temperature follows the saturation curve. An equation for the pressure as a function of temperature known as the Antoine equation can be derived by setting the rate of wall accretion equal to the rate of wall sublimation as shown in Equation 4.12.

$$p(T) = \nu \frac{n_{\text{ice}} R m_{\text{H}_2\text{O}}}{S_{\text{stick}} p_{\lambda,\text{average}}} \left(\frac{8 k_B T_{\text{wall}}}{\pi m_{\text{H}_2\text{O}}}\right)^{-1/2} T \exp\left(-\frac{E_a}{k_b T_{\text{wall}}}\right) \tag{4.12}$$

From Equation 4.12, the pre-exponential factor ν is calibrated to a value of about $\nu = 1.244 \times 10^{16}$ s^{-1} and was used as a constant throughout this work. This value is verified by plotting the pressure as a function of temperature and comparing with the saturation curves shown in Figure 4.4. The calibrated Antoine equation closely matches the saturation curves with an error of less than 1%.

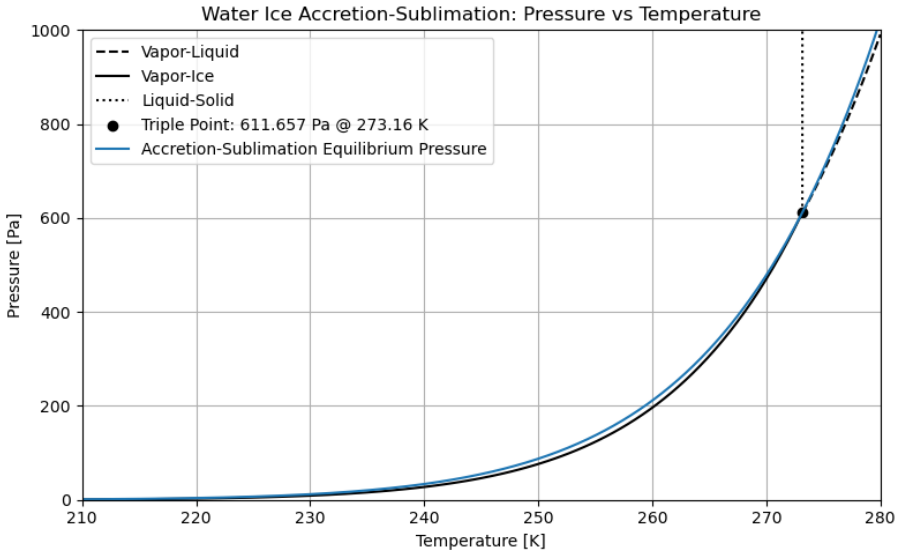

Figure 4.4: Phase diagram of water with a curve for the Accretion-Sublimation equilibrium pressure calibrated to match the associated saturation curve

4.2. Coupled Wall Interactions in the Icy Steam Model

In this section, the framework for coupled wall interactions in the icy steam model is described and forms the basis for this work. In the Icy Steam Model, wall coupling plays a critical role in regulating mass, momentum, and energy exchange at the flow–wall interface. These interactions are driven by wall accretion and sublimation processes that are highly sensitive to local thermodynamic conditions, including temperature gradients and pressure variations.

As the vapour accretes or sublimates at the wall, latent heat release or absorption significantly alters the local heat flux and can lead to time-dependent wall geometry evolution. Capturing these coupled wall interactions is essential for accurately modelling the transient dynamics of plume generation and for predicting observable features such as vent mass fluxes, plume structure, and mass fraction.

4.2.1. Conservation Equations

The conservation equations used in the Icy Steam model are almost identical to those for the Wet Steam Model and are repeated in Equation 4.13 for clarity. The first equation corresponds to the conservation of mass with the sink/source terms on the RHS associated with nucleation, grain growth, wall accretion and wall sublimation. The second equation corresponds to the conservation of momentum with the sink/source terms on the RHS applicable for momentum. The viscous stress tensor, total energy, total enthalpy and total enthalpy of the droplet given by Equation 3.48, Equation 3.49, Equation 3.50, and Equation 3.51 respectively. The third equation represents the conservation of energy with the sink/source terms on the RHS applicable for energy.

$$\begin{aligned}
&\frac{\partial \rho}{\partial t} + \nabla \cdot \left(\rho \vec{U}\right) = S_m \\
&\frac{\partial}{\partial t}\left(\rho \vec{U}\right) + \nabla \cdot \left(\rho \vec{U}\vec{U}\right) = -\nabla p + \nabla \cdot \tau + S_U \\
&\frac{\partial}{\partial t}\left(\rho E\right) + \nabla \cdot \left(\rho \vec{U} E + p\vec{U}\right) = \nabla \left(k_{\text{eff}} \nabla T + \left(\tau \cdot \vec{U}\right)\right) + S_h
\end{aligned} \tag{4.13}$$

Similarly, the additional transport equations are given by Equation 4.14 and Equation 4.15. Equation 4.14 describes the evolution of solid phase mass fraction f, and Equation 4.15 is used for the evolution of the grain number per unit mass of vapour.

$$\frac{\partial}{\partial t}\left(\rho f\right) + \nabla \cdot \left(\rho f \vec{U}\right) = S_f \tag{4.14}$$

$$\frac{\partial}{\partial t}\left(\rho N\right) + \nabla \cdot \left(\rho N \vec{U}\right) = S_N \tag{4.15}$$

The source terms due to nucleation and growth for the conservation of droplet number and mass fraction are given by Equation 4.16 and Equation 4.17. For Equation 4.16, the only contribution the

number of grains changing comes from new ice particles being formed by the process of nucleation. However, for Equation 4.17 the contribution to the mass fraction changing is due to the additional mass due to new ice particles being formed, as well as the added mass due to the growth of the ice particles.

$$S_N = J \tag{4.16}$$

$$S_f = \frac{4}{3}\pi r^{*\,3}\rho_i J + 4\pi r^2 N \rho_i \frac{dr}{dt}\rho_v \tag{4.17}$$

Two additional source/sink terms are included for wall accretion and wall sublimation given by Equation 4.18 and Equation 4.19 respectively. These source/sink terms are just the mass flows due to accretion and sublimation at the wall given by Equation 4.3 and Equation 4.10 respectively. It is emphasised that these source terms are only applicable to the cells adjacent to the wall and are zero elsewhere. Since wall accretion is the process in which the water vapour molecules deposit ice on the wall, it extracts mass, momentum and energy from the flow and therefore it is a sink term represented by the negative sign in Equation 4.18. Conversely, wall sublimation adds mass, momentum and energy to the flow and is therefore a source term.

$$S_a = -\dot{m}_a = -S_{\text{stick}}\dot{m}f_{\text{accretion}} \tag{4.18}$$

$$S_s = \dot{m}_s = r_{\text{sublimation}} \cdot n_{\text{ice}} \cdot \frac{m_{\text{H}_2\text{O}}}{N_A} \tag{4.19}$$

The source terms on the RHS of the conservation of mass, energy and momentum are expressed by Equation 4.20, Equation 4.21 and Equation 4.22 respectively, where H_g is the total enthalpy of the grain.

$$S_m = -S_f - S_a + S_s \tag{4.20}$$

$$S_U = \vec{U} \cdot S_m \tag{4.21}$$

$$S_h = \Delta H_{dep} \cdot S_s - H_g \cdot S_f - H_v \cdot S_a \tag{4.22}$$

4.2.2. Nucleation in Enceladus' Plumes

For Enceladus length scales where the channel length is of the order of hundreds of meters to several kilometers (Dotson 2018), it is expected that there are three phases present in the flow: water vapour, liquid water and ice. At the start of the channel where the temperature and pressure are the highest, liquid water nucleation is dominant and liquid water droplets grow. As the flow progresses in the channel, the temperature and pressure both decrease leading to a higher supersaturation. The supercooled water droplets subsequently nucleate to ice grains and begin to grow along the channel. Toward the end of the channel where the pressure and temperature are the lowest, the water vapour may nucleate spontaneously to ice and they will grow until they leave the channel. This complex three-phase phenomena is summarised below.

- Liquid water nucleation from the supercooled vapour phase
  - Droplet growth of supercooled liquid water droplets
  - Subsequent ice nucleation from the supercooled liquid water phase
  - Grain growth of ice grains
- Ice nucleation from the supercooled vapour phase
  - Grain growth of ice grains

The idea of including a 3-phase condensation-freezing and deposition model was considered for this work but was later scraped due to time constraints. Whilst such a model would reflect a high-fidelity model to simulate Enceladus' plumes, it was decided to proceed with the a 2-phase model with ice nucleation from the supercooled vapour phase. In addition, a 3-phase model would impose a higher computational cost for the CFD solver and the focus of this work is rather on performing multiple simulations to analyse the effect of wall interactions. The nucleation model is then based on the classical nucleation rate given by Equation 4.23 with the correction given by Equation 4.24 using the surface tension of water followed by grain growth discussed in subsection 3.4.2.

$$J_{CNT} = q_c \left(\frac{\rho_v^2}{\rho_l}\right) \sqrt{\frac{2\sigma_{l,v}}{\pi m^3}} \exp\left(-\frac{4\pi {r^*}^2 \sigma_{l,v}}{3k_B T}\right) \tag{4.23}$$

$$J = J_{CNT} \exp\left(A + \frac{B}{T}\right) \tag{4.24}$$

4.3. Methodology

To investigate the coupled dynamics of sublimation and accretion in icy vapour channels relevant to Enceladus' plumes, an automated simulation framework was developed integrating compressible multiphase flow modelling with evolving wall geometries. This framework is hosted in the PlumesCFD[1] repository and executed through a Python-based control script (`runSimulation.py`) that coordinates mesh generation, boundary condition assignment, simulation monitoring, wall interaction updates, and mesh regeneration across multiple time steps. A flow diagram of the framework is shown in Figure 4.6 and is outlined below.

Geometry and Mesh Generation: Channel geometries are initialised from experimental or idealised profiles that the user can create using a channel designer shown in Figure 4.5. Here users can either create a channel by changing the amplitude and frequency of three harmonic functions or by a custom function. Alternatively, users can also load a channel using a csv file called `channel_data.csv` with the first column denoting the x-coordinates the second column denoting the y-coordinates. These coordinates define the evolving upper wall of the domain. A custom Gmsh script (`createGmshGeoFile.py`) generates a structured mesh with user-defined vertical and horizontal cell divisions, including options for non-uniform structured grid refinement and geometric bumps. The mesh is converted to OpenFOAM format via `gmshToFoam`, and wall cell information is extracted for subsequent wall interaction modelling.

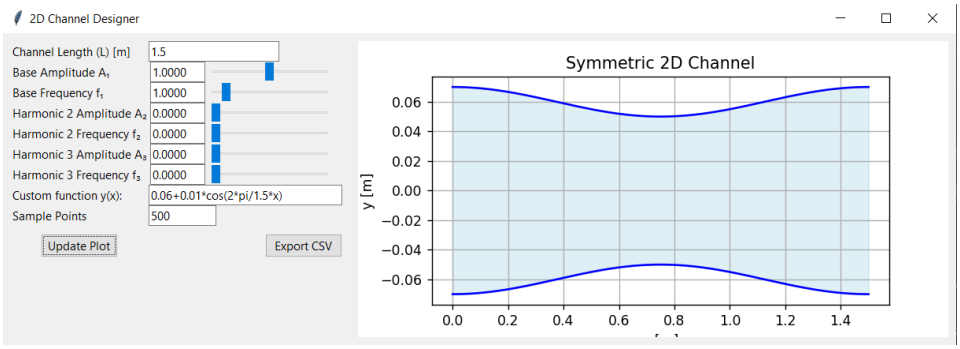

Figure 4.5: Example of a generated convergent-divergent nozzle using the channel designer tool

Flow Initialisation and Solver Coupling: Flow fields such as pressure, temperature, velocity, and Mach number are initialised using a quasi-1D isentropic approximation computed in (`quasi1DIsentropic.py`), based on the channel's varying cross-section. These fields serve as initial conditions for the compressible multiphase solver (`rhoCentralFoam_2ph`), a modified version of OpenFOAM's (`rhoCentralFoam`) that incorporates homogeneous nucleation dynamics and accretion/-sublimation source terms (`mdot_a`, `mdot_s`) defined on boundary faces. These terms are initialised only during the first run and then dynamically updated based on local wall behaviour.

CFD Transient Simulation Until Convergence: With the flow fields initialised, a CFD simulation of (`rhoCentralFoam_2ph`) is performed based on the equations for the Icy Steam Model in subsection 4.2.1. After each time-step is finished, (`monitorConvergence.py`) the residuals between the current time-step and the previous time-step are cheked to ensure the solver has converged.

Wall Interaction Loop and Time Evolution: After each transient simulation reaches steady state (as monitored by residual thresholds in `monitorSimulation.py`), the framework calculates the net rate

[1] `https://github.com/Sebastian2597/PlumesCFD`

of change in wall height (dRw/dt) using the extracted mass fluxes of accretion and sublimation at the top wall. A dynamic time step, constrained by safety factors and thresholds, is used to integrate this rate until the cumulative change approaches a set percentage of the local channel height or wall closure occurs. The updated wall geometry is then interpolated and used to regenerate the Gmsh mesh for the next simulation cycle.

Convergence, Termination, and Automation: The simulation proceeds iteratively until either (1) the physical time exceeds a user-defined limit, (2) the maximum number of allowed cycles is reached, or (3) the user terminates the simulation. All intermediate results, including field values and geometry snapshots, are archived for post-analysis in structured folders. This automated loop enables self-consistent coupling between vapour dynamics and ice wall evolution under various thermal boundary conditions and initial geometries.

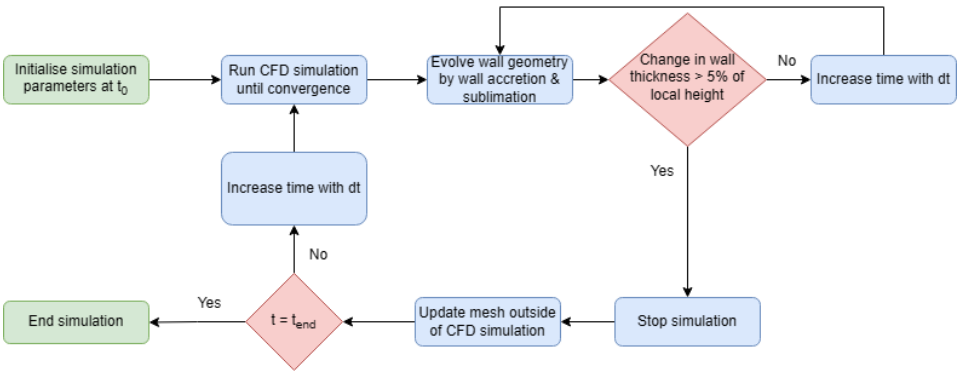

Figure 4.6: Flow diagram of the Coupled Wall Interactions in the Icy Steam Model methodology

As mentioned, the updated wall geometry needs to be interpolated to regenerate the Gmsh mesh. This is because there is a mismatch between the number and location of the Gmsh points and the OpenFOAM points due to the nature of converting the mesh using `gmshToFoam`. This is shown in Figure 4.7 where the blue crosses are the Gmsh points and the red dotted line represents the OpenFOAM points.

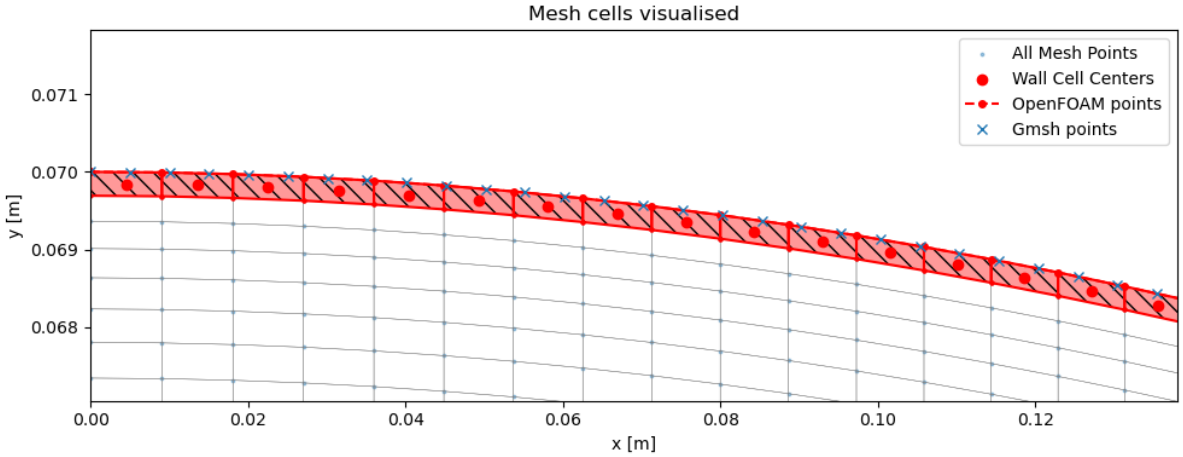

Figure 4.7: Diagram of the mesh zoomed-in at the wall to show the mismatch in OpenFOAM points and Gmsh points.

To reconcile this mismatch and ensure that the updated wall geometry can be accurately reinserted into the Gmsh mesh, an interpolation step is performed. SciPy's `UnivariateSpline` provides a convenient interface for fitting and evaluating splines in one step. In this approach, the original wall coordinates x and their corresponding values y are used directly to construct a smoothing spline. By default, `UnivariateSpline` selects the smoothing factor s automatically using generalised cross-

validation (GCV). This smoothing factor governs the balance between closely following the original data and producing a smooth, well-behaved curve.

In the present application, the spline is evaluated at the prescribed Gmsh sample points to produce an interpolated wall profile. This smoothed representation is particularly valuable when the OpenFOAM data contain small numerical oscillations or irregularities at the boundary. By applying an adaptive smoothing process, the regenerated Gmsh geometry remains both stable and physically consistent across iterative mesh updates.

5

OpenFOAM Setup

In order to solve the equations in the Icy Steam Model, a Computational Flow Dynamics (CFD) software is required. This chapter outlines the chosen CFD software including the chosen solver and how it works. In section 5.1 the reasoning for why OpenFOAM was chosen is described. In section 5.2 the numerical formulation of the solver rhoCentralFoam is outlined. In section 5.3, the geometry and mesh that were used for this work to answer the research questions are shown and discussed along with a solver convergence and grid convergence check. Lastly, section 5.4 and section 5.5 the boundary conditions and initial conditions for the OpenFOAM simulations are described for this work.

5.1. Methodology

For this thesis, the open-source CFD software OpenFOAM was used. Karagiannis (2020) implemented the Wet Steam Model in OpenFOAM to capture the condensation physics applicable for micronozzle flows. An existing solver for general compressible flows called rhoCentralFoam was adopted and extensively modified by Karagiannis (2020) to account for mild rarefaction effects within the micronozzle and to model condensation under supersonic conditions. Fontes (2023) modified the Wet Steam model implementation in OpenFOAM by Karagiannis to be applicable for Enceladus' plumes. Therefore, to investigate the posed questions of this work, OpenFOAM was chosen for several reasons. Firstly, the complex and evolving nature of condensation modelling of Enceladus' channels required a flexible and fully customisable framework; its open-source nature removed licensing constraints and supported the goal of reproducible research. Furthermore, the existence of the Wet Steam model implementation for Enceladus' plumes by Fontes (2023) provided a foundational basis for this work allowing for the focus for implementing a coupled wall interactions framework.

5.2. Solver Definition

The solver is a modified version of `rhoCentralFoam` which is a density-based solver in which the continuity equation is used to solve for the density, and the equation of state is used to solve for the pressure. The `rhoCentralFoam` solver is based on a combination of central-difference and upwind schemes (Canteros, Maria Laura and Polanský, Jiří 2024). This solver was preferred over sonicFoam, which is a pressure-based solver, as `rhoCentralFoam` results in better performance and resolution accuracy despite being more sensitive to initial conditions (Canteros, Maria Laura and Polanský, Jiří 2024; Marcantoni et al. 2012). Furthermore, this solver was chosen for modelling Enceladus' plumes as it can capture shock phenomena, transient behaviour and allows for the inclusion of turbulence and heat transfer (Harvey and Thompson 2020).

5.2.1. Computational Method

The rhoCentralFoam solver can be described by introducing the conservation equation for an arbitrary source field. Consider a conservation equation with a source term for an arbitrary field variable Ψ that can be a scalar or vector field represented by Equation 5.1.

$$\frac{\partial(\rho\mathbf{\Psi})}{\partial t} + \nabla \cdot [\mathbf{u}(\rho\mathbf{\Psi})] = S_{\mathbf{\Psi}} \tag{5.1}$$

Convective Terms

The convective terms in the conservation equations can be integrated over the control volume by converting the volume integral into a surface integral by using the divergence theorem and then it can be linearised as seen in Equation 5.2. In the linearised equation, it shows the summation over all cell faces of ϕ_f which is the volumetric flux.

$$\int_V \nabla \cdot [\mathbf{u}\mathbf{\Psi}] dV = \int_S d\mathbf{S} \cdot [\mathbf{u}\mathbf{\Psi}] = \sum_f [\mathbf{S}_f \cdot \mathbf{u}_f] \mathbf{\Psi}_f \approx \sum_f \phi_f \mathbf{\Psi}_f \tag{5.2}$$

Normally for incompressible flows, the velocity of the cell is interpolated using central differencing and the flux of the cell is interpolated using a scheme with some upwinding to ensure the solution is stable. However, since `rhoCentralFoam` is a compressible flow solver, one must consider that flow properties are transported by the propagation of waves in addition to the flow. This means that when interpolating the flux, it must be stabilised by transport that can happen in any direction (Greenshields et al. 2010). Therefore, interpolation has to be done in both directions for each face that is denoted as f_+ and f_- for the outward and inward direction respectively. Consider two computational cells in Figure 5.1 denoted by the owner cell P and neighbouring cell N. A flow property located at the centroids of the cells can be interpolated onto its face f.

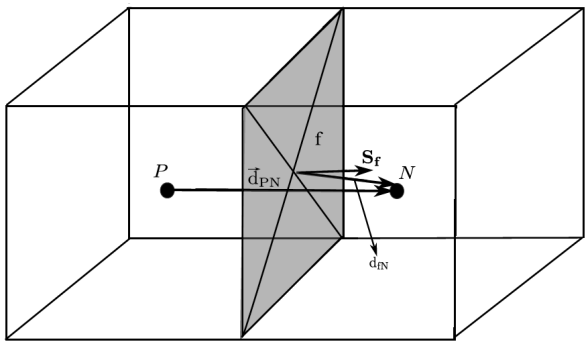

Figure 5.1: Illustration of the fundamental variable definitions and conservation laws used in the base rhoCentralFoam solver. The solver solves the compressible Navier–Stokes equations in conservative form using a central-upwind scheme. Fluxes across control volume positive face from the owner cell P and negative face from the neighbouring cell N are shown. This figure serves as the foundation for the extended `rhoCentralFoam` solver developed in this work, which incorporates additional source terms for nucleation, condensation, and wall sublimation (Marcantoni et al. 2012).

For the convective terms, this interpolation can then be computed using the outward and inward faces using Equation 5.3 with an additional diffusion term that is a function of the volumetric flux ω_f and is necessary for when the convective term is part of a substantial derivative. This volumetric flux is related to the maximum speed of propagation of any discontinuity that may occur at a face (Greenshields et al. 2010).

$$\sum_f \phi_f \mathbf{\Psi}_f = \sum_f [\alpha\phi_{f+}\mathbf{\Psi}_{f+} + (1-\alpha)\phi_{f-}\mathbf{\Psi}_{f-} + \omega_f(\mathbf{\Psi}_{f-} - \mathbf{\Psi}_{f+})] \tag{5.3}$$

The parameter α is a weighing factor that differs based on the interpolation scheme used. For `rhoCentralFoam`, there are two interpolation schemes that can be used: Kurganov and Tadmor (KT) scheme and Kurganov-Noelle-Petrova (KNP) scheme. For the KT scheme, the weighing factor is equal to 0.5 meaning that the contributions to the f_+ and f_- faces are equal and is therefore a central scheme. For the KNP scheme, has a weighting that is favoured in the upwinding direction as seen in Equation 5.4 and is called central-upwind.

$$\alpha = \begin{cases} \frac{1}{2} & \text{for the KT scheme} \\ \frac{\psi_{f+}}{\psi_{f+}+\psi_{f-}} & \text{for the KNP scheme} \end{cases} \tag{5.4}$$

The volumetric fluxes present in Equation 5.3 and Equation 5.4 with their corresponding local speed of propagation are computed using Equation 5.5 where $c_{f_\pm}$ is the local speed of sound at the face and is equal to $\sqrt{\gamma R T_{f\pm}}$.

$$\begin{aligned} \mathbf{\Psi}_{f_+} &= \max\left(c_{f_+}\left|\mathbf{S_f}\right| + \phi_{f_+}, c_{f_-}\left|\mathbf{S_f}\right| + \phi_{f_-}, 0\right) \\ \mathbf{\Psi}_{f_-} &= \max\left(c_{f_+}\left|\mathbf{S_f}\right| - \phi_{f_+}, c_{f_-}\left|\mathbf{S_f}\right| - \phi_{f_-}, 0\right) \end{aligned} \tag{5.5}$$

Finally, the diffusive volumetric flux necessary for the convective terms can be calculated using Equation 5.6 for the different schemes. For the two new conservation equations present in the Wet Steam Model & the Icy Steam Model, they are interpolated using a second-order upwind scheme due to these variables experiencing large gradients when nucleation begins.

$$\omega_f = \begin{cases} \alpha \max\left(\Psi_{f_+}, \Psi_{f_-}\right) & \text{for the KT scheme} \\ \alpha\left(1-\alpha\right)\left(\Psi_{f_+} + \Psi_{f_-}\right) & \text{for the KNP scheme} \end{cases} \tag{5.6}$$

Gradient Terms

For the gradient terms in the conservation equations, they can be discretised in much the same way as for the convective terms. The linearisation of the gradient terms is calculated using Equation 5.7 and consequently the interpolation is computed using Equation 5.8 which is similar to that of the interpolation for the linearised convective terms but without the added diffusion term.

$$\int_V \nabla \mathbf{\Psi} dV = \int_S d\mathbf{S}_f \mathbf{\Psi} \approx \sum_f \mathbf{S}_f \mathbf{\Psi}_f \tag{5.7}$$

$$\sum_f \mathbf{S}_f \mathbf{\Psi}_f = \sum_f \left[\alpha \mathbf{S}_f \mathbf{\Psi}_{f+} + (1-\alpha)\mathbf{S}_f \mathbf{\Psi}_{f-}\right] \tag{5.8}$$

Source Terms

In finite-volume methods, the convergence to the solution is generally improved when the coefficient matrix resulting from the discretization of the governing equations is diagonally dominant. In other words, when the magnitude of each diagonal entry exceeds the sum of the magnitudes of the off-diagonal entries in the corresponding row. This property promotes numerical stability and accelerates convergence. However, in equations such as those governing momentum or species transport, the source terms often depend on the variable being solved. In regions where metastable deposition occurs, this phenomenon exhibits highly impulsive behaviour, leading the rate of change of these source terms to dominate over other terms in the respective equations.

Direct inclusion of such rapidly varying source terms in the solution matrix can disrupt diagonal dominance and negatively affect convergence. To address this, the source terms can be linearised by expanding them into a Taylor series and retaining terms up to first order. This results in a formulation that separates the source term into an active (variable-dependent) and a passive component, thus restoring a structure more favourable to convergence. For an arbitrary source term in the conservation equations it can be linearised by a Taylor expansion as shown below.

$$S_{\Psi,i} = S_{\Psi,i-1} + S'_{\Psi,i}\left(\Psi_i - \Psi_{i-1}\right) \tag{5.9}$$

5.2.2. Code Summary

In order to highlight and summarise how the modified code of `rhoCentralFoam` for two-phase flow, a simple flow chart is presented in Figure 5.2. Furthermore, pseudo-code for this solver is provided in Appendix A. This flow chart consists of three main sections, where the case setup for the OpenFOAM software is defined, followed by the solution where the OpenFOAM simulation runs a specific case and lastly, a section including the user-defined functions (UDF) added to `rhoCentralFoam`. This flowchart can be explained as follows.

- **Initialisation and Setup:** The simulation begins with initialisation of mesh, model definition, boundary and initial conditions for the flow fields such as density ρ, velocity $\vec{U}$, pressure p, temperature T.
- **Time Loop:** The core of the simulation runs within a pseudo-time loop, iterating through time steps toward a steady-state solution. Within this loop, the main physics modules are executed in order.
- **Interpolation:** Inside the loop, it performs interpolations of primitive fields (like density ρ, momentum $\rho\vec{U}$, and grain mass fraction ρf) onto the cell faces. This is a common step in finite volume methods for calculating fluxes.
- **Thermophysical Properties:** It accesses and utilises thermophysical properties such as specific heat at constant pressure (c_p), specific heat at constant volume (c_v), the ratio of specific heats (γ), and the speed of sound (c) from the thermo object.
- **Flux Calculations:** The code calculates various flux-related quantities, including $c_{f+}|\mathbf{S}_f|$, $c_{f-}|\mathbf{S}_f|$, ϕ_{f+}, ϕ_{f-}, ψ_{f+}, ψ_{f-} and $\alpha\mathbf{S}_f$. These are used in the numerical schemes for solving the conservation equations.
- **Solving Conservation Equations:** The code then proceeds to solve the conservation equations for:
  - **Mass (ρ):** Including the sink terms due to nucleation, grain growth and wall accretion, and source terms for wall sublimation given by Equation 4.20, Equation 4.17, Equation 4.18 and Equation 4.19.
  - **Momentum (ρU):** Including the same source and sink terms but multiplied by the velocity field using Equation 4.21.
  - **Energy (ρE):** Accounting for the energy source/sink terms due to nucleation, grain growth, wall accretion and wall sublimation given by Equation 4.22.
  - **grain number (ρN):** With the nucleation rate as a source term given by Equation 4.16.
  - **Grain Mass Fraction (ρf):** Incorporating source terms for nucleation and growth using Equation 4.17.
  - **Corrections and Updates:** After solving the main equations, it corrects boundary conditions for various fields (U, e, N, f, p) and updates thermophysical properties.
- **Wall Interactions Modelling:** The wall accretion and wall sublimation based on the density field at the nearest cell to the wall given by Equation 4.3 and the temperature at the wall given by Equation 4.10 respectively. This contributes to boundary mass fluxes, which enter as source terms in the governing equations.
- **Phase Change Modelling:** A significant portion of the code deals with phase change, specifically deposition. It performs a loop over all cells and calculates:
  - **Critical Radius:** r^* based on thermodynamic properties and surface tension using Equation 3.12.
  - **Nucleation Rate:** Using Becker-Döring theory with Wölk and Strey (2001) correction in Equation 3.28.
  - **Grain Growth Rate:** Computed based on a kinetic-limited model developed by Gyarmathy (1976) and modified by Young (1980) applicable for low pressure flows given by Equation 3.69.
  - **Source Terms:** Sink/source terms are updated based on nucleation and growth.
  - **Residual Calculation and Convergence Check:** The RMS difference between the current and previous iterations is computed for each variable. These residuals are used to monitor convergence. If the residuals fall below a specified threshold, the solver exits; otherwise, it proceeds to the next pseudo-time iteration.

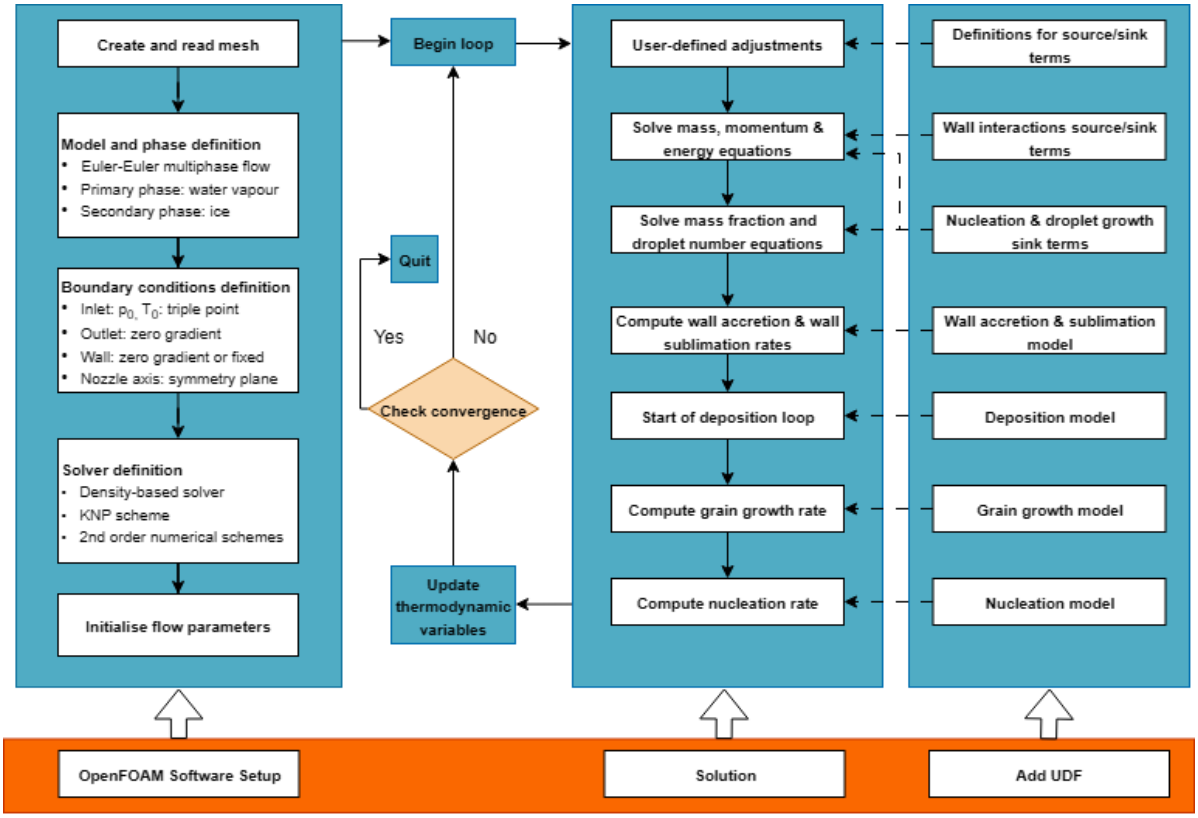

Figure 5.2: Flowchart of the adapted `rhoCentralFoam` solver developed in this thesis. The solver extends the standard `rhoCentralFoam` by incorporating non-equilibrium homogeneous deposition, grain growth, and wall phase-change processes such as accretion and sublimation. The flowchart outlines the sequential steps of the pseudo-time loop, including the evaluation of condensation source terms, update of nucleation and grain properties, computation of fluxes using a central-upwind scheme, and residual monitoring for convergence.

5.2.3. Numerical Schemes

The choice of numerical schemes in this work is guided by the need for second-order accuracy in the discretisation of the conservation laws, as such precision is generally required to produce reliable results in simulations involving non-equilibrium condensation phenomena (Blondel 2014; Karagiannis 2020). To keep this subsection concise, only the schemes employed are described, accompanied by brief justifications.

Temporal discretisation is handled using the second-order Crank–Nicolson method, with a weight factor of 0.9, in accordance with OpenFOAM guidelines (Crank and Nicolson 1947). Divergence terms are managed by the high-resolution method of Kurganov and Petrova (2007), which is inherently embedded in the solver and therefore does not require additional discretisation schemes. An exception is made for the divergence of the stress tensor, which is computed explicitly and thus discretised using a second-order Gauss linear scheme.

The Total Variation Diminishing (TVD) limiter associated with the Kurganov–Petrova scheme plays a key role in controlling numerical oscillations. A comparative study by Blondel (2014) found that the limiters by van Leer (1979) and Albada et al. (1997) offered the best trade-off between accuracy and stability in simulations of metastable condensation. Based on these findings, the van Albada limiter is employed in the work of Karagiannis (2020) and is therefore also used here.

In regions where nucleation initiates, extremely steep gradients arise in the solid-phase variables making TVD schemes overly diffusive. Instead, a second-order unbounded linear-upwind reconstruction scheme is used for these variables, as it is better suited to capture such sharp spatial transitions (Warming and Beam 1976).

Other terms are discretised with standard approaches. The Laplacian term in the energy equation is treated with a second-order Gauss linear scheme. The surface-normal gradient of the velocity, also appearing in the energy equation, is evaluated using a corrected central-difference surface-normal gradient scheme. Finally, all remaining gradient terms in the governing equations are discretised using

a least-squares scheme, with extrapolated values constrained by the local extrema of neighbouring cells to ensure numerical stability.

5.3. Geometry & Mesh

The geometry of the channels between the surface of Enceladus and its subsurface ocean is critical in understanding how material is transported in the plume system. Since the true shapes of these channels are unknown, considering a range of plausible geometries allows for a better exploration of the physical processes involved, including phase change, sublimation, ice deposition, flow choking, and heat exchange.

C.J. Hansen et al. (2020) and Ingersoll and Pankine (2010) suggest vent conditions may favour choked flow, requiring a constriction in the geometry by means of a throat. Furthermore, other authors have also considered convergent-divergent geometries for computational models to reproduce the observed plume structure, supporting this interpretation (Andrew P Ingersoll and Ewald 2011). It was necessary to consider only a few channels to analyse due to the short duration of this project. It was decided to analyse the convergent-divergent channel and the multiple throats channel. By focusing on these two geometries, the modelling framework can capture the essential flow regimes of choked flow & viscous flow, explore realistic geological scenarios, and retain manageable complexity for computational fluid dynamics simulations.

5.3.1. Meshes

Structured meshes were generated using the program Gmsh, with mesh grading applied to resolve regions of high gradients such as throats, and boundary layers at the wall. The meshes had an inflation towards the throat with cells being concentrated there. This was done using Gmsh's bump function of 0.9. Furthermore, the meshes had vertical refinement near the walls to capture the boundary layer and the wall interactions. This vertical refinement ensured that the maximum y+ value in the mesh was about 3 since all simulations were done using laminar flow. All meshes were generated with 18,000 cells and was later adjusted based on a grid convergence check that is further discussed in subsection 5.3.2. Furthermore, all meshes are axisymmetric about the centreline and therefore to reduce computational cost, the simulation is only run on half the channel.

Convergent-Divergent Channel

The convergent-divergent channel is illustrated in Figure 5.3. This design is inspired by Laval nozzle shapes and aims to capture the supersonic expansions expected in high-velocity venting scenarios. The channel narrows toward a throat and then widens again, mimicking Laval nozzle-like conditions that promote supersonic flow and enhanced nucleation. This design introduces strong pressure and temperature gradients across the domain. The channel geometry is represented by Equation 5.10 and was used in the work of Fontes (2023).

$$y(x) = 0.06 + 0.01 \cos\left(\frac{2\pi}{L}x\right) \tag{5.10}$$

The mesh for this geometry, presented in Figure 5.4, reflects these considerations. Fine streamwise resolution is applied near the throat region to resolve the steep gradients in velocity, pressure, and supersaturation that arise during expansion. Vertical refinement near the walls is also retained to accommodate wall flux modelling, particularly where sublimation rates are sensitive to local temperature and flow conditions. The mesh design ensures numerical accuracy in capturing both upstream compression and downstream rarefaction waves.

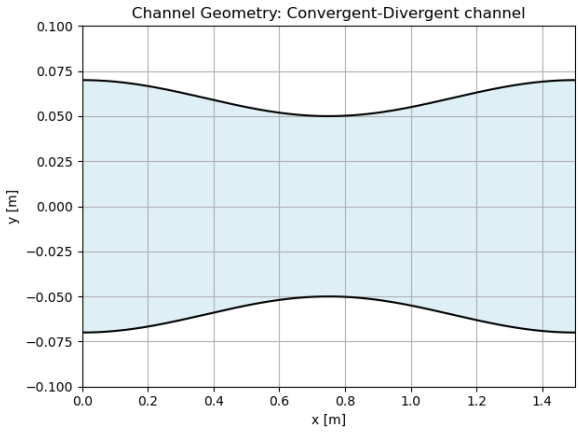

Figure 5.3: Geometry of the convergent-divergent channel

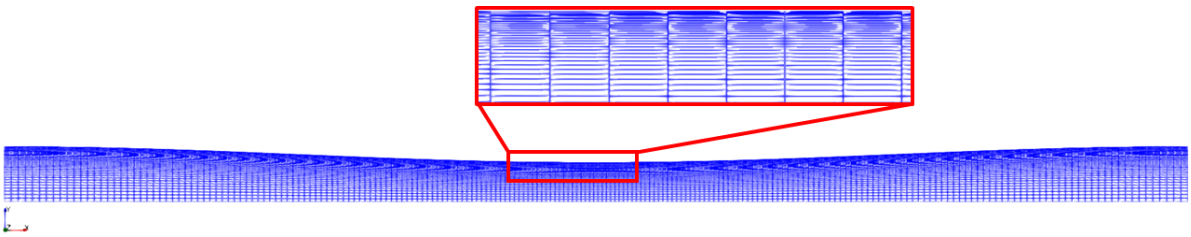

Figure 5.4: Structured mesh for the convergent-divergent channel

Multi-Throat Channel

The multiple throats channel is illustrated in Figure 5.5. This channel uses the same principle of contracting and expanding the flow but has irregular constrictions and expansions. The geometry is based on a superposition of sinusoids given by Equation 5.11 where ξ is a uniformly distributed random number between 0 and 1, A_i are the amplitudes of the modes given by Equation 5.12, and k_i are the wave numbers given by Equation 5.13(Schmidt et al. 2008b). In Equation 5.12, a is given by the smallest diameter of the channel. To stay consistent with the convergent-divergent channels, similar geometry constraints are imposed resulting in a maximum length of 1.5 m and a maximum height of 0.09 m. Then the geometry was constructed by setting $L = 1.5\ m$, $D_{\text{exit}} = 0.09\ m$, $D_{\text{throat}} = 0.063\ m$, $L_0 = 0.6\ m$ and $x^* = 1.11\ m$.

$$y(x) = \sum_i A_i \sin\left(k_i x + 2\pi\xi\right) \tag{5.11}$$

$$A_i = \frac{a}{\sqrt{1 + (k_i L_0)^2}} \tag{5.12}$$

$$k_i = \frac{1}{2}\left(\frac{2\pi}{L}\right) i < k_c = \left(\frac{2\pi}{L_0}\right) \tag{5.13}$$

The associated mesh is displayed in Figure 5.6, where increased mesh refinement is applied in regions with strong geometric curvature and at each constriction. The mesh is carefully graded to resolve steep flow gradients across multiple throats and to prevent numerical diffusion in highly non-uniform regions. This configuration is particularly useful for investigating flow choking, shock formation, and multi-region nucleation phenomena that may arise in more realistic vent systems.

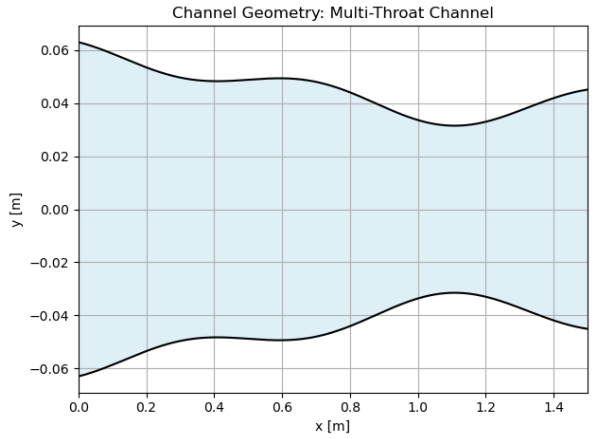

Figure 5.5: Geometry of the multi-throat channel with multiple constrictions and expansions along the length.

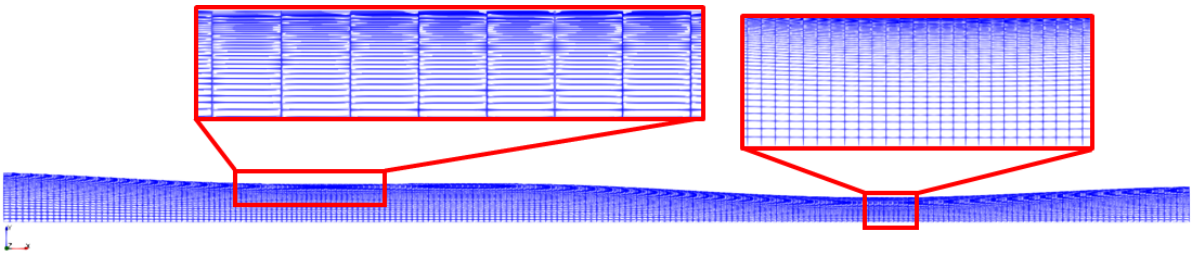

Figure 5.6: Structured mesh for the multi-throat channel geometry.

Solver Convergence

In order for the transient simulation to reach steady state, its thermodynamic variables need to have converged to a solution with little variation between each successive pseudo-time due to machine error. Figure 5.7 presents the root mean square (RMS) percentage difference over pseudo-time for a set of key flow and phase-change variables. It gives insight into how each variable converges over iterations, revealing both stable and problematic aspects of the solver performance for this coupled two-phase CFD model.

At the very beginning of the simulation, several variables exhibit extreme RMS differences—most notably the nucleation rate J and grain number N, which spike above 10^{20}%. These enormous initial transients are not unexpected, as previously mentioned the nucleation rate involves exponential dependencies on supersaturation. Similarly, grain radius r_{grain} and pressure show sharp early peaks, though they stabilise quickly. For the other variables, Mach number, pressure, and grain radius quickly drop to very low RMS differences (on the order of 10^{-5}% and remain stable throughout the pseudo-time. Velocity U_x and supersaturation S_{sat} converge within 0.01–0.1%, showing small residual oscillations but overall stability. The grain growth rate dr/dt and mass fraction f settle within 0.01−1%, suggesting well-behaved interaction between the condensation and growth models. This confirms that the base flow (momentum and thermodynamics) and particle evolution models are numerically stable and converge satisfactorily.

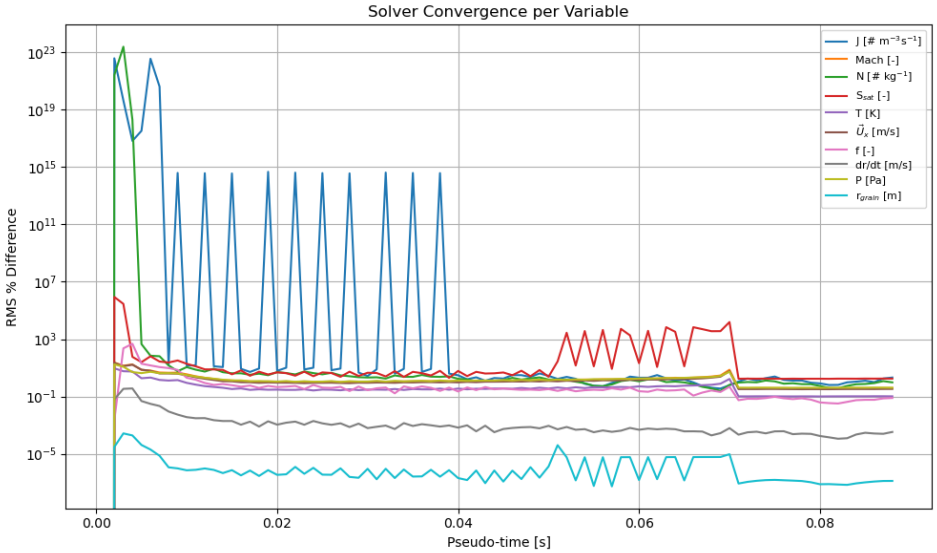

Figure 5.7: Comparison of the RMS percentage difference for different simulation variables at different simulation pseudo-times

The Courant number is a non-dimensional parameter that measures the ratio of the physical time a fluid particle takes to cross a cell to the numerical time step shown in Equation 5.14. In explicit and semi-implicit time integration schemes, it plays a crucial role in determining the numerical stability and convergence behaviour of the solver. For compressible flow solvers like the adapted `rhoCentralFoam`, maintaining a Courant number below 1 is typically necessary to avoid numerical instabilities, though lower values (e.g. < 0.5) are often preferred for stiff, coupled physics like phase change and nucleation.

$$Co = \frac{U\Delta t}{\Delta x} \tag{5.14}$$

In the current simulations, the Courant number was actively monitored and maintained below a conservative threshold (typically Co < 0.3) throughout the pseudo-time integration. This constraint ensures that information propagates smoothly across the mesh and that gradients are accurately captured without introducing spurious oscillations or numerical diffusion.

5.3.2. Grid Convergence

To assess the influence of mesh resolution on solution accuracy, a grid convergence study was performed using three progressively refined computational meshes: extra coarse, coarse, and fine. The baseline mesh used 18,000 cells based on the same geometry that Fontes (2023) used. The extra coarse, coarse and fine meshes that were used had 4500, 8988 and 36040 cells respectively. The objective was to evaluate the convergence behaviour of key flow thermodynamic variables such as pressure, temperature, velocity and Mach number as well as nucleation and growth variables such as nucleation rate, grain growth, grain number and average grain size along the channel centerline. The results, depicted in Figure 5.8 compare these variables across the three meshes and provides clear insights into the sensitivity of the solution to grid refinement.

Before comparing the results for the three meshes, it is necessary to explain the behaviour of each variable along the channel. Firstly, the pressure, temperature and density decrease along the channel due to the flow contraction until it reaches choked conditions at the throat shown by the vertical dashed line. After reaching choked conditions, the flow expands and the pressure, temperature and density further decreases. Due to the decrease of pressure, the supersaturation increases beyond 1 resulting in nucleation occurring at around x/L of 0.6. Once nucleation occurs, it releases latent heat into the flow which locally increases the temperature and decreases the pressure and density. This trend is reflected in the velocity and hence Mach number, the flow accelerates throughout the channel but locally slows down due to nucleation locally increasing the pressure. Furthermore, as nucleation begins, the average grain size abruptly increases due to the high supersaturation ratio but then decreases as the production of smaller grains by nucleation outweighs the growth of the grains. Eventually nucleation slows down

and grain growth remains high such that the average grain growth starts to increase. As a consequence, the mass fraction sharpy increases until nucleation stops and then increases only due to grain growth.

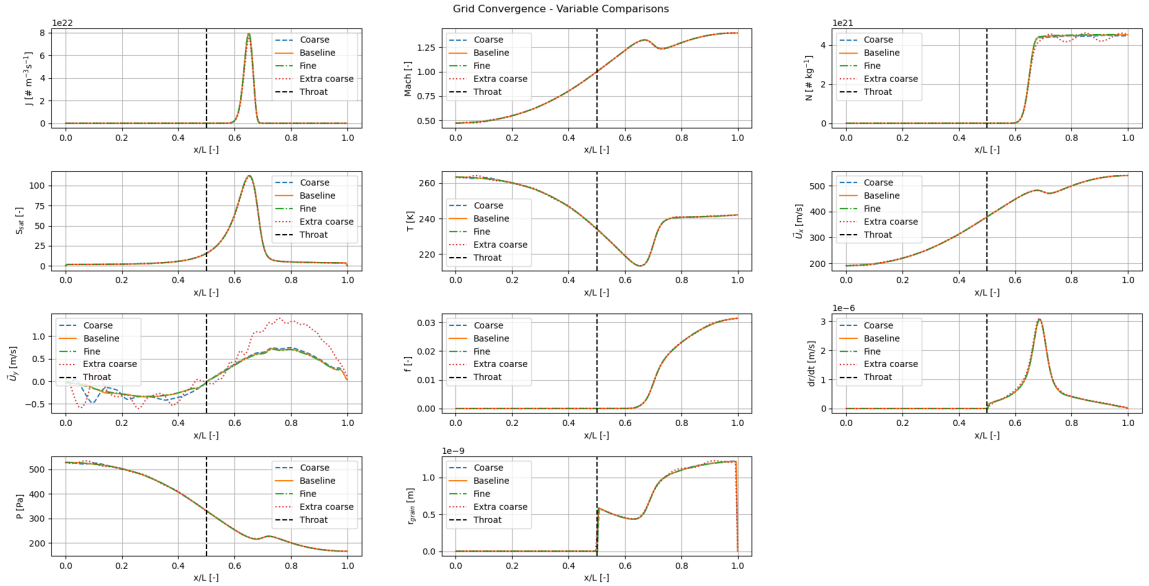

Figure 5.8: Comparison of different simulation variables for the extra coarse mesh: 4500 cells, coarse mesh: 8988 cells, baseline mesh: 18,000 cells and fine mesh 36040 cells. From left to right: nucleation rate, Mach number, grain number, supersaturation, temperature, velocity along channel, velocity along the channel height, mass fraction, grain growth, pressure and mean grain size.

The centerline pressure profile reveals a noticeable discrepancy between the extra coarse and finer meshes, particularly near the throat and downstream expansion region. The extra coarse mesh underpredicts the pressure drop and fails to capture sharp pressure gradients, resulting in a smoother, less accurate profile. In contrast, the coarse and fine meshes show strong agreement, both capturing the steep pressure gradient and downstream pressure recovery with high fidelity. This suggests that the pressure solution has converged between the coarse and fine resolutions.

The temperature distribution follows a similar trend. The extra coarse mesh produces a broader temperature peak, likely due to numerical diffusion, which blurs the thermal boundary layers and smooths out local temperature extrema. As the mesh is refined, the temperature profile becomes sharper and more physically realistic. The coarse and fine meshes again show near-identical temperature curves, indicating that thermal gradients are well resolved and the solution is effectively mesh-independent at these finer resolutions.

The velocity profile in y-direction along the centerline provides perhaps the clearest indication of grid sensitivity. On the extra coarse mesh, the velocity peak is noticeably flattened and shifted, reflecting an inability to accurately resolve the acceleration and expansion of the flow through the throat. With mesh refinement, the velocity profiles sharpen and shift toward the correct spatial location, with the coarse and fine meshes displaying excellent agreement throughout the domain, especially in capturing the acceleration near the throat and subsequent deceleration in the expansion section.

These observations are confirmed by looking atFigure 5.9 that shows the root-mean-square values of the difference of the variables along the centerline from the fine mesh and the other meshes. It is clear that making a finer mesh decreases the overall RMS up, however, the gain in accuracy is quickly diminished compared to the increase in computational cost. It is noted that this RMS error in the nucleation rate and grain number is very high in the order of 10^{21}. However, this is not apparent when looking at Figure 5.8. This is because when the mesh size has changed, the nucleation rate peak and the sudden increase in the grain number is shifted slightly and since the magnitude of both variables are high results in this high value of the RMS error. Nevertheless, it does not mean that the grid resolution is poor and is therefore more meaningful to look at the other variables to assess the grid resolution.

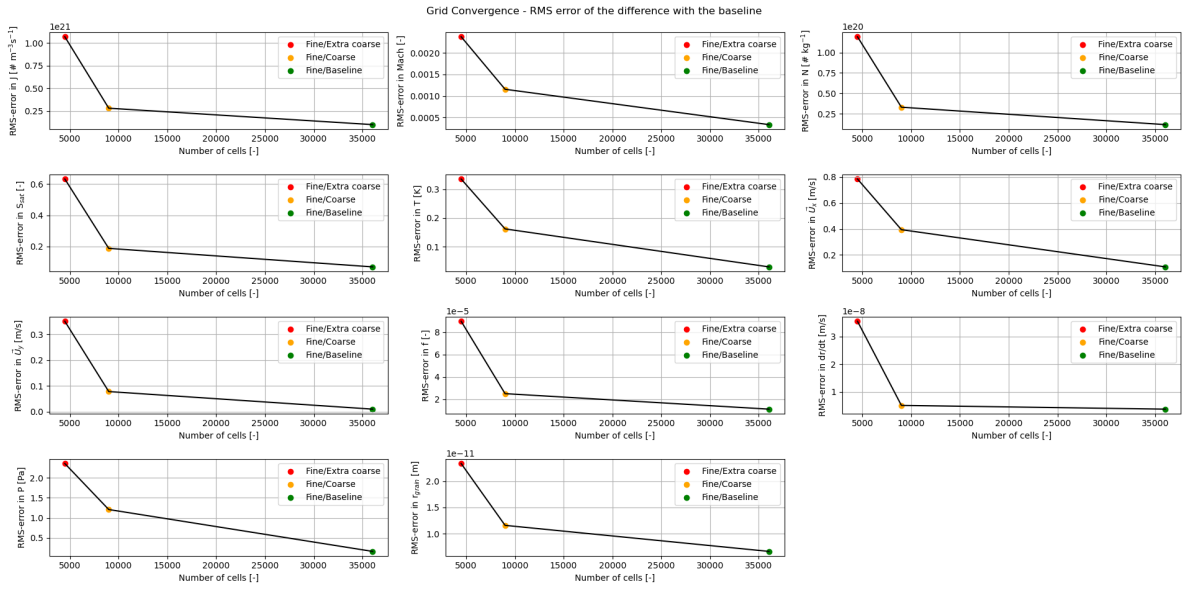

Figure 5.9: RMS error difference in simulation variables for the fine/extra coarse mesh, fine/coarse mesh and fine/baseline mesh

Overall, the grid convergence study confirms that the extra coarse mesh is inadequate for resolving critical flow features, while the coarse and fine meshes yield converged and physically consistent results. Since the difference between the coarse and fine mesh solutions is negligible, the coarse mesh is deemed sufficiently accurate for use in subsequent simulations, offering an optimal trade-off between computational cost and solution fidelity.

5.4. Boundary Conditions

It is important to correctly define the boundary conditions to properly define the simulation case. For all cases, there are four boundaries namely the inlet at the start of the channel, the outlet and the end of the channel, the wall which is the top boundary of the channel and the symmetry axis along the centreline.

Inlet: Stagnation conditions are imposed for both pressure and temperature at the triple point of water (611.657 Pa, 273.16 K) to ensure a subsonic compressible inflow. For the velocity field, a zero-gradient condition is applied, allowing the flow to be fully pressure-driven expected for Enceladus' plumes (Matson et al. 2012).

Outlet: Since the outflow is supersonic and cannot affect the upstream flow, no thermodynamic properties are explicitly set. Instead, zero-gradient conditions are applied to both pressure and temperature. For velocity, an inletOutlet boundary condition is used. This behaves as a zero-gradient condition when the flow exits the domain and switches to a fixed-value condition in the case of flow reversal.

Wall: In all simulations, wall friction is included and heat exchange is included for when defining the isothermal wall and linear temperature wall cases described in chapter 7. However, for adiabatic wall the heat exchange is zero ad onl viscosity and heat conduction is included. For the velocity boundary condition at the wall, a no-slip condition is applied. and the wall temperature is fixed at $T_w = 273.16$ K, while other variables still use zero-gradient conditions.

Symmetry Axis: This is not a physical boundary but a computational simplification to halve the domain size. Therefore, a the gradients normal to the channel axis are set to zero for all flow variables.

Solid Phase Variables: For the solid-phase variables namely, the grain number N and solid fraction f, zero-gradient conditions are applied at all boundaries. This ensures their evolution is governed solely by the flow field.

5.5. Initial Conditions

In order to start the OpenFOAM simulation, the fields need to be initialised. It is crucial to choose the initialisation such that speed of convergence is maximised. In compressible flows, the solution of propagation is limited by a time step based on the local speed of sound. As a result, convergence tends to be slow in regions where the flow remains subsonic. A first step would be to initialise the pressure, temperature and velocity to a fixed value by Riemann initial conditions. This was implemented by Fontes (2023) by specifying the static pressure to be 600 Pa in the converging region and 300 Pa in the diverging region, with the temperature and velocity being uniformly 270 K and 190 m/s respectively. Whilst this does speed up convergence compared to just prescribing a singular value, it is limited for other channel shapes and therefore can be improved by adjusting the initial conditions closer to the true solution. Instead, the pressure, temperature and velocity is initialised based on the quasi-1D isentropic flow equations presented in Equation 3.30. For example, in the case of the baseline channel, the pressure, temperature and velocity fields can be visualised. Whilst these initial conditions are not the true solution since they are quasi-1D and are also for isentropic flow with no shockwaves or phase changes occurring, they are a good first guess leading to convergence occurring faster requiring fewer pseudo time-steps.

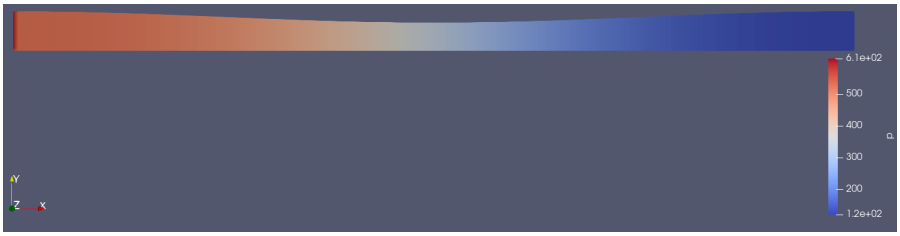

(a) Pressure field

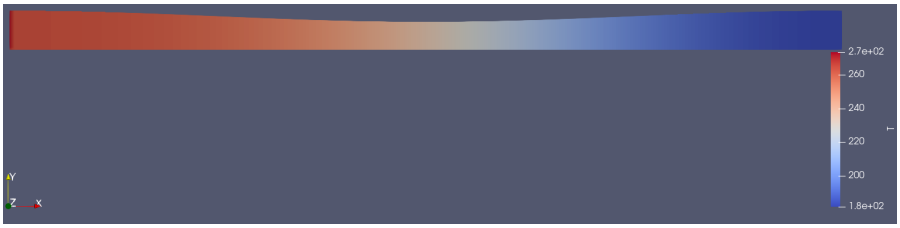

(b) Temperature field

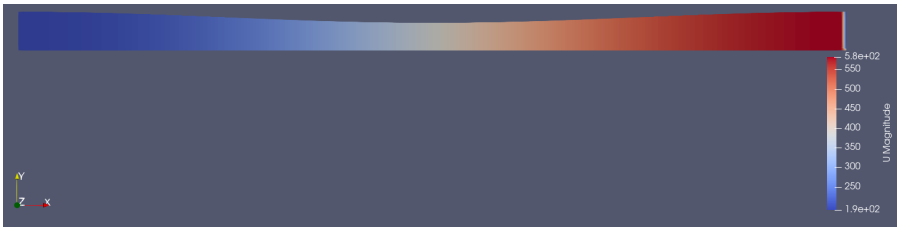

(c) Magnitude of the velocity field

Figure 5.10: Initial conditions for the pressure, temperature and velocity fields for the Icy Steam model by using quasi-1D isentropic flow model

6

Verification & Validation

It is crucial when working on new models to ensure that they are verified and validated. This chapter focuses on the steps undertaken to verify and validate the models both for the Wet Steam Model and the Wall Accretion & Sublimation Models. In section 6.1, a brief overview is given of the verification checks that were performed. In section 6.2, the Wet Steam Model and Wall Accretion & Sublimation models are analysed and compared to experimental data found in literature.

6.1. Verification

The first step in verifying the OpenFOAM model was to replicate the results obtained by Fontes (2023) using the Wet Steam Model. This ensured that the Wet Steam Model was correctly installed and integrated into OpenFOAM before any changes were made to the model.

In order to ensure the program works as intended several safeguards were implemented into the model to ensure numerical stability and physical realism. At the point where nucleation first begins, the computed values of nucleation rate J, grain mass fraction f, grain number N, and grain radius r are prone to numerical artifacts, such as division by zero or unphysical values.

The nucleation rate J depends implicitly on the logarithm of the supersaturation ratio S. This ratio transitions smoothly from subsaturation to supersaturation during the expansion. However, when $S = 1$, the logarithmic term becomes zero, rendering the critical radius undefined. This reflects the physical reality that grain formation cannot begin before vapour becomes supersaturated. To avoid this singularity, deposition is only computed when $S > 1 + \epsilon$, where ϵ is the machine precision. Additionally, nucleation is assumed to be active only if at least one cluster forms in a control volume during a time-step; this corresponds to the condition $\rho_v J \Delta t > 1 + \epsilon$ where ρ_v is the gas density and Δt is the time-step.

Similarly, the grain growth rate depends on the radius r, which is only defined when grains exist with $r \geq r^*$ To ensure physical consistency, the grain growth rate is computed only when the number of droplets per control volume exceeds unity. For a cell of volume cell V_{cell}, this requires $\rho_v N V_{cell} > 1 + \epsilon$

The minimum possible radius of a grain cluster is taken to be the diameter of a bonded pair of molecules, approximately 2.75×10^{-10} m (Huang et al. 2013). This value is imposed as a lower bound on the radius. A similar lower limit is placed on the grain mass fraction f, set to $f = 10^{-12}$ following the work of Hric and Halama (2014).

6.2. Validation

In order to validate the models, two separate validation comparisons were performed and analysed. Firstly, the Wet Steam Model was compared with experimental data for a selected channel obtained from Moore (1973). Secondly, the models for wall accretion and wall sublimation were validated by comparing the results of a simulated channel with an analytical expression obtained from Nakajima and Ingersoll (2016).

6.2.1. Wet Steam Model

A variety of experimental datasets exist in the literature for validating condensation models applicable for the Wet Steam Model. Among the most frequently cited are those by Barschdorff et al. (1972), Moses and Stein (1978), and Moore (1973). However, these studies are limited to typically higher pressures and temperatures of the range of 350 K and 30 kPa compared to what is used in this work. Most of the studies typically report centerline pressure, temperature, velocity, in some cases, nucleation related variables such as the nucleation rate, droplet growth and droplet size.

In this work, the widely used Nozzle A from Moore (1973) is selected due it as being used as a reliable benchmark in Wet Steam Model validation (Gerber and Kermani 2004). This nozzle provides pressure measurements along the centerline and a single data point for droplet size.

As indicated in the previous figure, the simulation and experimental pressure ratio results differ only slightly near the channel throat, likely due to uncertainties in the actual geometry at that location. Limited information is available on the average droplet radius in the experiment, but data from a single measurement point suggests that both simulation and experiment yield values of the same order of magnitude (10^{-8} m).

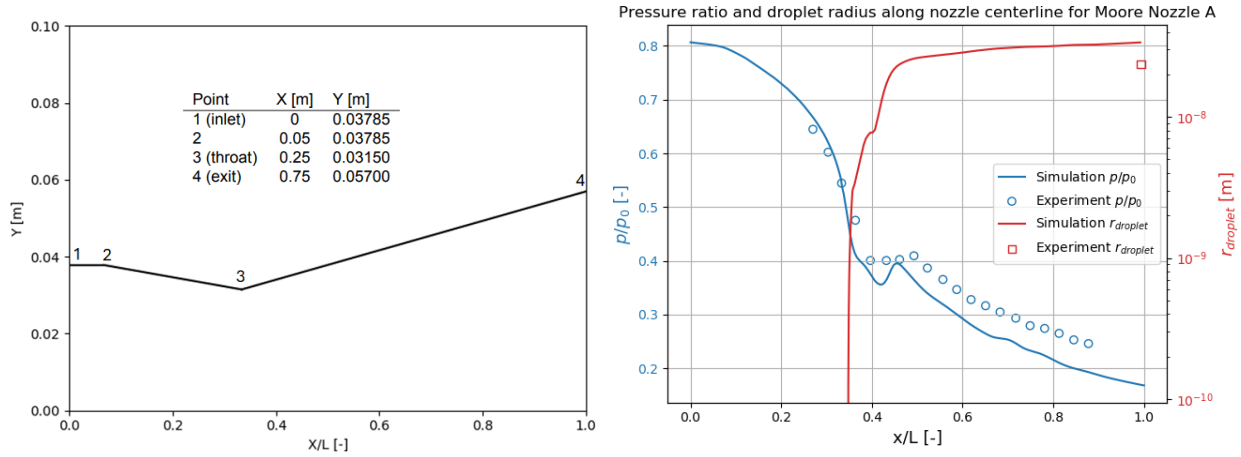

(a) Geometry of the Moore Nozzle A (Moore 1973)

(b) Pressure ratio and droplet radius values along the nozzle centreline

Figure 6.1: Validation of the Wet Steam Model for Moore Nozzle A from simulation and experimental data

It is also interesting to look at the thermodynamic and nucleation variables along the channel centreline to form an understanding of the underlying physics happening in a supersonic nozzle with condensation. The thermodynamic variables for pressure, temperature, density, Mach number and supersaturation along the centreline are shown in Figure 6.2. The nucleation variables for nucleation rate, droplet number mass fraction, droplet growth rate and average droplet radius along the centreline are shown in Figure 6.3. As steam expands through the nozzle, the saturation ratio rapidly exceeds unity and continues to rise steeply, reaching a maximum value just above 8–11. This strong supersaturation lowers the local critical radius, making the formation of stable liquid clusters energetically favourable. Nucleation then occurs at rates on the order of $10^{20}\ m^{-3}s^{-1}$, with droplets immediately beginning to form and grow.

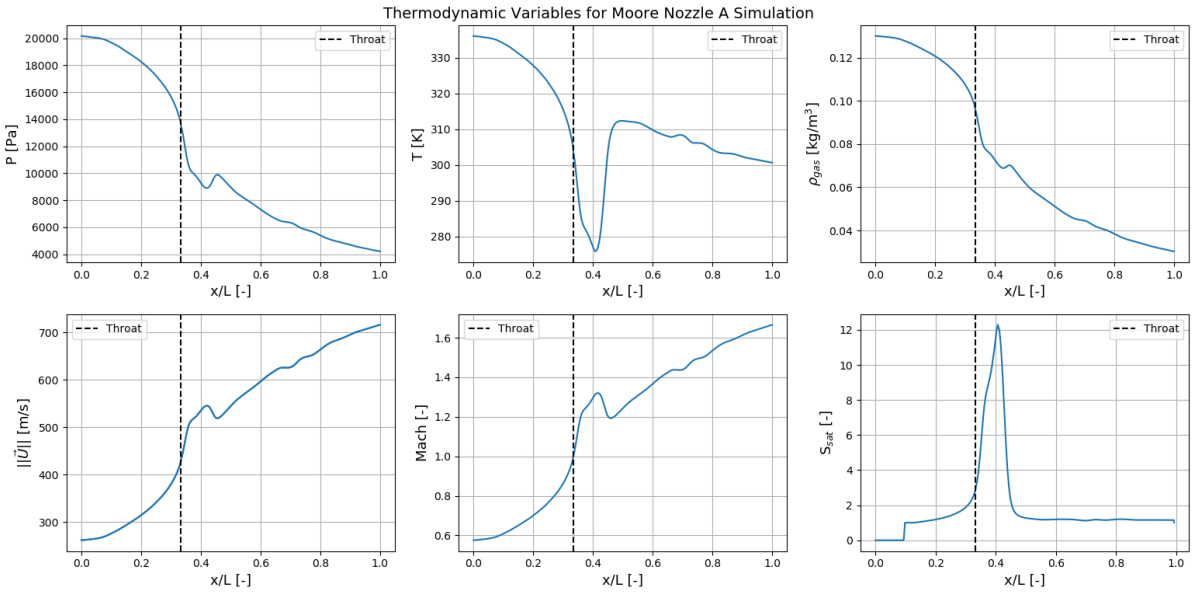

Figure 6.2: Simulation thermodynamic variables along the nozzle centreline for Moore Nozzle A with an adiabatic wall. From left to right: pressure, temperature, density, velocity, Mach number and supersaturation.

As condensation proceeds, latent heat is released, reducing subcooling and causing a local pressure rise. This in turn lowers the supersaturation ratio, thereby slowing the process of nucleation and driving the supersaturation towards 1. Once supersaturation decreases sufficiently, nucleation ceases and the droplet number density remains approximately constant, with only minor variations due to convection. Meanwhile, even once the supersaturation ratio approaches unity and nucleation has already stopped, droplets continue to grow as long as the vapour remains supercooled. This is further confirmed by observing that the mass fraction continues to increase even though nucleation has stopped.

The associated pressure rise slows the expansion, producing a deceleration of the flow that is reflected in a dip in the velocity profile. The temperature increase simultaneously raises the local speed of sound, further reducing the Mach number.

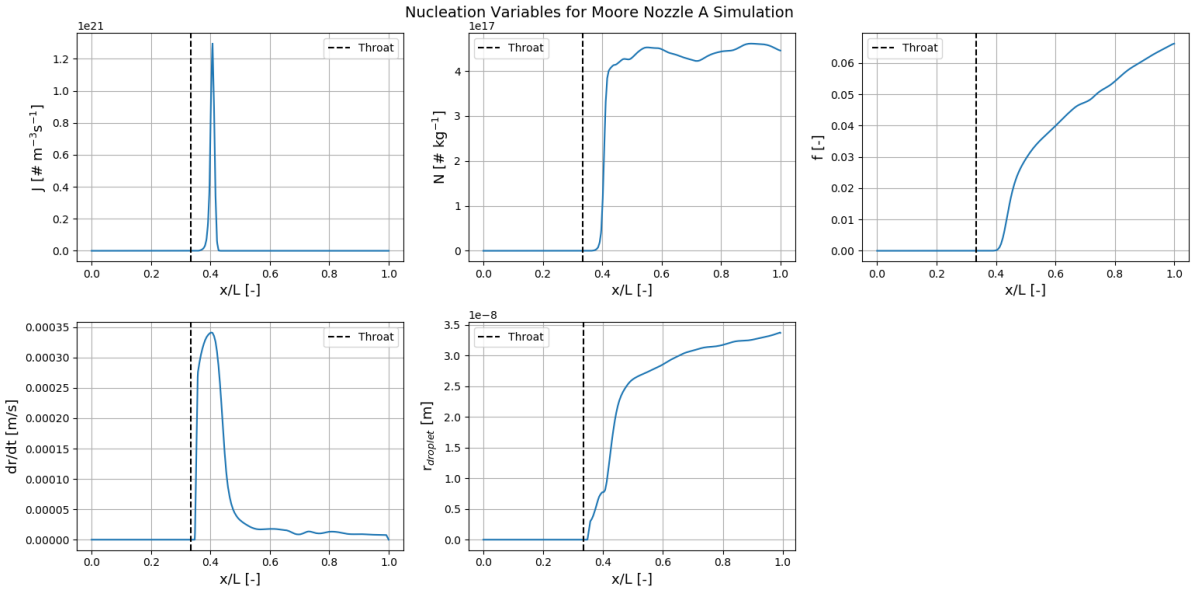

Figure 6.3: Simulation nucleation variables along the nozzle centreline for Moore Nozzle A with an adiabatic wall. From left to right: nucleation rate, droplet number, mass fraction, droplet growth rate and average droplet radius.

6.2.2. Wall Accretion & Sublimation

Validation of the wall mass flux comprising both accretion and sublimation was carried out by comparing the results of the multi-throat channel with an empirical formula from Nakajima and Ingersoll (2016) given by

$$E = 2\left(\frac{p}{\sqrt{2\pi RT/M}} - \frac{p_{sat}}{\sqrt{2\pi RT_w/M}}\right) \tag{6.1}$$

In Equation 6.1, E denotes the wall mass flux into the walls per unit area, p and T are the pressure and temperature of the adjacent wall cell respectively, M is the molar mass, R is the gas constant and p_{sat} is the saturation pressure given by

$$p_{sat}(T_w) = \exp\left((-2663.5/T_w + 12.537)\ln(10)\right) \tag{6.2}$$

The comparison between the mass flux from simulation and from Equation 6.1 is shown in Figure 6.4. The plot demonstrates similar results but the wall fluxes are overestimated in the simulation. Part of the discrepancy can be attributed to the choice of sticking coefficient. In reality, the sticking coefficient will be lower than 1 and hence reduces the wall accretion mass flux. Furthermore, the sticking coefficient directly affects the calibrated pre-exponential factor for the wall sublimation mass flux. A lower sticking coefficient will also result in a lower wall sublimation mass flux.

Another source of difference lies in the modelling approach. In this work, wall flux is calculated using a more physically based method that explicitly considers individual molecular collisions with the wall. In contrast, the validation data are based on an analytical relation that neglects both the redistribution of the flow following collisions and the fact that only part of the flow interacts directly with the walls. In the analytical approach, the flow is assumed to fully redistribute after each collision, such that the near-wall particle layer is always in equilibrium with the wall (Ingersoll and Pankine 2010). However, in reality, particles that do not collide with the wall and are not necessarily equilibrated with it.

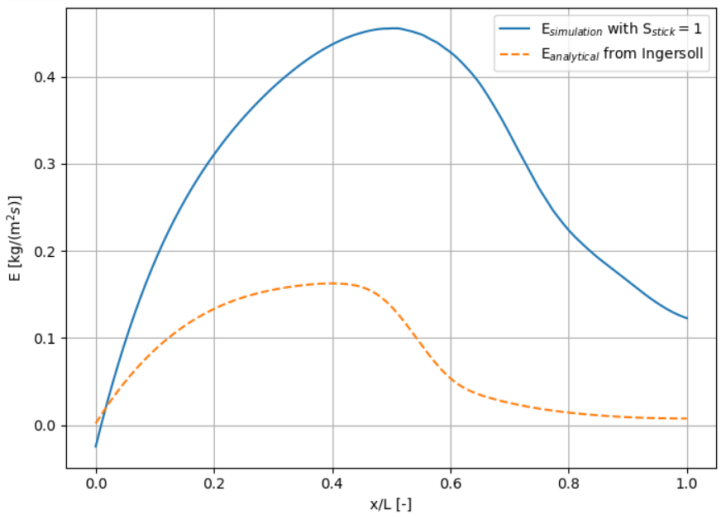

Figure 6.4: Validation of models for wall accretion & sublimation by computing the the total wall mass flux per unit area E and comparing it with an analytical relation obtained from Nakajima and Ingersoll (2016)

7

Results: A Parametric Study

The test cases presented in Table 7.1 are designed to systematically explore the influence of channel geometry, thermal boundary conditions, and wall-phase interactions on vapour transport and deposition in icy cracks, with direct relevance to cryovolcanic activity on Enceladus. Cases 1 and 2 isolate the effects of wall accretion by simulating vapour flow through the baseline convergent-divergent nozzle for an adiabatic wall and an isothermal wall. Cases 3 and 4 mirror this structure but focus on wall sublimation, examining how adiabatic and isothermal heating can drive mass loss from the channel walls. Cases 5 to 8 combine both accretion and sublimation processes to capture more realistic boundary evolution. In case 8, a multi-throat geometry is introduced to study the role of a more complex geometry on phase-change dynamics and wall interactions.

Table 7.1: Definitions of all test cases that was done for this work

Test Case	Channel	Wall Temperature	Wall Interactions
1	Baseline	Adiabatic	
2	Baseline	Isothermal: 273 K	Wall Accretion
3	Baseline	Adiabatic	
4	Baseline	Isothermal: 273 K	Wall Sublimation
5	Baseline	Adiabatic	
6	Baseline	Isothermal: 273 K	Both
7	Baseline	Linear: 273-200 K	
8	Multi-Throat	Linear: 273-200 K	Both

The thermodynamic properties inside the channel, particularly gas density and temperature, are strongly influenced by both (i) the compressible nature of the flow in a constricting channel and (ii) phase change processes within the flow. Nucleation, grain growth and wall accretion deplete vapour mass and release latent heat, which changes the gas state and indirectly affects the conditions driving wall accretion and sublimation.

For the adiabatic cases, there is a no-slip condition at the wall which enforces zero velocity. This creates a velocity gradient that increases the residence time of vapour molecules and icy particles in the near-wall region. Furthermore, there is no heat exchange with the solid boundary, meaning that any thermal effects are confined to the gas side. This leads to a thermal boundary layer that sustains elevated local supersaturation near the wall.

For the isothermal case, the wall has a fixed temperature that can be a cold wall where the wall temperature is lower than the adiabatic wall temperature or a hot wall where the wall temperature is higher. A thermal boundary layer is present where the temperature varies from the wall until it reaches the freestream temperature T_∞. It is emphasised that the isothermal case means that the temperature of the wall is fixed but it can still have wall temperature distribution along the channel. In other words, the wall temperature can have a gradient along the channel but none of the flow physics affects the temperature at the wall.

7.1. Cases 1 and 2: Channels with Wall Accretion

The two cases deal with channels that experience deposition in the bulk flow and wall accretion. The first case considers an adiabatic wall whereas the second case considers an isothermal wall at 273 K.

7.1.1. Case 1: Baseline Channel With Adiabatic Wall

The temporal evolution of the baseline channel due to wall accretion for an adiabatic wall is shown in Figure 7.1. Figure 7.1a shows a sequence of wall profiles with increasing simulation time. It can be observed that wall accretion occurs predominantly at the inlet and decreases in magnitude towards the outlet.

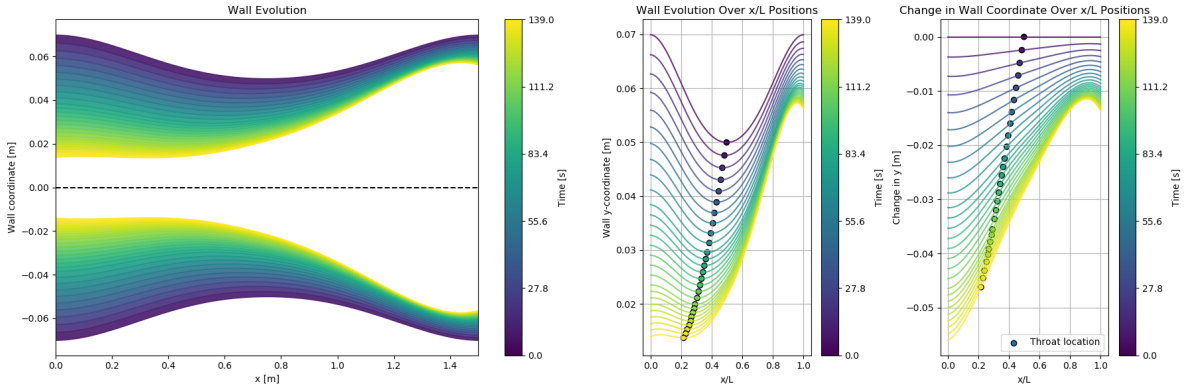

(a) Wall evolution as time progresses due to wall accretion for the baseline channel with an adiabatic wall

(b) Wall geometry evolution as time progresses due to wall accretion for the baseline channel with an adiabatic wall

Figure 7.1: Wall evolution as time progresses due to wall accretion for the baseline channel with an adiabatic wall

It is observed in Figure 7.1b that the geometrical throat moves upstream and that the change in the wall geometry is largest at the inlet and lowest at the outlet. This reduction in throat size results in a monotonic increase in the exit-to-throat area ratio (A_e/A^*). The change in the wall geometry due to accretion can be explained by looking at Figure 7.2. Figure 7.2 shows several thermodynamic variables such as temperature, density and pressure at the wall as well as the mass fluxes per unit area for wall accretion $\dot{m}_a$, wall sublimation $\dot{m}_s$ and the total wall mass flux per unit area $\dot{m}_{tot}$.

Analysing the spatial evolution, the density and pressure of the vapour decrease along the channel due to the compression of the channel until it reaches choked conditions before being expanded. At x/L of 0.6 there is a local increase in density and pressure due to localised nucleation occurring in the bulk flow. The temperature profile generally shows a decreasing trend due to the compression-expansion until the onset of nucleation in the bulk flow where the temperature increases due to the release of latent heat and from grain growth. The temperature increase due to the release of latent heat and from grain growth compete with the decreasing temperature due to expansion process. From Equation 4.3, the rate of wall accretion is directly proportional to $\rho_g \cdot \sqrt{T}$ and therefore follows similar trend to the density curve.

Analysing the temporal evolution, as the throat contracts and consequently A_e/A^* increases, it leads to a stronger expansion and hence shows the density decreasing over time. This effect effectively reduces the rate of wall accretion. However, the rate of wall accretion is also dependent of the wall temperature or in this case the wall-adjacent cell temperature.

At early simulation times the wall-adjacent cell temperature shows a three-stage pattern: expansion cooling, a small local heating, a subsequent cooling, and then a larger downstream heating. This results from a localised nucleation/growth event in the core that injects latent heat into the flow and briefly entrains into the boundary layer (first heating). Directly downstream the flow still experiences fresh expansion and reduced local condensation (vapour depletion), producing a transient cooling dip. Further downstream particle growth and advected enthalpy accumulate where expansion cooling is weaker, producing the final temperature rise. As wall accretion advances, the nucleation region shifts upstream and becomes more spatially distributed. The heat release therefore becomes continuous and advected, the intermediate cooling zone disappears, and only a single downstream temperature increase remains.

As a result of both the temperature and density profiles along the wall, the rate of wall accretion is the highest at the inlet and progressively decreases towards the vent. However, towards the vent the increase in temperature becomes so high that increase in $\sqrt{T}$ exceeds the decrease in ρ_{gas} resulting in rounded off outlet shape in Figure 7.1a.

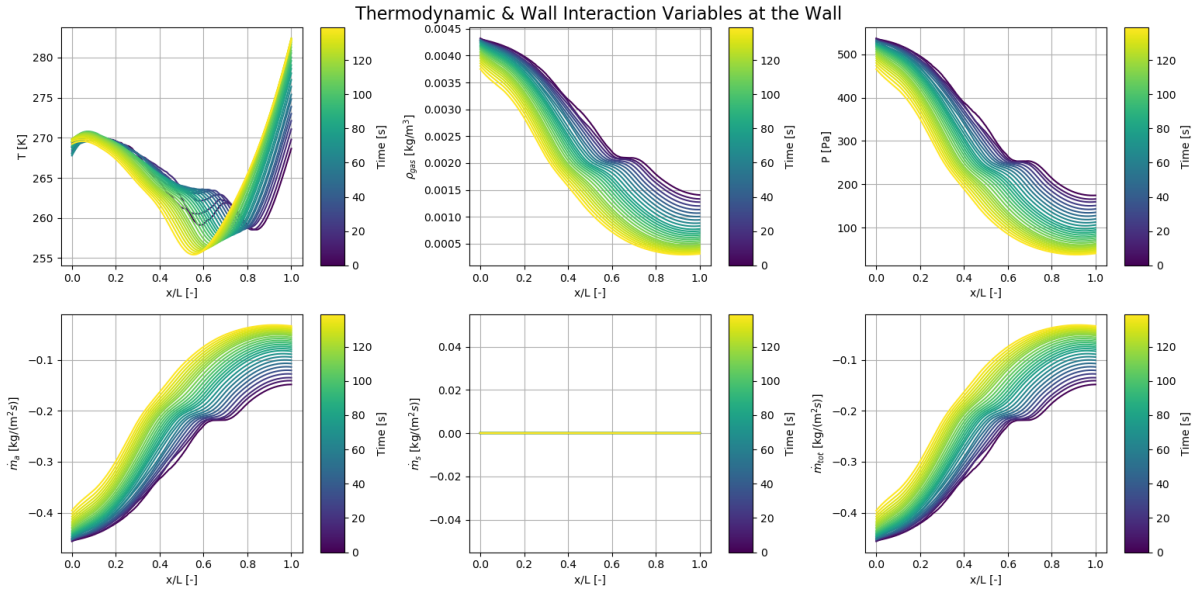

Figure 7.2: Thermodynamic and wall related variables at the wall as time progresses due to wall accretion for the baseline channel with an adiabatic wall

Figure 7.3 shows the centreline evolution of thermodynamic such as pressure, temperature, density, velocity, Mach number and supersaturation over several simulation times. Figure 7.4 shows the centreline evolution of nucleation variables such as nucleation, grain number, mass fraction, grain growth and average grain size.

Analysing the spatial evolution, the pressure, temperature and density decrease along the channel again due to the flow contraction and expansion. Similarly, for the first epoch, nucleation begins at around x/L of 0.5 resulting in the local increase in pressure, temperature and density. This is accompanied by an increase in flow velocity and hence Mach number along the channel followed by a local decrease at x/L of 0.65 until nucleation ceases. As the flow expands, supersaturation increases until nucleation occurs and then decreases as the flow comes back to equilibrium. This is reflected in Figure 7.4 where the nucleation rate begins at x/L of 0.5 which causes an increase in the grain number. As nucleation begins, the average grain size abruptly increases because of the high supersaturation ratio but then decreases as the production of smaller grains by nucleation outweighs the growth of the grains. Eventually, as nucleation reduces, the average grain size increases as grain growth remains high.

Analysing the temporal evolution, the increase in A_e/A^* over time causes an overall decrease in the pressure, while downstream pressure increase due to nucleation reduces over time. When accretion shifts the deposition onset upstream, growth continues over a longer axial distance (nucleation earlier, growth longer). The growth contribution therefore appears as a broad downstream source of latent heat rather than a tight, localised pulse.

Similarly, the temperature also decreases with time due to the throat moving upstream with a local increase in temperature towards the vent due to the heat from grain growth exceeding the heat lost due to expansion.

The supersaturation peak shifts slightly upstream as the throat narrows, and this migration is accompanied by strong localised spikes in the nucleation rate and grain number density. The average grain size, generally increases and occurs earlier in the channel.

These effects translate into a monotonic increase in downstream solid mass fraction. The velocity and Mach number generally increases with simulation time. These trends indicate that the throat progressively approaches choked conditions earlier in time.

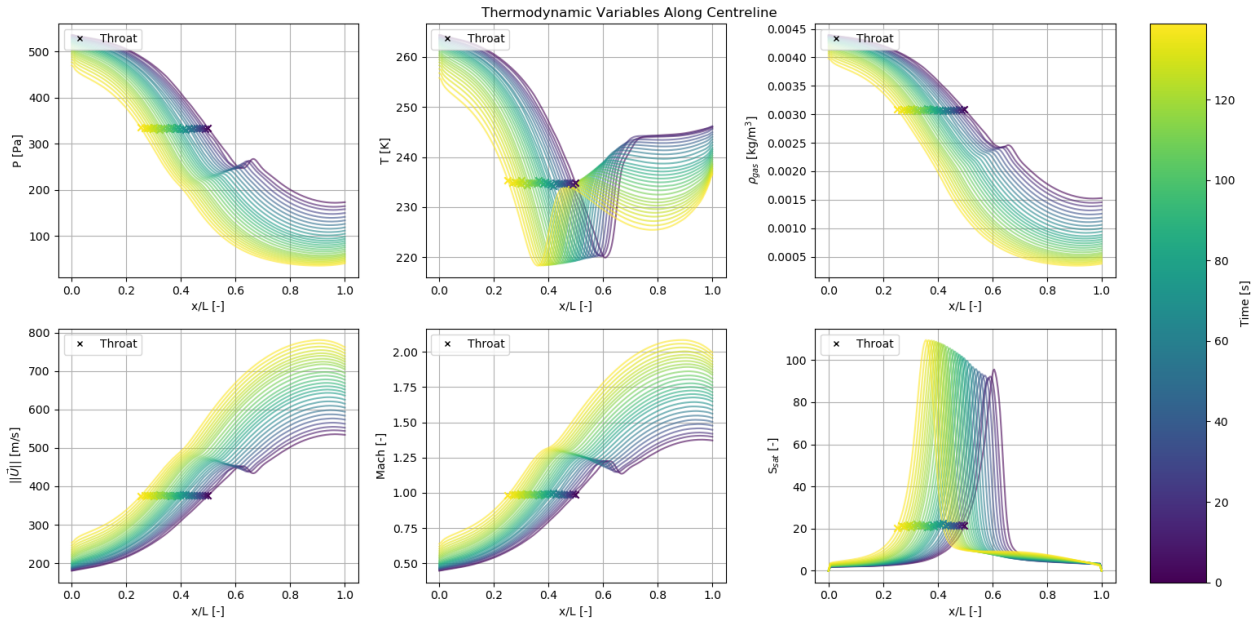

Figure 7.3: Thermodynamic parameters along the channel centreline as time progresses due to wall accretion for the baseline channel with an adiabatic wall. From left to right: pressure, temperature, density, velocity, Mach number, and supersaturation

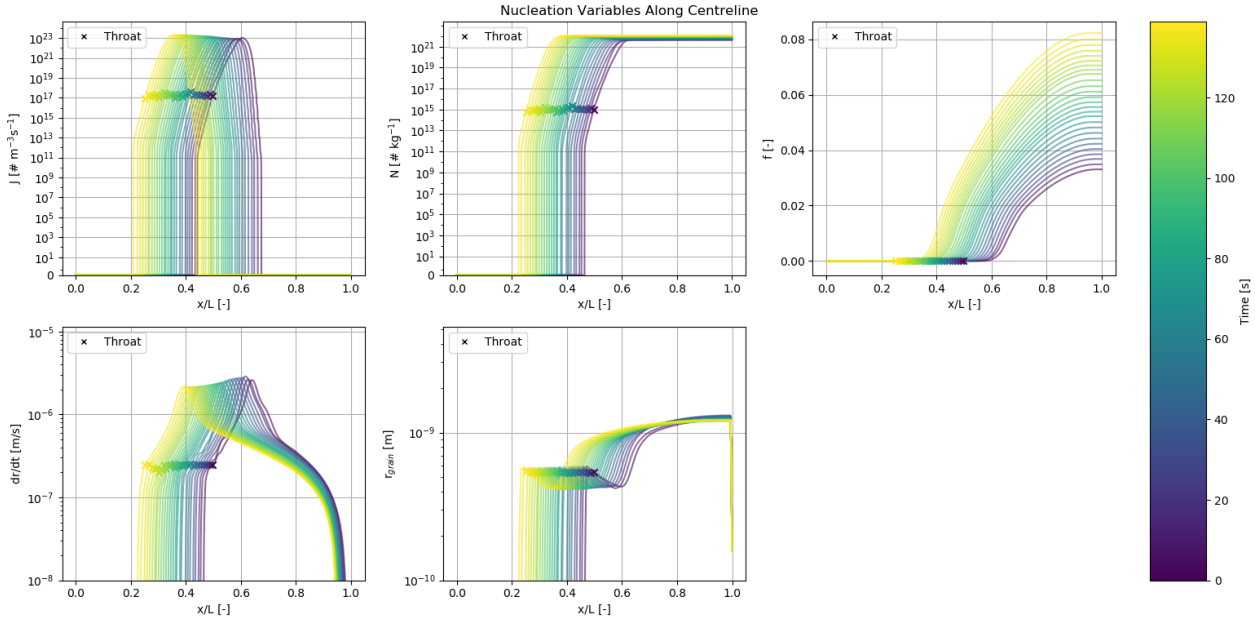

Figure 7.4: Nucleation parameters along the channel centreline as time progresses due to wall accretion for the baseline channel with an adiabatic wall. From left to right: nucleation, grain number, mass fraction, grain growth and average grain size

Figure 7.5 integrates the results by presenting the evolution of both the pressure-temperature (p-T) trajectory along the centreline and at relevant points such as the inlet, throat, Wilson point and outlet. The p–T plots demonstrate that as accretion progresses, fluid parcels experience stronger cooling earlier in the channel, crossing deeper into the metastable supersaturated region shown by the Wilson point and triggering nucleation closer to the throat. The inlet starts at a lower temperature and pressure because of the lower area ratio and since the throat moves upstream, it has a higher pressure and temperature for the latest epochs. For the outlet, the pressure and temperature decrease monotonically for the latest epochs.

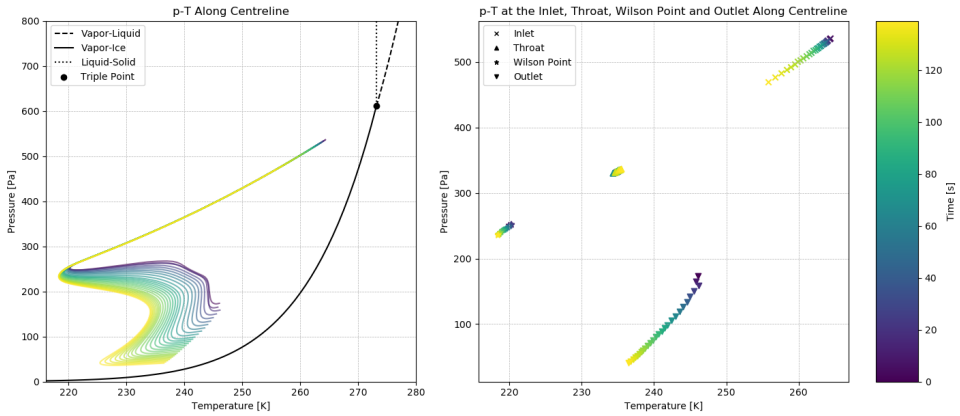

Figure 7.5: Evolution of pressure-temperature along the centreline as time progresses due to wall accretion for the baseline channel with an adiabatic wall

Figure 7.6 shows how the throat size and location evolves in time. The throat size decreases monotonically with time and the throat moves upstream. The throat size shows a linear trend whereas the location of the throat shows a near linear trend. Furthermore, A_e/A^* shows an accelerating growth with increasing time. From Figure 7.6 it appears that for the baseline channel with only wall accretion for an adiabatic wall that the throat will narrow and move upstream towards the inlet and will close with time.

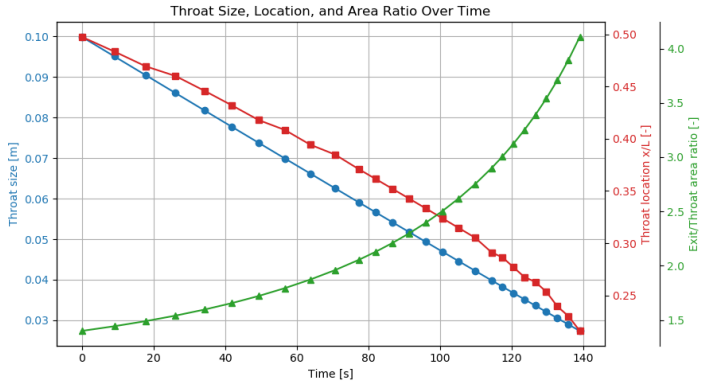

Figure 7.6: Channel throat evolution as time progresses as time progresses due to wall accretion for the baseline channel with an adiabatic wall

7.1.2. Case 2: Baseline Channel With Isothermal $T_w = 273\ K$

The temporal evolution of the baseline channel due to wall accretion for an isothermal wall at 273 K is shown in Figure 7.7. The wall evolution shown in Figure 7.7a shows a very similar behaviour to the adiabatic case (case 1). Figure 7.7b shows that the channel walls continue to narrow over time solely due to wall accretion, but the rate and spatial distribution of accretion are modified by the fixed wall temperature. Unlike in the adiabatic case, where near-wall vapour retained its energy, here the gas adjacent to the wall is warmed up to 273 K.

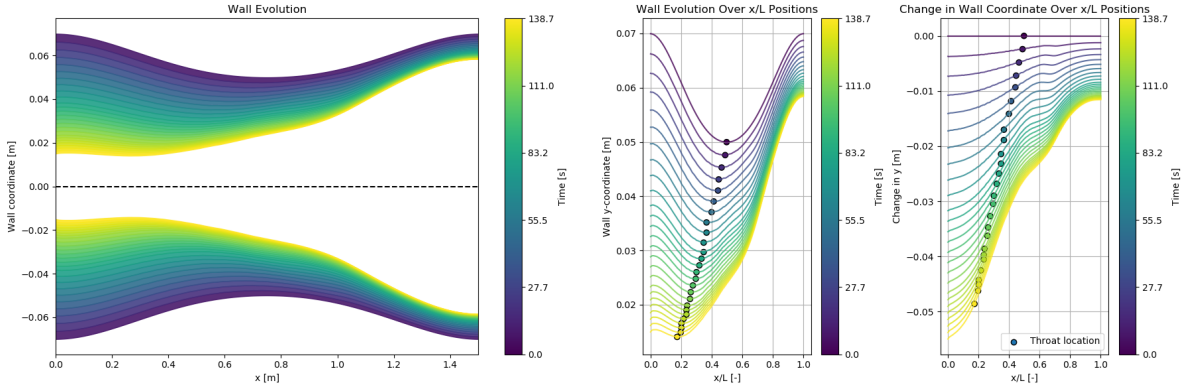

(a) Wall evolution as time progresses due to wall accretion for the baseline channel with an isothermal wall $T_w = 273\ K$

(b) Wall geometry evolution as time progresses due to wall accretion for the baseline channel with an isothermal wall $T_w = 273\ K$.

Figure 7.7: Wall evolution as time progresses due to wall accretion for the baseline channel with an isothermal wall $T_w = 273\ K$

Figure 7.8 shows several thermodynamic variables such as temperature and the wall mass fluxes per unit area. Analysing the spatial evolution, the behaviour of the curves along the channel follows the same reasoning as case 1 due to the expansion of the flow leading to a decreasing density, pressure with a local increase due to nucleation occurring in the bulk flow.

Analysing the temporal evolution, since the temperature is fixed to 273 K results in the channel being warmer than the adiabatic case for the majority of the channel until x/L of 0.9-1.0. However, since wall accretion is dependent on the square of the temperature, this effect is minor. Furthermore, since the temperature is fixed it shows a more moderate accretion mass flux per unit area after x/L 0.6 compared to case 1. This is because in case 1, the temperature starts to increase after x/L 0.6 due to nucleation occurring in the bulk flow.

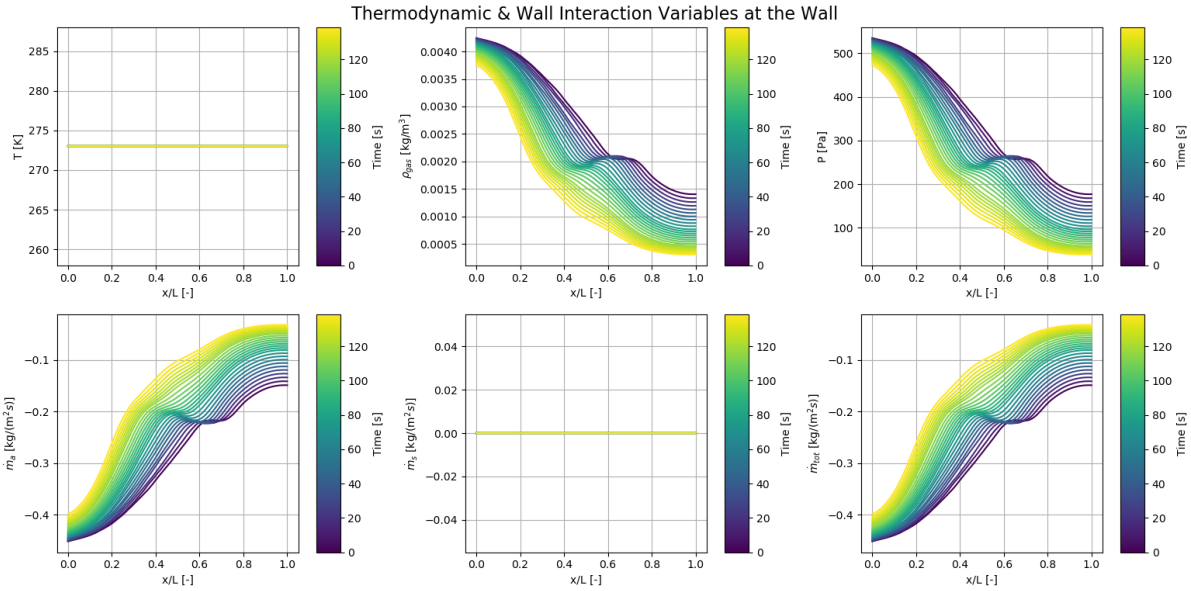

Figure 7.8: Thermodynamic and wall related variables at the wall as time progresses due to wall accretion for the baseline channel with an isothermal wall $T_w = 273\ K$.

Figure 7.9 and Figure 7.10 shows the centreline evolution of key flow and nucleation variables respectively across several simulation times. Analysing the spatial evolution, similarly to case 1 the pressure, temperature and density decrease along the channel due to contraction and expansion. As the flow expands and supersaturation increases, nucleation is triggered which injects latent heat into the flow. This is reflected by the local increase in pressure, temperature and density and decrease in

Mach number. The rise in nucleation increases the grain number and the average grain size. As new grains are nucleated, they grow which increases the mass fraction. The spatial evolution is generally the same for all cases with the same channel and will therefore will not be repeated for succeeding cases.

Analysing the temporal evolution, similarly to case 1, the nucleation occurs earlier and is enhanced. This is due to the throat becoming smaller and moving upstream promoting a higher expansion ratio. The same conclusions can therefore be drawn from the adiabatic case.

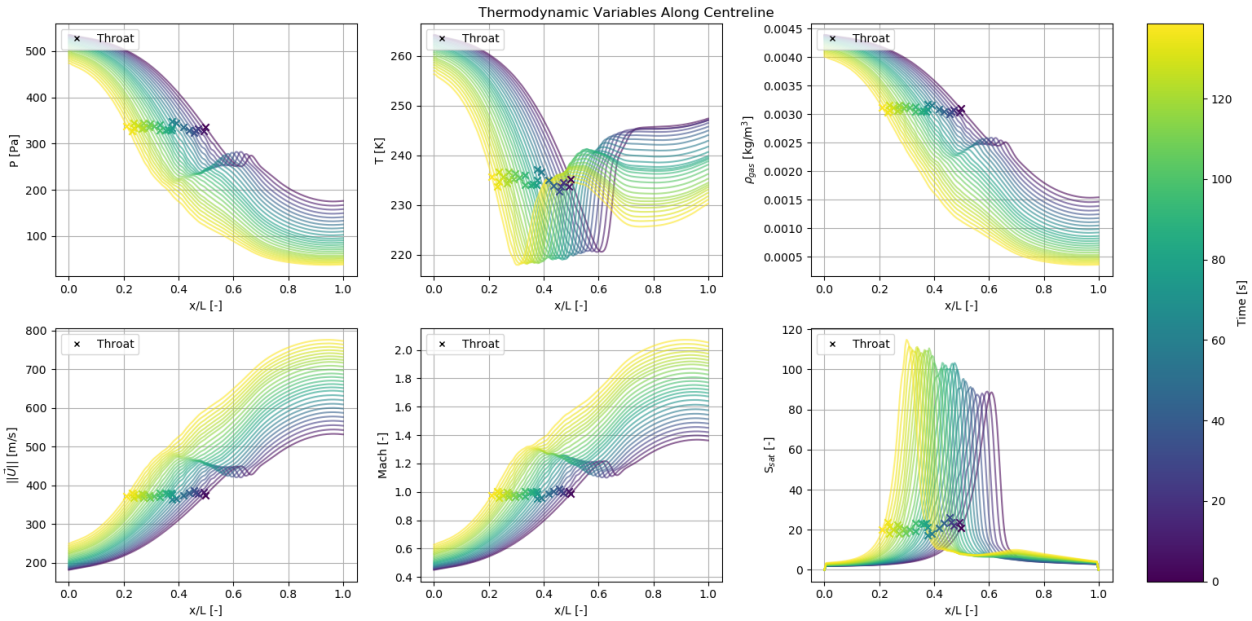

Figure 7.9: Simulation parameters along the channel centreline as time progresses due to wall accretion for the baseline channel with an isothermal wall $T_w = 273\ K$. From left to right: pressure, temperature, density, velocity, Mach number, supersaturation, nucleation rate, grain number and mass fraction

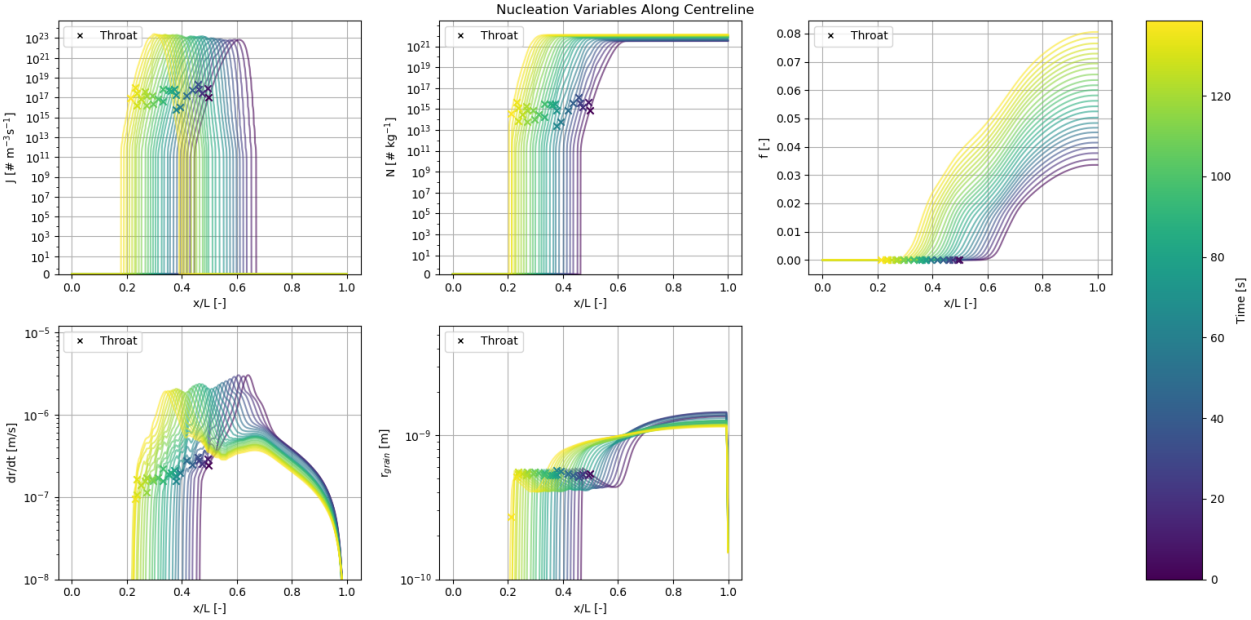

Figure 7.10: Simulation parameters along the channel centreline as time progresses due to wall accretion for the baseline channel with an isothermal wall $T_w = 273\ K$. From left to right: pressure, temperature, density, velocity, Mach number, supersaturation, nucleation rate, grain number and mass fraction

Figure 7.11 shows p-T curves along the centreline. Similarly to the adiabatic case, the vapour experiences stronger cooling earlier in the channel, allowing it to cross deeper into the metastable supersaturated region before nucleation begins. Furthermore, it can be seenFigure 7.6 that the heating due to grain growth is slightly lower for the isothermal case leading to a lower temperature at the outlet compared to the adiabatic case.

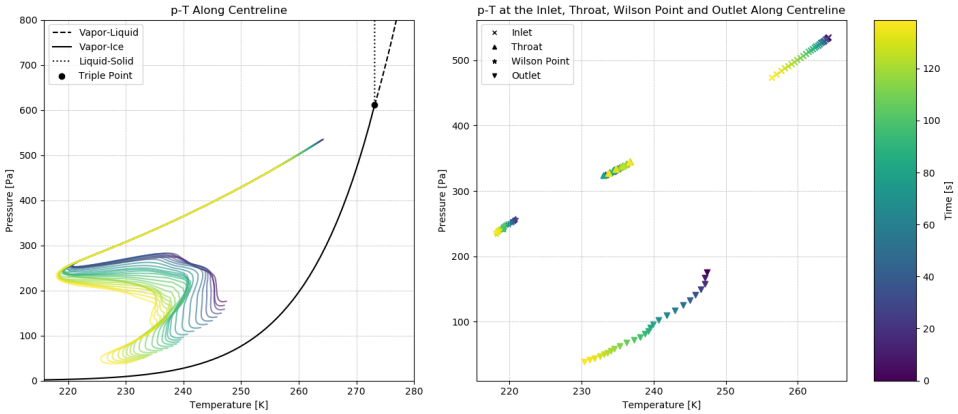

Figure 7.11: Evolution of pressure-temperature along the centreline as time progresses due to wall accretion for the baseline channel with an isothermal wall $T_w = 273\ K$.

Figure 7.6 shows how the throat evolves in time. Again, the throat size decreases monotonically with time resulting an effective increase in A_e/A^* and the throat moves upstream. Similarly to the adiabatic case, the linear trend of the throat size reduction and moving upstream results in the channel will close with time.

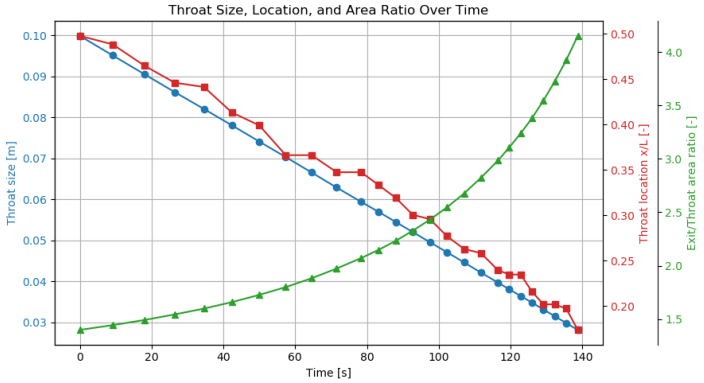

Figure 7.12: Channel throat evolution as time progresses as time progresses due to wall accretion for the baseline channel with an isothermal wall $T_w = 273\ K$

7.2. Cases 3 and 4: Channels with Wall Sublimation

The third and fourth cases deal with channels that experience deposition in the bulk flow and wall sublimation. Case 3 considers an adiabatic wall, whereas case 4 considers an isothermal wall at 273 K.

7.2.1. Case 3: Baseline Channel With Adiabatic Wall

The temporal evolution of the baseline channel due to wall sublimation for an adiabatic wall is shown in Figure 7.13. Figure 7.13b shows a sequence of wall profiles with increasing simulation time. It can be observed that wall sublimation occurs strongly at the inlet and decreases in magnitude towards the outlet. Since there is no wall accretion, the wall opens up monotonically. It is evident then in this case that the throat moves upstream towards the vent.

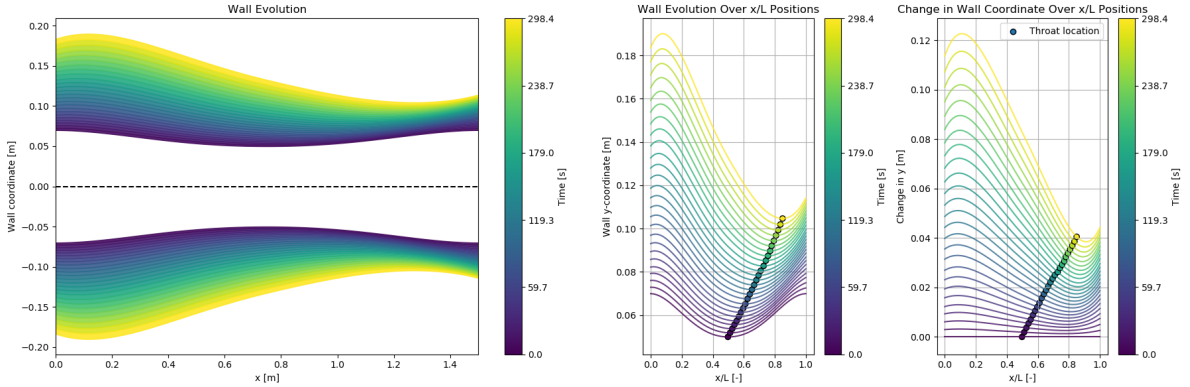

(a) Wall evolution as time progresses due to wall sublimation for the baseline channel with an adiabatic wall

(b) Wall geometry evolution as time progresses due to wall sublimation for the baseline channel with an adiabatic wall

Figure 7.13: Wall evolution as time progresses due to wall sublimation for the baseline channel with an adiabatic wall

The behaviour of wall sublimation can be explained by observing Figure 7.14. Figure 7.14 shows several thermodynamic variables such as temperature and the wall mass fluxes per unit area. Analysing the spatial evolution, the curves follow the same trend as cases 1 and 2.

Analysing the temporal evolution, in contrast cases 1 and 2, is that the wall temperature for the first epoch decreases until it reaches the throat at the local x/L of 0.5 and then starts to increase to about 270 K. However, for later times this increase diminishes as the throat moves downstream until at a certain time it decreases instead of increasing. Then at the final times since the throat has moved upstream, the temperature increase due to latent heat from nucleation occurs towards the vent at around the local x/L of 0.9. Since wall sublimation is only affected by the wall temperature, it shows the same trend. The effect of nucleation and grain growth in the bulk flow then is propagated downstream and affects the cells adjacent to the wall.

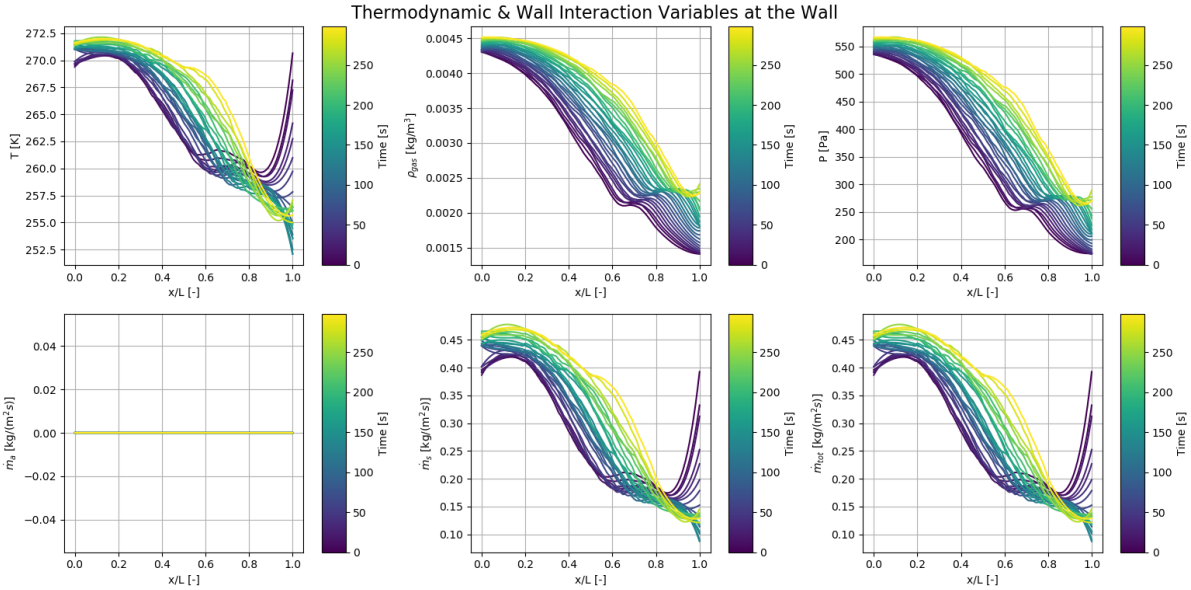

Figure 7.14: Thermodynamic and wall related variables at the wall as time progresses due to wall sublimation for the baseline channel with an adiabatic wall

Figure 7.15 and Figure 7.16 shows the centreline evolution of key flow and nucleation variables across several simulation times.

Analysing the temporal evolution, as expected, the process of wall sublimation is opposite to that of wall accretion. Since A_e/A^* decreases and the throat moves downstream, it results in an overall increase in pressure and hence temperature. Therefore, the cooling due to the expansion of the geom-

etry takes longer for the flow to become supersaturated. This is reflected by the downstream shifting of the local increase in pressure and density. This downstream migration is accompanied by reduced localised spikes in the nucleation rate and grain number density. Furthermore, the nucleation rates show a factor of about 100 lower compared to cases 1 and 2 due to the lower supersaturation caused by the weaker expansion.

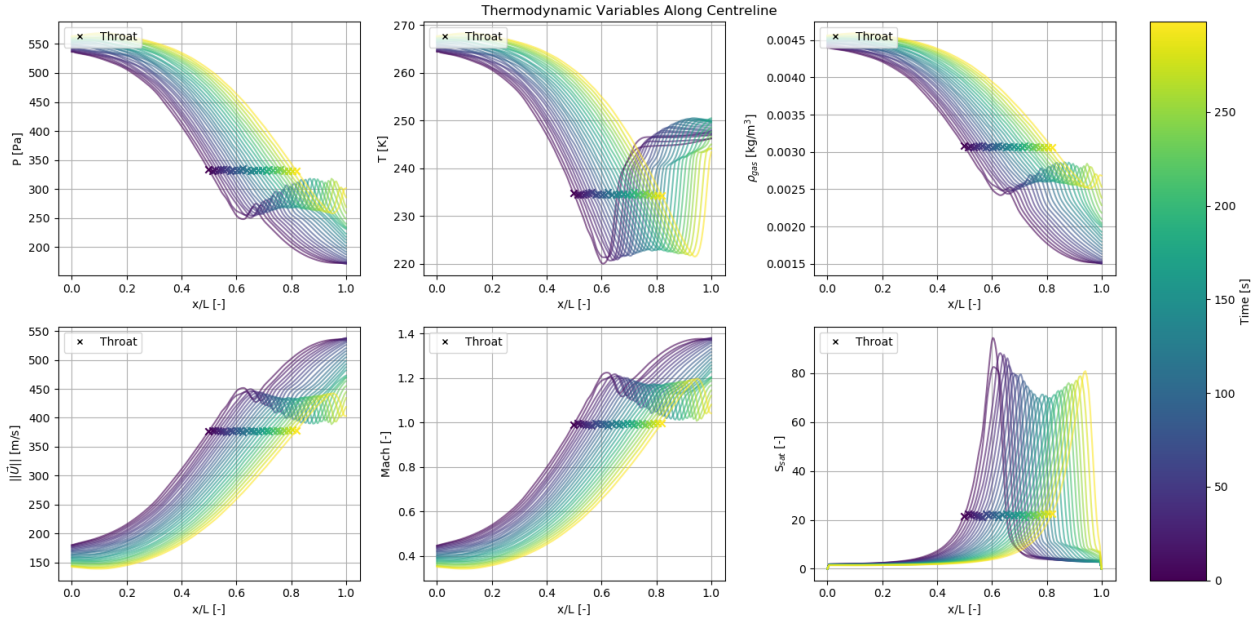

Figure 7.15: Simulation parameters along the channel centreline as time progresses due to wall sublimation for the baseline channel with an adiabatic wall. From left to right: pressure, temperature, density, velocity, Mach number, supersaturation, nucleation rate, grain number and mass fraction.

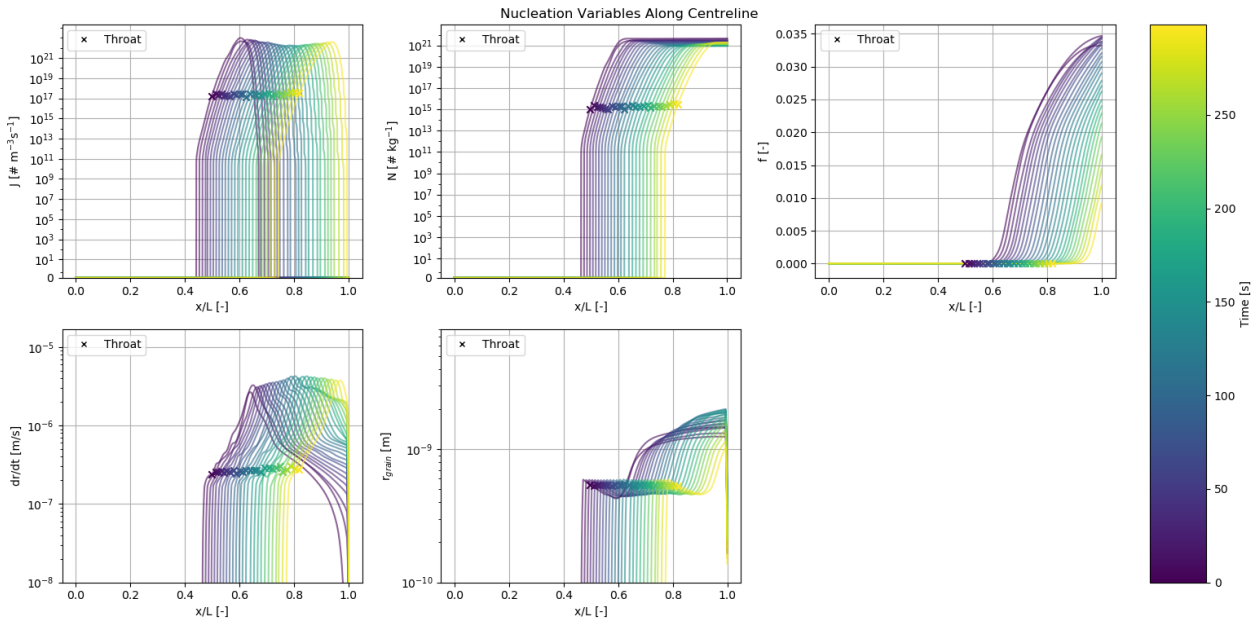

Figure 7.16: Simulation parameters along the channel centreline as time progresses due to wall sublimation for the baseline channel with an adiabatic wall. From left to right: pressure, temperature, density, velocity, Mach number, supersaturation, nucleation rate, grain number and mass fraction

Figure 7.17 shows the pressure versus temperature along the centreline. The pressure and temperature at the inlet move closer to triple point conditions with evolving time. Moreover, it experiences

more cooling although since the throat moves upstream it does not cross as deep into the metastable supersaturated region compared to the first epoch.

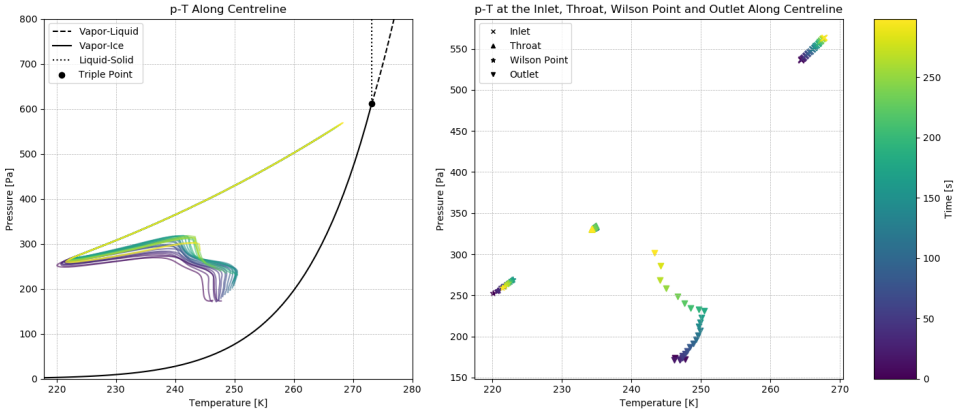

Figure 7.17: Evolution of pressure-temperature along the centreline as time progresses due to wall sublimation for the baseline channel with an adiabatic wall

Figure 7.18 shows how the throat evolves in time. Both the throat size and movement of the throat location show a positive near linear trend. The A_e/A^* area ratio initially gradually decreases over time and after about 25 seconds it decreases faster. It is evident that for the baseline channel with only wall sublimation for an adiabatic wall, the throat will move towards the vent and will continually open.

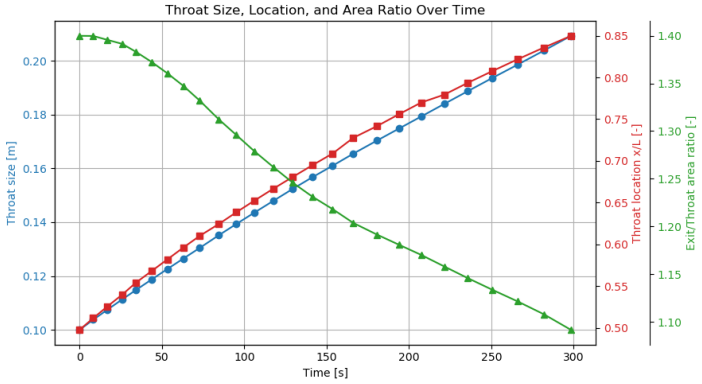

Figure 7.18: Channel throat evolution as time progresses as time progresses due to wall sublimation for the baseline channel with an adiabatic wall

7.2.2. Case 4: Baseline Channel With Isothermal $T_w = 273\ K$

The temporal evolution of the baseline channel due to wall sublimation for an isothermal wall at 273 K is shown in Figure 7.19. Figure 7.19 shows the wall opens up uniformly throughout the channel. This is in contrast to cases 1, 2 and 3 since wall sublimation is only dependent on the wall temperature which is fixed for the isothermal case. The result is a much simpler geometry progression where the throat size increases and stays at the same location of 0.5 x/L.

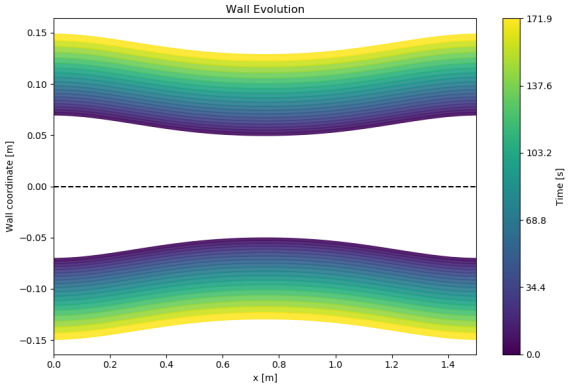

Figure 7.19: Wall evolution as time progresses due to wall sublimation for the baseline channel with an isothermal wall $T_w = 273\ K$

Figure 7.20 shows several thermodynamic variables at the wall and the wall mass fluxes per unit area. Analysing the temporal evolution, the imposed constant temperature enforces steady sublimation, while density and pressure at the wall decrease as the channel expands due to the higher A_e/A^*.

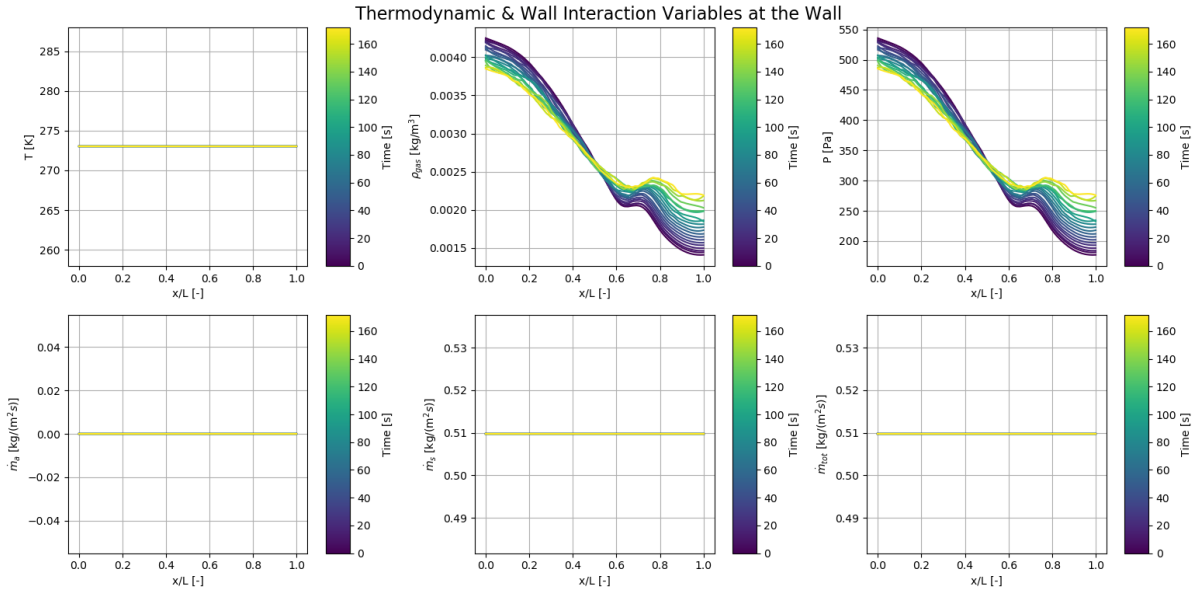

Figure 7.20: Thermodynamic and wall related variables at the wall as time progresses due to wall sublimation for the baseline channel with an isothermal wall $T_w = 273\ K$.

Figure 7.21 and Figure 7.22 shows the centreline evolution of key flow and nucleation variables respectively across several simulation times.

Analysing the temporal evolution, Figure 7.21 shows smoother gradients of pressure, temperature, and density compared to Case 3. Supersaturation is reduced, which limits nucleation activity and results in relatively low grain numbers and mass fraction. In this case, even though nucleation and grain number decrease with time, grain growth and grain number increase with time. This is because the lower A_e/A^* reduces the supersaturation since the expansion is less extreme. Since the channel changes uniformly, the thermodynamic variables such as pressure, temperature, density, velocity and Mach number are not shifted with time like in cases 1-3 but are instead rotated about the throat. Since the velocity is lower downstream of the throat, the flow spends a longer time in the expansion allowing for the grains to grow more.

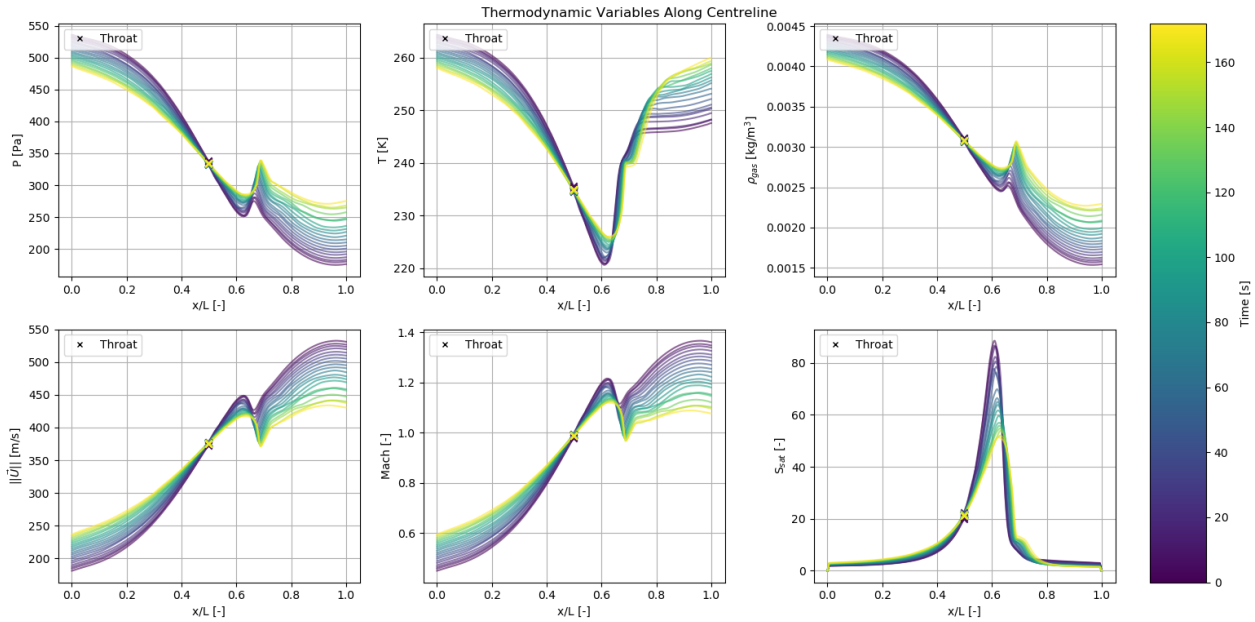

Figure 7.21: Simulation parameters along the channel centreline as time progresses due to wall sublimation for the baseline channel with an isothermal wall $T_w = 273\ K$. From left to right: pressure, temperature, density, velocity, Mach number, supersaturation, nucleation rate, grain number and mass fraction

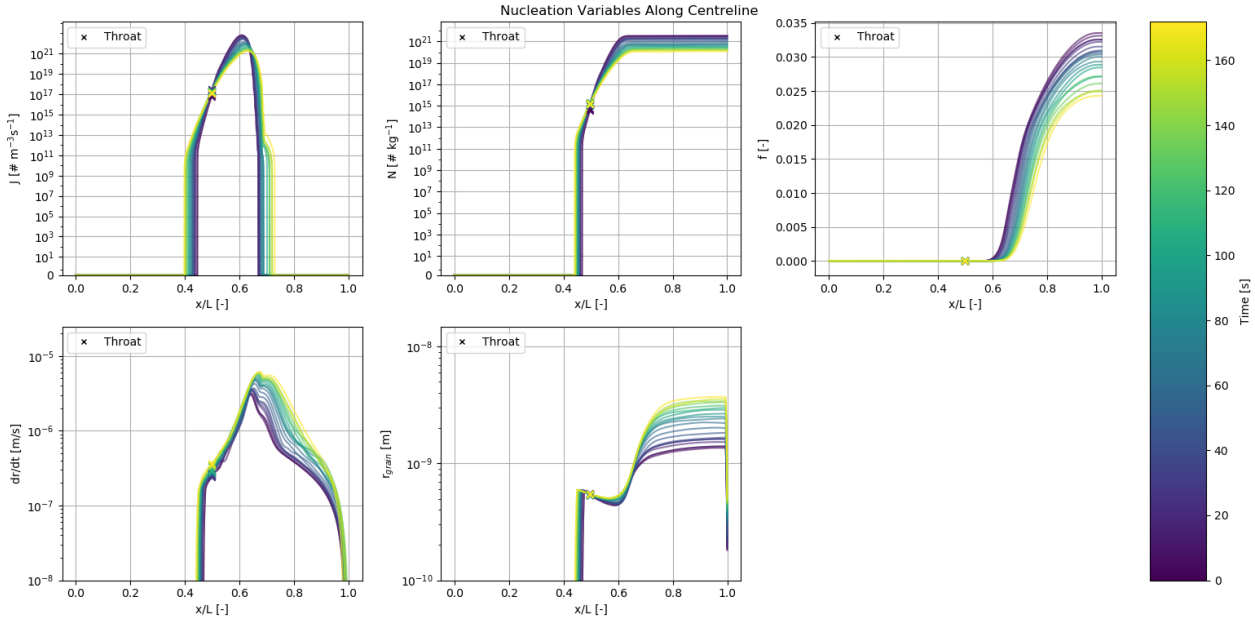

Figure 7.22: Simulation parameters along the channel centreline as time progresses due to wall sublimation for the baseline channel with an isothermal wall $T_w = 273\ K$. From left to right: pressure, temperature, density, velocity, Mach number, supersaturation, nucleation rate, grain number and mass fraction

Figure 7.23 shows the pressure versus temperature along the centreline. The p-T path shifts upward and to the right with time due to the decrease of A_e/A^*. This results in fluid parcel experiencing less cooling in the channel and does not cross as deep into the metastable supersaturated region. At the inlet, the temperature and pressure tend to decrease with time contrary to case 3. This is because in the isothermal case, the thermodynamic variables are not shifted upwards but rotated about the throat.

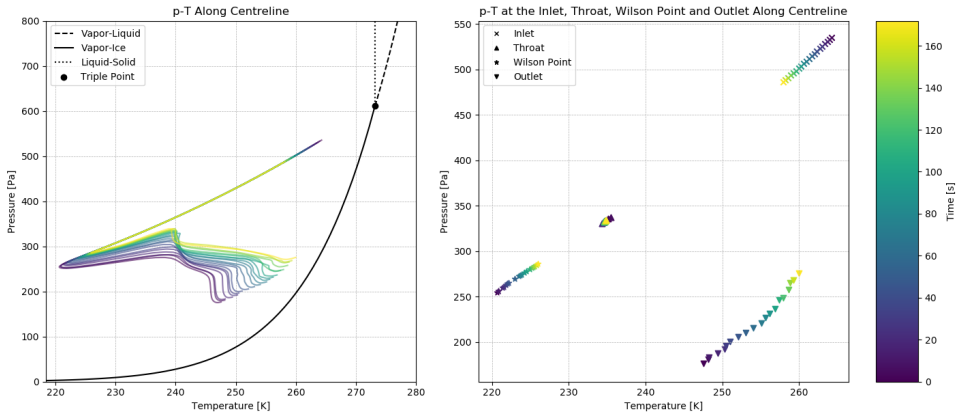

Figure 7.23: Evolution of pressure-temperature along the centreline as time progresses due to wall sublimation for the baseline channel with an isothermal wall $T_w = 273\ K$.

Figure 7.24 shows how the throat evolves in time. As expected, the throat size shows a clear linear trend with the throat location being constant. The A_e/A^* ratio shows an decaying trend. Therefore, the baseline channel with only wall sublimation for an isothermal wall of 273 K will keep widening with the consequence of nucleation and hence mass fraction diminishing.

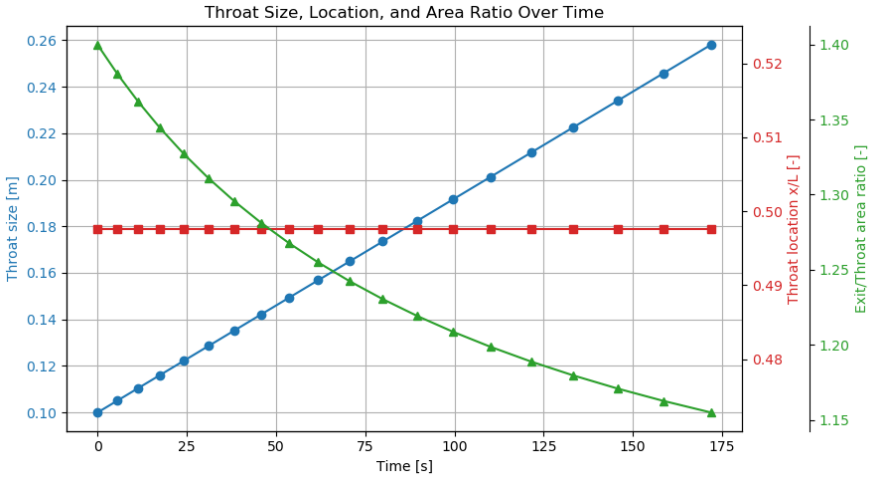

Figure 7.24: Channel throat evolution as time progresses as time progresses due to wall sublimation for the baseline channel with an isothermal wall $T_w = 273\ K$.

7.3. Cases 5-8: Channels with Wall Accretion & Wall Sublimation

The last cases deal with channels with that experience deposition in the bulk flow, wall accretion and wall sublimation. Case 5 considers the baseline channel with an adiabatic wall. Case 6 considers the baseline channel with an isothermal wall. Case 7 considers the baseline channel with a linear wall temperature from 273 K to 200 K. Lastly, case 8 considers the multi-throat channel with a linear wall temperature from 273 K to 200 K.

7.3.1. Case 5: Baseline Channel With Adiabatic Wall

The temporal evolution of the baseline channel due to wall accretion and wall sublimation for an adiabatic wall is shown in Figure 7.25. In this case, the wall geometry has drastically changed compared to the previous cases. Wall accretion is dominant towards the inlet and beginning of the channel with wall sublimation being dominant towards the vent. However, as time evolves, wall sublimation becomes increasingly more dominant towards the end of the channel and at some point skyrockets. This phenomenon is further explored below in Figure 7.26 and Figure 7.27.

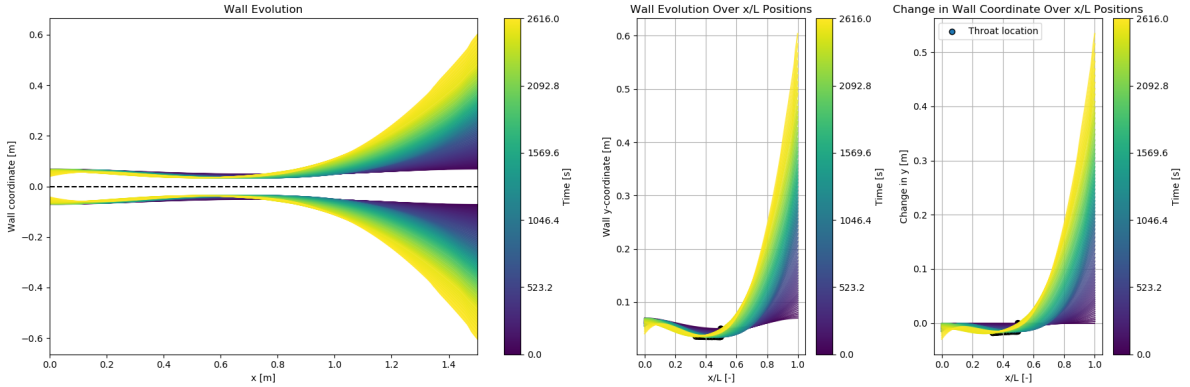

(a) Wall evolution as time progresses due to wall accretion & sublimation for the baseline channel with an adiabatic wall

(b) Wall geometry evolution as time progresses due to wall accretion & sublimation for the baseline channel with an adiabatic wall

Figure 7.25: Wall evolution as time progresses due to wall accretion & sublimation for the baseline channel with an adiabatic wall

Figure 7.26 shows several thermodynamic variables such as temperature and the wall mass fluxes per unit area. Analysing the temporal evolution, the wall temperature follows a similar pattern to the wall temperature in case 2 with the exception of the temperature rapidly increasing towards the end of the channel. This increase in temperature drastically increases the wall sublimation mass flux per unit area resulting in the observed geometry.

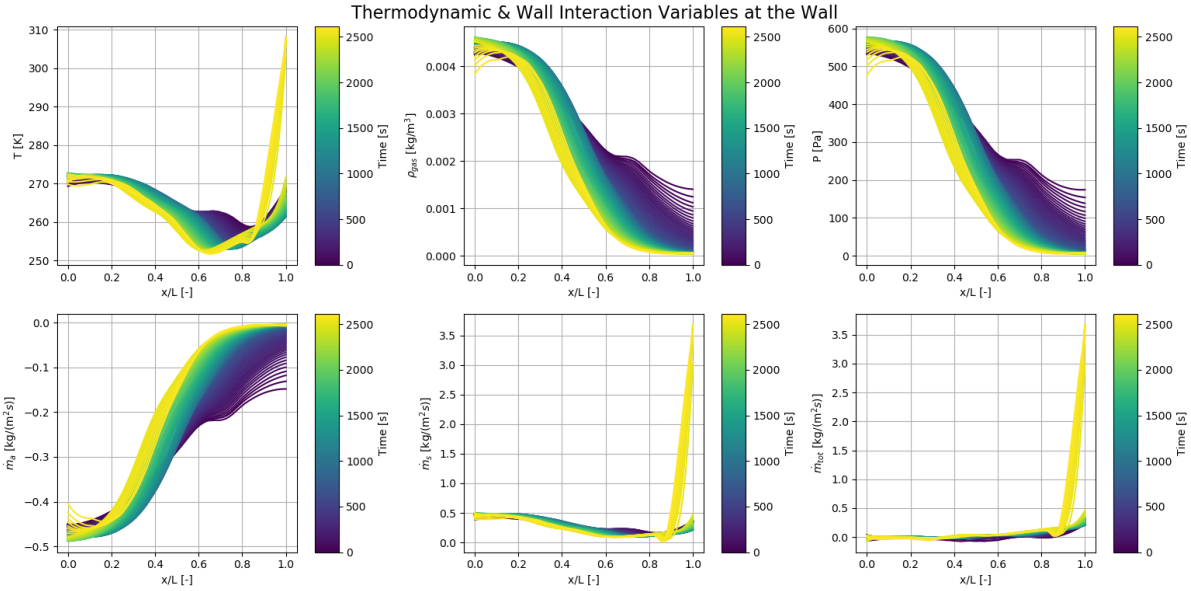

Figure 7.26: Thermodynamic and wall related variables at the wall as time progresses due to wall accretion & sublimation for the baseline channel with an adiabatic wall

The reason behind this drastic increase in temperature towards the end of the channel can be explained by looking at Figure 7.27. Figure 7.27 shows a 2D contour of the velocity for the latest epoch. At around a local x/L of 0.8, the flow completely separates from the channel as it cannot follow the curved wall. This introduces strong velocity and thermal gradients leading to the sudden increase in wall temperature.

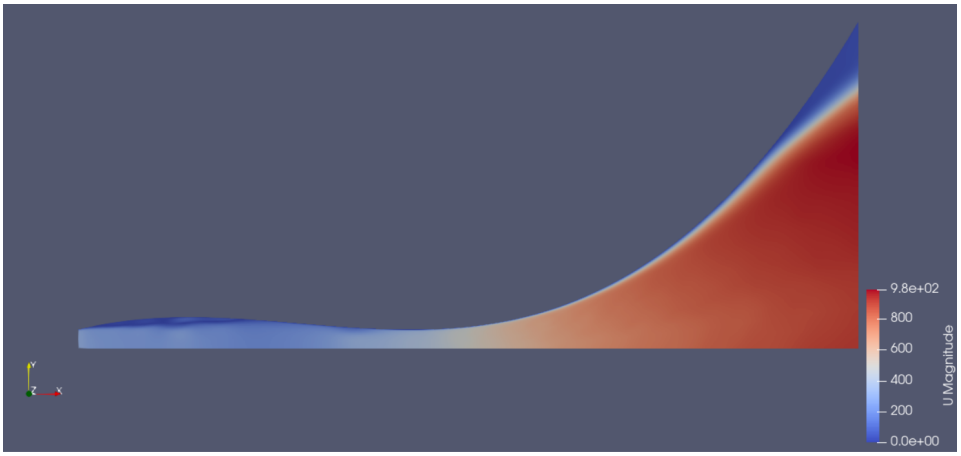

Figure 7.27: A 2D contour plot of the magnitude of the velocity vector along the baseline channel with wall accretion & wall sublimation for an adiabatic wall at the latest epoch

Figure 7.28 and Figure 7.29 shows the centreline evolution of key flow and nucleation variables respectively across several simulation times.

Analysing the temporal evolution compared to Case 4, the gradients are higher with the parameters shifted slightly upstream. The overall trend reflects gentle opening with some small constrictions throughout the channel. Supersaturation exhibits mild peaks tied to compressible-flow adjustments due to the wall accretion in the channel. However, as the simulation progresses the vent begins to drastically open which increases A_e/A^* and locally increases supersaturation. At some epoch, the supersaturation is high enough that nucleation can be sustained for longer. As a result, nucleation and grain growth is enhanced and is shifted upstream resulting in a higher mass fraction. The grain growth and grain size reduces and is shifted upstream since the vapour spends less time in the expansion region.

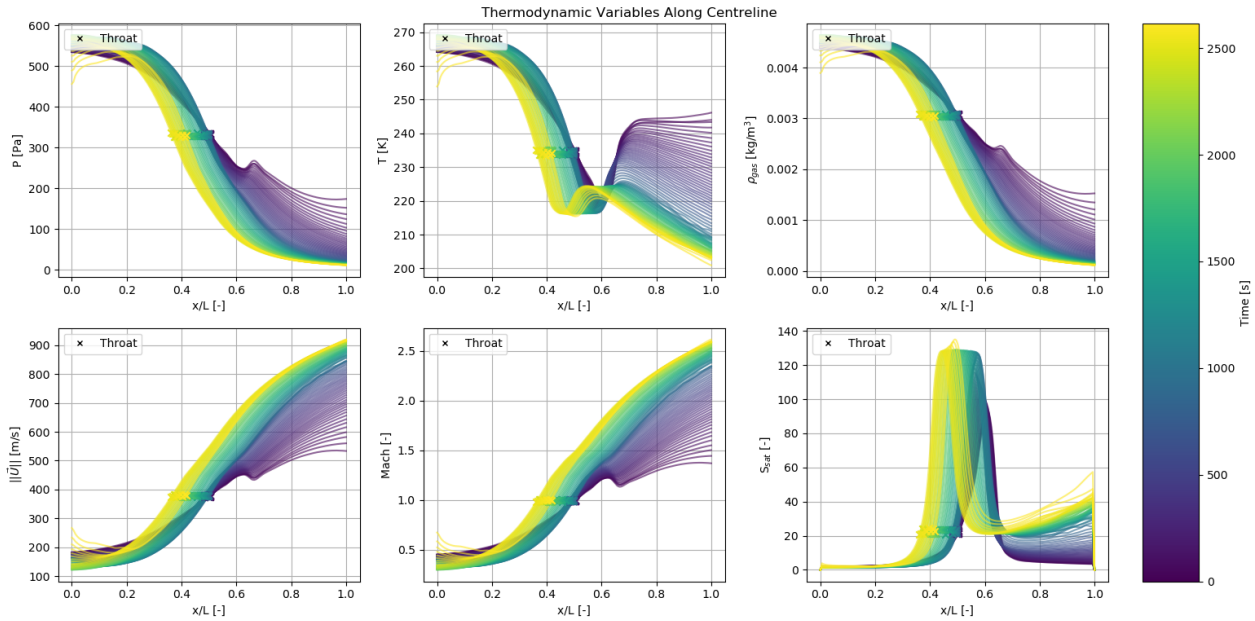

Figure 7.28: Simulation parameters along the channel centreline as time progresses due to wall accretion & sublimation for the baseline channel with an adiabatic wall. From left to right: pressure, temperature, density, velocity, Mach number, supersaturation, nucleation rate, grain number and mass fraction

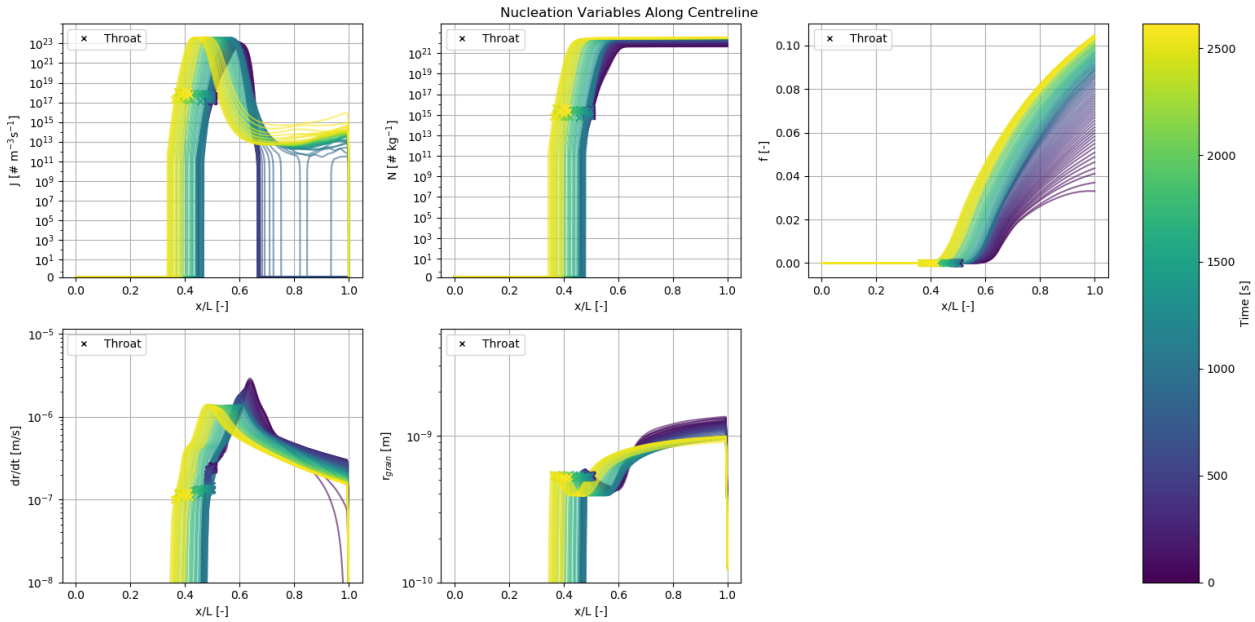

Figure 7.29: Simulation parameters along the channel centreline as time progresses due to wall accretion & sublimation for the baseline channel with an adiabatic wall. From left to right: pressure, temperature, density, velocity, Mach number, supersaturation, nucleation rate, grain number and mass fraction

Figure 7.30 shows the pressure versus temperature along the centreline. The p-T curve shows overall downward progression similar to cases 1 and 2, but with local deviations. The increase in A_e/A^* results in a stronger expansion allowing the fluid parcel to go deeper into the metastable supersaturated region. Furthermore, since the grain growth reduces with time, the temperature recovery due to grain growth is much weaker allowing the fluid parcel to follow a more isentropic trend after nucleation stops.

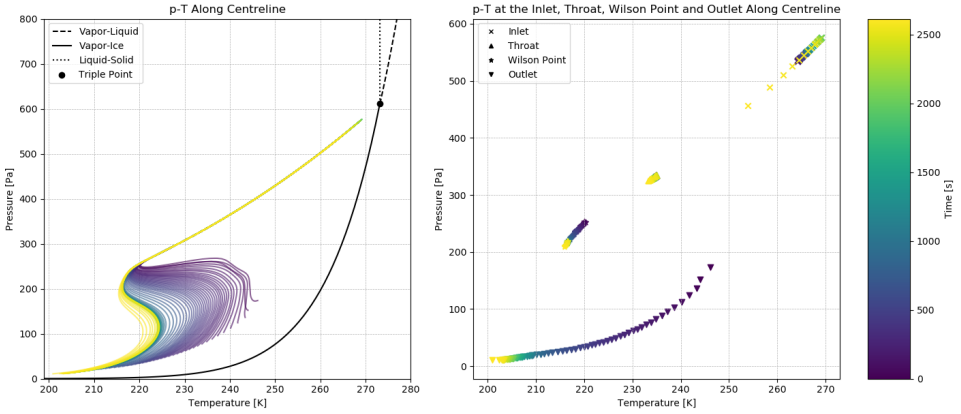

Figure 7.30: Evolution of pressure-temperature along the centreline as time progresses due to wall accretion & sublimation for the baseline channel with an adiabatic wall

Figure 7.31 shows how the throat evolves in time. Since wall accretion is dominated in parts of the channel, the throat size decreases and has a tendency to shift downstream. However, at some later epoch around 850 seconds, the throat shifts upstream for a bit before shifting downstream again. This is because the wall fluxes change due to the influence of the wall geometry has on the thermodynamic variables at the wall. For a certain wall geometry, wall accretion will have a lower value compared to wall sublimation resulting in the throat shifting upstream. Whereas, at other epochs the wall geometry will dictate a higher wall accretion resulting in the throat shifting downstream. Lastly, as the vent continually opens due to wall sublimation it increases the A_e/A^*.

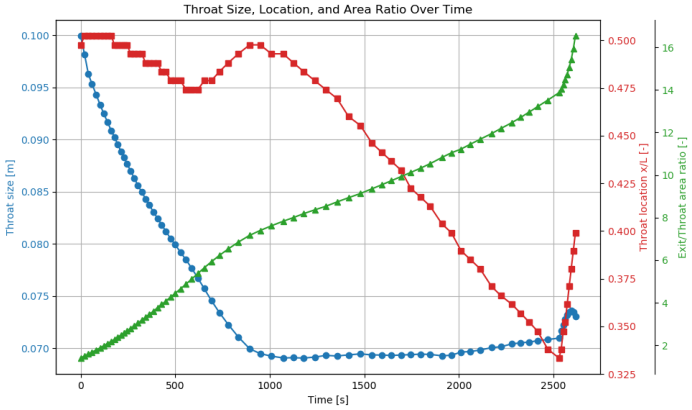

Figure 7.31: Channel throat evolution as time progresses as time progresses due to wall accretion & sublimation for the baseline channel with an adiabatic wall

7.3.2. Case 6: Baseline Channel With Isothermal $T_w = 273\ K$

The temporal evolution of the baseline channel due to wall accretion and wall sublimation for an isothermal wall at 273 K is shown in Figure 7.32. Since the wall temperature is set to 273 K, sublimation dominates everywhere, producing uniform wall recession and net widening across the channel. In Figure 7.32b, the throat moves upstream until it reaches the inlet and the simulation terminates.

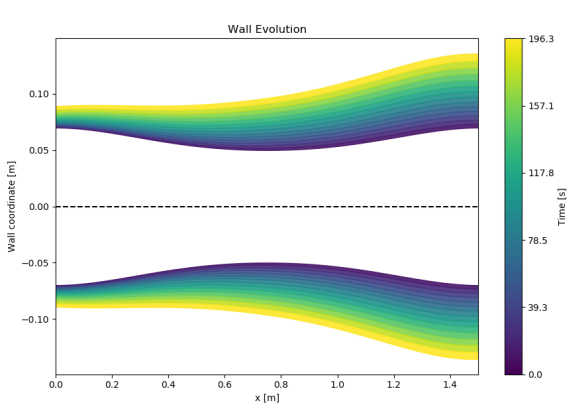

(a) Wall evolution as time progresses due to wall accretion & sublimation for the baseline channel with an isothermal wall $T_w = 273\ K$

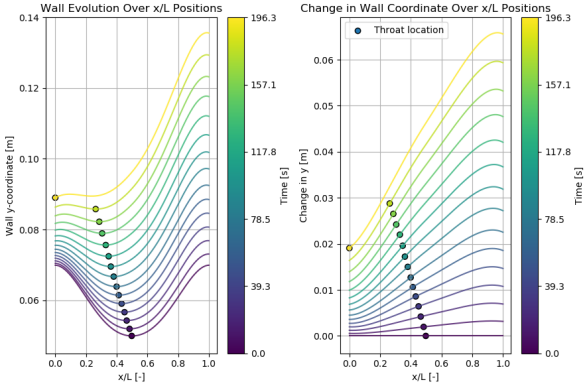

(b) Wall geometry evolution as time progresses due to wall accretion & sublimation for the baseline channel with an isothermal wall $T_w = 273\ K$

Figure 7.32: Wall evolution as time progresses due to wall accretion & sublimation for the baseline channel with an isothermal wall $T_w = 273\ K$

Figure 7.33 shows several thermodynamic variables such as temperature and the wall mass fluxes per unit area. The isothermal wall maintains a steady thermal driving for sublimation. Analysing the temporal evolution, the density and pressure are shifted downwards as the channels widens in contrast to case 3. This is because the A_e/A^* ratio increases with time whereas in case 3 it decreases with time. Since the density decreases with time, so does the accretion mass flux per unit area. The consequence is that the total mass flux per unit area becomes larger over time and explains why the wall sublimates more towards the vent.

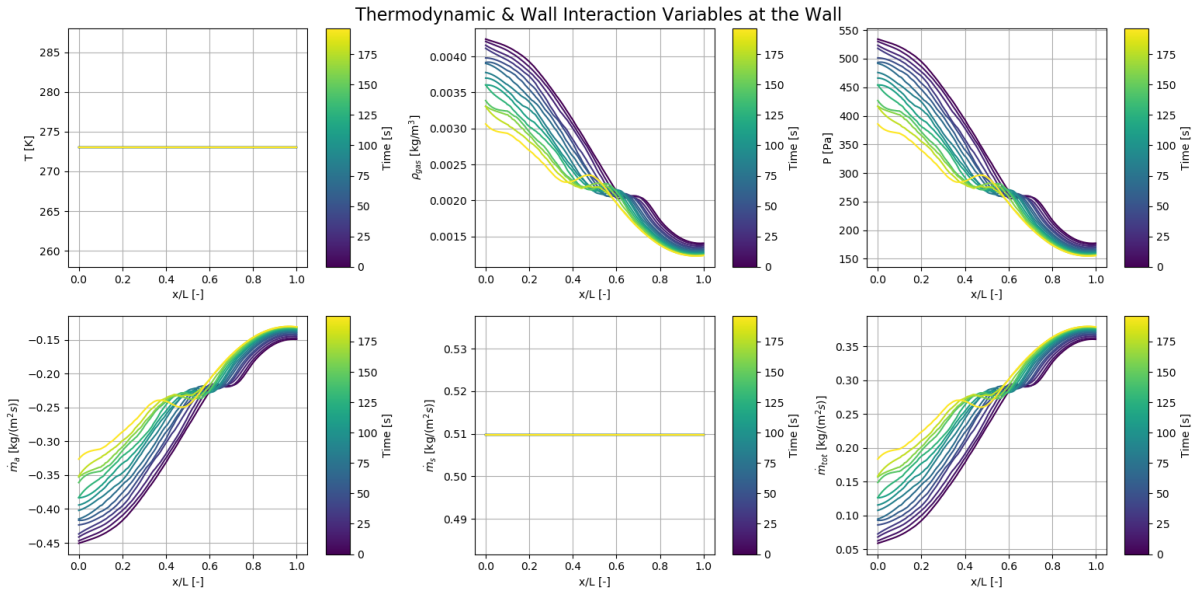

Figure 7.33: Thermodynamic and wall related variables at the wall as time progresses due to wall accretion & sublimation for the baseline channel with an isothermal wall $T_w = 273\ K$.

Figure 7.34 and Figure 7.35 shows the centreline evolution of key flow and nucleation variables respectively across several simulation times. Analysing the temporal evolution, whilst the A_e/A^* ratio increase results in a decrease in the density over time, the nucleation rate is actually reduced. This is because even though overall the density as decreased with time, its slope has also decreased meaning that its expansion is more gradual. This means a lower supersaturation leading to the lower nucleation rate and grain number. This also means that the Mach number growth is also more gradual along the channel resulting in a longer residence time for the icy grains to grow.

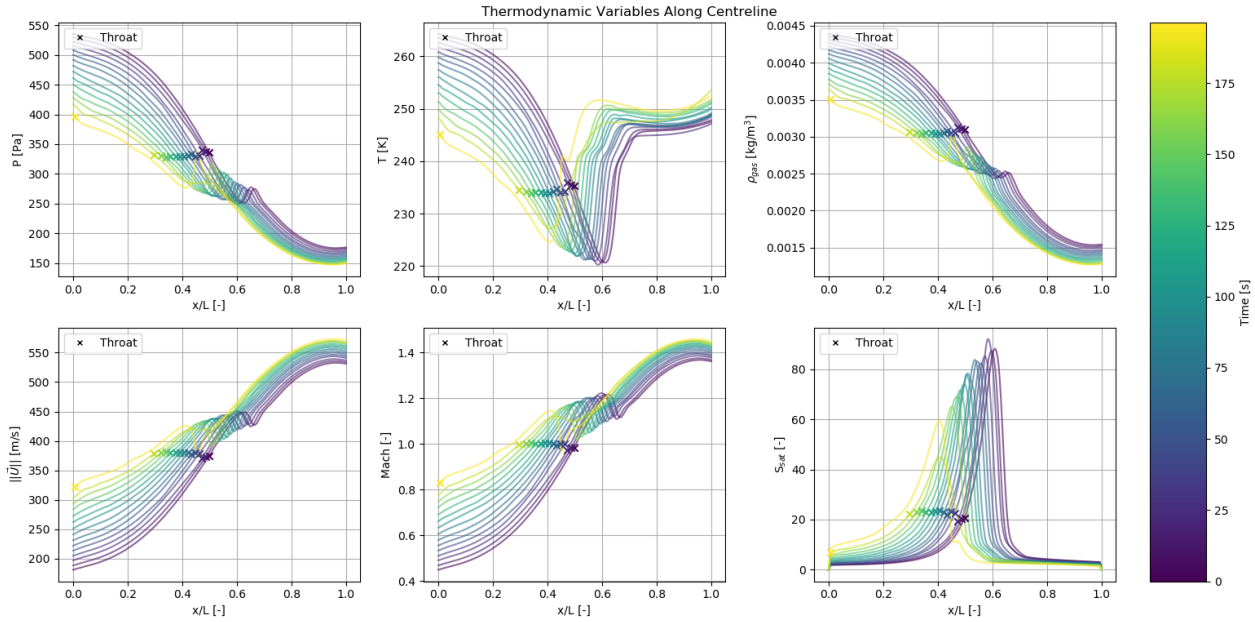

Figure 7.34: Simulation parameters along the channel centreline as time progresses due to wall accretion & sublimation for the baseline channel with an isothermal wall $T_w = 273\ K$. From left to right: pressure, temperature, density, velocity, Mach number, supersaturation, nucleation rate, grain number and mass fraction

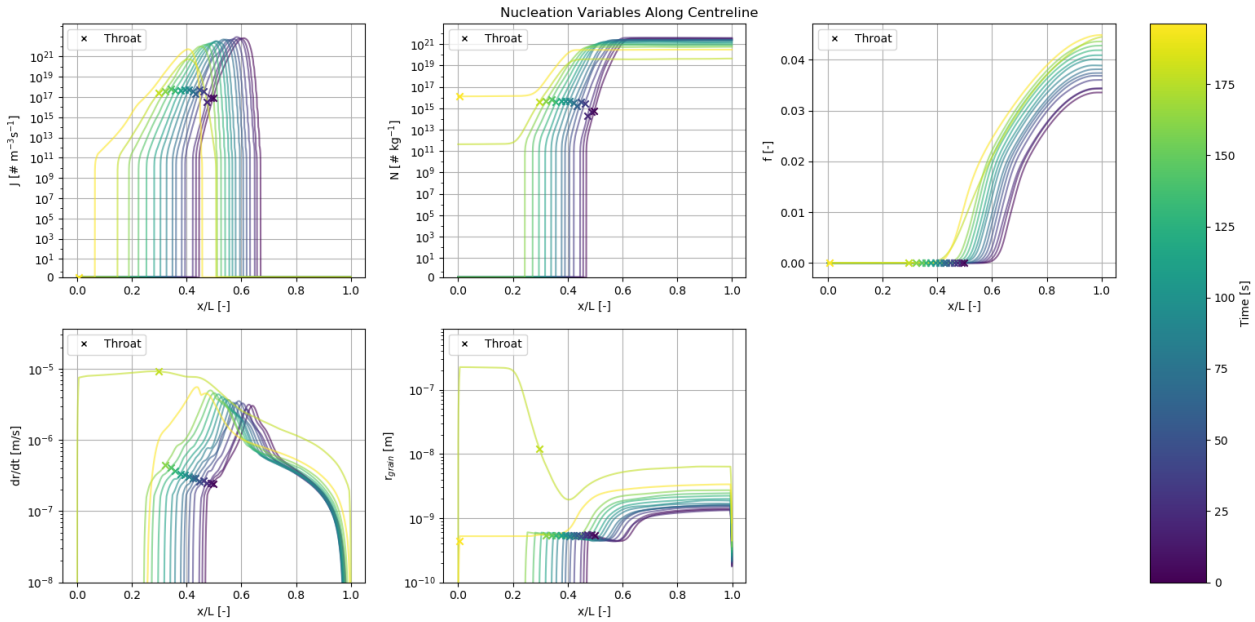

Figure 7.35: Simulation parameters along the channel centreline as time progresses due to wall accretion & sublimation for the baseline channel with an isothermal wall $T_w = 273\ K$. From left to right: pressure, temperature, density, velocity, Mach number, supersaturation, nucleation rate, grain number and mass fraction

Figure 7.36 shows the p-T curves along the centreline. The fluid parcel experiences more gradual cooling and so it does not cross as deep into the metastable supersaturated region as time progresses. Since the expansion still increases, the temperature and pressure at the inlet decrease but at the Wilson point it increases. Since grain growth is higher with increasing time, the temperature recovery due to grain growth is more pronounced and leads to a higher temperature at the outlet.

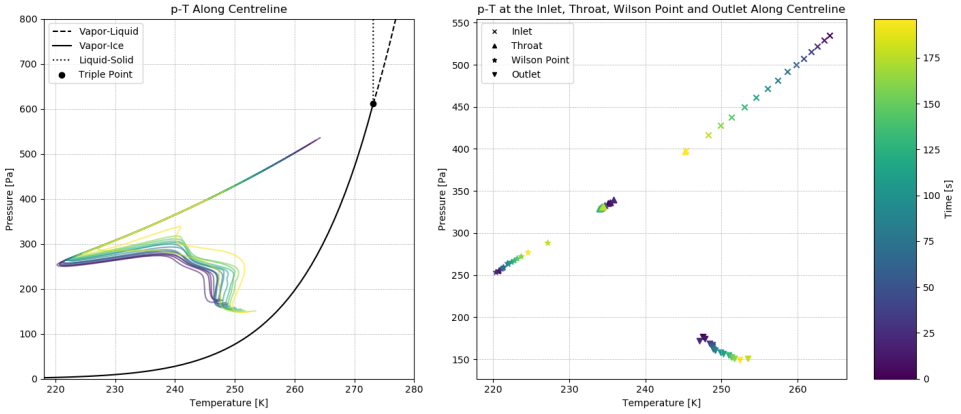

Figure 7.36: Evolution of pressure-temperature along the centreline as time progresses due to wall accretion & sublimation for the baseline channel with an isothermal wall $T_w = 273\ K$.

Figure 7.37 shows how the throat evolves in time. It clearly shows that the throat size increases as the throat moves upstream until it reaches the inlet. Furthermore, the A_e/A^* ratio increases with a linear trend similar to the throat size. Therefore, for the baseline channel with wall accretion and wall sublimation for an isothermal wall at 273 K, the wall will continuously open with the throat shifting towards the inlet.

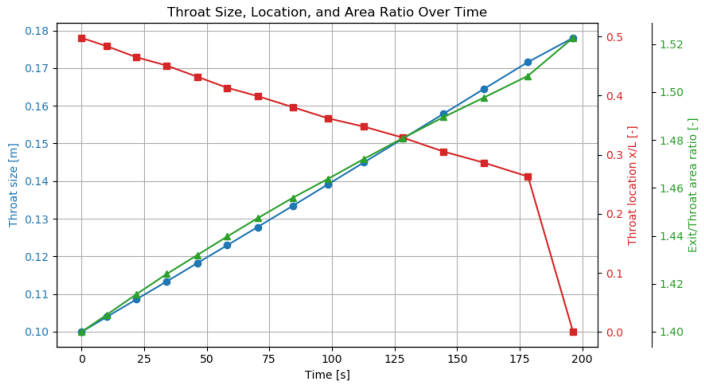

Figure 7.37: Channel throat evolution as time progresses due to wall accretion & sublimation for the baseline channel with an isothermal wall $T_w = 273\ K$

7.3.3. Case 7: Baseline Channel With Linear Wall Temperature: $T_w = 273$-$200\ K$

The temporal evolution of the baseline channel due to wall accretion and wall sublimation for a linear wall temperature from 273 K to 200 K is shown in Figure 7.38. Deposition strengthens downstream as the wall cools, and accretion becomes significant toward the throat, leading to progressive narrowing in that region. As a consequence, the throat moves upstream as seen in Figure 7.38b.

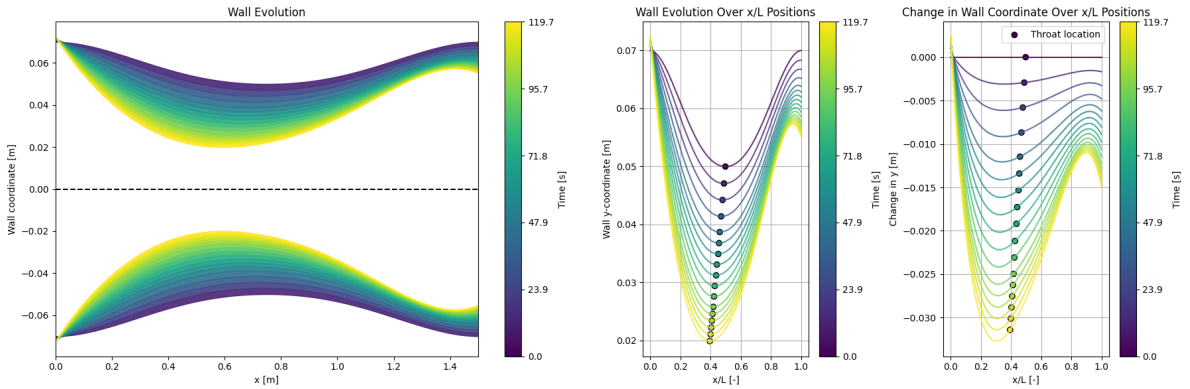

(a) Wall evolution as time progresses due to wall accretion & sublimation for the baseline channel with a linear wall temperature from 273 K at the inlet to 200 K at the vent

(b) Wall geometry evolution as time progresses due to wall accretion & sublimation for the baseline channel with a linear wall temperature from 273 K at the inlet to 200 K at the vent

Figure 7.38: Wall evolution as time progresses due to wall accretion & sublimation for the baseline channel with a linear wall temperature from 273 K at the inlet to 200 K at the vent

Figure 7.39 shows several thermodynamic variables such as temperature and the wall mass fluxes per unit area. Analysing the temporal evolution, sublimation persists near the warmer inlet, but the wall mass flux turns toward accretion. This is because as the wall temperature decreases downstream, it produces a net negative wall mass flux in the cold segment. Along the channel, the sublimation mass flux per unit area reduces with an exponential decay whereas the accretion mass flux per unit area reduces with the decrease of the density along the channel. This results in a location along the channel, in this case around 0.25-0.3 x/L where the total mass flux per unit area is maximised. As time progresses the flow parameters rotate clockwise from the location where the total mass flux per unit area is maximised. This is because even though the A_e/A^* increases, the inlet widens which for subsonic flow reduces the temperature, pressure and density.

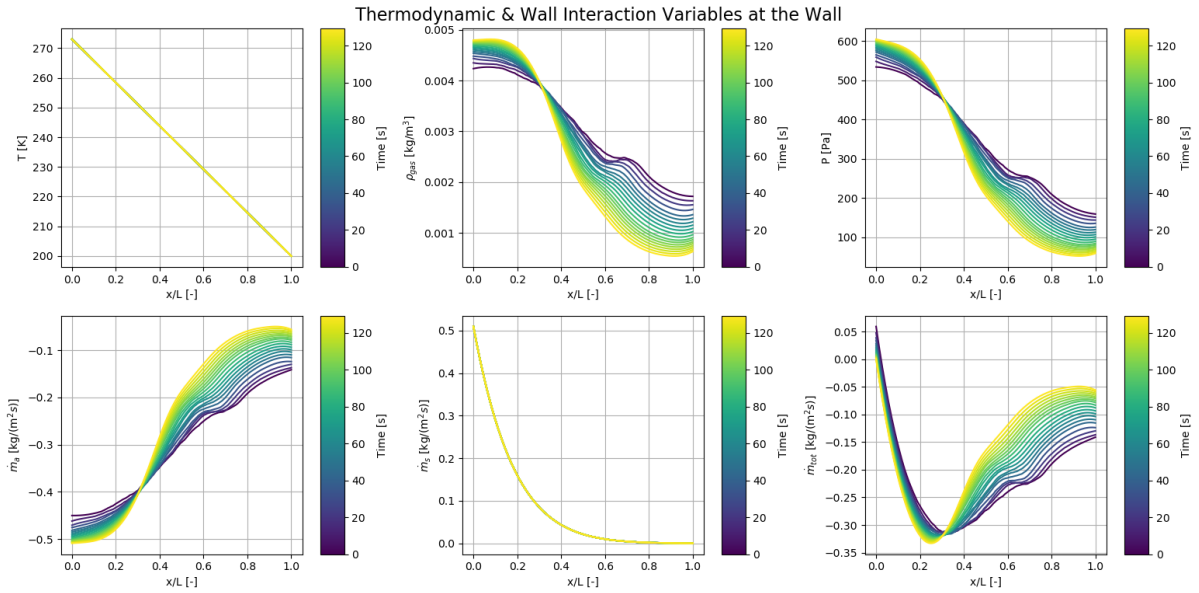

Figure 7.39: Thermodynamic and wall related variables at the wall as time progresses due to wall accretion & sublimation for the baseline channel with a linear wall temperature from 273 K at the inlet to 200 K at the vent

Figure 7.40 and Figure 7.41 shows the centreline evolution of key flow and nucleation variables respectively across several simulation times.

Analysing the temporal evolution, since the A_e/A^* increases, this results in a decrease in pressure, density and an increase in Mach number once accretion dominates in the channel. Furthermore, since the thermodynamic variables rotate clockwise, their gradients become steeper, which increases the supersaturation. This leads to an enhanced and broader nucleation region and hence a higher grain number and mass fraction. The grain growth and size decreases with time since the vapour has less residence time in the expansion region.

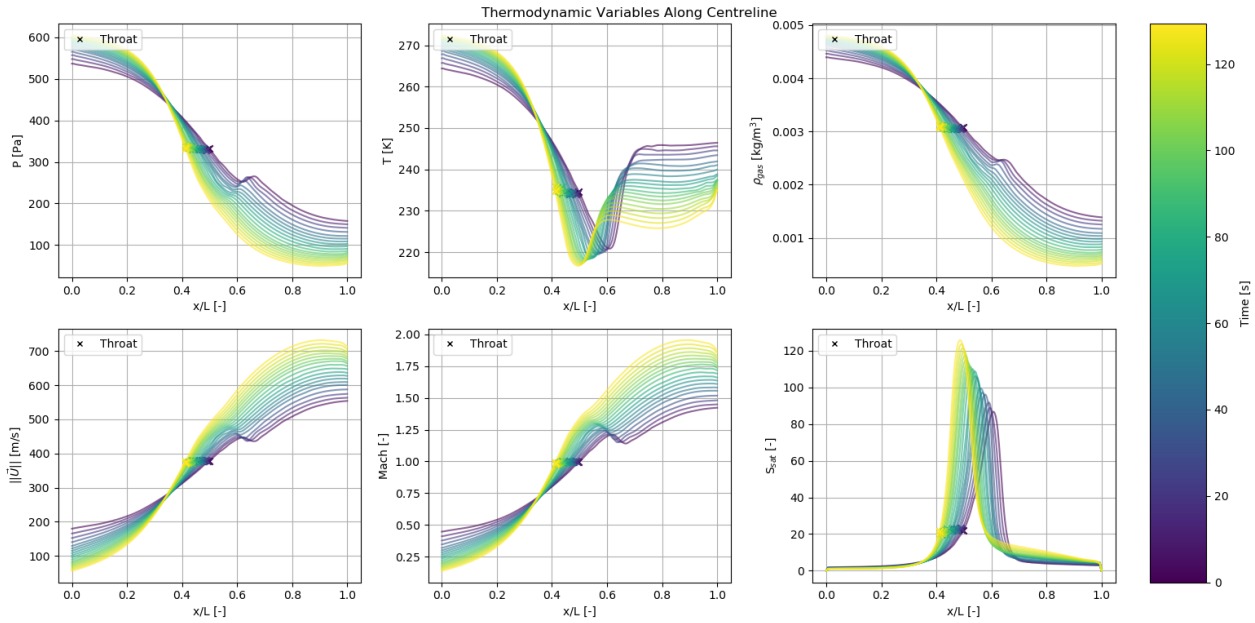

Figure 7.40: Simulation parameters along the channel centreline as time progresses due to wall accretion & sublimation for the baseline channel with a linear wall temperature from 273 K at the inlet to 200 K at the vent. From left to right: pressure, temperature, density, velocity, Mach number, supersaturation, nucleation rate, grain number and mass fraction

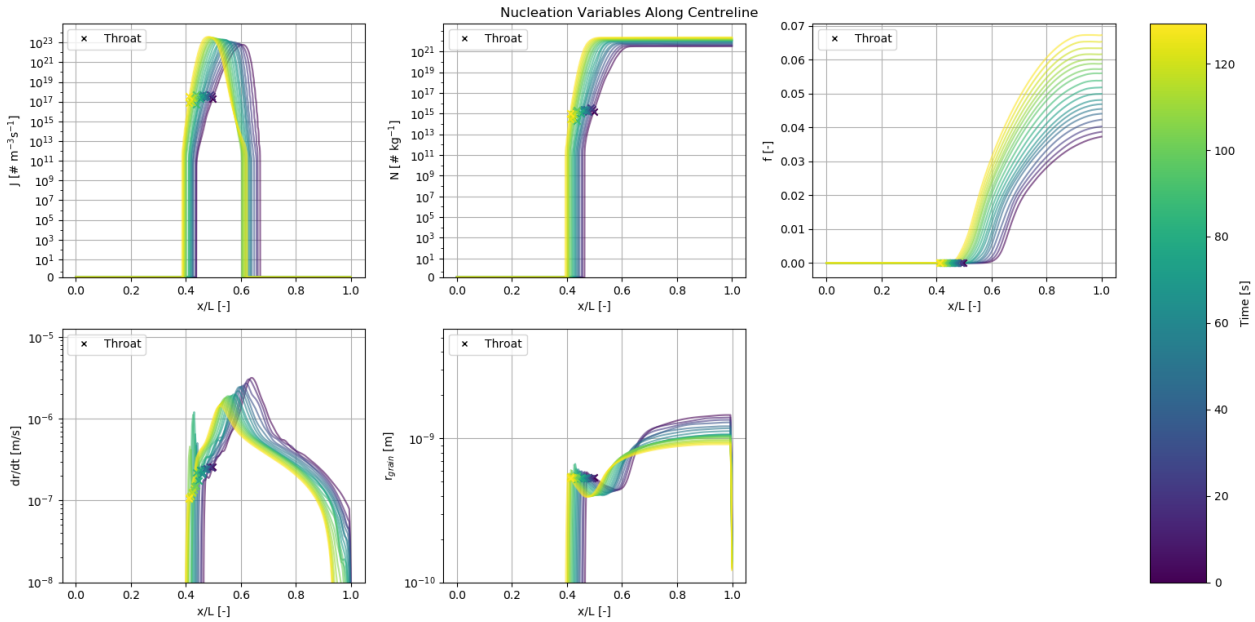

Figure 7.41: Simulation parameters along the channel centreline as time progresses due to wall accretion & sublimation for the baseline channel with a linear wall temperature from 273 K at the inlet to 200 K at the vent. From left to right: pressure, temperature, density, velocity, Mach number, supersaturation, nucleation rate, grain number and mass fraction

Figure 7.42 shows the p-T curves along the centreline. Due to the higher supersaturation, the vapour spends more time in the supersaturated state shown by the Wilson point. Due to sublimation at the start of the channel, the pressure and temperature at the inlet increase until it reaches triple point conditions. At this point wall accretion and wall sublimation begin to equilibrate.

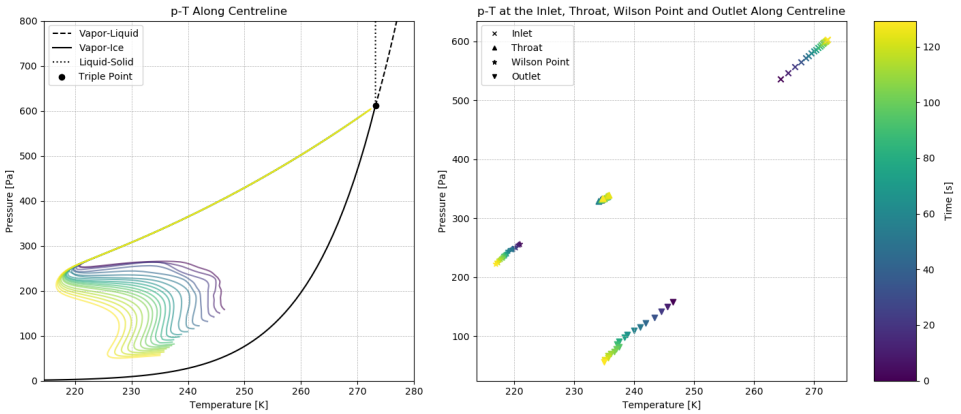

Figure 7.42: Evolution of pressure-temperature along the centreline as time progresses due to wall accretion & sublimation for the baseline channel with a linear wall temperature from 273 K at the inlet to 200 K at the vent

Figure 7.43 shows how the throat evolves in time. The throat behaves similarly to the wall accretion cases 1 and 2 where the throat size and location decreases linearly and the A_e/A^* ratio shows an accelerating growth. Therefore, for the baseline channel with wall accretion & sublimation for a linear wall temperature from 273 K to 200 K, the channel transitions to an accretion-dominated downstream segment due to the imposed wall-temperature gradient, yielding progressive narrowing toward the vent.

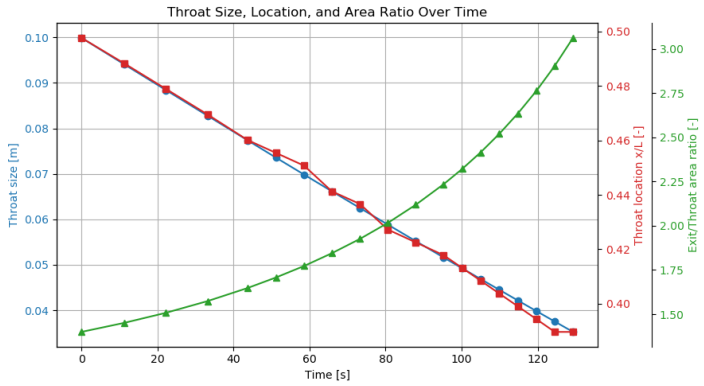

Figure 7.43: Channel throat evolution as time progresses due to wall accretion & sublimation for the baseline channel with a linear wall temperature from 273 K at the inlet to 200 K at the vent

7.3.4. Case 8: Multi-Throat Channel With Linear Wall Temperature: $T_w = 273\text{-}200\ K$

The temporal evolution of the multi-throat channel due to wall accretion and wall sublimation for a linear wall temperature from 273 K to 200 K is shown in Figure 7.44. Similarly, to case 7 the channel is dominated by sublimation at the inlet and then by accretion throughout the rest of the channel. Figure 7.44b shows that comparably to case 7, the throat shifts upstream with the greatest change in the wall geometry occurs at 0.45 x/L.

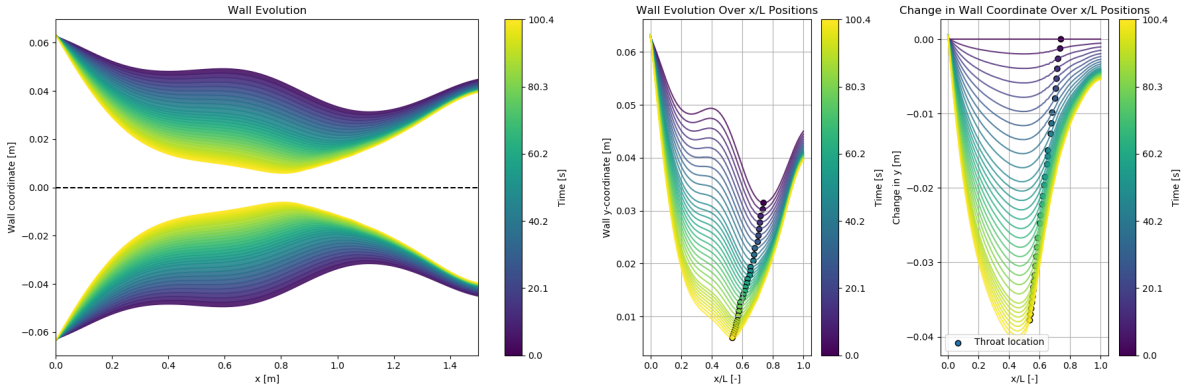

(a) Wall evolution as time progresses due to wall accretion & sublimation for the multi-throat channel with a linear wall temperature from 273 K at the inlet to 200 K at the vent

(b) Wall geometry evolution as time progresses due to wall accretion & sublimation for the multi-throat channel with a linear wall temperature from 273 K at the inlet to 200 K at the vent

Figure 7.44: Wall evolution as time progresses due to wall accretion & sublimation for the multi-throat channel with a linear wall temperature from 273 K at the inlet to 200 K at the vent

Figure 7.45 shows several thermodynamic variables such as temperature and the wall mass fluxes per unit area. Analysing the temporal evolution, similar to case 7, Figure 7.45 indicates that the flow parameters rotate clockwise with respect to the location where the total mass flux per unit area is maximised. In this case, it occurs around 0.42-0.5 x/L.

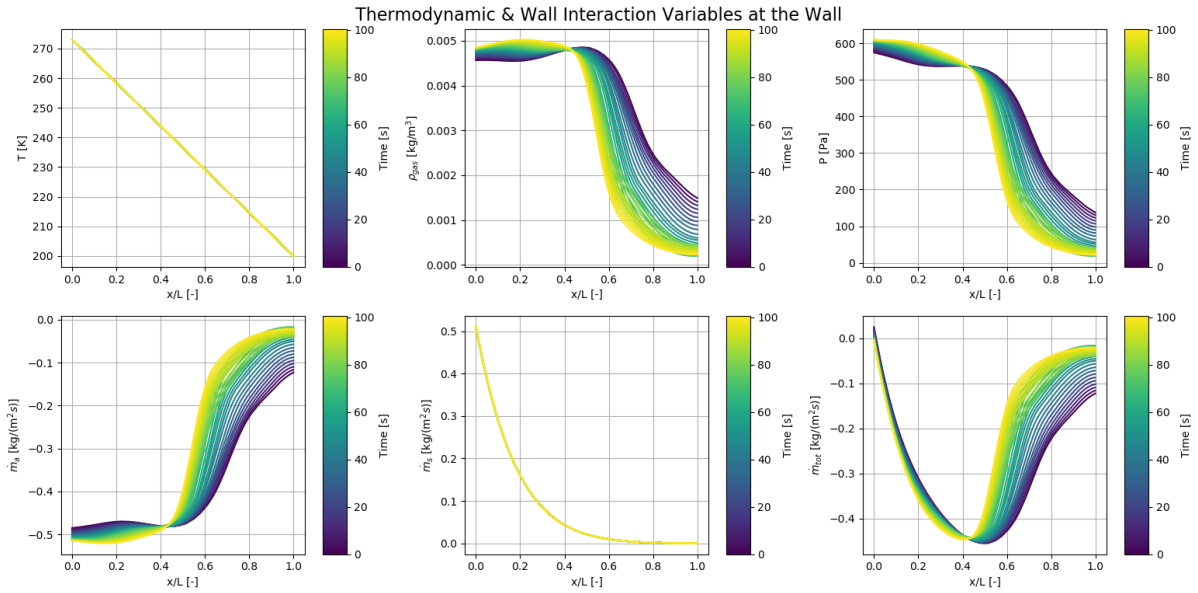

Figure 7.45: Thermodynamic and wall related variables at the wall as time progresses due to wall accretion & sublimation for the multi-throat channel with a linear wall temperature from 273 K at the inlet to 200 K at the vent

Figure 7.46 shows the centreline evolution of key flow and nucleation variables across several simulation times.

Analysing the temporal evolution, similar to case 7, the downstream contraction intensifies compressible-flow effects, leading to steeper gradients in pressure, temperature, density, and Mach number. Within this narrowed region, supersaturation rises, which promotes enhanced nucleation and grain growth.

In contrast to case 7, since the throat is located more downstream, the compression-expansion is weaker resulting in a lower nucleation rate. Furthermore, nucleation also occurs much closer to the outlet. As the throat moves upstream due to the dominant wall accretion, the compression-expansion becomes stronger resulting in a lower pressure and density. At some epoch, this compression-expansion becomes so strong that nucleation is not strong enough to drive the flow fully back to equilibrium. The result is that nucleation extends for longer before it ceases. This is accompanied by an increase in the grain growth and consequently the grain size.

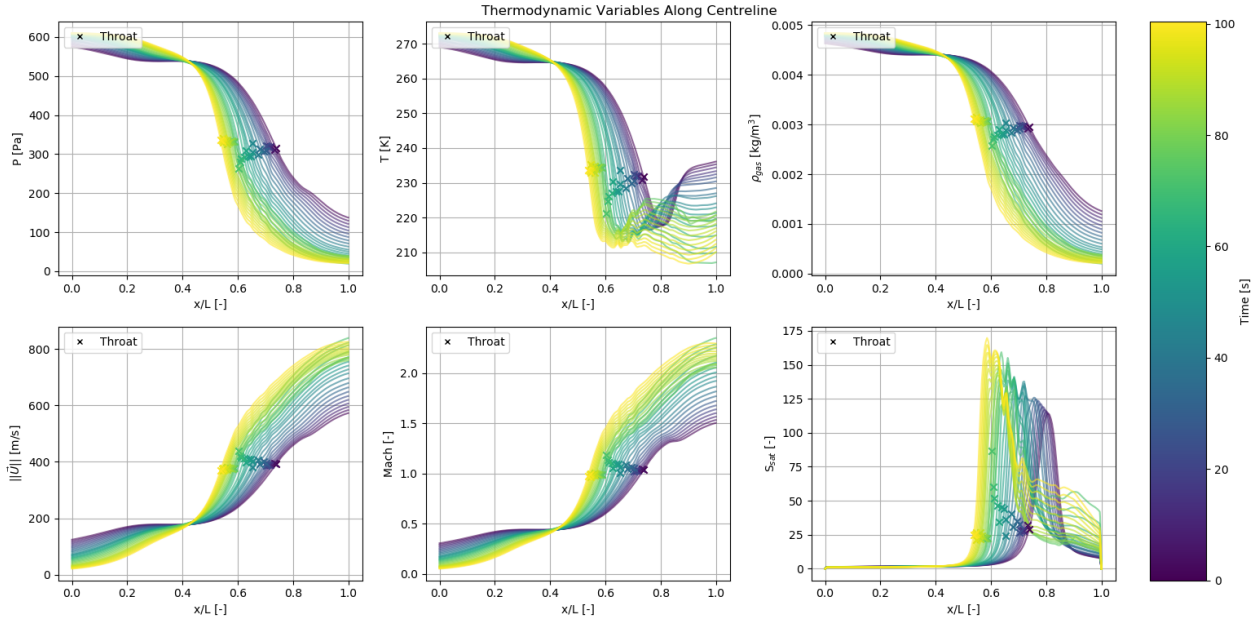

Figure 7.46: Simulation parameters along the channel centreline as time progresses due to wall accretion & sublimation for the multi-throat channel with a linear wall temperature from 273 K at the inlet to 200 K at the vent. From left to right: pressure, temperature, density, velocity, Mach number, supersaturation, nucleation rate, grain number and mass fraction

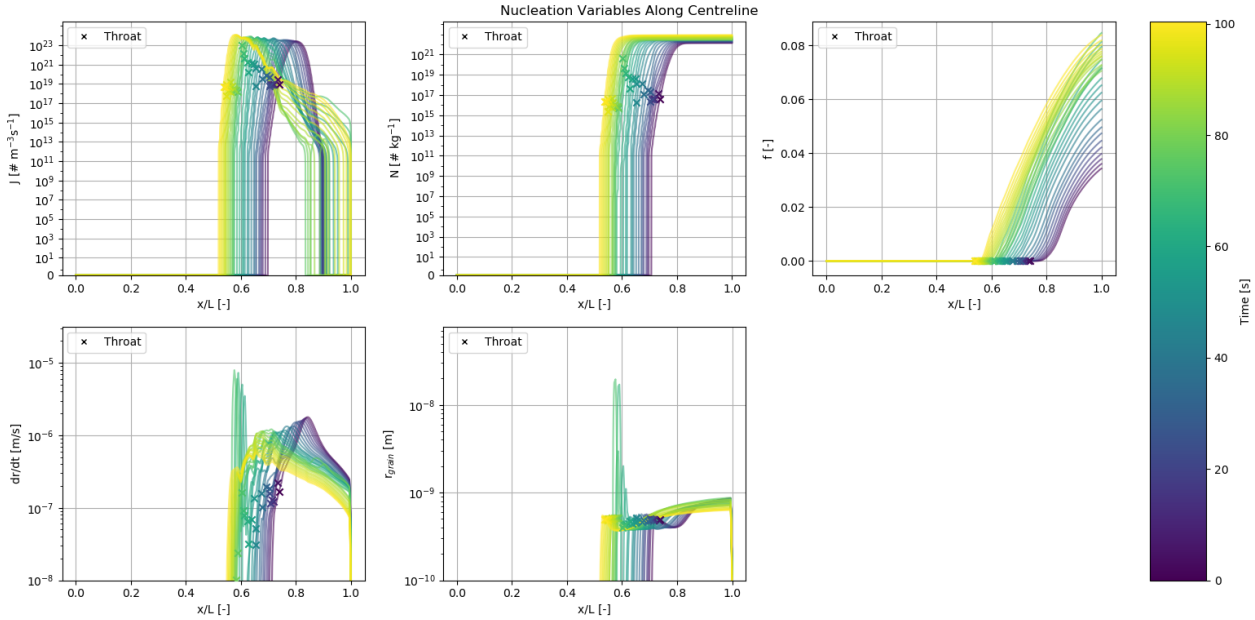

Figure 7.47: Simulation parameters along the channel centreline as time progresses due to wall accretion & sublimation for the multi-throat channel with a linear wall temperature from 273 K at the inlet to 200 K at the vent. From left to right: pressure, temperature, density, velocity, Mach number, supersaturation, nucleation rate, grain number and mass fraction

Figure 7.48 shows the p-T curves along the centreline. Figure 7.48 shows similar behaviour to case 7. The inlet moves towards triple point conditions, whereas the fluid parcels moves deeper into the metastable supersaturated region given by the Wilson point.

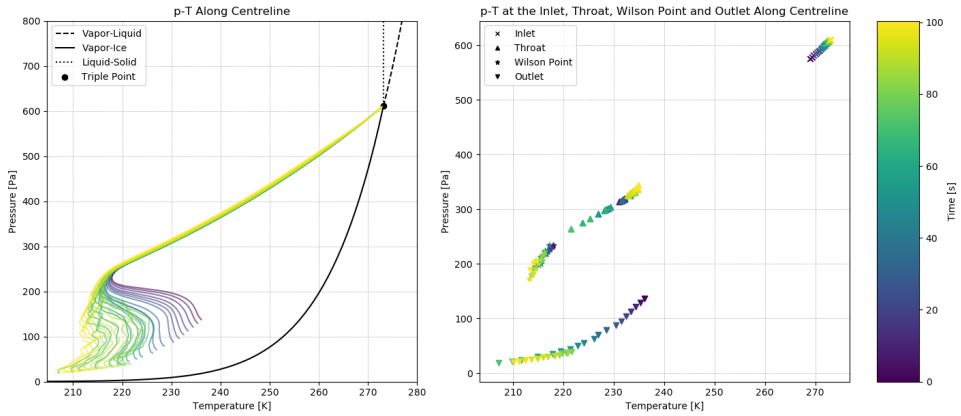

Figure 7.48: Evolution of pressure-temperature along centreline as time progresses due to wall accretion & sublimation for the multi-throat channel with a linear wall temperature from 273 K at the inlet to 200 K at the vent

Figure 7.49 shows how the throat evolves in time. It shows progressive throat contraction, accelerating growth in A_e/A^* and the throat moving downstream over time in a near linear trend. Therefore, for the multi-throat channel with wall accretion & sublimation with a linear wall temperature from 273 K to 200 K, the throat will continuously become smaller and shift downstream.

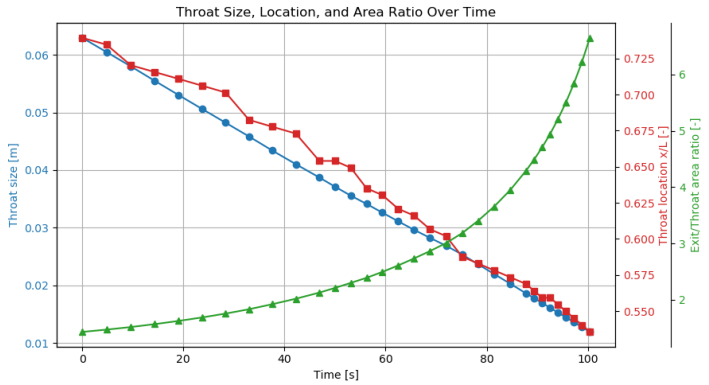

Figure 7.49: Channel throat evolution as time progresses due to wall accretion & sublimation for the multi-throat channel with a linear wall temperature from 273 K at the inlet to 200 K at the vent

7.4. Discussion

The parametric study presented in Table 7.2 demonstrates how wall thermal boundary conditions and phase-change mechanisms directly control channel evolution and flow thermodynamics. In the accretion-dominated cases (Cases 1–2), the channel throat consistently narrows and migrates upstream, leading to a monotonic increase in the exit-to-throat area ratio (A_e/A^*). This geometric constriction enhances the local expansion ratio and promotes earlier supersaturation, shifting nucleation upstream. The adiabatic wall (Case 1) supports stronger local supersaturation due to the absence of heat exchange, whereas the isothermal wall at 273 K (Case 2) constrains the wall-adjacent gas temperature, resulting in reduced accretion flux compared to the adiabatic case. Despite this difference, both scenarios converge on the same outcome: enhanced nucleation earlier in the channel and progressive choking of the throat, implying eventual closure under continued accretion.

By contrast, sublimation-only cases (Cases 3–4) exhibit opposite geometric and thermodynamic trends. In Case 3, the adiabatic wall produces throat widening with downstream migration, accompanied by diminished nucleation due to delayed cooling and weaker supersaturation. The isothermal wall at 273 K (Case 4) enforces a uniform sublimation flux, yielding a throat that expands while maintaining a fixed axial location. In both cases, A_e/A^* decreases with time, suppressing supersaturation and reducing nucleation rates. The comparison between accretion-only and sublimation-only cases highlights a clear dichotomy: accretion accelerates constriction and upstream migration of the throat

with enhanced nucleation, while sublimation drives widening and delays or suppresses phase-change activity.

The mixed accretion–sublimation cases (Cases 5–8) display more complex behaviour due to the competition between opposing wall fluxes. In Case 5 (adiabatic), accretion dominates the inlet while sublimation progressively strengthens downstream, particularly after flow separation at x/L $\approx$ 0.8 induces sharp increases in wall temperature. This dual behaviour yields net widening at the vent with narrowing upstream, and nucleation that is initially enhanced but later reduced as sublimation dominates. In Case 6 (isothermal, 273 K), sublimation dominates across the entire channel, producing uniform widening and throat migration upstream until termination at the inlet. In this case, the gradual increase in A_e/A^* results in reduced supersaturation, weaker nucleation, and diminished grain number density compared to Case 5.

The linear wall-temperature gradient cases (Cases 7–8) introduce spatially varying accretion sublimation regimes. In Case 7 (baseline channel), sublimation is localised near the warmer inlet, while accretion dominates downstream as the wall cools toward 200 K. This leads to progressive narrowing of the throat with upstream migration and accelerating growth in A_e/A^*. Thermodynamically, this configuration generates steepened gradients in pressure and temperature, amplifying supersaturation and yielding enhanced nucleation and higher solid mass fractions. The multi-throat geometry in Case 8 further intensifies these effects: the downstream constrictions strengthen compressible-flow adjustments, producing larger supersaturation peaks, enhanced nucleation, and accelerated throat contraction with near-linear downstream migration.

Overall, the study shows that the morphology of icy vents is governed by the competition between wall accretion and sublimation, modulated by wall thermal forcing and geometry. Accretion-driven narrowing favours enhanced and upstream-shifted nucleation, whereas sublimation-driven widening reduces or delays nucleation. In mixed cases, the axial distribution of wall temperature critically determines whether accretion or sublimation dominates, leading to non-monotonic throat evolution. The trends in A_e/A^*, throat position, and nucleation behaviour underscore the sensitivity of vent dynamics to thermal boundary conditions, implying that even modest spatial temperature variations can fundamentally alter vent evolution and the timing and location of plume particle formation.

Table 7.2: Summary of the results of the parametric study on how wall accretion and wall sublimation affect the geometry evolution and flow/thermodynamics

Case	Channel, Wall Accretion/Sublimation, Wall Condition	Geometry Evolution	Flow/Thermodynamics	Dominant Process
Case 1	Baseline channel, wall accretion, adiabatic wall	Throat narrows & moves upstream	Nucleation enhanced & shifts upstream	Accretion
Case 2	Baseline channel, wall accretion, isothermal wall T= 273 K	Throat narrows & moves upstream	Nucleation enhanced & shifts upstream	Accretion
Case 3	Baseline channel, wall sublimation, adiabatic wall	Throat widens & moves downstream	Nucleation diminished & shifts downstream	Sublimation
Case 4	Baseline channel, wall sublimation, isothermal wall T= 273 K	Uniform widening, throat location remains unchanged	Nucleation diminished & remains at the same location	Sublimation
Case 5	Baseline channel, wall accretion & sublimation, adiabatic wall	Net widening at vent due to flow separation. Throat narrows & moves mostly upstream	Nucleation is initially enhanced & moves upstream followed by a slight decrease downstream movement	Sublimation with the inlet to the middle of the channel accretion
Case 6	Baseline channel, wall accretion & sublimation, isothermal wall T= 273 K	Overall widening, throat moves upstream towards inlet	Nucleation diminished & shifts upstream	Sublimation
Case 7	Baseline channel, wall accretion & sublimation, linear wall temperature from 273 K to 200 K	Inlet widens, throat narrows & moves upstream	Nucleation enhanced & shifts upstream	Sublimation at the inlet, accretion downstream of inlet
Case 8	Multi-throat channel, wall accretion & sublimation, linear wall temperature from 273 K to 200 K	Inlet widens, throat narrows & moves upstream	Nucleation enhanced & shifts upstream	Sublimation at the inlet, accretion downstream of inlet

8

Application for Enceladus

In this chapter, a similarity study is conducted to connect the results discussed in chapter 7 to the observations of Enceladus taken by the Cassini spacecraft. In order to accomplish this, a scaled-up multi-throat channel is used. In section 8.1, the parameters of interest of Enceladus are elaborated. This is followed by the chosen scaled model for Enceladus in section 8.2. Finally, in section 8.3 an analysis and comparison is made for the scaled model for Enceladus with the observations from Cassini.

8.1. Enceladus Parameters

Cassini observations have provided estimates for key plume properties such as ejection velocity, grain size, and solid fraction. Ejection velocities have been derived by fitting UVIS and INMS data, yielding values between 350 and 950 m/s (Dong et al. 2011; Schmidt et al. 2008b). Grain sizes are typically in the range of 0.1–1 μm (Hedman et al. 2009; Schmidt et al. 2008b). However, larger particles up to 75 μm have also been suggested (Kempf et al. 2010). These grains likely fall back onto Enceladus' surface near the vents and thus escape detection by Cassini's Visual and Infrared Mapping Spectrometer (VIMS). As mentioned in chapter 2, solid fractions in Enceladus' plume of 0.07–0.20 have been proposed (Kieffer et al. 2009).

The aperiodic variations of Enceladus' plume analysed by Ingersoll et al. (2020) shown in Figure 2.12a is digitised in Figure 8.1. The mean anomaly has been converted into time from periapsis based on Enceladus' orbital period of 32.9 hours. The y-axis is also modified by dividing the slab density to the maximum slab density value in the datapoints from August 2nd. A curve is plotted through the datapoints for each date. The dashed vertical line shows a vertical slice through the datapoints which is displayed on the right plot. The vertical slice passes through three points and shows that the activity increases by about 4-5% from June 18th to August 2nd before reducing by about 14% in August 28th.

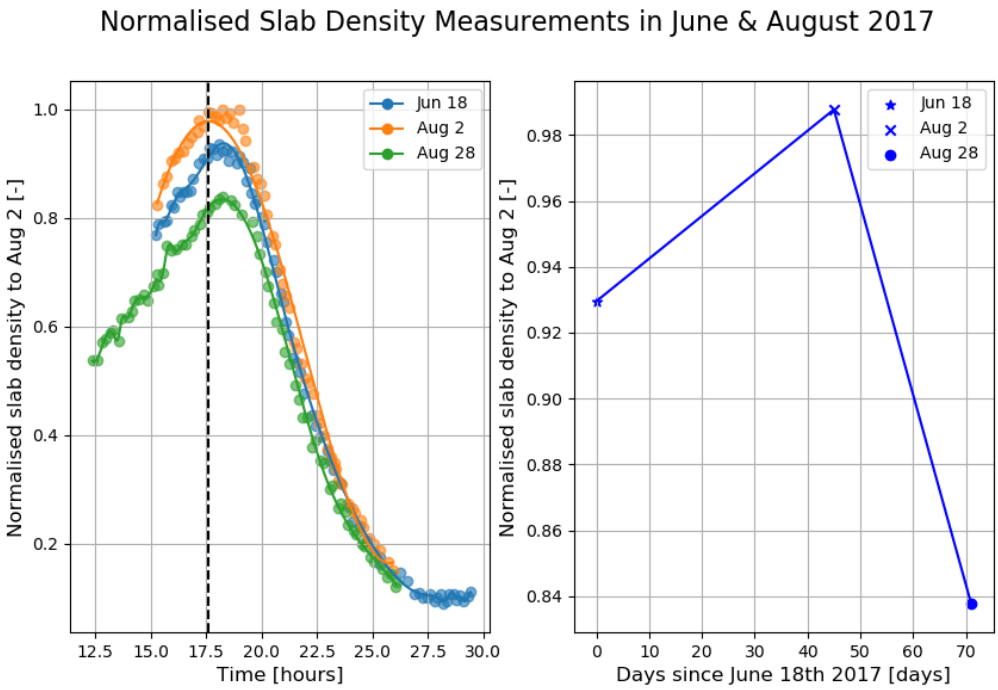

Figure 8.1: Digitised plot of Ingersoll et al. (2020) aperiodic data. Left: Normalised slab density at 100 km to the maximum at August 2, 2017 against time from periapsis for June 18, 2017, August 2, 2017, and August 28, 2017. Right: Normalised slab density at 100 km for a vertical slice at around t=17.5 hours from periapsis

8.2. Scaled Model of Enceladus

As mentioned in subsection 4.2.2, the crevasses of Enceladus have channel lengths in the order of hundreds of meters to several kilometers. Creating meshes for such channels proves impractical because of the large number of cells and the small cell size required to capture the effects on the wall. Instead, a scaled channel is created from the multi-throat channel analysed in subsection 7.3.4. This scaled channel is shown in Figure 8.2 and is scaled lengthwise by a factor of 10 compared to the multi-throat channel resulting in a length of 15 m. For this mesh 213,543 cells were used in order to capture the flow physics and wall phenomena.

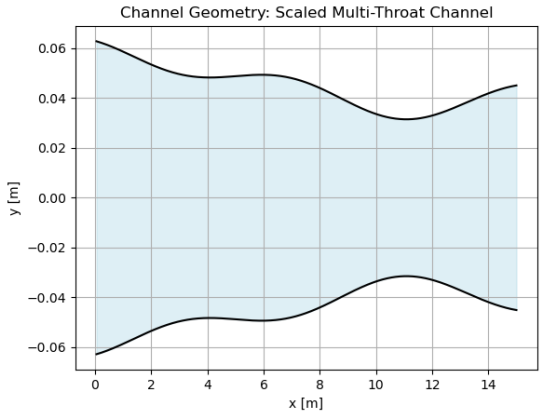

Figure 8.2: Scaled geometry of the multi-throat channel used for Enceladus length scale comparison

During the simulations, it was noticed that the simulation would take a couple of days before steady state was reached. This is because with a longer channel, a stronger shockwave occurs due to the onset of nucleation compared to the channels with a length of 1.5 m. The consequence is that the steady

state solution lies further away from the quasi-1D flow solution which is used as the initial condition. The solution to remedy this problem was to run the first simulation until steady state conditions are reached using the quasi-1D flow initialisation and then for succeeding simulations to use the steady-state solution of the previous simulation as an initialisation. However, for each simulation the wall progresses and therefore the mesh is slightly different. In order to use the steady-state solutions of the previous simulation which had a slightly different mesh, an OpenFOAM command was used to map the fields using nearest neighbour interpolation.

8.3. Analysis

The simulation results for the scaled Enceladus length scale channel are shown below. Figure 8.3b reveals that wall evolution in the scaled channel follows the same fundamental pattern observed in Case 8, but with enhanced spatial resolution and more pronounced effects. The channel exhibits sublimation-dominated behaviour near the warmer inlet, transitioning to accretion-dominated conditions in the cooler downstream regions. The most significant geometric changes occur at approximately 0.4-0.5 x/L, consistent with the location where the balance between wall accretion and sublimation fluxes is maximised. Unlike the shorter 1.5 m channel, the extended length allows for more gradual spatial transitions and provides greater opportunity for wall interaction effects to accumulate over the flow path.

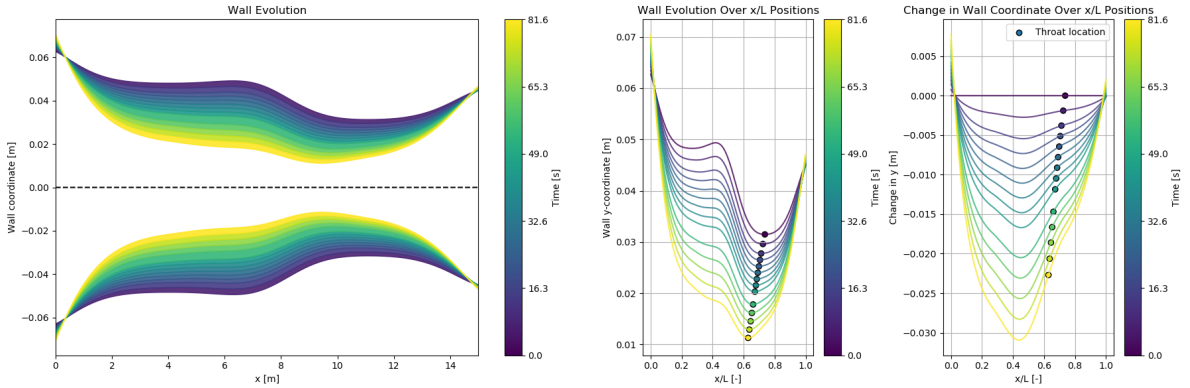

(a) Wall evolution as time progresses due to wall accretion & sublimation for the scaled Enceladus length scale channel

(b) Wall geometry evolution as time progresses due to wall accretion & sublimation for the scaled Enceladus length scale channel

Figure 8.3: Wall evolution as time progresses due to wall accretion for the scaled Enceladus length scale channel

The centreline profiles for the thermodynamic variables shown in Figure 8.4 show the characteristic clockwise “rotation” observed in case 8 in pressure, temperature, and density curves as the channel evolves. As the throat narrows, pressure drops more steeply, velocities accelerate, and Mach numbers increase faster than in the smaller-scale simulations.

The centreline profiles for the nucleation variables shown in Figure 8.4. Comparing to case 8, due to the longer residence time in the channel, the cooling rate is lower. This results in smaller super-saturation peaks and hence weaker nucleation. The same conclusions can be made for the temporal evolution of the channel when comparing with case 8. Since the compression-expansion becomes stronger, it eventually overpowers nucleation and supersaturation begins to increase.

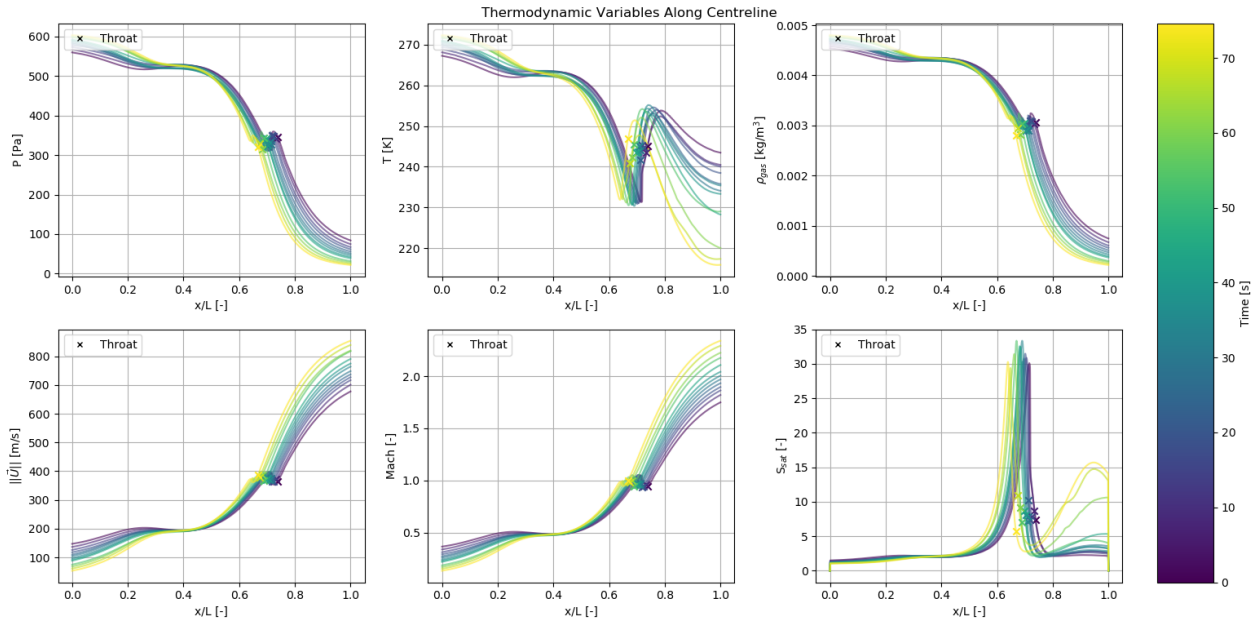

Figure 8.4: Thermodynamic parameters along the channel centreline as time progresses due to wall accretion & sublimation for the scaled Enceladus length scale channel with a linear wall temperature from 273 K at the inlet to 200 K at the vent. From left to right: pressure, temperature, density, velocity, Mach number, and supersaturation

The vent velocities range from 680 m/s to 830 m/s with the vent mass fraction ranging from 0.064 to 0.098. The grain size at the vent reaches around 0.02 μm. Fontes (2023) found a power-lass regression for the grain size with the expansion parameter given by $\epsilon \equiv \frac{A_e/A^*}{L_{\text{div}}}$ where L_{div} is the length between the throat and the outlet. The power law is given by $r = a\epsilon^b$ where $a = 3\times10^{-9}$ and $b = -1.137$. Applying this power law for a channel with 150 m results in grain sizes of the order of 0.1 μm. These results are in line with Cassini data obtained from UVIS and INMS discussed in section 8.1.

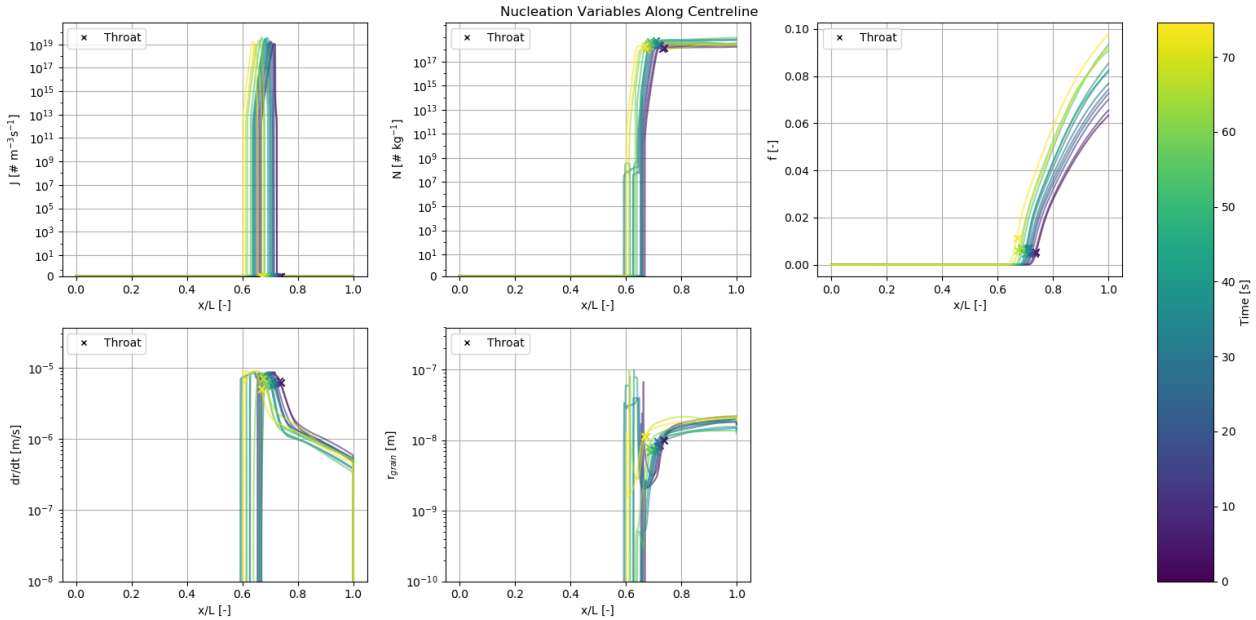

Figure 8.5: Simulation parameters along the channel centreline as time progresses due to wall accretion & sublimation for the scaled Enceladus length scale channel with a linear wall temperature from 273 K at the inlet to 200 K at the vent. From left to right: pressure, temperature, density, velocity, Mach number, supersaturation, nucleation rate, grain number and mass fraction

Looking at Figure 8.6, this plot compares the temporal evolution of normalised integrated mass flux

over the channel outlet for two different channel lengths: the 1.5 m multi-throat channel from Case 8 in chapter 7 and the 15 m scaled channel. Both curves are normalised by their respective maximum values, allowing direct comparison of the relative temporal behaviour despite potentially different absolute mass flux magnitudes. The x-axis shows its simulation time evolution.

The non-monotonic feature in the 1.5 m channel curve, with a sharp increase and recovery near 76 seconds is particularly noteworthy. This behaviour is most likely the result of a nucleation shock shifting relative to the throat, producing a sudden change in the pressure distribution and hence the outlet flux. The absence of such irregularities in the 15 m channel indicates that these effects are scale-dependent or that the 15 m channel may exhibit this feature later on if the simulation was continued for longer.

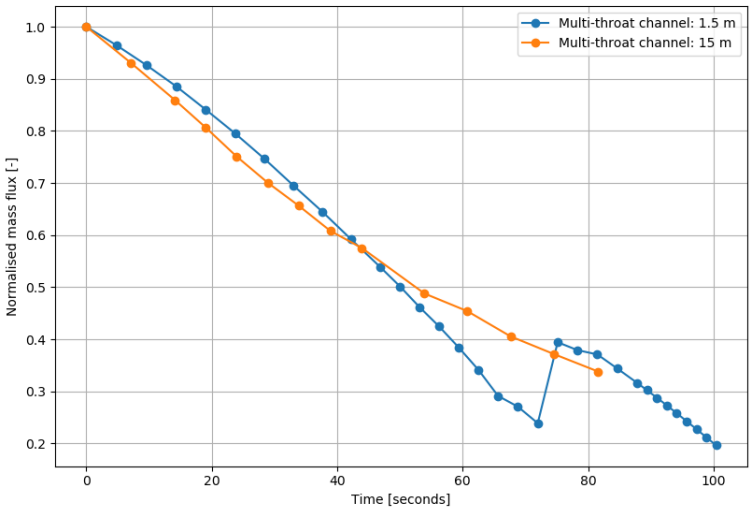

Figure 8.6: Integrated mass flux over channel outlet normalised by its corresponding maximum plotted over time for the multi-throat channel with a length of 1.5 m and 15 m.

In order to compare the mass flux in Figure 8.6 with the column/slab density at 100 km in Figure 8.1, the simulation time must be scaled. This scaling parameter is related to the exit-to-throat area given by

$$\tau_s = \frac{(A_e/A^*)_t - (A_e/A^*)_0}{(A_e/A^*)_{\text{max}} - (A_e/A^*)_0} \tag{8.1}$$

In Equation 8.1, $(A_e/A^*)_t$ is the area ratio for a certain epoch, $(A_e/A^*)_0$ is the area ratio for the first epoch and $(A_e/A^*)_{\text{max}}$ is the maximum area ratio achieved in the simulation. This scaling provides a common basis for comparing the 1.5 m and 15 m multi-throat channels as they evolve due to wall accretion and sublimation and to analyse it with Cassini data.

Figure 8.7 shows the normalised mass flux plotted against the dimensionless τ_s scaling parameter. The general trend in both channels is a monotonic decrease in normalised mass flux as τ_s increases, consistent with the physical expectation that as the throat constricts, the total mass output is reduced. This behaviour contrasts with Cassini observations, which showed an increase in plume brightness from June to August 2017, followed by a decline by late August. A direct one-to-one mapping of the Cassini points onto these curves is therefore not possible. However, this discrepancy opens up important avenues for interpretation.

First, the simulations capture only one phase of the vent cycle. This is the closure phase, whereas the Cassini data reflect the integrated behaviour of an evolving vent system. For instance, using the August 2nd data point and using that as an anchor at a normalised output of 1 for a τ_s of 0, the August 28th data point then follows with a normalised output of 0.78. Therefore, the model provides a mechanism for the observed decline in plume activity following August 2nd, 2017.

It is plausible that the June–August rise corresponds to an initial widening phase, potentially driven by sublimation, as identified in Cases 3 and 4 of the parametric study. Whereas the subsequent decline

(August 2nd to August 28th) reflects the choking phase captured here. In this interpretation, the current model reproduces only the decay portion of the observed variability. However, the issue could lie in the model itself.

The fundamental limitation is that the current model captures only accretion-dominated geometric evolution under fixed boundary conditions. As demonstrated in the parametric study, Cases 3 and 4 showed that wall sublimation can produce channel widening, but the linear temperature profile (273K to 200K) used here ensures accretion dominates downstream where cooling promotes ice deposition. The thesis findings indicate that achieving reversible vent behaviour may require either cyclic thermal forcing or spatially varying conditions not present in the current setup.

Secondly, the link between outlet mass flux and slab density at 100 km is not strictly linear. The mass flux is a measure of total outflow rate, whereas the slab density at 100 km depends additionally on the ejection velocity, plume expansion, and particle entrainment. As the throat narrows, the simulations show that exit velocities increase markedly, which could transiently enhance the ability of the vent to loft and sustain grains to high altitudes, even while the total mass flux is declining. This effect provides a possible explanation for the initial rise in brightness despite decreasing mass flux but warrants further study.

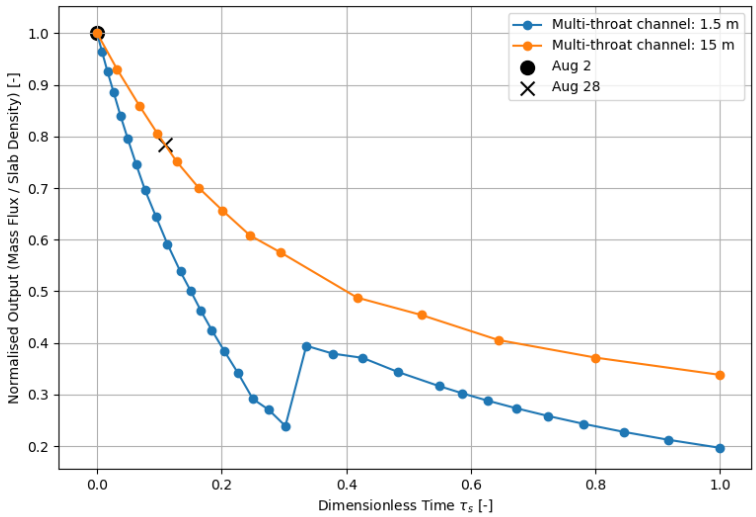

Figure 8.7: Integrated mass flux over channel outlet normalised by its corresponding maximum plotted over a scaled time based on the exit-to-throat area ratio for the multi-throat channel with a length of 1.5 m and 15 m. The Cassini data point for August 2nd is plotted as an anchor.

The results demonstrate that for larger channels, wall interaction processes can operate on timescales potentially relevant to Enceladus. Furthermore, wall accretion may indeed play an important role in the decline in plume activity observed from August 2nd to August 28th. However, the monotonic nature of the geometric evolution cannot alone account for the cyclic plume variability documented by Ingersoll et al. (2020). The thesis findings suggest that realistic modelling would require incorporating the thermal cycling and pressure variations, which were beyond the scope of the current isothermal and fixed-pressure boundary conditions.

9

Recommendations

The present study highlights several important avenues for future research to improve the understanding and modelling of vapour flows and phase-change dynamics in Enceladus-like icy vent systems. While the modelling framework employed here captures a wide range of physical phenomena including the coupled wall interactions, nucleation and grain growth, it is based on several assumptions. These assumptions merit further scrutiny through more sophisticated modelling and experimental validation.

A critical assumption in this work is that the vapour phase behaves as a perfect, continuous gas. However, at the extremely low pressures characteristic of Enceladus' plumes, the gas density becomes sufficiently low that rarefaction effects may play a significant role. This challenges the validity of the continuum approximation and suggests that future studies should consider kinetic models, such as those based on the Boltzmann equation or direct simulation Monte Carlo (DSMC) techniques, particularly in the near-vent and free-expansion regions. A hybrid approach, combining Navier–Stokes solvers for denser regions and DSMC for the rarefied portions, could provide a more accurate and computationally efficient framework for simulating the full plume structure.

Another area deserving attention is the treatment of solely water vapour to liquid water homogeneous nucleation with growth of icy grains. As mentioned in subsection 4.2.2, for homogeneous nucleation there should exist a complex three-phase mechanism in the channels. Furthermore, only homogeneous nucleation was considered for this work, yet heterogeneous nucleation should also be possible in the plumes due to the existence of foreign particles both in the solid and gaseous phase. Including the three-phase phenomena and heterogeneous nucleation in the model would improve the fidelity of the simulations.

Thermal modelling of the channel walls also warrants further refinement. This study explored a range of idealised wall temperatures (adiabatic, isothermal, and linear gradients), but real vents on Enceladus likely experience dynamic thermal environments influenced by tidal heating, sunlight exposure, and subsurface oceanic feedback. Therefore, future models should include time-dependent wall heating and cooling scenarios, coupled to subsurface thermal models, to simulate transient behaviour during plume activation and shutdown. Including this transient phase could be especially important, as startup and shutdown periods may introduce non-equilibrium effects that dramatically influence condensation and ice grain formation.

In terrestrial gas flows, it is common practice to assume that micron- or submicron-scale particles are sufficiently small to follow the motion of the gas phase, especially when the characteristic length scales are large enough that grain inertia is negligible. For Enceladus' plume vents, however, the characteristic dimensions can be on the order of a few meters or less, and the grain sizes resulting from vapour deposition are believed to range from nanometers up to submicron scales. This raises a natural concern as to whether the standard tracer particle assumption remains valid in this extraterrestrial cryovolcanic setting.

The gravitational acceleration at the surface of Enceladus is approximately $g \approx 0.113\ m/s^2$ nearly two orders of magnitude smaller than Earth's. In the context of plume dynamics, the vertical momentum imparted by high-velocity gas expansion far exceeds any contribution from gravity. For example, a parcel of gas travelling upward at 750 m/s would rise tens of kilometres before gravity causes a significant change in its velocity. On the length scales of the channel itself in the order of hundreds of

meters, the change in momentum due to gravity is negligible compared to that caused by pressure and inertial forces. However, if one were interested in modelling the trajectories of the icy particles from the channel to above the surface, then the gravitational acceleration would have to be included.

Taken together, these recommendations emphasise the need for more physically detailed, experimentally informed, and computationally advanced modelling approaches to accurately represent the unique plume dynamics observed on Enceladus. As future spacecraft missions target these cryovolcanic jets, a better understanding of the vent-scale processes will be essential to interpreting remote observations and unravelling the moon's subsurface structure and habitability.

10

Conclusion

The aim of this thesis was to investigate whether the temporal variations in Enceladus' plume activity can be explained through ice deposition, wall accretion and wall sublimation processes within subsurface channels. To address this overarching research question, a two-dimensional two-phase CFD framework was adapted to incorporate wall interactions, specifically accretion and sublimation, and applied across two different channel geometries. The findings from this work provide several insights into the dynamic evolution of plume vents and their implications for Enceladus' observed plume variability.

> *Q1: How do different channel geometries affect the plume characteristics (velocity, number of particles, solid fraction and average particle size)?*

The simulations demonstrated that geometry exerts a first-order control on plume properties. Convergent-divergent channels reproduced enhanced supersonic expansion, leading to stronger nucleation rates and higher grain numbers. Multi-throat geometries introduced localised regions of compression and expansion. However, nucleation occurs predominantly around the area where there is the highest compression-expansion which is the throat. A higher A_e/A^* results in a stronger compression-expansion and therefore enhances nucleation but reduces grain growth due to the shorter residence times. Finally, the location nucleation and grain growth is highly dependent on the throat location. These results indicate that channel architecture can strongly modulate the plume's velocity distribution, solid fraction, and particle size evolution, and may therefore contribute to the heterogeneity in plume observations.

> *Q2: How does the channel geometry change in time due to the coupling between the plume flow and wall accretion?*

Under wall accretion conditions, simulations showed progressive narrowing of the channel, particularly at the inlet and throat. The throat generally migrated upstream as wall accretion advanced, causing a reduction in cross-sectional area. This narrowing increased the exit-to-throat area ratio (Ae/A^*), which in turn altered the pressure, density, and nucleation environment of the plume. While accretion tended to constrict the vent and shift the plume's origin upstream, the process was not uniform, as accretion was highly sensitive to the interplay between local density, wall temperature, and flow conditions.

> *Q3: How does the channel geometry change in time due to the coupling between the plume flow and wall sublimation?*

In contrast, wall sublimation produced a net widening of channels. For the adiabatic case, sublimation was strongest near the inlet whereas for the isothermal case it was uniform. For both cases, sublimation resulted in the migration of the throat downstream. This widening reduced supersaturation and consequently lowered nucleation activity in some scenarios, though the longer residence time in the expansion zone allowed grains to grow larger. In cases with more complex wall temperature

profiles, sublimation could act in opposition to accretion, with the balance between these processes determining whether the vent narrowed or opened over time. For an adiabatic wall, accretion was dominated inside the channel until the vent where sublimation dominated due to flow separation. For an isothermal wall either accretion or sublimation can be dominant depending on the chosen wall temperature. For a linear wall temperature, accretion and sublimation can be dominant in different parts of the channel.

Taken together, these findings suggest that accretion and sublimation act as competing mechanisms that can drive channels either toward closure or toward widening, depending on the balance of wall fluxes. Importantly, the temporal evolution of the vent geometry feeds back into plume behaviour, influencing velocity fields, particle production, and grain size distributions. Therefore, it is crucial to carefully model the temperature evolution of the channel walls.

Q4: How does a 2D CFD model with wall interactions compare to observations from the Cassini spacecraft?

The application of the model to scaled multi-throat channels allowed a first comparison with Cassini's observations of aperiodic variability. When normalised mass flux is plotted against the dimensionless parameter τ_s, the simulations show a clear decay in mass output as the channel closes. By contrast, Cassini data show both a rise (June to August 2017) and a subsequent fall (August to late August 2017) in plume brightness. This indicates that the present simulations capture only part of the observed cycle: specifically, the decay phase consistent with the observed decline between August 2nd and August 28th.

A direct mapping of Cassini slab density to modelled mass flux is complicated by the non-linear relationship between outflow and observed brightness at altitude. While total mass flux decreases as the vent narrows, exit velocities increase, potentially leading to more efficient grain lofting and temporarily brighter plumes. This effect provides a plausible explanation for the June–August rise, even though the mass flux itself was declining.

Can the temporal variations in Enceladus' plume activity be explained by deposition and sublimation of ice in the cracks?

The results of this thesis indicate that wall accretion and sublimation within subsurface cracks are capable of driving significant temporal changes in vent geometry. Therefore, they play a central role in shaping the variability of Enceladus' plumes. Accretion systematically narrows channels, reducing mass flux while increasing exit velocities and enhancing nucleation, whereas sublimation produces net widening, lowering nucleation rates but permitting larger grain growth. These two processes are strongly coupled to the flow field, and their competition determines whether vents evolve toward choking or widening over time.

When compared to Cassini's observations of aperiodic plume variability, the CFD framework reproduces decline in plume brightness following August 2nd, 2017. However, the model does not capture the preceding rise in activity, reflecting important limitations in the current framework. The main limitation is the simplified treatment of wall temperature: the linear gradient assumption constrains sublimation–accretion balance in a way that may not fully reflect natural conditions. For instance, transient heating Ftand non-linear gradients are likely to play a role. These limitations may suppress widening phases in the model, thereby underestimating the potential for plume brightening during the early part of the cycle.

Therefore, while wall accretion and sublimation alone may not fully explain all aspects of Enceladus' plume variability, they provide a mechanism for the observed aperiodic decline in activity. More broadly, the findings underscore the importance of vent-scale wall processes in shaping the temporal variability of cryovolcanic activity.

References

Abramov, O. and Spencer J. (2009). “Endogenic heat from Enceladus’ south polar fractures: New observations, and models of conductive surface heating”. In: *Icarus* 199.1, pp. 189–196. ISSN: 0019-1035. DOI: https://doi.org/10.1016/j.icarus.2008.07.016. URL: https://www.sciencedirect.com/science/article/pii/S0019103508002893.

Albada, G. D. van et al. (1997). “A Comparative Study of Computational Methods in Cosmic Gas Dynamics”. In: *Upwind and High-Resolution Schemes*. Ed. by M. Yousuff Hussaini et al. Berlin, Heidelberg: Springer Berlin Heidelberg, pp. 95–103. ISBN: 978-3-642-60543-7. DOI: 10.1007/978-3-642-60543-7_6. URL: https://doi.org/10.1007/978-3-642-60543-7_6.

Amann-Winkel, Katrin et al. (Feb. 2016). “Colloquium: Water’s controversial glass transitions”. In: *Rev. Mod. Phys.* 88 (1), p. 011002. DOI: 10.1103/RevModPhys.88.011002. URL: https://link.aps.org/doi/10.1103/RevModPhys.88.011002.

Anderson, J.D. (1991). *Fundamentals of Aerodynamics*. McGraw-Hill Aeronautical and aerospace engineering series. McGraw-Hill Companies. ISBN: 9780070016804. URL: https://books.google.nl/books?id=LJ-hAAAACAAJ.

Averill, Bruce A and Patricia Eldredge (2012). “Principles of general chemistry”. In: *Creative Commons*.

Azzini, Lucia (2019). “Numerical investigation of dense condensing flows for next-generation power units”. English. Dissertation (TU Delft). Delft University of Technology. DOI: 10.4233/uuid:6c84e51e-4111-4638-ae70-24a510db3ca5.

Bakhtar, F et al. (Dec. 2005). “Classical Nucleation Theory and Its Application to Condensing Steam Flow Calculations”. In: *Proceedings of The Institution of Mechanical Engineers Part C-journal of Mechanical Engineering Science - PROC INST MECH ENG C-J MECH E* 219, pp. 1315–1333. DOI: 10.1243/095440605X8379.

Barschdorff, D. et al. (Dec. 1972). “Homogeneous Nucleation in Steam Nozzle Condensation”. In: *Nature Physical Science* 240.103, pp. 166–167. DOI: 10.1038/physci240166a0.

Batista, Enrique R. et al. (Dec. 2005). “What Determines the Sticking Probability of Water Molecules on Ice?” In: *Phys. Rev. Lett.* 95 (22), p. 223201. DOI: 10.1103/PhysRevLett.95.223201. URL: https://link.aps.org/doi/10.1103/PhysRevLett.95.223201.

Becker, R and Werner Döring (1954). *Kinetic treatment of the nucleation in supersaturated vapors*. 1374. National Advisory Commitee for Aeronautics.

Berne, A. et al. (Oct. 2023). “A Relationship Between Jet Activity and Strike-Slip Motion over the Tiger Stripes on Enceladus”. In: DOI: 10.21203/rs.3.rs-3405798/v1.

Blondel, Frédéric (Jan. 2014). “Unsteady couplings of wet steam in steam turbine flows”. Theses. Ecole Centrale de Lyon. URL: https://theses.hal.science/tel-00985725.

Brown, R. et al. (2006). “Composition and Physical Properties of Enceladus’ Surface”. In: *Science* 311.5766, pp. 1425–1428. DOI: 10.1126/science.1121031. eprint: https://www.science.org/doi/pdf/10.1126/science.1121031. URL: https://www.science.org/doi/abs/10.1126/science.1121031.

Buch, V. and Q. Zhang (Oct. 1991). “Sticking Probability of H and D Atoms on Amorphous Ice: A Computational Study”. In: *ApJ* 379, p. 647. DOI: 10.1086/170537.

Canteros, Maria Laura and Polanský, Jiří (2024). “Review and comparison of two OpenFOAM® solvers: rhoCentralFoam and sonicFoam”. In: *EPJ Web of Conf.* 299, p. 01005. DOI: 10.1051/epjconf/202429901005. URL: https://doi.org/10.1051/epjconf/202429901005.

Cassini imaging team, NASA (Mar. 2006). *PIA07800: Enceladus the Storyteller*. URL: https://photojournal.jpl.nasa.gov/catalog/pia07800.

— (Dec. 2008). *PIA11133: A Tectonic Feast.* URL: https://photojournal.jpl.nasa.gov/catalog/PIA11133.

— (Feb. 2010). *PIA11688: Bursting at the Seams: the Geyser Basin of Enceladus.* URL: https://photojournal.jpl.nasa.gov/catalog/PIA11688f.

Chan, W.F. et al. (1993). “The electronic spectrum of water in the discrete and continuum regions. Absolute optical oscillator strengths for photoabsorption (6–200 eV)”. In: *Chemical Physics* 178.1, pp. 387–400. ISSN: 0301-0104. DOI: https://doi.org/10.1016/0301-0104(93)85078-M. URL: https://www.sciencedirect.com/science/article/pii/030101049385078M.

Chodas, Mark et al. (2023). “Enceladus Vent Explorer Mission Architecture Trade Study”. In: *2023 IEEE Aerospace Conference*, pp. 1–16. DOI: 10.1109/AERO55745.2023.10115635.

Cmglee (Aug. 2014). *Phase diagram of water simplified.svg*. URL: https://en.wikipedia.org/wiki/File:Phase_diagram_of_water_simplified.svg.

Crank, J. and P. Nicolson (1947). “A practical method for numerical evaluation of solutions of partial differential equations of the heat-conduction type”. In: *Mathematical Proceedings of the Cambridge Philosophical Society* 43.1, pp. 50–67. DOI: 10.1017/S0305004100023197.

Crow-Willard, Emma N. and Robert T. Pappalardo (2015). “Structural mapping of Enceladus and implications for formation of tectonized regions”. In: *Journal of Geophysical Research: Planets* 120.5, pp. 928–950. DOI: https://doi.org/10.1002/2015JE004818. eprint: https://agupubs.onlinelibrary.wiley.com/doi/pdf/10.1002/2015JE004818. URL: https://agupubs.onlinelibrary.wiley.com/doi/abs/10.1002/2015JE004818.

Cui, J. et al. (2011). “A new time- and space-dependent model for predicting frost formation”. In: *Applied Thermal Engineering* 31.4, pp. 447–457. ISSN: 1359-4311. DOI: https://doi.org/10.1016/j.applthermaleng.2010.09.022. URL: https://www.sciencedirect.com/science/article/pii/S1359431110004187.

Cuppen, H. M. et al. (July 2010). “H2 reformation in post-shock regions”. In: *Monthly Notices of the Royal Astronomical Society: Letters* 406.1, pp. L11–L15. ISSN: 1745-3925. DOI: 10.1111/j.1745-3933.2010.00871.x. eprint: https://academic.oup.com/mnrasl/article-pdf/406/1/L11/3512394/406-1-L11.pdf. URL: https://doi.org/10.1111/j.1745-3933.2010.00871.x.

Dong, Y. et al. (2011). “The water vapor plumes of Enceladus”. In: *Journal of Geophysical Research: Space Physics* 116.A10. DOI: https://doi.org/10.1029/2011JA016693. eprint: https://agupubs.onlinelibrary.wiley.com/doi/pdf/10.1029/2011JA016693. URL: https://agupubs.onlinelibrary.wiley.com/doi/abs/10.1029/2011JA016693.

Dotson, Renée (2018). *Enceladus and the Icy Moons of Saturn*. University of Arizona Press. ISBN: 9780816537075. URL: http://www.jstor.org/stable/j.ctv65sw2b (visited on 06/01/2023).

Dougherty, M. K. et al. (2018). “Enceladus as an Active World: History and Discovery”. In: *Enceladus and the Icy Moons of Saturn*. Ed. by Paul M. Schenk et al., p. 3. DOI: 10.2458/azu_uapress_9780816537075-ch001.

Dougherty, Ralph C. and Louis N. Howard (Nov. 1998). “Equilibrium structural model of liquid water: Evidence from heat capacity, spectra, density, and other properties”. In: *The Journal of Chemical Physics* 109.17, pp. 7379–7393. ISSN: 0021-9606. DOI: 10.1063/1.477344. eprint: https://pubs.aip.org/aip/jcp/article-pdf/109/17/7379/10794855/7379_1_online.pdf. URL: https://doi.org/10.1063/1.477344.

Fabrikant, Ilya I. et al. (2017). “Chapter Nine - Recent Progress in Dissociative Electron Attachment: From Diatomics to Biomolecules”. In: ed. by Ennio Arimondo et al. Vol. 66. Advances In Atomic, Molecular, and Optical Physics. Academic Press, pp. 545–657. DOI: https://doi.org/10.1016/bs.aamop.2017.02.002. URL: https://www.sciencedirect.com/science/article/pii/S1049250X17300034.

Farnsworth, K.K. et al. (2024). “Chapter 10 - Titan, Enceladus, and other icy moons of Saturn”. In: *Ices in the Solar-System*. Ed. by Richard J. Soare et al. Elsevier, pp. 315–356. ISBN: 978-0-323-99324-1. DOI: https://doi.org/10.1016/B978-0-323-99324-1.00011-0. URL: https://www.sciencedirect.com/science/article/pii/B9780323993241000110.

Fassnacht, S. R. (Dec. 2004). “Estimating Alter-shielded gauge snowfall undercatch, snowpack sublimation, and blowing snow transport at six sites in the coterminous USA”. In: *Hydrological Processes* 18.18, pp. 3481–3492. DOI: 10.1002/hyp.5806.

Feder, J. et al. (1966). “Homogeneous nucleation and growth of droplets in vapours”. In: *Advances in Physics* 15.57, pp. 111–178. DOI: 10.1080/00018736600101264. eprint: https://doi.org/10.1080/00018736600101264. URL: https://doi.org/10.1080/00018736600101264.

Feistel, Rainer and Wolfgang Wagner (2007). “Sublimation pressure and sublimation enthalpy of H2O ice Ih between 0 and 273.16K”. In: *Geochimica et Cosmochimica Acta* 71.1, pp. 36–45. ISSN: 0016-

7037. DOI: https://doi.org/10.1016/j.gca.2006.08.034. URL: https://www.sciencedirect.com/science/article/pii/S0016703706020461.

Fladerer, Alexander and Reinhard Strey (Apr. 2006). “Homogeneous nucleation and droplet growth in supersaturated argon vapor: The cryogenic nucleation pulse chamber”. In: *The Journal of Chemical Physics* 124.16, p. 164710. ISSN: 0021-9606. DOI: 10.1063/1.2186327. eprint: https://pubs.aip.org/aip/jcp/article-pdf/doi/10.1063/1.2186327/15385046/164710_1_online.pdf. URL: https://doi.org/10.1063/1.2186327.

Fletcher, Neville H (1962). “The physics of rainclouds”. In: *Quarterly Journal of the Royal Meteorological Society* 88.378, pp. 559–559. DOI: https://doi.org/10.1002/qj.49708837821. eprint: https://rmets.onlinelibrary.wiley.com/doi/pdf/10.1002/qj.49708837821. URL: https://rmets.onlinelibrary.wiley.com/doi/abs/10.1002/qj.49708837821.

Fontes, T. (Jan. 2023). “Icy plumes on Enceladus”. MSc thesis. TU Delft Aerospace Engineering.

Fransen, M.A.L.J. et al. (2014). “On the growth of homogeneously nucleated water droplets in nitrogen : an experimental study”. English. In: *Experiments in Fluids* 55.July, pp. 1780–1/17. ISSN: 0723-4864. DOI: 10.1007/s00348-014-1780-y.

Frommert, H. and C. Kronberg (May 2013). “William Herschel (1738–1822)”. In: *The Messier Catalog*. Retrieved May 23, 2023.

Gao, Peter et al. (2016). “Aggregate particles in the plumes of Enceladus”. In: *Icarus* 264, pp. 227–238. ISSN: 0019-1035. DOI: https://doi.org/10.1016/j.icarus.2015.09.030. URL: https://www.sciencedirect.com/science/article/pii/S0019103515004443.

Gerber, A.G. and M.J. Kermani (2004). “A pressure based Eulerian–Eulerian multi-phase model for non-equilibrium condensation in transonic steam flow”. In: *International Journal of Heat and Mass Transfer* 47.10, pp. 2217–2231. ISSN: 0017-9310. DOI: https://doi.org/10.1016/j.ijheatmasstransfer.2003.11.017. URL: https://www.sciencedirect.com/science/article/pii/S001793100300646X.

Goldsby, D. L. and D. L. Kohlstedt (2001). “Superplastic deformation of ice: Experimental observations”. In: *Journal of Geophysical Research: Solid Earth* 106.B6, pp. 11017–11030. DOI: https://doi.org/10.1029/2000JB900336. eprint: https://agupubs.onlinelibrary.wiley.com/doi/pdf/10.1029/2000JB900336. URL: https://agupubs.onlinelibrary.wiley.com/doi/abs/10.1029/2000JB900336.

Goldstein, D. B. et al. (2018). “Enceladus Plume Dynamics: From Surface to Space”. In: *Enceladus and the Icy Moons of Saturn*. Ed. by Paul M. Schenk et al., p. 175. DOI: 10.2458/azu_uapress_9780816537075-ch009.

Greenshields, Christopher J et al. (2010). “Implementation of semi-discrete, non-staggered central schemes in a colocated, polyhedral, finite volume framework, for high-speed viscous flows”. In: *International journal for numerical methods in fluids* 63.1, pp. 1–21.

Gyarmathy, George (1976). *Condensation in flowing steam*.

Handle, Philip H. et al. (2017). “Supercooled and glassy water: Metastable liquid(s), amorphous solid(s), and a no-man’s land”. In: *Proceedings of the National Academy of Sciences* 114.51, pp. 13336–13344. DOI: 10.1073/pnas.1700103114. eprint: https://www.pnas.org/doi/pdf/10.1073/pnas.1700103114. URL: https://www.pnas.org/doi/abs/10.1073/pnas.1700103114.

Hansen, C et al. (Dec. 2008). “Water vapour jets inside the plume of gas leaving Enceladus”. In: *Nature* 456, pp. 477–9. DOI: 10.1038/nature07542.

Hansen, C. J. et al. (2006). “Enceladus’ Water Vapor Plume”. In: *Science* 311.5766, pp. 1422–1425. DOI: 10.1126/science.1121254. eprint: https://www.science.org/doi/pdf/10.1126/science.1121254. URL: https://www.science.org/doi/abs/10.1126/science.1121254.

Hansen, C. J. et al. (2011). “The composition and structure of the Enceladus plume”. In: *Geophysical Research Letters* 38.11. DOI: https://doi.org/10.1029/2011GL047415. eprint: https://agupubs.onlinelibrary.wiley.com/doi/pdf/10.1029/2011GL047415. URL: https://agupubs.onlinelibrary.wiley.com/doi/abs/10.1029/2011GL047415.

Hansen, C.J. et al. (2020). “The composition and structure of Enceladus’ plume from the complete set of Cassini UVIS occultation observations”. In: *Icarus* 344. Cassini Mission Science Results, p. 113461. ISSN: 0019-1035. DOI: https://doi.org/10.1016/j.icarus.2019.113461. URL: https://www.sciencedirect.com/science/article/pii/S0019103519302325.

Hansen, James E. (1971). “Multiple Scattering of Polarized Light in Planetary Atmospheres Part II. Sunlight Reflected by Terrestrial Water Clouds”. In: *Journal of Atmospheric Sciences* 28.8, pp. 1400–

1426. DOI: https://doi.org/10.1175/1520-0469(1971)028<1400:MSOPLI>2.0.CO;2. URL: https://journals.ametsoc.org/view/journals/atsc/28/8/1520-0469_1971_028_1400_msopli_2_0_co_2.xml.

Harvey, Eleanor and H Thompson (2020). "Combining a density-based compressible solver with a multiphase model". In: *Proceedings of CFD with OpenSource Software*, pp. 1–65.

Hasegawa, Tatsuhiko I. and Eric Herbst (Mar. 1993). "New gas-grain chemical models of quiscent dense interstellar clouds :the effects of H2 tunnelling reactions and cosmic ray induced desorption." In: *mnras* 261, pp. 83–102. DOI: 10.1093/mnras/261.1.83.

Hasini, Hasril et al. (2012). "Numerical Modeling of Wet Steam Flow in Steam Turbine Channel". In: *Mechanical Engineering*. Ed. by Murat Gokcek. Rijeka: IntechOpen. Chap. 19. DOI: 10.5772/37394. URL: https://doi.org/10.5772/37394.

Hedman, M et al. (July 2013). "An observed correlation between plume activity and tidal stresses on Enceladus". In: *Nature* 500. DOI: 10.1038/nature12371.

Hedman, M. M. et al. (Mar. 2009). "Spectral observations of the Enceladus plume with Cassini-VIMS". In: *The Astrophysical Journal* 693.2, p. 1749. DOI: 10.1088/0004-637X/693/2/1749. URL: https://dx.doi.org/10.1088/0004-637X/693/2/1749.

Helfenstein, Paul and C. Porco (Sept. 2015). "Enceladus' Geysers: Relation to Geological Features". In: *aj* 150.3, 96, p. 96. DOI: 10.1088/0004-6256/150/3/96.

Hill, Philip G. (1966). "Condensation of water vapour during supersonic expansion in nozzles". In: *Journal of Fluid Mechanics* 25.3, pp. 593–620. DOI: 10.1017/S0022112066000284.

Hodgson, Anthony W. (1984). "Homogeneous nucleation". In: *Advances in Colloid and Interface Science* 21.3, pp. 303–327. ISSN: 0001-8686. DOI: https://doi.org/10.1016/0001-8686(84)85003-4. URL: https://www.sciencedirect.com/science/article/pii/0001868684850034.

Hou, Youmin et al. (2020). "Water and Ice Nucleation on Solid Surfaces". In: *Ice Adhesion*. John Wiley & Sons, Ltd. Chap. 2, pp. 55–85. ISBN: 9781119640523. DOI: https://doi.org/10.1002/9781119640523.ch2. eprint: https://onlinelibrary.wiley.com/doi/pdf/10.1002/9781119640523.ch2. URL: https://onlinelibrary.wiley.com/doi/abs/10.1002/9781119640523.ch2.

Howett, C. J. A. et al. (2011). "High heat flow from Enceladus' south polar region measured using 10–600 cm-1 Cassini/CIRS data". In: *Journal of Geophysical Research: Planets* 116.E3. DOI: https://doi.org/10.1029/2010JE003718. eprint: https://agupubs.onlinelibrary.wiley.com/doi/pdf/10.1029/2010JE003718. URL: https://agupubs.onlinelibrary.wiley.com/doi/abs/10.1029/2010JE003718.

Hric, Vladimír and Jan Halama (Nov. 2014). "Numerical Solution of Transonic Wet Steam Flow in Blade-to-Blade Cascade with Non-equilibrium Condensation and Real Thermodynamics". In: *EPJ Web of Conferences* 92. DOI: 10.1051/epjconf/20159202025.

Hsu, Hsiang-Wen et al. (Mar. 2015). "Ongoing hydrothermal activities within Enceladus". In: *Nature* 519, pp. 207–10. DOI: 10.1038/nature14262.

Huang, Yongli et al. (Oct. 2013). "Size, separation, structural order, and mass density of molecules packing in water and ice". In: *Scientific reports* 3, p. 3005. DOI: 10.1038/srep03005.

Iess, L. et al. (2014). "The Gravity Field and Interior Structure of Enceladus". In: *Science* 344.6179, pp. 78–80. DOI: 10.1126/science.1250551. eprint: https://www.science.org/doi/pdf/10.1126/science.1250551. URL: https://www.science.org/doi/abs/10.1126/science.1250551.

Ingersoll, A. et al. (2020). "Time variability of the Enceladus plumes: Orbital periods, decadal periods, and aperiodic change". In: *Icarus* 344. Cassini Mission Science Results, p. 113345. ISSN: 0019-1035. DOI: https://doi.org/10.1016/j.icarus.2019.06.006. URL: https://www.sciencedirect.com/science/article/pii/S0019103519301186.

Ingersoll, Andrew P and Shawn P Ewald (2011). "Total particulate mass in Enceladus plumes and mass of Saturn's E ring inferred from Cassini ISS images". In: *Icarus* 216.2, pp. 492–506.

— (2017). "Decadal timescale variability of the Enceladus plumes inferred from Cassini images". In: *Icarus* 282, pp. 260–275. ISSN: 0019-1035. DOI: https://doi.org/10.1016/j.icarus.2016.09.018. URL: https://www.sciencedirect.com/science/article/pii/S0019103516305905.

Ingersoll and A. Pankine (2010). "Subsurface heat transfer on Enceladus: Conditions under which melting occurs". In: *Icarus* 206.2. Cassini at Saturn, pp. 594–607. ISSN: 0019-1035. DOI: https://doi.org/10.1016/j.icarus.2009.09.015. URL: https://www.sciencedirect.com/science/article/pii/S0019103509003984.

Jacobson, R. (Oct. 2022). “The Orbits of the Main Saturnian Satellites, the Saturnian System Gravity Field, and the Orientation of Saturn’s Pole*”. In: *The Astronomical Journal* 164.5, p. 199. DOI: 10.3847/1538-3881/ac90c9. URL: https://dx.doi.org/10.3847/1538-3881/ac90c9.

Jones, G. H. et al. (2009). “Fine jet structure of electrically charged grains in Enceladus’ plume”. In: *Geophysical Research Letters* 36.16. DOI: https://doi.org/10.1029/2009GL038284. eprint: https://agupubs.onlinelibrary.wiley.com/doi/pdf/10.1029/2009GL038284. URL: https://agupubs.onlinelibrary.wiley.com/doi/abs/10.1029/2009GL038284.

Kamenik, Blaž et al. (2024). “Simulation of ice deposition in a freeze dryer condenser: A computational fluid dynamics study”. In: *Applied Thermal Engineering* 247, p. 123019. ISSN: 1359-4311. DOI: https://doi.org/10.1016/j.applthermaleng.2024.123019. URL: https://www.sciencedirect.com/science/article/pii/S1359431124006872.

Kang, Taiyoung et al. (2020). “Supercooling preservation technology in food and biological samples: A review focused on electric and magnetic field applications”. In: *Food science and biotechnology* 29, pp. 303–321.

Kantrowitz, Arthur (Sept. 1951). “Nucleation in Very Rapid Vapor Expansions”. In: *The Journal of Chemical Physics* 19.9, pp. 1097–1100. ISSN: 0021-9606. DOI: 10.1063/1.1748482. eprint: https://pubs.aip.org/aip/jcp/article-pdf/19/9/1097/18799146/1097_1_online.pdf. URL: https://doi.org/10.1063/1.1748482.

Karagiannis, A (2020). “Numerical Examination of Non-Equilibrium Condensation in Supersonic Micronozzles”. In: URL: http://resolver.tudelft.nl/uuid:abe34357-627e-4df4-92eb-73e590ab79a6.

Kelton, Ken and Alan Lindsay Greer (2010). *Nucleation in condensed matter: applications in materials and biology*. Vol. 15. Elsevier.

Kempf, Sascha et al. (2010). “How the Enceladus dust plume feeds Saturn’s E ring”. In: *Icarus* 206.2. Cassini at Saturn, pp. 446–457. ISSN: 0019-1035. DOI: https://doi.org/10.1016/j.icarus.2009.09.016. URL: https://www.sciencedirect.com/science/article/pii/S0019103509004084.

Kieffer, Susan W. et al. (2009). “A redetermination of the ice/vapor ratio of Enceladus’ plumes: Implications for sublimation and the lack of a liquid water reservoir”. In: *Icarus* 203.1, pp. 238–241. ISSN: 0019-1035. DOI: https://doi.org/10.1016/j.icarus.2009.05.011. URL: https://www.sciencedirect.com/science/article/pii/S0019103509002115.

Kirchoff, Michelle R. and Paul Schenk (2009). “Crater modification and geologic activity in Enceladus’ heavily cratered plains: Evidence from the impact crater distribution”. In: *Icarus* 202.2, pp. 656–668. ISSN: 0019-1035. DOI: https://doi.org/10.1016/j.icarus.2009.03.034. URL: https://www.sciencedirect.com/science/article/pii/S0019103509001213.

Konstantinidis, Konstantinos et al. (2015). “A lander mission to probe subglacial water on Saturn’s moon Enceladus for life”. In: *Acta Astronautica* 106, pp. 63–89. ISSN: 0094-5765. DOI: https://doi.org/10.1016/j.actaastro.2014.09.012. URL: https://www.sciencedirect.com/science/article/pii/S0094576514003610.

Kurganov, Alexander and G. Petrova (Mar. 2007). “A Second-Order Well-Balanced Positivity Preserving Central-Upwind Scheme for the Saint-Venant System”. In: *Communications in mathematical sciences* 5. DOI: 10.4310/CMS.2007.v5.n1.a6.

Lai, Der-Shaiun and Jaikrishnan Kadambi (Feb. 1993). “Generation of monodisperse droplets by spontaneous condensation of flow in nozzles”. In.

Lamanna, G. (2000). “On nucleation and droplet growth in condensing nozzle flows”. English. Phd Thesis 1 (Research TU/e / Graduation TU/e). Applied Physics and Science Education. ISBN: 90-386-1649-X. DOI: 10.6100/IR539104.

Manga, Michael and Emily Brodsky (2006). “Seismic triggering of eruptions in the far field: Volcanoes and Geysers”. In: *Annual Review of Earth and Planetary Sciences* 34.1, pp. 263–291. DOI: 10.1146/annurev.earth.34.031405.125125. eprint: https://doi.org/10.1146/annurev.earth.34.031405.125125. URL: https://doi.org/10.1146/annurev.earth.34.031405.125125.

Manka, Alexandra et al. (2012). “Freezing water in no-man’s land”. In: *Phys. Chem. Chem. Phys.* 14 (13), pp. 4505–4516. DOI: 10.1039/C2CP23116F. URL: http://dx.doi.org/10.1039/C2CP23116F.

Marcantoni, Luis F Gutiérrez et al. (2012). “High speed flow simulation using openfoam”. In: *Mecánica Computacional* 31.16, pp. 2939–2959.

Marzouki, Riadh (Oct. 2020). *Synthesis Methods and Crystallization*. Rijeka: IntechOpen. ISBN: 978-1-83880-224-0. DOI: 10.5772/intechopen.77471. URL: https://doi.org/10.5772/intechopen.77471.

Matson, Dennis L. et al. (2012). "Enceladus: A hypothesis for bringing both heat and chemicals to the surface". In: *Icarus* 221.1, pp. 53–62. ISSN: 0019-1035. DOI: https://doi.org/10.1016/j.icarus.2012.05.031. URL: https://www.sciencedirect.com/science/article/pii/S0019103512002138.

Matsuo, K. et al. (Feb. 1986). "Studies of condensation shock waves. II - Relation between condensation shock wave and condensation zone". In: *JSME International Journal Series B* 29, pp. 439–443.

Mer, Victor K. La (1952). "Nucleation in Phase Transitions." In: *Industrial & Engineering Chemistry* 44.6, pp. 1270–1277. DOI: 10.1021/ie50510a027. eprint: https://doi.org/10.1021/ie50510a027. URL: https://doi.org/10.1021/ie50510a027.

Minissale, Marco et al. (2022). "Thermal Desorption of Interstellar Ices: A Review on the Controlling Parameters and Their Implications from Snowlines to Chemical Complexity". In: *ACS Earth and Space Chemistry* 6.3, pp. 597–630. DOI: 10.1021/acsearthspacechem.1c00357. eprint: https://doi.org/10.1021/acsearthspacechem.1c00357. URL: https://doi.org/10.1021/acsearthspacechem.1c00357.

Mmarso (May 2020). *Critical radius nanoparticle*. URL: https://en.wikipedia.org/wiki/File:Critical_radius1.svg.

Moore, Michael J (1973). "Predicting the fog-drop size in wet-steam turbines". In: *Wet steam*.

Moses, C. A. and G. D. Stein (Sept. 1978). "On the Growth of Steam Droplets Formed in a Laval Nozzle Using Both Static Pressure and Light Scattering Measurements". In: *Journal of Fluids Engineering* 100.3, pp. 311–322. ISSN: 0098-2202. DOI: 10.1115/1.3448672. eprint: https://asmedigitalcollection.asme.org/fluidsengineering/article-pdf/100/3/311/5633230/311_1.pdf. URL: https://doi.org/10.1115/1.3448672.

Nakajima, M. and A. Ingersoll (2016). "Controlled boiling on Enceladus. 1. Model of the vapor-driven jets". In: *Icarus* 272, pp. 309–318.

Neumann, W. and Kruse A. (Aug. 2019). "Differentiation of Enceladus and Retention of a Porous Core". In: *The Astrophysical Journal* 882.1, p. 47. DOI: 10.3847/1538-4357/ab2fcf. URL: https://dx.doi.org/10.3847/1538-4357/ab2fcf.

Nicholson, Philip D. et al. (1996). "Observations of Saturn's Ring-Plane Crossings in August and November 1995". In: *Science* 272.5261, pp. 509–515. DOI: 10.1126/science.272.5261.509. eprint: https://www.science.org/doi/pdf/10.1126/science.272.5261.509. URL: https://www.science.org/doi/abs/10.1126/science.272.5261.509.

Nimmo, F. et al. (July 2014). "Tidally Modulated Eruptions on Enceladus: Cassini ISS Observations and Models". In: *The Astronomical Journal* 148.3, p. 46. DOI: 10.1088/0004-6256/148/3/46. URL: https://dx.doi.org/10.1088/0004-6256/148/3/46.

Oosthuizen, P.H. and W.E. Carscallen (1997). *Compressible Fluid Flow*. McGraw-Hill series in aeronautical and aerospace engineering. McGraw-Hill. ISBN: 9780071154260. URL: https://books.google.nl/books?id=3OMnPwAACAAJ.

Ostwald, Wilhelm (1897). "Studien über die bildung und umwandlung fester körper: 1. Abhandlung: Übersättigung und überkaltung". In: *Zeitschrift für physikalische Chemie* 22.1, pp. 289–330.

Peeters, P. et al. (2002). "The nucleation behavior of supercooled water vapor in helium". English. In: *Journal of Chemical Physics* 117.12, pp. 5647–5653. ISSN: 0021-9606. DOI: 10.1063/1.1501885.

Pellicer, J. et al. (July 2002). "On the experimental values of the water surface tension used in some textbooks". In: *American Journal of Physics* 70.7, pp. 705–709. ISSN: 0002-9505. DOI: 10.1119/1.1477431. eprint: https://pubs.aip.org/aapt/ajp/article-pdf/70/7/705/7530867/705_1_online.pdf. URL: https://doi.org/10.1119/1.1477431.

Pollack, J. and Cuzzi J. (1980). "Scattering by Nonspherical Particles of Size Comparable to a Wavelength: A New Semi-Empirical Theory and Its Application to Tropospheric Aerosols". In: *Journal of Atmospheric Sciences* 37.4, pp. 868–881. DOI: 10.1175/1520-0469(1980)037<0868:SBNPOS>2.0.CO;2. URL: https://journals.ametsoc.org/view/journals/atsc/37/4/1520-0469_1980_037_0868_sbnpos_2_0_co_2.xml.

Porco, C. et al. (2006). "Cassini Observes the Active South Pole of Enceladus". In: *Science* 311.5766, pp. 1393–1401. DOI: 10.1126/science.1123013. eprint: https://www.science.org/doi/pdf/10.1126/science.1123013. URL: https://www.science.org/doi/abs/10.1126/science.1123013.

Porco, C. et al. (July 2014). “How the geysers, tidal stresses, and thermal emission across the south polar terrain of Enceladus are related”. In: *The Astronomical Journal* 148.3, p. 45. DOI: 10.1088/0004-6256/148/3/45. URL: https://dx.doi.org/10.1088/0004-6256/148/3/45.

Porco, C. et al. (Mar. 2018). “Enceladus’ Plume Temporal Variability from Analysis of Cassini ISS Images”. In: *49th Annual Lunar and Planetary Science Conference*. Lunar and Planetary Science Conference, 2003, p. 2003.

Postberg, F. et al. (2008). “The E-ring in the vicinity of Enceladus: II. Probing the moon’s interior—The composition of E-ring particles”. In: *Icarus* 193.2. Saturn’s Icy Satellites from Cassini, pp. 438–454. ISSN: 0019-1035. DOI: https://doi.org/10.1016/j.icarus.2007.09.001. URL: https://www.sciencedirect.com/science/article/pii/S0019103507003867.

Postberg, F. et al. (2018). “Plume and Surface Composition of Enceladus”. In: *Enceladus and the Icy Moons of Saturn*. Ed. by Paul M. Schenk et al., p. 129. DOI: 10.2458/azu_uapress_9780816537075-ch007.

Postberg, Frank et al. (July 2009). “Sodium salts in E-ring ice grains from an ocean below the surface of Enceladus”. In: *Nature* 459, pp. 1098–101. DOI: 10.1038/nature08046.

Potter, M.C. and C.W. Somerton (2013). *Schaum’s Outline of Thermodynamics for Engineers, 3rd Edition*. Schaum’s Outline Series. McGraw Hill LLC. ISBN: 9780071830836. URL: https://books.google.nl/books?id=S4IlAgAAQBAJ.

Pruppacher, Hans R et al. (1998). *Microphysics of clouds and precipitation*.

Qiu, Guodong et al. (2024). “Development and validation of a numerical model for frost growth based on nucleation theory”. In: *International Journal of Heat and Mass Transfer* 221, p. 125137. ISSN: 0017-9310. DOI: https://doi.org/10.1016/j.ijheatmasstransfer.2023.125137. URL: https://www.sciencedirect.com/science/article/pii/S0017931023012826.

Ren, Jiahui et al. (2025). “Numerical simulation for ice crystal formation in high-pressure supersonic humid air low-temperature flow”. In: *International Communications in Heat and Mass Transfer* 164, p. 108928. ISSN: 0735-1933. DOI: https://doi.org/10.1016/j.icheatmasstransfer.2025.108928. URL: https://www.sciencedirect.com/science/article/pii/S0735193325003549.

Rovira-Navarro, Marc et al. (2022). “The Tides of Enceladus’ Porous Core”. In: *Journal of Geophysical Research: Planets* 127.5. e2021JE007117 2021JE007117, e2021JE007117. DOI: https://doi.org/10.1029/2021JE007117. eprint: https://agupubs.onlinelibrary.wiley.com/doi/pdf/10.1029/2021JE007117. URL: https://agupubs.onlinelibrary.wiley.com/doi/abs/10.1029/2021JE007117.

Schmidt, Jürgen et al. (2008a). “Formation of enceladus’ dust plume”. In: *Nature* 451.7250, pp. 685–687.

Schmidt, Jürgen et al. (2008b). “Slow dust in Enceladus’ plume from condensation and wall collisions in tiger stripe fractures”. In: *Nature* 451.7179, pp. 685–688.

Schoenfeld, Ashley M. and An Yin (2024). “Quantifying tidal versus non-tidal stresses in driving time-varying fluxes of Enceladus’ plume eruptions”. In: *Icarus* 415, p. 116064. ISSN: 0019-1035. DOI: https://doi.org/10.1016/j.icarus.2024.116064. URL: https://www.sciencedirect.com/science/article/pii/S0019103524001246.

Shapiro, Ascher H (1953). “The dynamics and thermodynamics of compressible fluid flow”. In: *New York: Ronald Press*.

Skrotzki, J. et al. (2013). “The accommodation coefficient of water molecules on ice – cirrus cloud studies at the AIDA simulation chamber”. In: *Atmospheric Chemistry and Physics* 13.8, pp. 4451–4466. DOI: 10.5194/acp-13-4451-2013. URL: https://acp.copernicus.org/articles/13/4451/2013/.

Smith, B. et al. (1982). “A New Look at the Saturn System: The Voyager 2 Images”. In: *Science* 215.4532, pp. 504–537. DOI: 10.1126/science.215.4532.504. eprint: https://www.science.org/doi/pdf/10.1126/science.215.4532.504. URL: https://www.science.org/doi/abs/10.1126/science.215.4532.504.

Solar System Exploration, NASA (Aug. 2013). *Enceladus: Facts & Figures*. Retrieved May 31, 2023. URL: https://web.archive.org/web/20131016093801/http://solarsystem.nasa.gov/planets/profile.cfm?Object=Sat_Enceladus%5C&Display=Facts.

Solé, R.V. (2011). *Phase Transitions*. Phase Transitions v. 16. Princeton University Press. ISBN: 9780691150758. URL: https://books.google.nl/books?id=8RcLuv-Ll2kC.

Spahn, Frank et al. (2006). “E ring dust sources: Implications from Cassini’s dust measurements”. In: *Planetary and Space Science* 54.9. Physics of Dusty Rings, pp. 1024–1032. ISSN: 0032-0633. DOI: https://doi.org/10.1016/j.pss.2006.05.022. URL: https://www.sciencedirect.com/science/article/pii/S0032063306001024.

Spencer, J. and F. Nimmo (2013). “Enceladus: An Active Ice World in the Saturn System”. In: *Annual Review of Earth and Planetary Sciences* 41.1, pp. 693–717. DOI: 10.1146/annurev-earth-050212-124025.

Spencer, J. et al. (2006). “Cassini Encounters Enceladus: Background and the Discovery of a South Polar Hot Spot”. In: *Science* 311.5766, pp. 1401–1405. DOI: 10.1126/science.1121661. eprint: https://www.science.org/doi/pdf/10.1126/science.1121661. URL: https://www.science.org/doi/abs/10.1126/science.1121661.

Spencer, J. et al. (2009). “Enceladus: An Active Cryovolcanic Satellite”. In: *Saturn from Cassini-Huygens*. Ed. by Michele K. Dougherty et al. Dordrecht: Springer Netherlands, pp. 683–724. ISBN: 978-1-4020-9217-6. DOI: 10.1007/978-1-4020-9217-6_21. URL: https://doi.org/10.1007/978-1-4020-9217-6_21.

Teolis, Ben D. et al. (2017). “Enceladus Plume Structure and Time Variability: Comparison of Cassini Observations”. In: *Astrobiology* 17.9. PMID: 28872900, pp. 926–940. DOI: 10.1089/ast.2017.1647.

Thomas, P.C. et al. (2007). “Shapes of the saturnian icy satellites and their significance”. In: *Icarus* 190.2. Deep Impact Mission to Comet 9P/Tempel 1, Part 2, pp. 573–584. ISSN: 0019-1035. DOI: https://doi.org/10.1016/j.icarus.2007.03.012. URL: https://www.sciencedirect.com/science/article/pii/S0019103507001315.

Tokar, R. L. et al. (2009). “Cassini detection of Enceladus’ cold water-group plume ionosphere”. In: *Geophysical Research Letters* 36.13. DOI: https://doi.org/10.1029/2009GL038923. eprint: https://agupubs.onlinelibrary.wiley.com/doi/pdf/10.1029/2009GL038923. URL: https://agupubs.onlinelibrary.wiley.com/doi/abs/10.1029/2009GL038923.

Travis, B.J. and G. Schubert (2015). “Keeping Enceladus warm”. In: *Icarus* 250, pp. 32–42. ISSN: 0019-1035. DOI: https://doi.org/10.1016/j.icarus.2014.11.017. URL: https://www.sciencedirect.com/science/article/pii/S0019103514006459.

van der Hijden, Nick (2021). “Linking Enceladus’ plume characteristics to the crevasse properties”. In: URL: http://resolver.tudelft.nl/uuid:6d340c03-8c63-4a7c-86b5-864df805f651.

van Leer, Bram (1979). “Towards the ultimate conservative difference scheme. V. A second-order sequel to Godunov’s method”. In: *Journal of Computational Physics* 32.1, pp. 101–136. ISSN: 0021-9991. DOI: https://doi.org/10.1016/0021-9991(79)90145-1. URL: https://www.sciencedirect.com/science/article/pii/0021999179901451.

Veeraghattam, Vijay K. et al. (July 2014). “The Sticking of Atomic Hydrogen on Amorphous Water Ice”. In: *apj* 790.1, 4, p. 4. DOI: 10.1088/0004-637X/790/1/4.

Verbiscer, A. et al. (2007). “Enceladus: Cosmic Graffiti Artist Caught in the Act”. In: *Science* 315.5813, pp. 815–815. DOI: 10.1126/science.1134681. eprint: https://www.science.org/doi/pdf/10.1126/science.1134681. URL: https://www.science.org/doi/abs/10.1126/science.1134681.

Vidmachenko, A. P. (Dec. 2023). “Seasonal activity of “tiger” stripes on Saturn’s moon Enceladus”. In: *Annali D’italia* 50, p. 35. DOI: 10.5281/zenodo.10432556.

Viisanen, Y. et al. (Sept. 1993). “Homogeneous nucleation rates for water”. In: *The Journal of Chemical Physics* 99.6, pp. 4680–4692. ISSN: 0021-9606. DOI: 10.1063/1.466066. eprint: https://pubs.aip.org/aip/jcp/article-pdf/99/6/4680/19217766/4680_1_online.pdf. URL: https://doi.org/10.1063/1.466066.

Villanueva, G. L. et al. (2023). *JWST molecular mapping and characterization of Enceladus’ water plume feeding its torus*. arXiv: 2305.18678 [astro-ph.EP].

Waite, J. Hunter et al. (2017). “Cassini finds molecular hydrogen in the Enceladus plume: Evidence for hydrothermal processes”. In: *Science* 356.6334, pp. 155–159. DOI: 10.1126/science.aai8703. eprint: https://www.science.org/doi/pdf/10.1126/science.aai8703. URL: https://www.science.org/doi/abs/10.1126/science.aai8703.

Waite J. H., Jr. et al. (July 2009). “Liquid water on Enceladus from observations of ammonia and ^{40}Ar in the plume”. In: *nat* 460.7254, pp. 487–490. DOI: 10.1038/nature08153.

Warming, R. F. and Richard M. Beam (1976). “Upwind Second-Order Difference Schemes and Applications in Aerodynamic Flows”. In: *AIAA Journal* 14.9, pp. 1241–1249. DOI: 10.2514/3.61457. eprint: https://doi.org/10.2514/3.61457. URL: https://doi.org/10.2514/3.61457.

Wegener, P. (1963). “Condensation phenomena in nozzles”. In: *Heterogeneous Combustion Conference*. DOI: 10.2514/6.1963-509. eprint: https://arc.aiaa.org/doi/pdf/10.2514/6.1963-509. URL: https://arc.aiaa.org/doi/abs/10.2514/6.1963-509.

Wegener, P.P. and L.M. Mack (1958). “Condensation in Supersonic and Hypersonic Wind Tunnels”. In: ed. by H.L. Dryden and Th. von Kármán. Vol. 5. Advances in Applied Mechanics. Elsevier, pp. 307–447. DOI: https://doi.org/10.1016/S0065-2156(08)70022-X. URL: https://www.sciencedirect.com/science/article/pii/S006521560870022X.

Wen, C. et al. (2020). “Non-equilibrium condensation of water vapour in supersonic flows with shock waves”. In: *International Journal of Heat and Mass Transfer* 149, p. 119109. ISSN: 0017-9310. DOI: https://doi.org/10.1016/j.ijheatmasstransfer.2019.119109. URL: https://www.sciencedirect.com/science/article/pii/S0017931019323816.

Wölk, Judith and Reinhard Strey (Nov. 2001). “Homogeneous Nucleation of H 2 O and D 2 O in Comparison: The Isotope Effect †”. In: *Journal of Physical Chemistry B - J PHYS CHEM B* 105, pp. 11683–11701. DOI: 10.1021/jp0115805.

Wölk, Judith et al. (Sept. 2002). “Empirical function for homogeneous water nucleation rates”. In: *The Journal of Chemical Physics* 117.10, pp. 4954–4960. ISSN: 0021-9606. DOI: 10.1063/1.1498465. eprint: https://pubs.aip.org/aip/jcp/article-pdf/117/10/4954/19234936/4954_1_online.pdf. URL: https://doi.org/10.1063/1.1498465.

Wyslouzil, Barbara E. and Judith Wölk (Sept. 2016). “Overview: Homogeneous nucleation from the vapor phase—The experimental science”. In: *The Journal of Chemical Physics* 145.21, p. 211702. ISSN: 0021-9606. DOI: 10.1063/1.4962283. eprint: https://pubs.aip.org/aip/jcp/article-pdf/doi/10.1063/1.4962283/15519309/211702_1_online.pdf. URL: https://doi.org/10.1063/1.4962283.

Yeoh, Seng Keat et al. (2015). “On understanding the physics of the Enceladus south polar plume via numerical simulation”. In: *Icarus* 253, pp. 205–222.

Young, J. B. (July 1992). “Two-Dimensional, Nonequilibrium, Wet-Steam Calculations for Nozzles and Turbine Cascades”. In: *Journal of Turbomachinery* 114.3, pp. 569–579. ISSN: 0889-504X. DOI: 10.1115/1.2929181. eprint: https://asmedigitalcollection.asme.org/turbomachinery/article-pdf/114/3/569/5940625/569_1.pdf. URL: https://doi.org/10.1115/1.2929181.

— (1980). *Spontaneous Condensation of Steam in Supersonic Nozzles: Part 1, Nucleation and Droplet Growth Theory; Part 2, Numerical Methods and Comparison with Experimental Results*. CUED/A-Turbo/TR pts. 1-2. University of Cambridge, Department of Engineering. URL: https://books.google.nl/books?id=Zu5fuAAACAAJ.

Zucker, R.D. and O. Biblarz (2019). *Fundamentals of Gas Dynamics*. Wiley. ISBN: 9781119481706. URL: https://books.google.nl/books?id=kreuDwAAQBAJ.

A

Pseudo-code for Deposition Model

```
for each cell in the domain:
Compute local saturation properties;

// Skip if no meaningful population or volume fraction
if (ρ * N * V_cell < 1.0) or (f < 1e-12):
    Set f = 0;
    Set N = 0;

// Proceed only if temperature is within valid deposition range
if (T < T_crit) and (T < T_sat(p)) and (T ≥ 173.16):
    Compute local solid grain properties;

    // Compute grain radius if valid population and volume fraction exist
    if (ρ * N * V_cell ≥ 1.0) and (f ≥ 1e-12):
        Compute r_droplet from f and N;
    else:
        Set r_droplet = 0;

    // Compute critical radius only in supersaturated conditions
    if (S ≥ 1):
        Compute r_crit;
    else:
        Set r_crit = 0;

    // Condensation and grain growth only if radius conditions are met
    if (r ≥ r_crit) and (r ≥ 2.75e-10):
        Compute droplet growth rate;
        Compute active component of mass source term;
    else:
        Set growth rate and source term to zero;

    // Nucleation only if critical radius is physical
    if (r_crit ≥ 2.75e-10):
        Compute nucleation rate (γ_nuc);

        // Suppress nucleation if less than one event per cell per timestep
        if (J * V_cell * Δt < 1.0):
            Set J = 0;
    else:
        Set r_crit = 0;
        Set J = 0;

    Compute remaining source terms;

else:
    // Outside valid temperature range: no condensation
    Set all condensation terms to zero;
```